Accretion characteristics in intermediate polars

Thesis

Faculty of Science, The Open University

Accretion Characteristics In Intermediate Polars

Tracey Louise Parker M.Phys.

Submitted for the degree of Doctor of Philosophy

April 2006

ProQuest LLC.
789 East Eisenhower Parkway
P.O. Box 1346
Ann Arbor, MI 48106 – 1346

CONTENTS

LIST OF FIGURES v

LIST OF TABLES viii

ABSTRACT ix

1 Introduction 1
1.1 X-ray Binaries . . . 1
1.1.1 Low Mass X-Ray Binaries (LMXB) . . . 2
1.1.2 High Mass X-Ray Binaries (HMXB) . . . 8
1.1.3 Microquasars . . . 10
1.2 Cataclysmic Variables (CVs) . . . 12
1.2.1 CV Characteristics and subtypes . . . 13
1.2.2 The period gap . . . 19
1.3 Magnetic CVs . . . 20
1.3.1 Polars (AM Her systems) . . . 21
1.3.2 Intermediate Polars . . . 23
1.4 Geometry of magnetic accretion in intermediate polars . . . 25
1.4.1 Magnetic Fields in WDs . . . 25
1.4.2 The Equation of motion in magnetic CVs . . . 26
1.4.3 The accretion flow . . . 30
1.4.4 Propeller System . . . 32
1.5 Table of known Intermediate Polars . . . 33
1.5.1 Notes to table . . . 33
1.5.2 References to Table . . . 36

2 X-ray Orbital Modulations in Intermediate Polars 37
2.1 Introduction . . . 37
2.2 Orbital Modulation . . . 38
2.3 Observations . . . 40
2.4 Data Reduction . . . 43
2.5 Results . . . 53
2.6 Discussion of Results . . . 90
2.6.1 V1025 Cen . . . 90
2.6.2 BG CMi . . . 90
2.6.3 V1223 Sgr . . . 91
2.6.4 V2400 Oph . . . 92
2.6.5 AO Psc . . . 92
2.6.6 YY Dra . . . 93
2.6.7 LS Peg . . . 93
2.6.8 V405 Aur . . . 94
2.6.9 V2306 Cyg . . . 94
2.6.10 FO Aqr . . . 95
2.6.11 PQ Gem . . . 96
2.6.12 V709 Cas . . . 96

2.6.13 TV Col . . . 97
2.6.14 TX Col . . . 97
2.6.15 AE Aqr . . . 98
2.6.16 V1062 Tau . . . 98
2.7 Summary of results . . . 98
2.8 Overall Discussion . . . 101

3 Magnetic model 105
3.1 Introduction . . . 105
3.2 An overview of HyDisc . . . 106
3.2.1 Basics . . . 106
3.2.2 Gas physics . . . 107
3.2.3 When a magnetic field is involved . . . 109
3.2.4 Introducing k . . . 112
3.2.5 Estimating Parameters . . . 113
3.2.6 Scaling k – constant density and size scale . . . 114
3.2.7 Scaling k – non-constant density and size scale . . . 115
3.2.8 Calculating B from k . . . 116
3.3 Two Versions of HyDisc . . . 118
3.4 Previous Uses of the Model . . . 118
3.5 My Work . . . 124

4 Accretion Flows from the Magnetic Model 125
4.1 Introduction . . . 125
4.2 n^3 model . . . 126
4.2.1 Discussion of accretion flows for the n^3 model . . . 139
4.2.2 Overall Conclusions . . . 141
4.3 n^6 model . . . 142
4.3.1 Discussion of accretion flows for the n^6 model . . . 155
4.3.2 Overall Conclusions . . . 157
4.3.3 n^3 model vs n^6 model . . . 157
4.4 Equilibrium Flows . . . 161
4.4.1 Data for equilibrium models . . . 166
4.4.2 Discussion . . . 169
4.5 Dipole angle variations . . . 177
4.6 Conclusions . . . 181

5 Doppler Tomography of Intermediate Polars 183
5.1 Introduction . . . 183
5.2 Background to the technique of Doppler tomography . . . 184
5.3 Assumptions that must be considered for mCV Doppler Tomography . . . 188
5.4 n^3 model Doppler Tomograms . . . 189
5.4.1 Discussion of the Doppler tomograms for the n^3 model . . . 202
5.4.2 Overall Conclusions . . . 213
5.5 n^6 model Doppler Tomograms . . . 218
5.5.1 Discussion of the Doppler Tomograms for the n^6 model . . . 230
5.5.2 Overall Conclusions . . . 239
5.6 Equilibrium Tomograms . . . 243
5.6.1 Discussion of equilibrium tomograms for the n^3 model . . . 248

5.6.2 Discussion of equilibrium tomograms for the n^6 model 250
5.7 Dipole angle and Inclination angle variations for a n^3 field 251
5.7.1 Discussion of Dipole angle and inclination angle variations 261
5.7.2 Overall Conclusions 268
5.8 Published observations of Doppler Tomography of IPs 269
5.9 Observational tomograms vs. model tomograms 287
5.9.1 V1025 Centauri 287
5.9.2 V405 Aurigae 291
5.10 Overall Chapter Conclusion 294

6 Conclusions and Further Work 297
6.1 Conclusions 297
6.2 Further Work 299

APPENDICES 302

A Current Information on Known Intermediate Polars 302
A.0.1 Aqr1 302
A.0.2 AE Aquarii 303
A.0.3 FO Aquarii 304
A.0.4 V1425 Aquilae 304
A.0.5 XY Arietis 305
A.0.6 V405 Aurigae 305
A.0.7 HT Camelopardaris 306
A.0.8 BG Canis Minoris 306
A.0.9 V709 Cassiopeia 307
A.0.10 V1025 Centauri 307
A.0.11 RR Chamaeleontis 308
A.0.12 DD Circinus 308
A.0.13 DW Cnc 308
A.0.14 TV Columbae 309
A.0.15 TX Columbae 309
A.0.16 UU Columbae 310
A.0.17 AP Crucis 310
A.0.18 V2306 Cyg 311
A.0.19 YY Draconis 312
A.0.20 PQ Geminorum 312
A.0.21 DQ Herculis 313
A.0.22 V533 Herculis 314
A.0.23 V795 Herculis 314
A.0.24 EX Hydrae 315
A.0.25 V2400 Oph 315
A.0.26 LS Pegasi 316
A.0.27 GK Persei 317
A.0.28 AO Piscium 317
A.0.29 HZ Puppis 318
A.0.30 VZ Pyxidis 318
A.0.31 WX Pyxidis 319
A.0.32 V1223 Sagittari 320

A.0.33 V697 Scorpii 320
A.0.34 V1062 Tauri 321
A.0.35 V381 Velorum 321
A.0.36 RX J0944.5+0357 321
A.0.37 1RXS J154814.5-452845 322
A.0.38 RX J0153.3+7446 323
A.0.39 RX J1039.7-0507 323
A.0.40 RX J2133.7+5107 323
A.0.41 HS0943+1404 324
A.0.42 Recently discovered IPs 324

B RXTE and ASCA Data Reduction 325
B.1 Archival data from *RXTE* and *ASCA* 325
B.2 *RXTE* data reduction 327
B.3 *ASCA* data reduction 329
B.3.1 *RXTE* data reduction in comparison with *ASCA* Data Reduction . 332

LIST OF FIGURES

1.1 Artist impression of a LMXB 4
1.2 Colour-colour diagram of a Z source and an atoll source 6
1.3 Combined colour-colour diagram of atoll sources 7
1.4 Artist impression of a Super Giant X-ray Binary 9
1.5 Artist impression of a Be star XRB 11
1.6 Comparison of a microquasar and a quasar 12
1.7 Artist impression of a cataclysmic variable 13
1.8 Artist impression of a Polar 21
1.9 Schematic view of an accretion column 22
1.10 Artist impression of an Intermediate Polar 25

2.1 Example ASCA 0.7-2keV source lightcurve and background lightcurve . . . 47
2.2 Example ASCA 2-10keV source lightcurve and background lightcurve . . . 48
2.3 Example RXTE 2-4keV source lightcurve and background lightcurve 48
2.4 Example RXTE 4-6keV source lightcurve and background lightcurve 49
2.5 Example RXTE 6-10keV source lightcurve and background lightcurve . . . 49
2.6 Example RXTE 10-20keV source lightcurve and background lightcurve . . . 49
2.7 Orbital Phase diagram 50
2.8 Orbital phase folded *ASCA* lightcurves and power spectra of the *ASCA* lightcurves of each object 54
2.1 (a) V1025 Cen 55
2.1 (b) BG CMi 56
2.1 (c) V1223 Sgr 57
2.1 (d) V2400 Oph 58
2.1 (e) AO Psc 59
2.1 (f) YY Dra 60
2.1 (g) LS Peg 61
2.1 (h) V405 Aur (1) 62
2.1 (i) V405 Aur (2) 63
2.1 (j) V2306 Cyg 64
2.1 (k) FO Aqr 65
2.1 (l) PQ Gem (1) 66
2.1 (m) PQ Gem (2) 67
2.1 (n) TV Col 68
2.1 (o) TX Col 69
2.1 (p) AE Aqr 70
2.1 (q) V1062 Tau 71
2.2 Orbital phase folded *RXTE* lightcurves and power spectra of the *RXTE* lightcurves of each object 72
2.2 (a) V1025 Cen 73
2.2 (b) BG CMi 74
2.2 (c) V1223 Sgr 75
2.2 (d) V2400 Oph 76
2.2 (e) AO Psc 77
2.2 (f) YY Dra 78

2.2 (g) V405 Aur 79
2.2 (h) FO Aqr 80
2.2 (i) PQ Gem 81
2.2 (j) V709 Cas 82
2.2 (k) TV Col 83
2.2 (l) TX Col 84
2.2 (m) V1062 Tau 85
2.3 Orbital modulation depths measured from (a) the *ASCA* data and (b) the *RXTE* data 89

3.1 Forces acting on a particle 'P' in the co-rotating reference frame of a binary system 107
3.2 Radius of Curvature 110
3.3 Field lines frozen into a plasma blob 111
3.4 Diamagnetic plasma blob 111

4.1 Accretion flows for the n^3 model ($k(r) \propto r^{-3}$) 127
4.2 Accretion flows for the n^6 model ($k(r) \propto r^{-6}$) 143
4.3 Spin phase variations – Stream Accretion 159
4.4 Spin phase variations – Disk Accretion 160
4.5 Spin phase variations – Propeller accretion 160
4.6 Spin phase variations – Ring accretion 160
4.7 Accretion flows at equilibrium spin period 161
4.8 Plot of equilibrium spin periods of intermediate polars for the n^3 model . . 173
4.9 Plot of equilibrium spin periods of intermediate polars for the n^6 model . . 174
4.10 Spin vs. orbital period plot with accretion characteristics for real IPs as assessed from the simulated n^3 data 175
4.11 Spin vs. orbital period plot with accretion characteristics for real IPs as assessed from the simulated n^6 data 176
4.12 Accretion flows for increasing magnetic co-latitude 177

5.1 Emission line profile from an accretion disk 185
5.2 How positional coordinates translate to Doppler coordinates 186
5.3 How Line profiles map to a Doppler image 187
5.4 A schematic layout of a Doppler tomogram 190
5.5 Tomograms for the n^3 model ($k(r) \propto r^{-3}$) 190
5.6 Overall result features from the n^3 field tomograms 216
5.7 Tomograms for the n^6 model ($k(r) \propto r^{-6}$) 218
5.8 Overall result features from the n^6 field tomograms 243
5.9 Tomograms from the simulated equilibrium accretion flows for the n^3 model 244
5.10 Tomograms from the simulated equilibrium accretion flows for the n^6 model 246
5.11 Doppler Tomograms for magnetic co-latitudes for varying inclination angles 251
5.12 Stroboscopic Doppler tomograms of FO Aqr 271
5.13 Doppler tomograms of BG CMi and PQ Gem 274
5.14 Doppler tomograms of AO Psc and Fo Aqr 276
5.15 Doppler tomograms of BG CMi and PQ Gem 277
5.16 Doppler tomograms of RX 1712 and EX Hya 277
5.17 Doppler tomogram of RX 1238-38 278
5.18 Doppler tomogram of EX Hya 278

5.19 Doppler tomograms of V405 Aur by Still et al. (1998) 280
5.20 Doppler tomograms of V405 Aur by Szkody et al. (2000) 281
5.21 Doppler tomogram of AE Aqr 283
5.22 Doppler tomogram of V1025 Cen 285
5.23 Orbital-cycle tomograms of V1025 Cen for selected ranges of beat-phase cycle phase 286
5.24 Doppler tomogram of RXJ0757.0+6306. 287
5.25 Model tomograms of V1025 Cen 290
5.26 Doppler tomogram of V1025 Cen 290
5.27 Model tomograms of V405 Aur 292
5.28 Doppler tomograms of V405 Aur 293
5.29 Doppler tomograms of V405 Aur 293

LIST OF TABLES

2.1 ASCA observations 40
2.2 RXTE observations 41
2.3 Orbital ephemerides 51
2.4 Orbital modulation depths for *ASCA* data 86
2.5 Orbital modulation depths for *RXTE* data 87
2.6 Modulation depth comparison data 100

4.1 Accretion flow distribution for the n^3 model 142
4.2 Accretion flow distribution for the n^6 model 158
4.3 Data tables of Equilibrium Spin Periods 166
4.4 Average percentage of material escaping/accreting the model for each accretion mechanism for equilibrium n^3 runs. 171
4.5 Average percentage of material escaping/accreting the model for each accretion mechanism for equilibrium n^6 runs 171

5.1 Published Doppler maps of IPs 270

Accretion Characteristics In Intermediate Polars

Tracey Louise Parker M.Phys.
April 2006

Faculty of Science, The Open University
Submitted for the degree of Doctor of Philosophy

This thesis concerns the class of interacting binaries known as intermediate polars (IPs). These are semi-detached magnetic cataclysmic variable systems in which a red dwarf secondary transfers material via Roche lobe overflow onto a white dwarf (WD). The magnetic field of the white dwarf ($\sim 10^6$ to 10^7Gauss) plays an important part in determining the type of accretion flow from the secondary. In chapter 1 I discuss binary systems in general, moving on to a more in depth look at Intermediate polars (IPs), their geometry and characteristics, ending with a brief look at all known IPs to date.

In the first part of the thesis I present an analysis of the X-ray lightcurves in 16 IPs in order to examine the possible cause of the orbital modulation. I show that X-ray orbital modulation is widespread amongst IPs, but not ubiquitous. The orbital modulation is most likely due to photoelectric absorption in material at the edge of the accretion disk. Assuming a random distribution of inclination angles, the fact that such a modulation is seen in seven systems out of sixteen studied (plus two eclipsing systems) implies that modulations are visible at inclination angles in excess of 60°. It is also apparent that these modulations can appear and disappear on timescales of ~years or months in an individual system, which may be evidence for precessing, tilted accretion disks.

In the second half of the thesis I use a particle hydrodynamical code known as HyDisc, to investigate the accretion flows in IPs, as a function of parameter space for two dipole models. One where we assume that the density and size scale of the blobs being accreted are constant which we refer to as the n^6 model, and the other where the size scale and density of the accreted blobs are not constant refered to as the n^3 model. I show that the accretion flow can take the form of an accretion disk, accretion stream, propeller accretion and ring accretion for the n^3 model and stream and disk accretion in the n^6 model, depending on the magnetic field strength, orbital period and spin period of the system.

IPs violate some of the assumptions of Doppler tomography, such as motion parallel to the orbital plane due to the accretion curtains and that accretion flow is constant throughout the orbital period, making the analysis more complex and the interpretations of observational tomograms flawed as they are based on false assumptions. We have therefore generated simulated tomograms from the simulated accretion flows so we can compare them with real tomograms from observed data and begin to interpret them better. In this way we can discover the nature of the accretion flows in real systems. We show that some of the tomogram features that are produced are in good agreement with those of published observations, but there are also a number of new features which arise corresponding to each of the accretion mechanisms of disks, streams, propellers, weak propellers and ring systems.

Chapter 1

Introduction

In this chapter I introduce the characteristics of the class of binaries which this thesis concentrates on, namely the intermediate polar systems. I start by giving the reader a brief background to the class of X-ray binaries. In section 1.3 I introduce the sub group of X-ray binaries known as magnetic cataclysmic variables of which IPs are a member. I present a detailed discussion of IPs, looking at their general characteristics, how they are classified, the proposed accretion mechanisms and their geometry. In the final part of this chapter I concentrate on individual systems and give a list all known IPs to date giving a brief description of the main characteristics of each system.

1.1 X-ray Binaries

The brightest Galactic X-ray sources are X-ray binary systems. These systems consist of a companion star and a compact object (a neutron star or black hole) which is the end point of stellar evolution. These pairs of stars produce X-rays if the stars are close enough together that material is pulled off the normal star by the gravity of the dense, compact object or if the compact star is able to accrete a fraction of the stellar wind emitted by

its companion. The X-rays come from the area around the compact object where the material that is falling toward it is heated to very high temperatures. X-ray binaries are conventionally divided into two classes, Low Mass X-ray Binaries (LMXB) and High Mass X-ray Binaries (HMXB), according to the nature of the companions to the compact object (Bradt & McClintock (1983)). This in turn dictates the type of accretion that occurs.

1.1.1 Low Mass X-Ray Binaries (LMXB)

Evolution

The standard evolutionary scenario for the majority of LMXBs begins with an initial binary containing a massive OB star and a low-mass star with a wide separation (Webbink et al. (1983); Kalogera & Webbink (1998 1996)). The massive primary star expands rapidly and transfers material faster than it can be swept up by the secondary, giving unstable mass transfer within the system. The transferred material over flows the primary's Roche lobe and the primary's envelope then engulfs both the stars. This is known as the common envelope phase and causes the two stars to spiral inward. During this process, energy is transfered to the envelope resulting in its ejection. This energy comes from the orbital energy of the system thus shrinking the orbital period (Paczynski (1976)) giving an evolved short-period binary. The massive star continues its evolution rapidly to the point of becoming a supernova (SN), resulting in the formation of a post-SN binary (PSNB) consisting of a neutron star or black hole with a low-mass companion, which turns into a LMXB when the latter attains Roche lobe contact, because of either nuclear evolution or orbital decay by gravitational radiation and magnetic braking. This, in turn, may produce a recycled millisecond pulsar at the end of mass transfer.

Characteristics

The LMXB consist of a compact object accreting matter from a companion whose mass is less than or comparable to that of the Sun $< \sim 2M_{\odot}$ (Hayakawa (1985)). These companions are cool, reddish type K or M stars and do not have strong winds. The orbit is compact enough for Roche lobe overflow to take place see Figure 1.1. The Roche lobe is essentially the volume around a star, inside which material is gravitationally bound to that star. The Roche lobe is an equipotential surface, that is a surface on which the potential is constant i.e where the gradient of the potential field is zero. The point at which the two Roche lobes of a star meet is known as the L_1 or inner Lagrangian point and is the point where the gravitational forces of each of the two stars are equal. If the binary system is close, the contact point can occur near the surface of the normal star so that some of the material in the star's outer edges (on the edge of the Roche lobe) finds itself no longer bound to the star. This "unbound" material flows from the companion to the compact object. Thus a "funnel point" is created for significant mass to flow out toward the compact star for accretion. The material that is "stripped" off the companion will tend to form a disk around the compact object, rather than falling directly in, as the material has angular momentum from its orbital motion. Since that angular momentum cannot just disappear, the material will orbit the compact object, forming an accretion disk. The material in the accretion disk will then slowly spiral in to the compact object, losing that angular momentum as it goes. This process heats up the material in the disk to temperatures of over 10^6K. It is this hot material that emits X-rays.

Subtypes of LMXB

- **LMXB Pulsars** - Most known accreting X-ray pulsars are members of High Mass X-ray Binaries (see next section), however there are a few systems which are LMXBs.

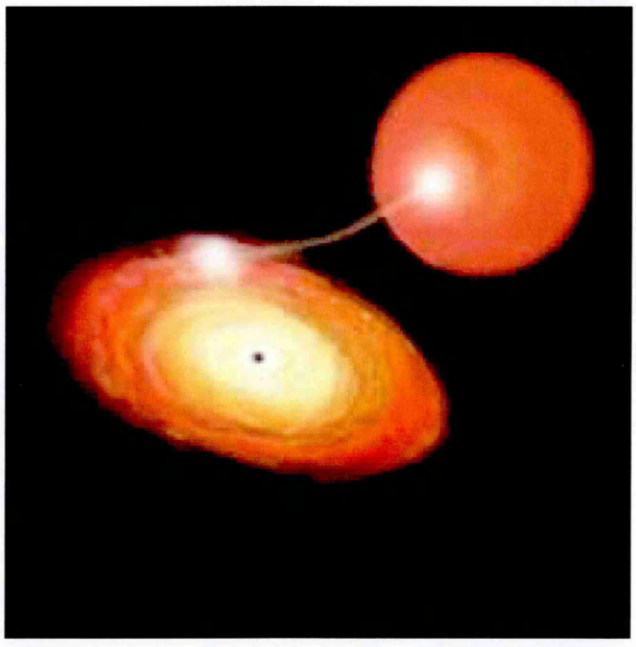

Figure 1.1: Artist impression of a LMXB, artist unknown

The compact object in the binary system is a neutron star with a strong magnetic field ($\sim 10^{12}$ Gauss) which affects the mass transfer from the companion star. In pulsars the strong magnetic field strength means that generally no accretion disk will form, though in some a thin disk is present. Matter streaming from the L_1 point is gravitationally captured by the neutron star when it comes close, it is then trapped by the magnetic field and from then on, it can only move following the magnetic field lines. They take it to the magnetic poles of the neutron star. Since all the field lines are converging there, the gas density is very large, the particles are decelerated and crash against the neutron star surface. In both cases, the particles release their energy in the form of X-rays that emerge in a narrow beam in the direction of the magnetic axis. In X-ray pulsars, the spin axis and the magnetic axis of the neutron star are not well aligned, so as the neutron star rotates about its spin axis, its magnetic poles will periodically sweep into view. As one pole and then the other comes into our line

of sight the beams are seen flashing by as the neutron star rotates. Thus they are seen to pulse in and out of our line of sight and so are hence referred to as an X-ray pulsar (see Bildsten et al. (1997)). The same situation arises in radio pulsars but they are powered by the neutron stars' rotation rather than by accretion and involve **isolated** neutron stars.

- **Atoll and Z sources** - Low mass X-ray binaries that contain neutron stars with weak magnetic fields can be divided into two classes, Z sources and atoll sources (Hasinger & van der Klis (1989)) based upon changes in both their spectral and timing properties as their luminosity changes. Z sources get their name from the Z-shaped track they produce on an X-ray colour-colour diagram, i.e. plots of a "hard" colour against a "soft" colour usually form the Z shape that is traced on time scales of hours to days, see Figure 1.2 (Wijnands (2001)). Atoll sources on the other hand, can be divided into two spectral states, a hard, low-luminosity 'island' or a soft, high-luminosity 'banana'. They trace a U-shaped or a C shaped track as the source evolves between the island and the banana on timescales of weeks to months, see Figure 1.2. Having said that, Muno et al. (2002) took colour-colour diagrams over a five year span with the Rossi X-ray Timing Explorer satellite of eight atoll and four Z sources and found that the clear distinction between the colour-colour diagrams of the atoll and Z sources we have just described was an artefact of incomplete sampling and that in fact the atoll sources traced out three-branched colour-colour patterns similar to the tracks of Z sources. However, Muno explains that the atoll sources trace this pattern over a large range of luminosity and on much longer time scales than the Z sources, and show much harder spectra when they are faint therefore keeping the two classes separate as a whole and not defined as one. Similar conclusions were reported independently by Gierliński & Done (2002); see Figure 1.3 for the combined

colour-colour diagram of atoll sources.

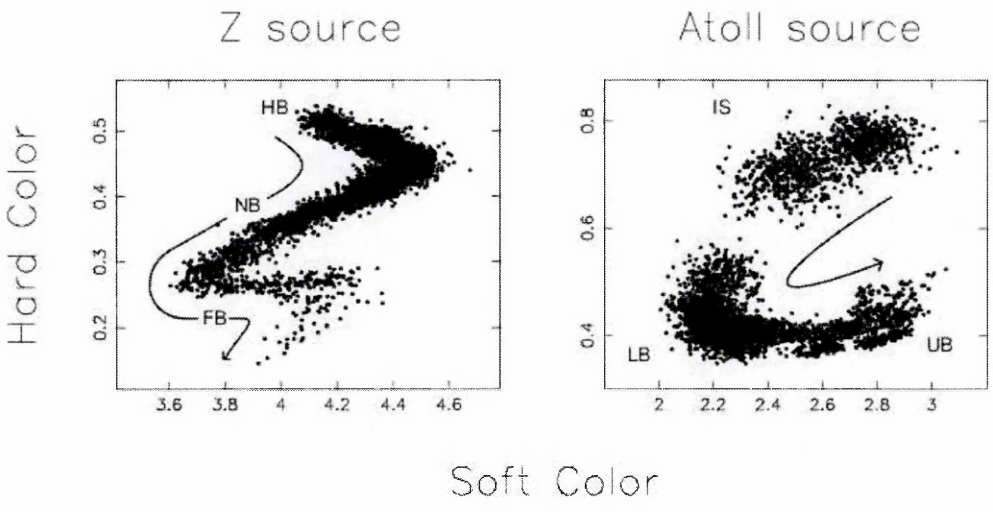

Figure 1.2: Colour-colour diagrams of Z (left) and atoll (right) sources. HB = horizontal branch, NB= normal branch, FB = flowing branch, LB = lower banana, UB = upper banana and IS = island. The figure was taken from Wijnands (2001)

- **Bursters** - X-ray bursts are thought to be due to thermonuclear flashes on the surfaces of neutron stars. They occur when the unburned matters ignite via unstable H/He burning on the surface of the neutron star and can last from a few seconds to a few minutes. The resulting spike in X-ray luminosity is called an X-ray burst. They are further classified as either type I or type II. Typical type I bursts have a faster rise than decay and the average energy of the X-rays decreases as the burst smoothly decays. Typical type II bursts stop abruptly without changing the average photon energy. For reviews about the X-ray bursts and the physics involved, see e.g. Bildsten (1998) and Lewin et al. (1993)

- **Quasi-Periodic Oscillations** - QPOs were discovered by the European X-ray Ob-

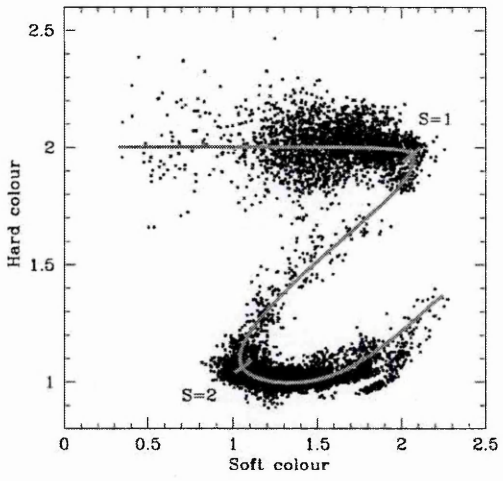

Figure 1.3: A Combined colour-colour diagram of atoll sources. The colours of three sources were linearly transformed so as to co-align all three systems at turns on the track. The sources clearly define a Z-shaped track (figure from Gierliński & Done (2002))

servatory Satellite (EXOSAT). QPOs are likely to originate very close to the neutron star member of the binary and related to the neutron star spin rate. As such they provide a new means of studying the neutron star properties, the effects of general relativity and the dynamics of mass accretion. Observationally a great deal remains to be done in detecting kilohertz QPOs in more X-ray binaries and studying their systematic behaviours (see van der Klis (1998) for a recent review).

- **Soft X-ray transients**

  Also known as X-ray novae, they consist typically of a K-type subgiant or dwarf that transfers mass to a black hole via an accretion disk. In some cases the compact object is a neutron star, but black holes appear to be more common. During quiescence mass accumulates in the disk, during outburst most of this disk falls into the black hole. The outburst in the disk is due to thermal-viscous instability, a similar mechanism to that of dwarf novae. During outburst the source brightens by about 12 magnitudes.

The system fades back to quiescence in a few months and disappears from the X-ray sky. During the outburst, the X-ray spectrum is "soft" (dominated by low-energy X-rays), hence the name Soft X-ray transients; for a review see White (1994).

1.1.2 High Mass X-Ray Binaries (HMXB)

Evolution

HMXBs are descendants of massive binaries. They contain large, massive blue stars (spectral types O and B) with masses in the range 10-40$M_{\odot}$ and a neutron star companion (in some occasions a black hole). Accretion generally occurs through capture of the companion's stellar wind, driven by its radiation pressure although contributions from Roche lobe overflow may also occur. The high mass companion sheds mass through a wind which flows isotropically from the companion, so a portion of it cannot help but run into the compact object. The potential energy of this fraction of the wind being captured is converted into X-rays see (Urpin et al. (1998)).

Conventionally HMXBs can be further divided into two subtypes (van Paradijs (1983)): those in which the primary is a giant or a supergiant and those in which the primary is a Be star, (see Liu et al. (2000)).

Subtypes of HMXB

- **OB Supergiant XRB** - When a massive star reaches the last stages of its life, after having consumed most of the hydrogen in its core, the outer layers begin expanding and the star grows enormously, becoming a supergiant. As it grows, the gravitational pull on its outer layers decreases. It is then when the gravitational attraction of an orbiting compact object in a close orbit can start distorting the shape of the supergiant and the dragging of matter towards the compact star begins. The technical

name for these systems is Supergiant Roche-lobe Overflow X-ray Binaries. As the supergiant expands, it increases in brightness. The outer layers of its atmosphere are continuously bombarded by very energetic photons. They push a stream of particles along with them. These particles dissipate into the empty space around the star at very high velocities. This is called a radiation-driven stellar wind. Sometimes, a neutron star in a rather distant orbit can pick up some of these particles and start the accretion process, becoming a weak X-ray source. These systems are known as Supergiant Stellar Wind X-ray Binaries (see Corbet (1986) for an overview of the OB supergiant systems), see Figure 1.4 for an artist impression of a SGXB.

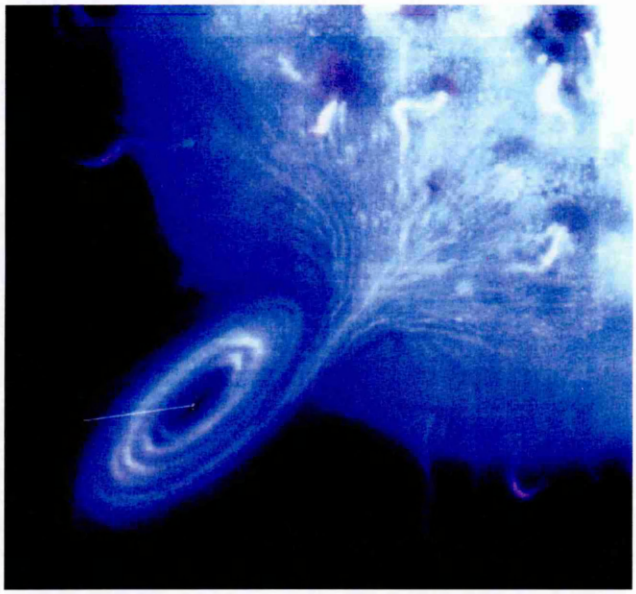

Figure 1.4: Artist impression of a SGXB, artist unknown

- **Be-star XRB** - Be-star X-ray binaries were first recognised as a class by Maraschi et al. (1976). If a neutron star is orbiting a star which has not reached the supergiant phase, it will not be able to steal any material from it and will not become an X-

ray source. The exception is the case when the normal star is surrounded by a circumstellar disk of material. These are the Be stars (stars of spectral class B which show emission lines), which are surrounded by matter that, for some reason, has escaped from the star. It is not very clear why circumstellar disks are formed. It is believed that it is related to internal disturbances caused by very rapid rotation. If the binary system contains a Be star and a neutron star, the orbit of the neutron star may take it inside the circumstellar disk at some moment. Then the neutron star will be able to accrete material and become an X-ray source, see Figure 1.5. Another possibility is that the Be star undergoes a sudden ejection of matter which will also turn on the X-ray source. As these sources are only on from time to time, they are known as X-ray transients (periods of enhanced X-ray emission which typically last longer than a week, but which are not representative of the usual observed emission from the source). Observed in the infrared, optical or ultraviolet, only the Be star is seen, the neutron star can only be seen in the X-ray range. More than 50 HMXB Be star systems are known, making them the most numerous class of HMXBs (see, van den Heuvel & Rappaport (1987) for a review)

1.1.3 Microquasars

Microquasars (Mirabel & Rodriguez (1998)) are a subset of XRBs found in both LMXB and HMXB. The compact object is either a black hole or neutron star. Like other XRBs the more-massive object is pulling material from its stellar companion. The material circles the massive object in an accretion disk before being pulled into it. The accretion disk is heated by viscous dissipation caused by friction which creates temperatures hot enough to cause the material to emit hard X-rays and gamma-rays.

It is magnetic processes that are believed to accelerate material from the compact

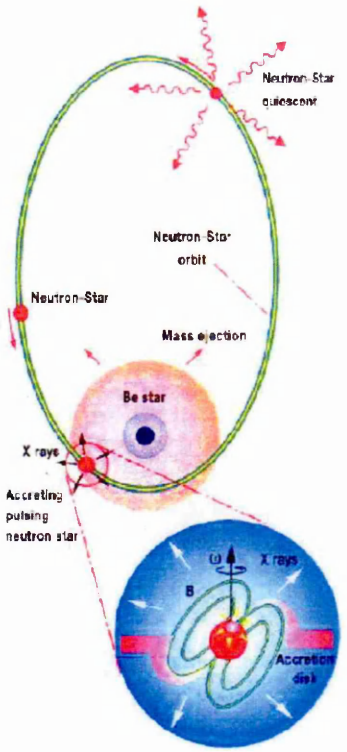

Figure 1.5: Artist impression of a Be star XRB, artist unknown

object into jets that are usually seen in these systems. The gravitational energy of the supermassive black hole is capable of accelerating the jets of subatomic particles to speeds approaching that of light. In some, blobs of material have been seen to move at apparent speeds greater than that of light, known as superluminal motion. The relativistic electrons produce synchrotron radiation from spiralling in the magnetic fields detected at radio wavelengths.

Microquasars behave like extragalactic quasars but at a reduced scale, hence their name. In microquasars the black hole is only a few solar masses instead of several million or billion solar masses; the accretion disk has mean thermal temperatures of several million degrees instead of several thousand degrees; and the particles ejected at relativistic speeds can travel up to distances of a few light years only, instead of several million light years

as in giant radio galaxies (Mirabel & Rodriguez (1998)). See Figure 1.6 for a comparison between the two systems.

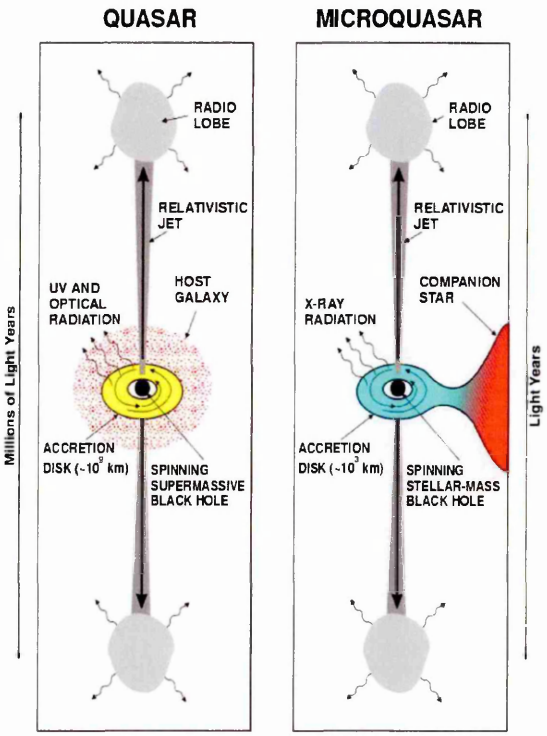

Figure 1.6: Image of a microquasar (left) compared to that of a quasar (right) taken from Mirabel & Rodriguez (1998)

1.2 Cataclysmic Variables (CVs)

There are probably over a million cataclysmic variables in the Galaxy, but only those close to our Sun (several hundred of them) with the nearest systems at distances of ~100 parsecs (300 light years) from Earth have been detected in X-rays so far. This is because CVs are fairly faint in X-rays; they are just above the coronal X-ray sources and far below the X-ray binaries in terms of how powerful their X-ray emissions are.

1.2.1 CV Characteristics and subtypes

CVs are close semi-detached binary systems consisting of a white dwarf (WD)(the primary), a collapsed star with a mass similar to the Sun in a volume similar to the Earth, and a low-mass, late type red dwarf companion (the secondary) a more or less normal star like our own Sun. By semi-detached we mean that the surface of the low mass star is defined by the Roche lobe. As the star evolves it fills the Roche lobe and transfers material between the two stars via the inner-Lagrangian point L_1. They are typically small with a binary system roughly the size of the Earth-moon system with an orbital period in the range of typically 1-10hrs, see Figure 1.7.

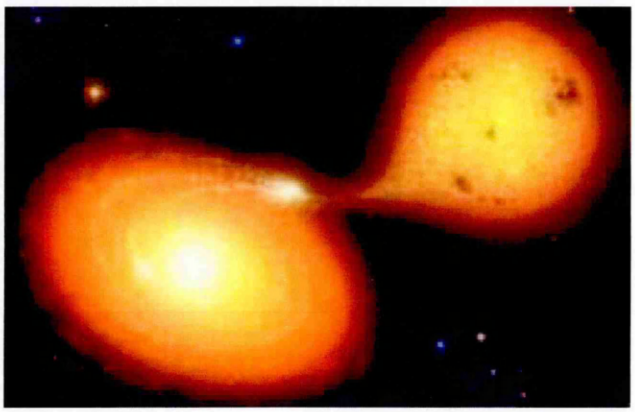

Figure 1.7: Artist impression of a cataclysmic variable by Mark Garlick, space-art.co.uk

Because of angular momentum conservation, the in-falling gas can't plunge directly onto the surface of the WD and so forms a disk - an accretion disk with the WD at its centre. The gas in the disk spirals down towards the WD radiating its gravitational potential energy as a result of viscous dissipation in the form of heat. This usually makes the accretion disk outshine both the red dwarf and the WD in visible light, see Warner (1995a) and Poyner (2001) for a comprehensive review of all types of CVs.

There are two principal energy sources in a cataclysmic variable: nuclear fusion and gravity (through accretion) .

Nuclear Energy

The material which flows onto the WD simply piles up on the surface of the WD and is rich in hydrogen since it comes from the envelope of the companion star. Hence the companion replenishes the WD's fuel supply as they have no nuclear fuel left after nuclear burning. The first material accreted compresses due to the weight of the recently added material. The compression causes the temperature and pressure of the accreted material to increase. After around 10,000 to 100,000 years of accretion, the conditions become right for nuclear burning. There is an explosion because the material is degenerate in a thin shell. The thermonuclear explosion causes the outer nuclear burning shell to be ejected leading to a Classical Nova outburst. Systems in which this process is seen to recur on a shorter timescale are known as recurrent novae.

A related class of objects is the Super Soft Sources (SSS). These are thought to be WDs accreting matter from a binary companion star with a rate sufficient to produce steady nuclear burning on the WD surface (Hasinger (1994), Kahabka & van den Heuvel (1997)).

Gravitational Energy (accretion)

The material accelerates as it falls onto the WD, at a speed of around 10,000 kilometres per second. In dwarf nova systems, the energy which powers the outbursts is gravitational in nature i.e. it comes from the energy the material gained by falling onto the WD. Dwarf nova outbursts are usually attributed to the release of gravitational energy resulting from thermal viscous instability in the accretion disk.

Since the WD is very dense, the gravitational potential energy is enormous, and some of it is converted into X-rays and optical/IR radiation during the accretion process. The efficiency of this process is typically around 0.03%. For comparison, the fusion of 4 hy-

drogen nuclei into a He nucleus has an efficiency of 0.7%. These efficiencies are much lower than those for accretion onto neutron stars ($\sim$ 10%) or black holes (up to $\sim$ 40%), observed in X-ray binary systems, but still high enough to make CVs much brighter in X-rays than typical stellar coronae.

We can show the efficiency of this process by the use of the following equations. The gravitational potential energy released by the accretion of a mass m on the surface of a body of mass M and radius R_* over a time Δt is given by:

$$\Delta E_{acc} = \frac{GM\Delta m}{R_*} \tag{1.1}$$

This energy however is immediately radiated away so the accretion luminosity is:

$$L_{acc} = \frac{\Delta E_{acc}}{\Delta t} \tag{1.2}$$

Substituting equation 1.1 into 1.2 give us:

$$L_{acc} = \frac{GM\Delta m}{R_*\Delta t} \tag{1.3}$$

As the mass Δm accretes in a time Δt, so the accretion rate denoted by $\dot{M}$ is dM/dt which is $\Delta m/\Delta t$, as the time interval becomes small. i.e:

$$L_{acc} = \frac{GM\dot{M}}{R_*} \tag{1.4}$$

The accretion efficiency, η, is defined as the accretion luminosity as a fraction of the rest mass energy, i.e:

$$L_{acc} = \eta\dot{M}c^2 \tag{1.5}$$

Combining Eq. 1.4 with Eq. 1.5 we therefore have:

$$\frac{GM\dot{M}}{R_*} = \eta \dot{M} c^2 \tag{1.6}$$

The $\dot{M}$ cancel out and if we then rearrange for η we get:

$$\eta = \frac{GM}{c^2 R_*} \tag{1.7}$$

as G and c^2 are constants we arrive at the final expression for the efficiency in terms of the mass and radius of the compact object:

$$\eta \propto \frac{M}{R_*} \tag{1.8}$$

In the accretion-dominated phase, CVs can be categorised into several different types:

1. Dwarf novae - Dwarf novae outbursts are intrinsically much less luminous events than classical nova outbursts. Their peak absolute magnitudes are at least 100 times weaker. All dwarf novae recur, with some recurring on times as short as a few weeks. They also have short durations, lasting a few days and can also exhibit a variety of unusual behaviours. Conventional dwarf novae are known as U Gem stars, but there are two other subtypes:- (Warner (1995a))

    - SU Ursae Majoris stars. These dwarf novae show two distinct kinds of outburst: normal dwarf nova outbursts, and superoutbursts, which last 5-10 times longer and are typically 0.7 magnitudes brighter than usual dwarf nova outbursts. Most superoutbursting dwarf novae have short orbital periods (less than 2 hours). During a superoutburst, an SU UMa star shows an additional modulation of the light curve, a superhump believed to arise from the hot spot where the accretion stream from the secondary collides with the accretion disk. Superhumps show up in the light curve as a modulation with a period slightly longer (a few percent)

than the orbital period, they have a much larger (~100 times) luminosity, which amounts to an amplitude of a few tenths of magnitude during superoutbursts. This is why these humps are called "super" ones. The most striking feature of the superhumps is found in its period: as noted above, the period of light variation is a few percent longer than the orbital period of the binary determined by radial velocity studies. The superhump period is believed to be due to a precessing accretion disk. At present, the existence of superhumps is considered to be the definition of a superoutburst, rather than its general outburst characteristics. It seems that the two crucial criteria for a system to show superhumps are the following: first, there must be a high rate of mass transfer through the accretion disk; and secondly, the mass-donating red star must be much less massive than the accreting WD (see Warner (1995a) and Warner (1995b) for more details).

- Z Camelopardalis (Z Cam) stars. These dwarf novae will occasionally get stuck in standstills during which their brightness is both below outburst stage and well above quiescent levels. They exhibit standstills about 0.7 magnitudes below the maximum brightness. Outbursts cease during these standstills for tens of days to years. (Warner (1995a))
- VY Sculptoris (VY Scl) stars. Also known as anti-dwarf novae, will spend most of their time in an outburst state, with occasional dips into quiescence that last for a few days.

2. Nova-like variables. The difference between the nova-like variables and dwarf novae is that nova-like variables have never been seen to undergo any outburst. The overall brightness varies only slightly about its mean level. In addition, the rate of mass transfer in the disks of nova-like variables is much higher than that in quiescent dwarf novae, and the accretion disks are thus very bright. Subtypes of nova like

variables include:-

- SW Sextantis stars. This group of stars has many unusual properties. If you observe a CV system edge-on, so that your line of sight is along the plane of the disk, you expect to see double-peaked emission lines. This is because the gas in one half of the disk is moving towards you, and its emission is thus blue-shifted, while the gas in the other half is moving away from you, and its emission is red-shifted. Despite being edge-on systems, the SW Sextantis stars have single-peaked emission lines (see Hellier (2000), Thorstensen et al. (1991) and the review by Warner (1995a)). It has been suggested that SW Sex stars may be magnetic in nature and related to intermediate polars (see section 1.3).
- AM Canum Venaticorum stars. These are an interesting group of double degenerate (2 WDs) CV systems that show permanent superhumps. They are helium-rich CVs: no hydrogen has ever been detected in any of them. They have much shorter orbital periods than the hydrogen-rich systems: the two stars of AM CVn itself whizz around each other every quarter of an hour (see reviews by Warner (1995c) and Solheim (1995)).
- Permanent Superhumpers. In many systems, which do not show eruptions, superhumps are observed. Patterson & Richman (1991) initially suggested the term 'permanent superhump' for the subclass of cataclysmic variables having quasi-periodicities slightly different from their binary orbital periods. Unlike SU UMa systems, which show this behaviour only during superoutbursts, permanent superhump systems show the phenomenon during their normal brightness state. However, their amplitudes are highly variable with typical full amplitudes at about 5-15%, sometimes even disappearing below the detection limits and from the light curves, so the term 'permanent superhump' is somewhat misleading.

During the last few years permanent superhumps have been found in almost 20 CVs. Superhumps can be either negative or positive and refer to them having periods that are either greater or smaller than that of the binary's orbital period. Positive superhumps are currently explained by the prograde precession of an elliptical accretion disk, relative to the orbit (Whitehurst (1988b), Osaki (1989), Lubow (1991)). It is proposed that negative superhumps arise when the disk also extends out of the orbital plane and the line of nodes undergoes retrograde precession due to the gravitational torque of the donor star (Harvey et al. (1995); Patterson et al. (1997); Patterson (1999); Wood et al. (2000); Murray et al. (2002)).

For the final two subtypes of CV,

3. Polars (AM Her systems)

4. Intermediate Polars (DQ Her systems)

See section 1.3.

1.2.2 The period gap

One of the most striking observed properties of cataclysmic variables, is that there are relatively few systems with an orbital period P in the range 2h$\lesssim P \lesssim$3h, usually referred to as the period gap, which cannot be explained by observational selection effects (see e.g. King (1988); Kolb (1996); Ritter (1996) for reviews). However the range of the period gap has now changed according to Katysheva & Pavlenko (2003) who put the gap closer, from 2.1 to 2.8 hours. Within this range they state that there are eighteen stars, eight are novalike magnetic systems (six polars and two intermediate polars), seven are SU UMa-type stars, two are former classical novae and one star is a novalike UX UMa-type variable.

The best explanation for this period gap was provided by Rappaport et al. (1983) and Spruit & Ritter (1983). At periods above the gap, angular momentum losses shrink the orbit, reducing the period and causing mass transfer. The secondary star is gradually forced out of thermal equilibrium and remains oversized for its mass compared with its main sequence radius. When the period reaches the upper edge of the gap, the angular momentum losses are sharply reduced. It is now able to shrink back to its main sequence radius and thus detaches from the Roche lobe, turning off mass transfer. Some angular momentum loss (e.g. via gravitational radiation) continues, and eventually reduces the binary separation (and period) to the point that the Roche lobe closes down on the star and mass transfer resumes.

1.3 Magnetic CVs

A magnetic cataclysmic variable star is a semi-detached binary system comprising a magnetic accreting WD, which has an appreciable magnetic field (up to several tens of millions of Gauss), and its mass-donating companion star. As with conventional CVs, the latter is usually, but not always, a late-type star near or on the main sequence. The binary orbital periods for such systems are most commonly between $\sim$ 80 min and several hours (see Ritter (1990) and Ritter & Kolb (2005)).

Usually magnetic X-ray emitting CVs are subdivided into Polars or AM Her systems, Intermediate polars (IPs) and DQ Herculis systems (a subset of IPs) depending on the geometry of the accretion flow (see Warner (1995a) and Patterson (1994a) for a comprehensive review of mCVs), and other parameters of the system.

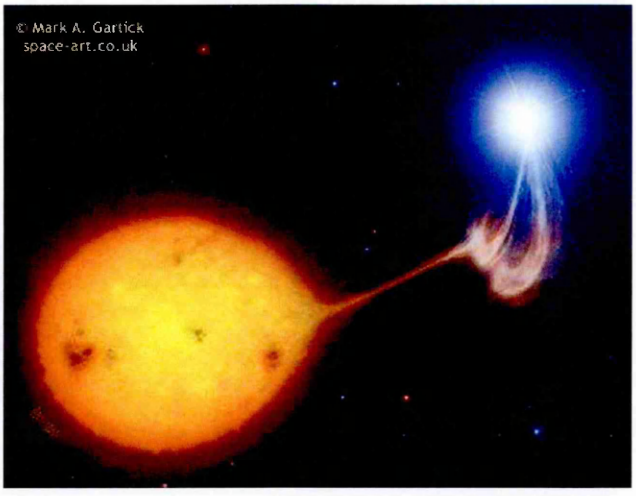

Figure 1.8: Artist impression of a polar by Mark Garlick, space-art.co.uk

1.3.1 Polars (AM Her systems)

In Polars, matter will overflow the Roche Lobe of the companion star, however, the magnetic field of the WD is strong enough to synchronise the rotation of the WD to that of the binary ($P_{spin} = P_{orb}$). Furthermore, the magnetic field is so strong, $\geq 10^7$G that no accretion disk can form. Instead, the accretion stream moves freely under gravity until a distance $\sim 10^{10}$cm from the WD, where it is thought to be threaded rather rapidly by the field and plunges straight down onto the magnetic pole or poles of the WD, see Figure 1.8. For gas flow concentrated in a stream, the ram pressure exceeds magnetic stresses over much of the binary separation. However the magnetic field takes over where the ram pressure is equal to the magnetic field pressure $P_{ram} \approx P_{mag}$ and the matter then couples directly onto the magnetic field. Until impact the material is essentially in free-fall towards the white dwarf, forming an accretion column, and thus reaching substantial velocities $\sim$ 5000kms^{-1} as it approaches the white dwarf. The collision with the surface generates a shock wave. The flux distribution from the accretion stream comprises three components:

- Hard X-ray bremsstrahlung (typically kT_{br} = 10 - 50 keV) emission by free electrons

in a post-shock region above the surface, where field lines intercept the WD atmosphere. The kinetic energy is thermalised, corresponding to energies of $\sim$ 30keV for photons, which is then radiated as hard X-rays;

- The electrons are also moving in the magnetic field and so produce cyclotron emission by spiralling around the magnetic field lines. The emission is predominantly in the optical and IR and is strongly polarised.

- The hard X-rays from the shock also irradiate and heat up the white dwarf surface below to a temperature $\sim 10^5$K producing an approximately blackbody spectrum in the UV or soft X-ray energies with kT_{bb} = 20 - 40eV. This component therefore originates from post-shock photons which are intercepted by the primary, absorbed, thermalised and remitted.

A schematic view of this process is shown in figure 1.9.

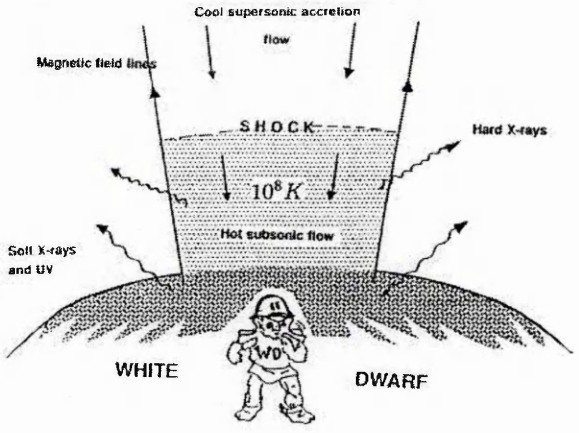

Figure 1.9: Accretion column onto a white dwarf indicating the various emission mechanisms that occur. Hard X-rays are emitted from the shock region, soft X-ray and UV emission is emitted from the surface. (Patterson (1994a))

One of the most distinctive properties of the optical light emitted by polars is that it is both linearly and circularly polarised. By observing changes in the intensity of polarised emission over the orbital cycle, the magnetic field strength of the WD and the magnetic field geometry can be discovered. For an up to date listing of polar systems see Ritter & Kolb (2005)

1.3.2 Intermediate Polars

Intermediate Polars (IPs) are systems which have weaker magnetic fields, about 10^6 to 10^7 Gauss, or wider separations between the companion star and the WD, compared to that of AM Her type systems. They are spin asynchronous systems, that is the spin period of the WD is shorter than the orbital period. The accretion flow in IPs from the secondary proceeds towards the WD in a range of ways depending on the mass-transfer rate, the field strength and WD spin period, see Figure 1.10 for an artist impression of an IP. The flow is usually assumed to be either through an accretion disk, accretion stream or some combination of both (disk overflow accretion) until it reaches the magnetospheric radius (see next section for accretion geometry). We investigate further possibilities for the accretion flow in Chapters 4 and 5. The basic accretion process onto the white dwarf in IPs is similar to that in polars, but the lower magnetic field leads to accretion over a larger area of the surface. The infalling material that originates from an accretion disk takes the form of arc-shaped accretion curtains, standing above the WD surface. At some distance from this surface, the accretion flow undergoes a strong shock, below which material settles onto the WD, releasing X-ray to optical emission as in polars. Since the magnetic axis is offset from the spin axis of the WD, this gives rise to the defining characteristic of the class, X-ray (and usually optical) emission pulsed at the WD spin period. Additionally, as the X-ray beam sweeps around the system, there is the possibility that some fraction

of the emission will be reprocessed from structures such as the companion star or bulge at the edge of an accretion disk. This will give rise to further optical emission pulsed at the lower orbital sideband of the spin frequency, i.e. the spin frequency of the white dwarf in the reference frame of the binary, also known as the beat frequency. Because the two stars move around each other, one rotation of the WD does not bring it back to the same position relative to the companion star - it always has to rotate just a little more to catch up with the companion. If radiation from the WD reflects off the red dwarf, for example, it will vary at the beat period. Several IPs show a dominant optical pulsation at this orbital sideband frequency. X-ray pulsation at the orbital sideband frequency can also arise due to an intrinsic modulation arising from pole-switching in the case of stream-fed accretion. Several IPs show this type of modulation too. Because the variations in the light of an intermediate polar can exhibit at least three periods - spin, orbital, and beat - IPs are observationally distinct from other cataclysmic variables.

Their X-ray spectra typically show strong Iron Kα emission lines and a high column density. The X-ray continuum is usually modelled in terms of thermal bremsstrahlung emission, possibly with multiple temperature components, see Cropper et al. (2000).

Hence, the following is a brief summary of the definitions which observers apply in deciding an IP candidate

- A stable optical periodicity showing up in the lightcurve, which is less than the orbital period ($P < P_{\rm orb}$)
- Coherent X-ray pulsations: usually arising from spin modulation of the WD.
- Optical periodicities: usually coincident with the X-ray periods, plus orbital sidebands.
- Circular polarisation (in some cases).

- Emission line variations: at the orbital, spin, and sometimes, sideband period(s).
- Hard ($kT \gtrsim$10 keV) thermal bremsstrahlung spectrum with lightcurves curves strongly affected by variable absorption and geometry.

About twenty confirmed IPs are now recognised with about 20 candidate systems having been proposed. They are usually detected by X-ray emission, optical emission or photometric and spectroscopic variations i.e by the presence of two modulations.

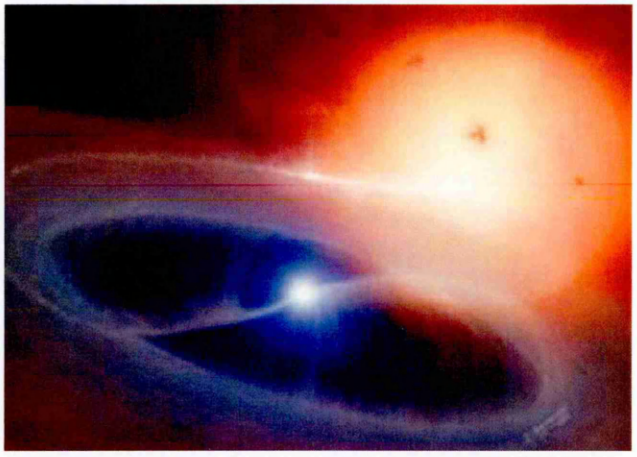

Figure 1.10: Artist impression of a intermediate polar by Mark Garlick, space-art.co.uk

DQ Her systems constitute a subset of the IPs. Observationally they are defined as rapidly rotating IPs lacking hard X-ray emission. The latter property probably results from the distance of the magnetospheric radius to the surface of the WD.

1.4 Geometry of magnetic accretion in intermediate polars

1.4.1 Magnetic Fields in WDs

The origin of magnetic fields within accreting WDs is not well understood. The intense magnetic field of the WD is believed to come from the original star which produced it.

Magnetic fields of isolated magnetic WDs are thought to be conserved during their stellar evolution from magnetic main sequence stars such as the Ap and Bp stars. About 5% of the main sequence A and B type stars display strong magnetic fields. These stars are known as the peculiar A stars, or Ap/Bp stars, as their magnetic fields lead to important chemical peculiarities (hence the "p") in their atmospheres usually with regard to the concentration of helium, which may be low, high, or variable. The Bp stars are generally considered to be a hot subgroup of the Ap stars.

Observational evidence from analysis of Zeeman spectroscopy, cyclotron spectroscopy and circular polarisation spectra shows that surface field distributions of magnetic white dwarfs tend in general to be complex and strongly nondipolar. The field topology can deviate drastically from that of a centred dipole and so are modelled by dipoles that are offset from the centre by 10-30%, (Wickramasinghe & Ferrario (2000), Schwope (1995)).

1.4.2 The Equation of motion in magnetic CVs

Accretion flow is a common phenomenon in astrophysical systems ranging from young stellar objects, interacting binaries, galaxies to galaxy clusters. When the magnetic field stress is larger than the ram pressure of the accreting material, the flow is confined to follow the magnetic-field lines. The accretion hydrodynamics in these systems are therefore dependent on the magnetic field geometry. We first start by looking at the gas dynamics in the flow. The equation of motion of the gas in a binary system can be written as:

$$\frac{\partial \mathrm{v}}{\partial t} + (\mathbf{v}\cdot\nabla)\mathbf{v} = -\nabla\Phi_{\mathrm{R}} - 2\Omega\wedge\mathbf{v} - \frac{1}{\rho}\nabla P - \frac{1}{\rho}\nabla\left(\frac{B^2}{8\pi}\right) + \frac{1}{\rho R_c}\left(\frac{B^2}{4\pi}\right)\hat{n} \qquad (1.9)$$

In order to see how this comes about we go back to first principles and consider a gas, with a velocity field $\mathbf{v}$, density ρ and temperature T, all defined as functions of position $\boldsymbol{r}$ and time t. Conservation of mass is made certain by the continuity equation:

$$\frac{\partial \rho}{\partial t} + \nabla \cdot (\rho \mathbf{v}) = 0 \tag{1.10}$$

Now the gas has a pressure P at each point due to the thermal motion of the particles. The perfect gas law, an equation of state, relates this pressure to the density and temperature of the gas and is as follows:

$$P = \frac{\rho k T}{\mu m_{\mathrm{H}}} \tag{1.11}$$

where μ is the mean molecular weight and m_{H} is the mass of a hydrogen atom.

Gradients in the pressure in the gas imply forces since momentum is transfered by this means. Conservation of momentum for each gas element then gives the Euler equation:

$$\rho \frac{\partial \mathbf{v}}{\partial t} + \rho \mathbf{v} \cdot \nabla \mathbf{v} = -\nabla P + \mathbf{f} \tag{1.12}$$

where $\mathbf{f}$ represents forces acting on the gas (unspecified at the moment), in terms of the force density, the force per unit volume.

Now any gas flow between two stars is governed by the Euler equation. Taken usually in the rotating reference frame of the binary system with orbital angular velocity Ω relative to an inertial frame, it introduces extra terms in the Euler equation to take account of the centrifugal and Coriolis forces and so equation (1.11) becomes:

$$\frac{\partial \mathbf{v}}{\partial t} + (\mathbf{v} \cdot \nabla)\mathbf{v} = -\nabla \Phi_{\mathrm{R}} - 2\Omega \wedge \mathbf{v} - \frac{1}{\rho}\nabla P \tag{1.13}$$

where $-2\Omega \wedge \mathbf{v}$ is the Coriolis force per unit mass and $-\nabla \Phi_{\mathrm{R}}$ is the gradient of the Roche potential which includes the effects of both gravitation and centrifugal force.

Euler's equation stands for a gas flow between two stars, however in IPs, we are dealing with plasma flow that feels the effects of a strong magnetic field. There are a number of effects produced by the field acting on the plasma. If the plasma has sufficiently high

electrical conductivity, then the plasma and the magnetic field move together. The following equations determine the conditions under which the gas follows the motion of the magnetic field, or the reverse in that the magnetic field is dragged around by the gas. We consider the magnetic forces on a plasma:

The magnetic field, $\mathbf{B}$, is directed by Maxwell's equation.

$$\nabla \cdot \mathbf{B} = \mathbf{0}, \tag{1.14a}$$

$$\nabla \wedge \mathbf{B} = \frac{1}{c}\frac{\partial \mathbf{E}}{\partial t} + \frac{4\pi}{c}\mathbf{j} \tag{1.14b}$$

with $\mathbf{E}$ = electric field and $\mathbf{j}$ = current density. We neglect the displacement current term ($\propto \partial\mathbf{E}/\partial t$) in astrophysics, as electric fields in the Universe do not change rapidly with time.

Each charge is subject to the Lorentz force $\mathbf{f}_{\text{mag}} = (e/c)\mathbf{v} \wedge \mathbf{B}$ (the force exerted on a charged particle in an electromagnetic field). However, we must consider 'n' charges per unit volume which gives the Lorentz force as $\mathbf{f}_{\text{mag}} = n(e/c)\mathbf{v} \wedge \mathbf{B}$. If we substitute the current density $\mathbf{j}$, defined as $\mathbf{j} = ne\mathbf{v}$ into the Lorentz force equation, we get the magnetic force density as:

$$\mathbf{f}_{\text{mag}} = \frac{1}{c}\mathbf{j} \wedge \mathbf{B}. \tag{1.15}$$

By using the second of Maxwell's equations (1.13b) without the displacement term we eliminate $\mathbf{j}$:

$$\begin{aligned} \nabla \wedge \mathbf{B} = \frac{4\pi}{c}\mathbf{j} \Longrightarrow \mathbf{j} = \frac{c}{4\pi}\nabla \wedge \mathbf{B} \\ \mathbf{f}_{\text{mag}} = \frac{1}{c}\frac{c}{4\pi}\nabla \wedge \mathbf{B} \wedge \mathbf{B} \end{aligned} \tag{1.16}$$

$$\mathbf{f}_{\text{mag}} = \frac{1}{4\pi}\nabla \wedge \mathbf{B} \wedge \mathbf{B} \tag{1.17}$$

using the vector expression $\nabla\ (A \cdot B)$ for any two vector fields, $\mathbf{A}$ and $\mathbf{B}$ we have:

$$\nabla(\mathbf{A}\cdot\mathbf{B}) = \mathbf{A}\wedge(\nabla\wedge\mathbf{B}) + (\mathbf{A}\cdot\nabla)\mathbf{B} + \mathbf{B}\wedge(\nabla\wedge\mathbf{A}) + (\mathbf{B}\cdot\nabla)\mathbf{A} \tag{1.18}$$

In this case, both fields are magnetic fields $\mathbf{B}$, so substituting $\mathbf{A}$ for $\mathbf{B}$ gives the following:

$$\nabla(\mathbf{B}\cdot\mathbf{B}) = \mathbf{B}\wedge(\nabla\wedge\mathbf{B}) + (\mathbf{B}\cdot\nabla)\mathbf{B} + \mathbf{B}\wedge(\nabla\wedge\mathbf{B}) + (\mathbf{B}\cdot\nabla)\mathbf{B} \tag{1.19}$$

If we then rearrange for the term in equation 1.17 and collect like terms, we get:

$$\begin{aligned}
\mathbf{B}\wedge(\nabla\wedge\mathbf{B}) &= \nabla(\mathbf{B}\cdot\mathbf{B}) - (\mathbf{B}\cdot\nabla)\mathbf{B} - \mathbf{B}\wedge(\nabla\wedge\mathbf{B}) - (\mathbf{B}\cdot\nabla)\mathbf{B} \\
\mathbf{B}\wedge(\nabla\wedge\mathbf{B}) + \mathbf{B}\wedge(\nabla\wedge\mathbf{B}) &= \nabla(\mathbf{B}^2) - (\mathbf{B}\cdot\nabla)\mathbf{B} - (\mathbf{B}\cdot\nabla)\mathbf{B} \\
2\mathbf{B}\wedge(\nabla\wedge\mathbf{B}) &= \nabla(\mathbf{B}^2) - 2(\mathbf{B}\cdot\nabla)\mathbf{B}
\end{aligned} \tag{1.20}$$

dividing through by 2 gives us,

$$\mathbf{B}\wedge(\nabla\wedge\mathbf{B}) = \frac{\nabla\mathbf{B}^2}{2} - (\mathbf{B}\cdot\nabla)\mathbf{B} \tag{1.21}$$

However,

$$\nabla\wedge\mathbf{B}\wedge\mathbf{B} = -\mathbf{B}\wedge(\nabla\wedge\mathbf{B}) \tag{1.22}$$

so we arrive at the final expression of:

$$\mathbf{B}\wedge(\nabla\wedge\mathbf{B}) = -\frac{\nabla\mathbf{B}^2}{2} + (\mathbf{B}\cdot\nabla)\mathbf{B} \tag{1.23}$$

Substituting 1.23 into 1.17 then gives us:

$$\mathbf{f}_{\text{mag}} = -\nabla\left(\frac{B^2}{8\pi}\right) + \frac{1}{4\pi}(\mathbf{B}\cdot\nabla)\mathbf{B} \tag{1.24}$$

Comparing this to Euler's equation (1.12), we can see that the first term on the right hand side follows a hydrostatic pressure of magnitude $B^2/8\pi$.

The second term on the right, behaves as a tension of magnitude $\mathbf{B}$ when $\mathbf{B} = (0,0,B(z))$ along the fieldlines, and we get the term $B^2/4\pi$.

Hence we arrive at the original expression stated in Eq. 1.9.

1.4.3 The accretion flow

In IPs, the accretion flow from the secondary proceeds towards the WD in a range of ways depending on the mass-transfer rate, the field strength and WD spin period. As noted earlier, the flow is usually either through an accretion disk, accretion stream or some combination of both (disk overflow accretion) until it reaches the magnetospheric radius. The inward spread of the accretion disk undergoing Keplerian rotation, will eventually be halted by the magnetic field at some radius R_{in} (the inner disk radius). R_{in} is the point at which the magnetic field removes angular momentum from the disk at a greater rate than viscous stresses, at which point it encounters a magnetic field strong enough to control the flow of material. From here, the matter streams from the inner edge of the disk along the magnetic field lines onto the poles of the WD, forming arc-shaped accretion curtains. At some distance from the surface, the accretion flow undergoes a strong shock, below which material settles onto the WD, releasing X-rays as it cools.

If the material accretes directly from an accretion stream, the proportion falling onto each pole of the WD will vary according to the rotation phase of the WD. Stream-fed (or disk overflow) accretion gives rise to X-ray emission that varies with the beat period

$$\frac{1}{P_{\rm beat}} = \frac{1}{P_{\rm spin}} - \frac{1}{P_{\rm orb}}$$

In order to understand the nature of the accretion flow, it is necessary to define some characteristic radii. The co-rotation radius, circularisation radius, inner disk and magne-

tospheric radius are all very close in terms of distance from the WD. The Magnetospheric Radius ($R_{\rm M}$), is the radius at which magnetic effects are able to overcome the ram pressure of the stream material. It is therefore approximately the same as R_{in}. Disk plasma can then thread onto the magnetic field lines from any point along its inner edge. The Co-rotation Radius ($R_{\rm co}$), is the radius at which the magnetic field rotates at the same rate as the local Keplerian frequency. It is where the angular velocity on a Keplerian orbit around the central accreting star equals the rotational angular velocity of this star. Hence, the time it takes to complete one Keplerian orbit at $R_{\rm co}$ is the same as the rotational period of the WD. The Circularisation Radius ($R_{\rm circ}$), is the radius at which a stream from L_1 point would first orbit the WD.

The spin rate of a magnetic WD accreting via a disk reaches an equilibrium when the rate at which angular momentum is accreted by the WD is balanced by the braking effect of the magnetic torque on the disk close to $R_{\rm in}$. Many models of this process find however that the point at which the accretion disk is disrupted ($R_{\rm in}$) is very close to the WD co-rotation radius ($R_{\rm co}$). The relation $R_{\rm in} \sim R_{\rm co}$ implies that a small magnetosphere results in fast equilibrium rotation as we expect for a magnetic system with a truncated accretion disk $R_{\rm in} \sim R_{\rm co} \ll R_{\rm circ}$. However the deciding criterion for the formation of a disk is whether or not there is room for the accreting gas stream to circulate without interference from the magnetic field, i.e., whether $R_{\rm circ} > R_{\rm mag}$ or not. Hence for IPs with sufficiently short orbital periods, the WD magnetic field is likely to prevent the formation of an accretion disk, and channel the in-falling matter on to large fractions of the WD surface. We investigate the conditions under which this occurs in Chapter 4. Most IP systems have spin periods of order 10-20min, and there is a strong tendency to observe $P_{\rm spin} \approx 0.1 P_{\rm orb}$. This relation is equivalent to the condition $R_{\rm circ} \approx R_{\rm co}$. Hence we have two distinct modes of mass transfer onto the WD: (i) if the magnetic moment is too small

to prevent formation of an accreting disk ($R_{\rm mag} < R_{\rm circ}$), then magnetically controlled accretion will be restricted to the region from the inner edge of the disk $R_{\rm in}$, down to the WD surface; (ii) if the magnetic moment is sufficiently large, no accretion disk can form ($R_{\rm mag} > R_{\rm circ}$) and the process of mass accretion is determined by the location of the threading region. As noted above, we investigate this process via simulations in Chapters 4 and 5.

1.4.4 Propeller System

In a propeller system such as AE Aquarii, the magnetic CV with the shortest spin period (33s) and one of the longest orbital periods (9.88hr), the WD spin period is observed to be lengthening at such a rate that the loss of spin energy far exceeds radiative output of the system. Doppler tomography reveals that AE Aquarii is actually centrifugally ejecting most of the matter transferred to it from the secondary. The high rotational motion of the field lines compensates for the weak magnetic field and produces a large torque which expels the material.

At the magnetospheric radius of $R_{\rm mag} \sim 10^{10}$cm, the accreting plasma couples to the magnetic field lines which are effectively fixed to the WD and therefore co-rotate with the WD. Hence the plasma is forced to co-rotate with the WD as well when it arrives at $R_{\rm mag}$. If $R_{\rm mag}$ just equals the co-rotation radius, then the angular velocity the plasma acquires at $R_{\rm mag}$ is just the Keplerian one, i.e the centrifugal and gravitational forces are in equilibrium. If $R_{\rm mag}$ is larger than the co-rotation radius, then the angular velocity the plasma acquires is larger than the local Keplerian value. If this is the case centrifugal forces dominate and the plasma is accelerated away from the WD. This is the propeller effect (see Wynn et al. (1997) and Meintjes & Venter (2005)), and we also investigate this further in Chapters 4 and 5 via accretion simulations.

1.5 Table of known Intermediate Polars

The following tables give a current list of identified Intermediate Polars. For a detailed description of each of these systems see appendix A.

1.5.1 Notes to table

1. *Equatorial Position.* Whenever possible, the J2000 coordinates of the IPs as measured in the Space Telescope Guide Star reference frame. The right ascension is given to the nearest 0.01s, while the declination is given to the nearest 0.1s; for objects that are very faint optically or not visible, the coordinates are given to a lesser accuracy. The internal accuracy of the Guide Star Catalogue is 0.4" in the north, and 0.6" in the south (Taff et al. 1990). For faint novae, the coordinates are taken from Duerbeck (1987), or from the literature (for recent novae), and are precessed to the J2000 equinox. For IPs 1 RXS J154814.5-452845 and RX J1039.7-0507 the right ascension and declination was taken from SIMBAD as they were not found in the Space Telescope Guide Star reference catalogue. The IP WGA J1958.2+3232 was found in neither of the two so the co-ordinates were taken from Israel et al. (1998).

2. *Magnitude.* For Novae, the primary sources are Duerbeck (1987), while for the non-novae, the catalogue of Ritter & Kolb (1998) is the prime source. When no other references to brightness were available, the GCVS values were used.

   Magnitude Definition

   B Johnson B

   V Johnson V

   J SRC J (unfiltered IIIa-J)

Table of known Intermediate Polars

Name	Alternative Name	Position (1) Equatorial	Oribtal Period(hr)	Spin Period(s)	Dist (pc)	V (2) Magnitude	Inc i	References
AE Aquarii	-	$20^h40^m09.02^s - 00°52'15.5''$	9.88	33.08	100±30	9.8-11.8	$50° < i < 70°$	(1)
FO Aquarii	H2215−086	$22^h17^m55.43^s - 08°21'04.6''$	4.85	1254	~ 400	13-14	~65°	(2)
V1425 Aquilae	Nova Aquilae 1995	$19^h05^m26.67^s - 01°42'14.0''$	6.14	5190	3.0±0.4	7.5-<19	-	(3),(4)
XY Arietis	H0253+193	$02^h56^m08.10^s + 19°26'34.0''$	6.06	206	270±100	13.5J-17.6J	$80° < i < 87°$	(5)
V405 Aurigae	RX J0558.0+5353	$05^h57^m59.29^s + 53°53'44.9''$	4.15	545	-	14.6	-	(6)
HT Camelopardaris	RX J0757.0+6306	$07^h57^m01.33^s + 63°06'01.4''$	1.43	515.1	-	~ 17.8	-	(7)
V709 Cassiopeiae	RX J0028.8+5917	$00^h28^m48.87^s + 59°17'21.8''$	5.34	312.8	-	~ 14	-	(8)
BG Canis Minoris	3A0729+103	$07^h31^m28.98^s + 09°56'22.6''$	3.23	913	-	14.3-15.4	55°- 75°	(9)
V1025 Centauri	RX J1238−38	$12^h38^m16.45^s - 38°42'46.2''$	1.41	2146.6	-	16.1	-	(10)
DD Circinus	H0857-242	$14^h23^m23.46^s - 69°40'45.3''$	2.34	670	-	20.1	~70°	(11)
DW Cancri	FBS 0756+164	$07^h58^m53.07^s + 16°16'45.4''$	1.43	2315	~ 200	14.8	-	(43)
TV Columbae	A0526−328	$05^h29^m25.44^s - 32°49'04.5''$	5.49	1911	368^{+17}_{-15}	13.6-14.1	~70°	(12)
TX Columbae	1H0542−407	$05^h43^m20.22^s - 41°01'55.2''$	5.72	1911	-	14.5B-15.8B	< 30°	(13),(14)
UU Columbae	RX J0512.2−3241	$05^h12^m13.12^s - 32°41'38.8''$	3.45	863.5	>740	17.25B-18.2B	-	(15)
AP Crucis	Nova Crucis 1936	$12^h31^m20.34^s - 64°26'24.3''$	5.12	1837	-	~ 18	-	(16),(17)
V2306 Cyg	WGA J1958.2+3232	$19^h58^m14.40^s + 32°32'42.0''$	4.35	733	-	16	-	(18),(19)
YY Draconis	3A1148+719	$11^h43^m38.34^s + 71°41'20.4''$	3.96	529	155±35	10.6B-16.7B	42° ± 5°	(20),(21)
PQ Geminorum	RE0751+14	$07^h51^m17.39^s + 14°44'24.6''$	5.2	834	-	14.1-14.5	-	(22)
DQ Herculis	Nova Herculis 1934	$18^h07^m30.38^s + 45°51'31.7''$	4.65	71.1	-	1.3-18.08	86.5°	(21),(24)
V533 Herculis	Nova Herculis 1963	$18^h14^m20.51^s + 41°51'22.8''$	3.53	63.63	-	-	-	(25)

0

Continuation Table of known Intermediate Polars

Name	Alternative Name	Position (1) Equatorial	Oribtal Period(hr)	Spin Period(s)	Dist (pc)	V (2) Magnitude	Inc i	References
V795 Herculis	PG 1711+336	$17^h12^m56.09^s + 33°31'21.4''$	2.60	1172	-	-	-	(26)
EX Hydrae	4U1228−29	$12^h52^m24.40^s - 29°14'56.7''$	1.64	4021.6	65±11	10.0-14.1	∼77 °	(27),(28)
V2400 Oph	RX J1713.6−2414	$17^h12^m36.45^s - 24°14'44.6''$	3.42	927	-	14.2-14.6	∼10 °	(29)
LS Pegasi	S193	$21^h51^m57.93^s + 14°06'53.8''$	4.2	1776	-	12-14	30°	(30)
GK Persei	Nova Persei 1901	$03^h31^m12.00^s + 43°54'15.7''$	47.92	351	470	0.2-13.9	$46° < i < 73°$	(31)
AO Piscium	H2252−035	$22^h55^m17.97^s - 03°10'40.4''$	3.59	805	∼ 400	13.3-15.0	∼60°	(32)
HZ Puppis	-	$08^h03^m22.79^s - 28°28'28.9''$	5.11	1212	-	7.7p-17.0B	-	(33)
VZ Pyxidis	H0857-242	$08^h59^m19.89^s - 24°28'55.1''$	1.78	-	-	11-17	-	(34)
WX Pyxidis	1E 0830.9-2238	$08^h33^m5.75^s - 22°48'32.6''$	6-9	1560	-	17.5	-	(44)
RR Chamaeleontis	Nova Chamaeleontis 1953	$13^h26^m23.44^s - 82°19'43.4''$	3.37	1950	-	18.4	-	(35)
V1223 Sagittari	4U1851−31	$18^h55^m02.24^s - 31°09'48.5''$	3.37	745.6	∼ 600	12.3-<16.8	16°- 40 °	(33),(36)
V697 Scorpii		$17^h51^m21.83^s - 37°24'55.2''$	4.49	11916	-	20.0	-	(11)
V1062 Tauri	H0459+246	$05^h02^m27.50^s + 24°45'22.7''$	9.95	3720	> 500	15.1B-16.1B	-	(37)
V381 Velorum		$10^h16^m58.90^s - 41°03'44.6''$	2.233	7320	-	-	-	(38)
-	1 RXS J154814.5−452845	$15^h48^m14.50^s - 45°28'46.0''$	9.37	693	-	14.6	-	(39)
-	RX J1039.7-0507	$10^h39^m47.00^s - 05°06'58.1''$	1.57	1444	-	-	-	(40)
-	RX J0944.5+0357	$09^h44^m31.80^s + 03°58'06.1''$	3.58	2162	-	16.3/16.5	30°-60°	(41)
-	RX J0524+42	$05^h24^m30.52^s + 42°44'50.4''$	2.617	8160	-	-	-	(42)
Aqr1	2236+0052	$22^h38^m43.80^s + 01°08'20.6''$	3.23	403.7	-	18.5	-	(11)
-	RX J0153.3+7446	$01^h53^m20.94^s + 74°46'21.7''$	3.94	1414	-	16	30°-60°	(45)
-	RX J2133.7+5107	$21^h33^m43.00^s + 51°07'20.0''$	7.19	570.82	-	-	$\lesssim$45°	(46)
-	HS094+1404	$09^h46^m34.50^s + 13°50'58.1''$	4.17	4150	-	-	-	(47)

1.5.2 References to Table

(1) Ikhsanov (2000)

(2) Mukai et al. (1994)

(3) Leibowitz et al. (1997)

(4) Lyke et al. (2001)

(5) Littlefair et al. (2001)

(6) Harlaftis & Horne (1999)

(7) Mukai et al. (1994)

(8) Bonnet-Bidaud et al. (2001a)

(9) de Martino et al. (1995a)

(10) Hellier et al. (2002b)

(11) Warner et al. (2003)

(12) McArthur et al. (2001a)

(13) Mouchet et al. (1991)

(14) Buckley & Sullivan (1992)

(15) Burwitz et al. (1996)

(16) Woudt & Warner (2002)

(17) Munari et al. (1997)

(18) Uslenghi et al. (2000)

(19) Israel et al. (1999)

(20) Szkody et al. (2002)

(21) Mateo et al. (1991)

(22) Howell et al. (1997)

(23) Silber et al. (1996)

(24) Zhang et al. (1995)

(25) Thorstensen & Taylor (2000)

(26) Rodríguez-Gil et al. (2002)

(27) Mauche (1999)

(28) Eisenbart et al. (2002)

(29) Hellier & Beardmore (2002)

(30) Szkody et al. (2001)

(31) Reinsch (1994)

(32) Hellier et al. (1996)

(33) Abbott & Shafter (1997)

(34) Kato & Nogami (1997)

(35) Jablonski & Steiner (1987)

(36) Watts et al. (1985)

(37) Remillard et al. (1994)

(38) Tovmassian et al. (2004)

(39) Haberl et al. (2002)

(40) Woudt & Warner (2003b)

(41) Woudt & Warner (2003a)

(42) Schwarz et al. (2004)

(43) Patterson et al. (2004)

(44) Schlegel (2005)

(45) Haberl & Motch (1995a)

(46) Bonnet-Bidaud *et al.* (2005)

(47) Rodríguez-Gil et al. (2005)

Chapter 2

X-ray Orbital Modulations in Intermediate Polars

In this chapter we start to delve deeper into the mechanisms of the accretion flow within IPs. This chapter concentrates on the stream-disc impact region or 'hot-spot' region as it is known. We ask questions such as what causes it, in which systems does it affect the observed X-ray emission, does it occur at different binary phases in different systems, what is the effect of the system inclination and other similar questions. We use archival data from the *RXTE* and *ASCA* satellites. We go through the reduction process and produce folded lightcurves and power spectra for each of the 16 systems we were able to use. Analysis for each system is presented with discussion and overall conclusions of our findings.

2.1 Introduction

As noted in chapter 1, observations of IPs reveal X-ray modulations at the spin period of the white dwarf (P_{spin}), at the orbital period (P_{orb}) in some systems and there may also be modulation at the beat period (P_{beat}). The X-ray flux may be modulated due to various factors.

Spin Modulation

- Absorption by and scattering in, the accretion curtain immediately above the shock.
- Self-occulation by the body of the WD.

Beat Modulation

- If a stream-fed component exists, the accretion rate on to each pole will vary with the beat period, resulting in a modulation at that period.

Orbital Modulation

- In the absence of an accretion disk, the accretion onto the WD poles may depend on binary phase, and so give rise to an orbitally modulated X-ray flux.
- The interaction of stream and disk could give rise to an additional emission component, whose visibility varies with orbital phase.
- If a disk is present, but it has a non-axisymmetric structure at its outer edge, local absorption of the X-ray flux could occur as the structure crosses the line of sight to the WD. This would reduce the X-ray flux periodically, with an energy dependence characteristic of photoelectric absorption.

This latter possibility, absorption at the edge of a disk, is the accepted explanation for X-ray orbital modulations seen in Low Mass X-ray Binaries (LMXBs) and is a likely candidate to operate in IPs too.

2.2 Orbital Modulation

Orbitally modulated X-ray flux has been reported in several IPs and three possible origins for such X-ray orbital modulations have been suggested as noted above. Hellier et al.

(1993) carried out the only previous systematic study of X-ray orbital modulations in IPs. They looked at the X-ray lightcurves of seven IPs observed by *EXOSAT*, and found orbital modulations to be probably present in each of them (TV Col, TX Col, AO Psc, FO Aqr, BG CMi, V1223 Sgr and EX Hya), although the evidence in V1223 Sgr was marginal. Hellier et al. (1993) concluded that these orbital modulations are similar to those seen in dipping LMXBs and have a similar cause. The implication noted by Hellier et al. is that IPs are all seen at high inclinations and are all disk fed. For comparison, observations of IPs using *ROSAT* and *Ginga* confirmed the presence of X-ray orbital modulations in FO Aqr (Norton et al. 1992b), BG CMi (Norton et al. 1992a), TX Col (Norton et al. 1997), and AO Psc (Taylor et al. 1997), and failed to find such modulation in V1223 Sgr (Taylor et al. 1997), YY Dra and V709 Cas (Norton et al. 1999). In addition XY Ari and EX Hya are the only IPs to show X-ray eclipses (Hellier 1997b; Rosen et al. 1991) and so are known to be at high inclination angles.

In order to extend the earlier studies, and investigate the preponderance of X-ray orbital modulations in the large number of IPs now known, we re-analysed 30 X-ray observations of 16 IPs obtained with *RXTE* and *ASCA* that are available in the archives. We have excluded observations of IPs that span less than two orbital periods of the system in question and we have not included observations of EX Hya and XY Ari in our analysis. The X-ray orbital modulation of EX Hya is well studied but difficult to disentangle from the spin modulation with which it is in a 3:2 resonance. The archival *RXTE* observations of XY Ari are all short and cover only a tiny phase range around the eclipse egress in each case, so the overall broad X-ray modulation (anti-phased with the X-ray eclipse) is not sampled.

Table 2.1: ASCA observations

Target name	Observation start time	Duration / s	GIS exposure / s	SIS exposure / s	Ref.
V1025 Cen	1997-01-14 08:46:26	131048	60832	48320	–
BG CMi	1996-04-14 18:17:33	198956	85440	72352	–
V1223 Sgr	1994-04-24 04:15:47	153904	59168	55552	[1]
V2400 Oph	1996-03-18 20:26:45	206031	83840	76320	–
AO Psc	1994-06-22 06:52:43	196679	82336	75808	[2]
YY Dra	1997-05-06 09:16:20	80064	32896	24448	[3]
LS Peg	1998-11-23 11:21:58	79728	29936	28176	[4]
V405 Aur (1)	1996-10-05 13:36:29	165263	82368	71323	–
V405 Aur (2)	1999-03-21 09:24:39	91570	44064	38272	–
V2036 Cyg	1998-05-15 03:18:51	56816	28352	25248	[5]
FO Aqr	1993-05-20 22:12:34	96176	37952	35552	[6],[7]
PQ Gem (1)	1994-11-04 21:44:28	189439	79872	71200	[8],[9]
PQ Gem (2)	1999-10-19 16:23:56	98800	42912	39296	–
TV Col	1995-02-28 06:03:42	102998	39936	36448	[10]
TX Col	1994-10-03 07:04:37	96992	41888	35680	[11]
AE Aqr	1995-10-13 23:40:13	85842	43968	39264	[12],[13]
V1062 Tau	1998-02-16 21:33:55	137264	61248	55136	[14]

References: [1] Beardmore et al. (2000), [2] Hellier et al. (1996), [3] Yazgan & Balman (2002), [4] Szkody et al. (2001), [5] Norton et al. (2002), [6] Beardmore et al. (1998), [7] Mukai et al. (1994), [8] James et al. (2002), [9] Mason (1997), [10] Rana et al. (2004), [11] Norton et al. (1997), [12] Eracleous (1999), [13] Choi et al. (1999), [14] Hellier et al. (2002a)

2.3 Observations

The data in this chapter were obtained with the Advanced Satellite for Cosmology and Astrophysics (*ASCA*) and the Rossi X-ray Timing Explorer satellite (*RXTE*). Table 2.1 shows details of the *ASCA* observations and Table 2.2 lists the *RXTE* observations that we have used. References in each table indicate papers where these observations have been previously reported, although in most cases, the authors do not comment on any X-ray orbital modulation.

Table 2.2: RXTE observations

Target name	Observation start time	Total exposure time / s	Ref.
V1025 Cen	1997-01-14 17:03:58.2	89437	–
BG CMi	1997-01-07 11:40:56.9	98894	–
V1223 Sgr	1998-11-30 22:28:07.7	136152	[1]
V2400 Oph	1996-03-12 21:17:04.7	89649	–
AO Psc	1997-09-06 01:09:00.3	94351	[2]
YY Dra	1996-03-13 08:57:09.8	29243	[3]
V405 Aur	1996-04-26 00:50:55.1	57899	–
FO Aqr	1997-05-14 19:01:23.2	180380	–
PQ Gem	1997-01-27 03:54:38.0	137874	[2],[4]
V709 Cas	1997-03-28 00:10:54.0	59485	[5]
TV Col	1996-08-10 14:57:53.9	83731	[6]
TX Col	1997-03-25 06:09:29.4	68555	–
V1062 Tau	1998-02-16 06:29:55.4	146526	[7]

References: [1] Revnivtsev et al. (2004), [2] Schlegel (1999), [3] Szkody et al. (2002), [4] James et al. (2002), [5] de Martino et al. (2002), [6] Rana et al. (2004), [7] Hellier et al. (2002a)

The Advanced Satellite for Cosmology and Astrophysics (ASCA) (formerly named Astro-D) was Japan's fourth cosmic X-ray astronomy mission, and the second for which the United States provided part of the scientific payload. The satellite was successfully launched on February 20, 1993. The project operated a general/guest observer programme for most of the mission. In this phase the observing program was open to astronomers based at Japanese and US institutions, as well as those located in member states of the European Space Agency. ASCA carried four large-area X-ray telescopes. At the focus of two of the telescopes was a Gas Imaging Spectrometer (GIS), while a Solid-state Imaging Spectrometer (SIS) was at the focus of the other two. ASCA was the first X-ray astronomy mission to combine imaging capability with a broad pass band, good spectral resolution, and a large effective area. The mission was also the first satellite to use CCDs for X-ray astronomy. With these properties, the primary scientific purpose of ASCA was the X-ray

spectroscopy of astrophysical plasmas-especially the analysis of discrete features such as emission lines and absorption edges.

ASCA performed imaging and spectroscopic observations simultaneously over an energy range of 0.5 – 10 keV. The Gas Imaging Spectrometers (GIS) had an energy resolution of $E/\Delta E$ ~13 at 6 keV and ~7 at 1.5 keV, and a circular field of view of $50'$ diameter. The Solid-state Imaging Spectrometers (SIS) had an energy resolution of ~50 at 6 keV and ~20 at 1.5 keV, and a square field of view of $20'$ x $20'$. See Tanaka et al. (1994) for a more extensive guide to *ASCA*.

The Rossi X-ray Timing Explorer (RXTE) is a satellite designed for time domain studies of cosmic X-ray sources. The mission carries two pointed instruments, the Proportional Counter Array (PCA) developed by GSFC to cover the lower part of the energy range, and the High Energy X-ray Timing Experiment (HEXTE) developed by UCSD covering the upper energy range. These instruments are equipped with collimators yielding a FWHM of one degree. In addition, RXTE carries an All-Sky Monitor (ASM) from MIT that scans about 80% of the sky every orbit, allowing monitoring at time scales of 90 minutes or longer. It was launched on December 30, 1995 from NASA's Kennedy Space Center. The mission is managed and controlled by NASA's Goddard Space Flight Center (GSFC) in Greenbelt, Maryland. It features unprecedented time resolution in combination with moderate spectral resolution to explore the variability of X-ray sources. Time scales from microseconds to months are covered in an instantaneous spectral range from 2 to 250 keV.

The instrument used for the observations presented here was the Proportional Counter Array (PCA; see Zhang et al. (1993)), which consists of five Proportional Counter Units (PCUs) with a total net area of 6500 cm^2. Each PCU is filled with xenon gas and split into three layers, plus a propane filled veto layer. The energy bandwidth of the instrument is 2–60 keV and it has a collimated field of view of 1° (FWHM). The energy resolution of the

PCA is ~18% at 6 keV (see Bradt et al. 1993, for more details). During the observations reported here, the PCA was mostly operated with all five PCUs functioning, however for some observations fewer were in use, but this is accounted for within the data reduction and the lightcurves are shown as counts per PCU against time.

2.4 Data Reduction

All the data used were extracted from the HEASARC archive and reduced using the standard routines of the FTOOLS package v5.2.

RXTE is a non-imaging satellite, which means that for light curve analysis, the background must be subtracted based on a previous model. The source and background counts have to be taken at different times: the background count is taken before and after the source, then an extrapolation between the two background models across the source area is calculated to give an estimation of the background count rate at the source. The background is defined to include anything that contributes non-source counts to the PCA instrument in orbit and includes the local particle environment, induced radioactivity of the spacecraft and the cosmic X-ray background. These vary as a function of time, so must be parameterized. The parameterized model is adjusted to fit a set of observations by the PCA of blank sky regions. Within ftools a package known as PCABACKEST produces synthetic background data by matching the background conditions of the observation with those in various model files. These model files contain actual background observations sorted by quantities such as the position of the spacecraft with respect to the South Atlantic Anomaly. These data files are then put through another routine to produce background lightcurves to subtract from the source lightcurves using the same selection and binning criteria as the source. This can of course lead to systematic errors, however values have been calculated for this error (see appendix 2) which observers can

use to estimate their sensitivity to fluctuations of faint sources in a given observation.

For the *RXTE* data reduction for our sources, we took the standard data products from the PCA and extracted the source lightcurves for each dataset using the tool SAEXTRACT for the appropriate good time intervals. The background data files were generated with the tool RUNPCABACKEST using background models appropriate for the source. We filtered out inappropriate or contaminated data by using the following criterion (see appendix 2 for more details):

1. **Earth elevation angle** – this is the angle between the target subtended by the satellite and the Earth's limb. We used a value of $> 5°$.

2. **Stable pointing** – this is the difference between the source position and the pointing of the satellite. Our pointing offset was taken as $< 0.02°$.

3. **Time since passage through South Atlantic Anomaly (SAA)** – The SAA is a 'hole' in the geomagnetic field which allows cosmic rays to penetrate further than usual and thus has an extremely high particle background rate. The particle dose received is related to the induced radioactivity in the detectors onboard the satellite which persists for several hours after SAA passage and must be accounted for to give accurate results. So, the parameterization of coordinates relative to the SAA represents the time since the peak of the last SAA passage. When the time since passage through South Atlantic Anomaly is between zero and 30 minutes, the background will increase dramatically, resulting in a lowering of the signal to noise. Hence we only used data acquired >25min after passage through the SAA.

4. **Electron contamination** – the PCA is subject to contamination from electrons trapped in the Earth's magnetosphere or from solar flare activity.

Background subtracted lightcurves were then constructed in 16s time bins in the energy

bands 2–4, 4–6, 6–10 and 10–20 keV.

ASCA data reduction was carried out in a similar way, with data from all four co-aligned instruments. Since *ASCA* is an imaging satellite, the background is much lower than in collimated instruments, and is easier to quantify. The background is a combination of both cosmic and instrumental (particle) background, so it is both variable in time and variable from one location of the sky to another. Depending on the brightness of the source, you can either use blank sky background (from the identical section of the detector taken from observation fields without any obvious sources) or local background (parts of the detector without obvious sources from your own observation).

The reduction was carried out using the standard screening criteria (using ASCASCREEN); filtering data for the following (a more detailed description can be found in appendix 2):

1. **Stable pointing** – as opposite. [0.01° recommended] For out data we used 0.02°.
2. **Earth elevation angle** – as opposite. [5° – 10° recommended] For our data we used 5°.
3. **PIXL rejection threshold** [100 recommended] – this identifies periods when the count rate per pixel exceeds a threshold due to background flares. For our data we used 75.
4. **Cut-off rigidity** [6 GeV/c recommended] – this identifies periods of high background based on cut-off rigidity, which is a local measure of the geomagnetic field to repel cosmic rays. For our data we used the recommended value.

Hot and flickering pixels were removed from the SIS events and SIS data were additionally screened for proximity to the bright Earth (the angle between the target and the Earth's bright limb, 20° – 40° recommended we used 10°) and time after passing through the South Atlantic Anomaly (SAA). Only well-calibrated events, with grades 0, 2, 3 or 4

were kept. The grade is a one-dimensional description of the shape of the charge cloud created by an event in a CCD. Certain grades are more likely to be true X-ray events. The combination of the grades we selected gave us the best calibration, and the combination provided a good compromise in resolution and signal-to-noise.

The GIS background consists of non-X-ray background (NXB, charged particles, gamma-rays) and the cosmic X-ray background. The GIS data like the SIS data were screened by filtering data for stable pointing; elevation angle and cut-off rigidity and additionally screened to remove the background ring and calibration source. In the GIS, non-X-ray events occur most often in the outer ring of the GIS field of view (FOV). Therefore we excluded this part of the FOV, as well as the internal calibration source which also appears at the edge of the FOV.

Light curves were extracted in 16s bins from each instrument in low (0.7–2keV) and high (2–10keV) energy bands, both from the source and from nearby source-free background region using XSELECT. Background subtraction was carried out and data from all four instruments were then combined accounting for different good times. Further details of the data reduction process may be found in Appendix B.

The RXTE PCA background is often systematics dominated – the background is large ($\sim$ 30 c/s/PCU over the entire band) and is modeled, not measured. The limit of the model is typically 1%, which sets the error. 1% of 30 is 0.3 c/s, so this is the lowest error you can ever achieve. The RXTE background is therefore comparable to the typical count rate observed from an IP with this satellite.

ASCA background is small (typically 0.02 c/s per point source extraction region) and is measured directly. If you observe an r c/s source for t seconds, you get total (src+bgd counts) of $(r+0.02)t$ with ASCA. So the statistical error in the count rate is:

$$\frac{\sqrt{r+0.2}}{\sqrt{t}} \tag{2.1}$$

And the relative error is:

$$\frac{\frac{\sqrt{r+0.2}}{r}}{\sqrt{t}} \tag{2.2}$$

So, for a typical ASCA count rate of 1 c/s in a 30ks exposure, the relative error is only 0.6%.

The following Figures, 2.1 - 2.6 show images of the raw lightcurve data for the background and source counts for ASCA and RXTE respectively, to illustrate the data reduction process described above. Figures 2.1 and 2.2. show excample lightcurves of ASCA data in the 0.7-2keV and 2-4keV energy bands respectively. Red indicates the lightcurve extracted from the source region and green indicates the lightcurve extracted from the background region, in 200 second bins. These lightcurves clearly illustrate that ASCA has a low background rate and thus the subtracted lightcurves have a low uncertainty. The RXTE lightcurves in Figures 2.3 - 2.6 also illustrate examples of raw data for both source (in red) and background (in green) lightcurves for the four energy bands of 2-4, 4-6, 6-10 and 10-20keV at 100 second time bin intervals.

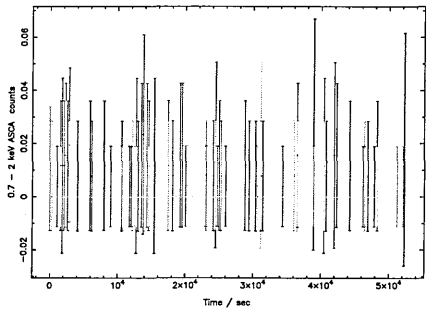

Figure 2.1: Example ASCA 0.7-2keV source lightcurve (red) and background lightcurve (green)

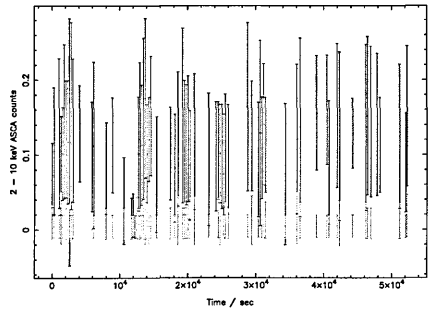

Figure 2.2: Example ASCA 2-10keV source lightcurve (red) and background lightcurve (green)

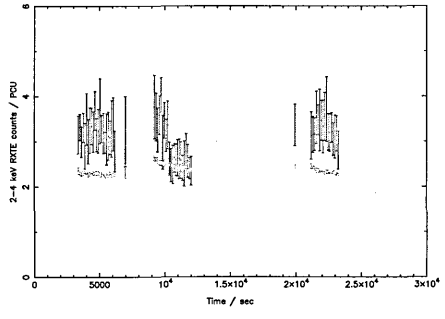

Figure 2.3: Example RXTE 2-4keV source lightcurve (red) and background lightcurve (green)

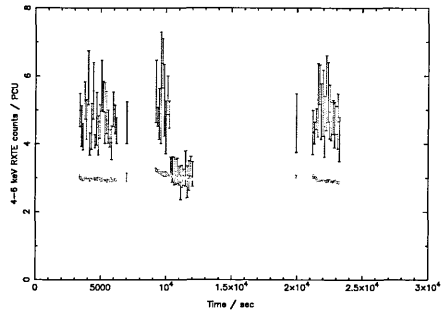

Figure 2.4: Example RXTE 4-6keV source lightcurve (red) and background lightcurve (green)

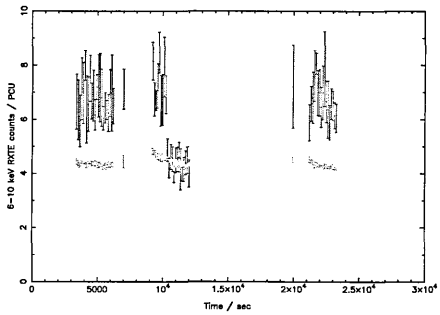

Figure 2.5: Example RXTE 6-10keV source lightcurve (red) and background lightcurve (green)

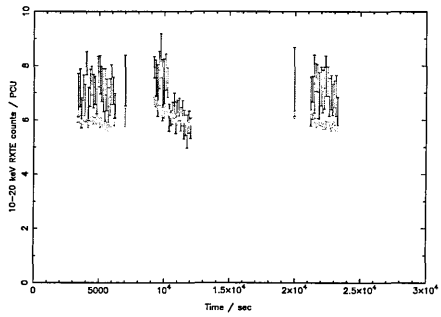

Figure 2.6: Example RXTE 10-20keV source lightcurve (red) and background lightcurve (green)

Lightcurves from both *RXTE* and *ASCA* data were then folded into 16 orbital phase bins according to the best available orbital ephemerides for each system, see Table 2.3. In each case the epoch of zero phase was adjusted to coincide with the presumed inferior conjunction of the secondary star. The published ephemerides of these systems are defined in various ways. If the ephemeris is based on optical photometric data, we assume that minimum light corresponds to the secondary star at inferior conjunction, or that maximum light indicates the WD at inferior conjunction. Similarly, if the ephemeris is based on spectroscopic data, we assume that red-to-blue crossing of the emission lines corresponds to the WD at superior conjunction, or that blue-to-red crossing of the absorption lines indicates the secondary star at inferior conjunction. Where no ephemeris is available, the phasing is arbitrary and zero phase is simply set to the start of the observation in each case. Figure 2.7 depicts the orbital phases seen in a binary system. according to the corrections we adopted.

Figure 2.7: Orbital Phase diagram

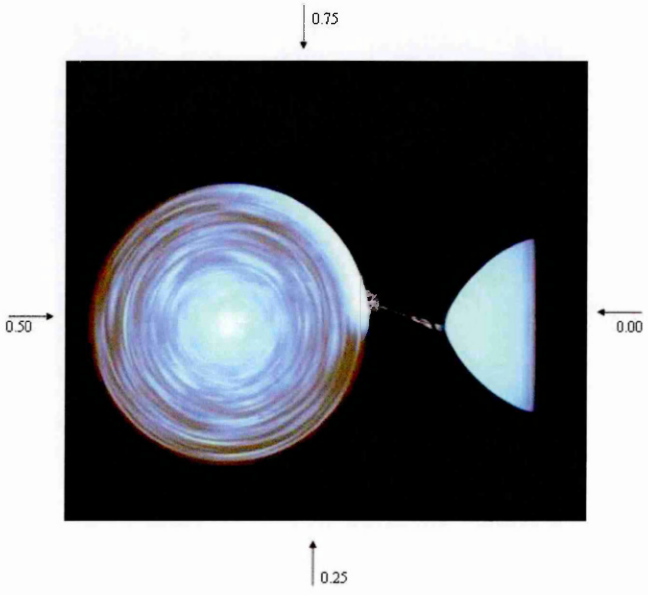

Table 2.3: Orbital ephemerides

Source	Orbital Ephemeris/HJD†	Ref.	Zero Phase/HJD (inf. conj. of 2^{ndary})	Accumulated phase error at epoch of X-ray observations
V1025 Cen*	0.05876	[1]	–	–
BG CMi	2445020.396(2)+0.13474854(10)E	[2]	2445020.396	*ASCA*(1): 0.03 ; *ASCA*(2): 0.03 ; *RXTE*: 0.03
V1223 Sgr	2444749.986(3)+0.1402440(4)E	[3]	2444750.056	*ASCA*: 0.10 ; *RXTE*: 0.13
V2400 Oph*	0.1429167	[4]	–	–
AO Psc	2444864.1428(28)+0.1496252(5)E	[5]	2444864.217	*ASCA*: 0.10 ; *RXTE*: 0.13
YY Dra	2446863.4376(5)+0.16537398(17)E	[6]	2446863.4376	*ASCA*: 0.02 ; *RXTE*: 0.02
LS Peg	2450358.8964(9)+0.174774(3)E	[7]	2450358.983	*ASCA*: 0.08
V405 Aur	2449474.6446(15)+0.172624(1)E	[8]	2449474.744	*ASCA*(1): 0.3 ; *ASCA*(2): 0.6 ; *RXTE*: 0.2
V2306 Cyg	2451762.9527(1)+0.181195(339)E	[9]	2451762.9527	*ASCA*: >1
FO Aqr	2444782.869(2)+0.2020596(1)E	[10]	2444782.869	*ASCA*: 0.011 ; *RXTE*: 0.014
PQ Gem	2449333.984(4)+0.216359(3)E	[11]	2449333.984	*ASCA*(1): 0.02 ; *ASCA*(2): 0.13 ; *RXTE*: 0.07
V709 Cas	2451048.0575(2)+0.2225(2)E	[12]	2451048.168	*RXTE*: >1
TV Col	2448267.4893(5)+0.2285999(2)E	[13]	2448267.4893	*ASCA*: 0.005 ; *RXTE*: 0.007
TX Col*	0.23825	[14]	–	–
AE Aqr	2449281.42222(8)+0.41165553(5)E	[15]	2449281.42222	*ASCA*: 0.0002
V1062 Tau*	0.41467	[16]	–	–

* - No ephemeris available.

† numbers in brackets in the ephemerides indicate the uncertainty on the last digit.

References: [1] Buckley et al. (1998), [2] Hellier (1997), [3] Jablonski & Steiner (1988), [4] Hellier & Beardmore (2002), [5] Kaluzny & Semeniuk (1988), [6] Haswell et al. (1997), [7] Taylor et al. (1999), [8] Thorstensen (1997), private communication, cited in Harlaftis & Horne (1999), [9] Zharikov et al. (2002), [10] Patterson et al. (1998b), [11] Hellier (1997), [12] Bonnet-Bidaud et al. (2001), [13] Hellier (1993), [14] Mouchet et al. (1991), [15] Casares et al. (1996), [16] Lipkin et al. (2004)

Power spectra of each lightcurve were constructed using the 1-dimensional CLEAN algorithm of H.J. Lehto, which utilises a variable gain. This is particularly suited to revealing

the signals in unevenly sampled, multiply-periodic data and is quite effective at removing signals at the frequency 1.75×10^{-4} Hz due to the sampling pattern imposed by the orbital period of both the *ASCA* and *RXTE* satellites (about 95 minutes in each case). Noise levels in CLEANed power spectra are notoriously difficult to calculate (Norton et al. 1996). However, we are in the fortunate position of knowing the expected system frequencies in advance, namely the various harmonics and sidebands of the spin and orbital frequencies of each system. Any power at a frequency other than those 'expected' can be considered spurious, and due to noise in the lightcurve. Normally when analyzing power spectra we would consider all peaks, however as we are only interested in the peaks that correspond to known spin and orbital frequencies these are the peaks that we analyse in this case. In order to estimate the noise level in a given power spectrum we therefore followed the prescription of Norton et al. (1996). This involved determining the power level above which there are n discrete noise peaks in the power spectrum, where we defined n in this case as 1% of the total number of independent frequency samples in the spectrum (typically several thousand, depending on the length and sampling of that data set). This power level therefore represents that at which there is a 1% chance that any individual frequency bin will contain a noise peak. Hence, if the power at any of the expected system frequencies is greater than this noise level, there is a 99% chance that the signal at that frequency is *not* due to noise. Such peaks are therefore considered as 'real'. Conversely, any peak that corresponds to one of the system frequencies, but which has a power below the noise level, is considered as spurious. This simple procedure allowed us to make a direct comparison between one data set and another. Power spectra for the systems are shown in Figures 2.1 and 2.2, with the noise level indicated by a dashed horizontal line in each case.

Finally, in order to quantify the degree of X-ray orbital modulation in each system, we found the best-fit sinusoid to each folded lightcurve, allowing the mean level, amplitude

and phase as free parameters. We recognise that many of the orbital modulations present may not be well fit by a sinusoid, but this is the simplest way of characterising the depth in each system in a systematic manner.

2.5 Results

The folded lightcurves for all the objects are shown in Figures 2.1 and 2.2 with the best-fit sinusoids over-plotted in each case. Modulation depths were calculated as the peak-to-peak amplitude of the sinusoid divided by the maximum level, and are shown in Tables 2.4 and 2.5, along with the fitted phase of minimum flux and the reduced chi-squared values for the sinusoid fit in each case. 1σ uncertainties on each parameter in the fit were calculated by rescaling the error bars on individual flux measurements so as to give a reduced chi-squared of unity for the best fit, and then finding the parameter range corresponding to an increase in reduced chi-squared of one. If the modulation really can be modelled as a sine wave, then we would expect $\chi^2_r = 1$. A $\chi^2_r \neq 1$ would in this case indicate that the errors are underestimated, and the scaling procedure above would account for this correctly. Alternatively, if the modulation is **not** a sine wave, then a $\chi^2_r \neq 1$ merely indicates that the model being fit to the data is not appropriate. In this case, scaling the error bars to produce a $\chi^2_r = 1$ may not be the best way of estimating the uncertainties in the modulation depth, but at least it provides a consistent way of doing so. Figures 2.3a and 2.3b illustrate the data from Tables 2.4 and 2.5 respectively. An X-ray orbital modulation is considered to be confirmed only if the depth is non-zero above the 3σ level in all energy bands of a given observation, and if the value for the phase of minimum flux is consistent between the various energy bands.

Figure 2.8: Upper panels: Orbital phase folded *ASCA* lightcurves of each object with the best fit sinusoid overplotted in each case. Lower panels: power spectra of the *ASCA* lightcurves of each object. The low frequency range is shown on an expanded scale in each case to aid visibility of the orbital components, despite the different tick marks the frequencies are the same; ω - indicates the spin frequency, Ω - indicates the orbital frequency and the horizontal dashed line indicates the noise level in the power spectra, for details see text.

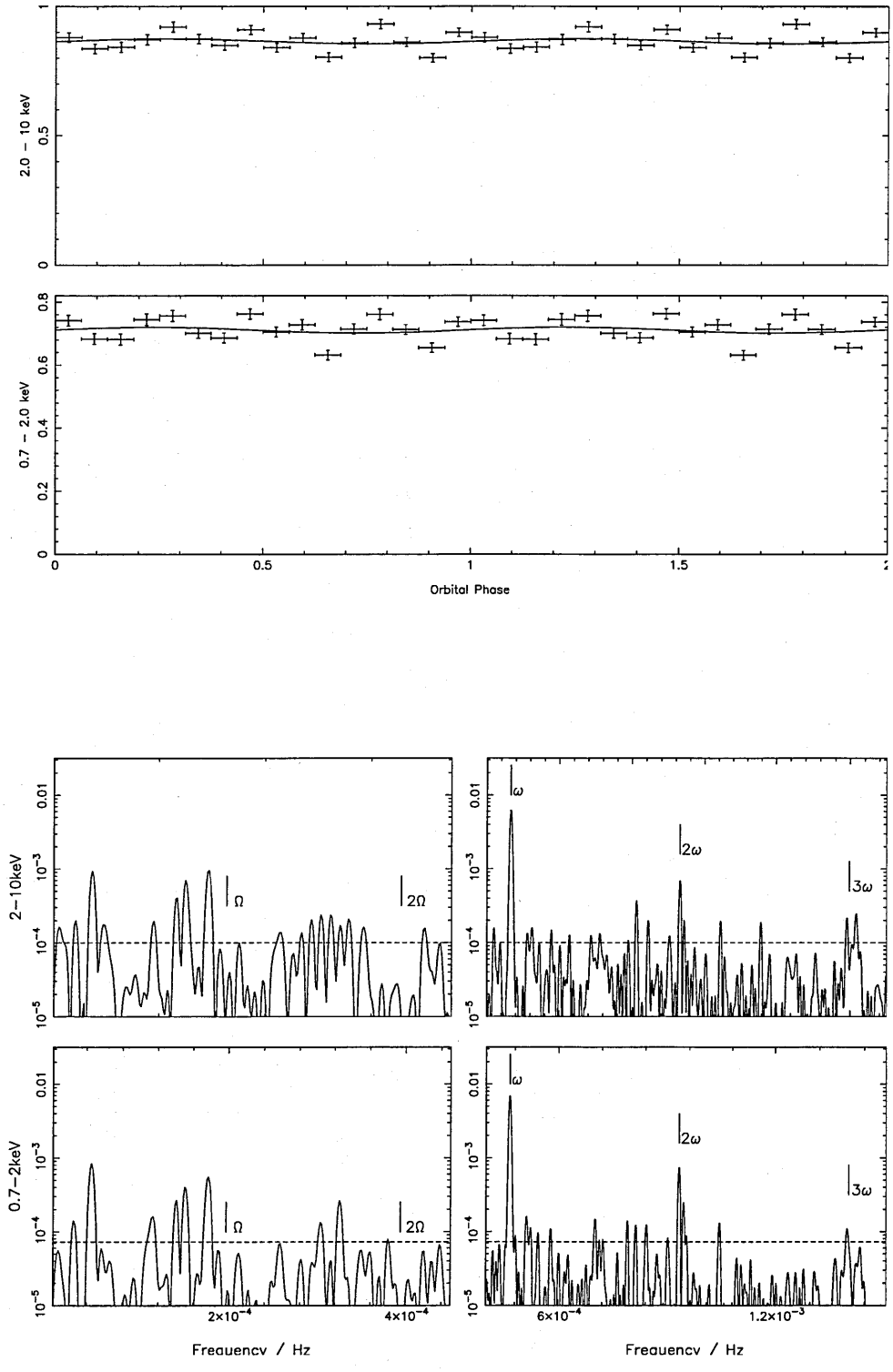

Figure 2.1: (a) V1025 Cen

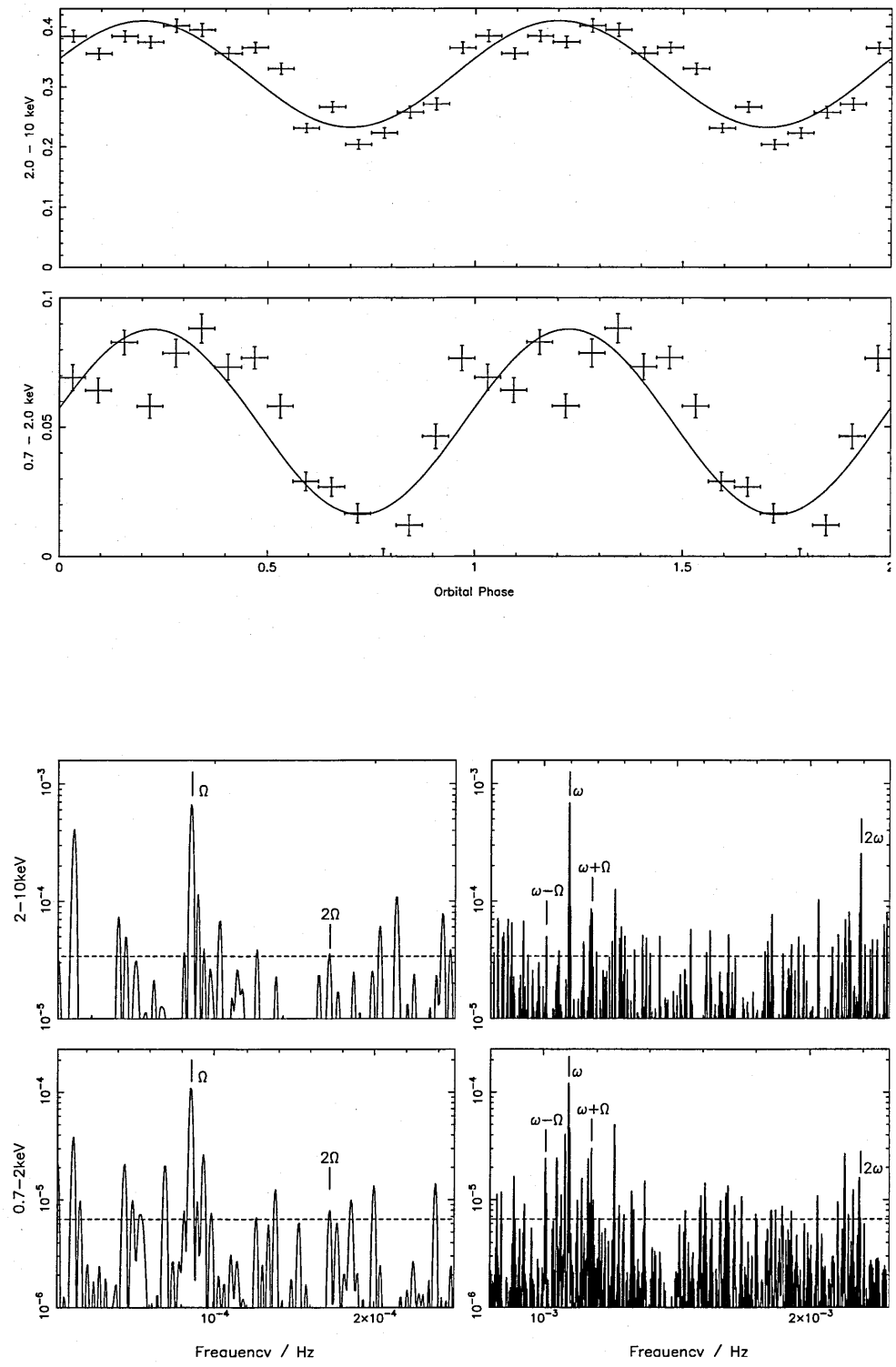

Figure 2.1: (b) BG CMi

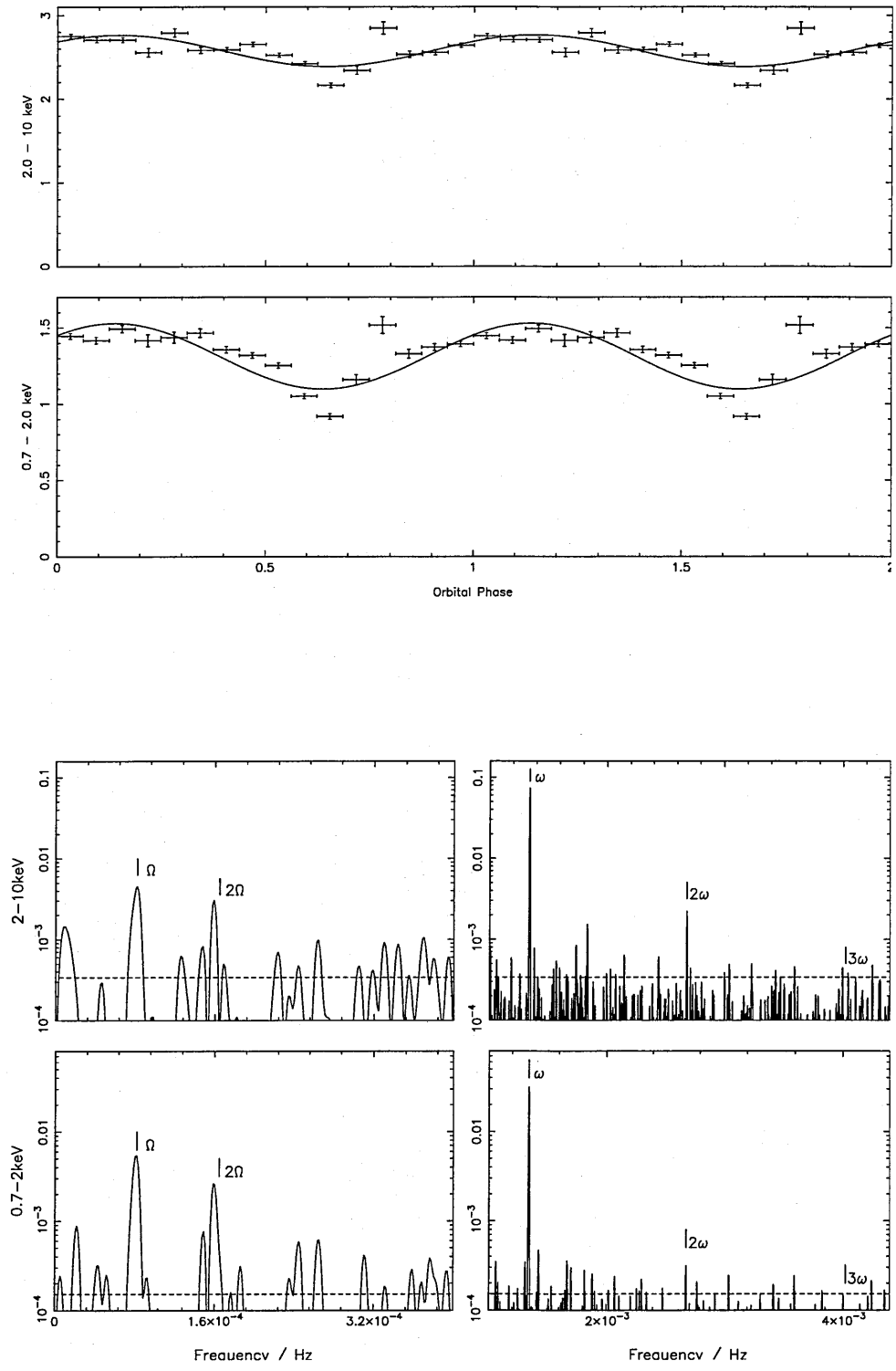

Figure 2.1: (c) V1223 Sgr

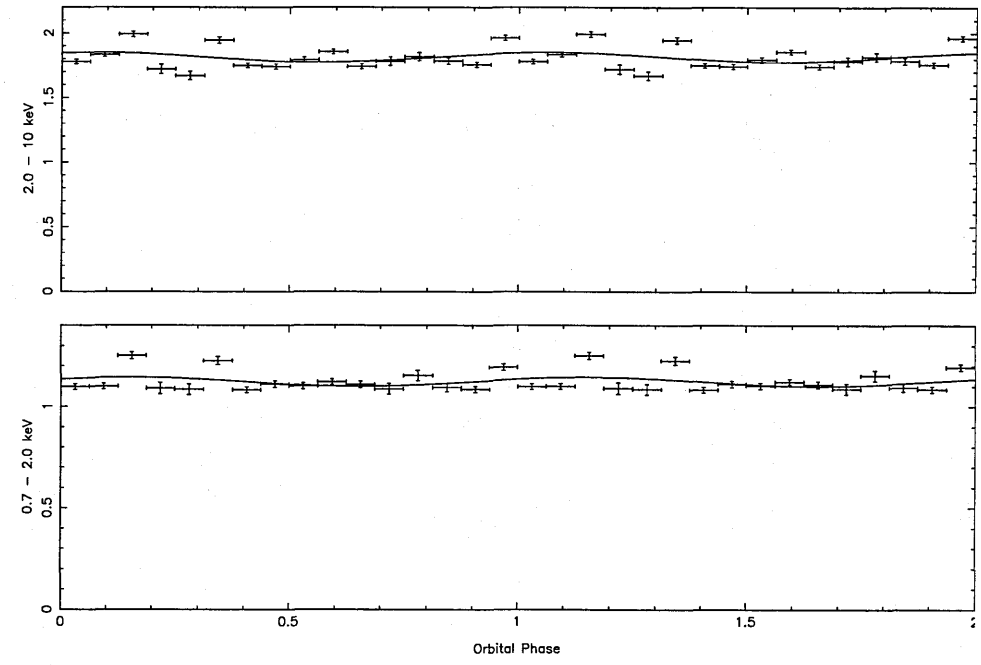

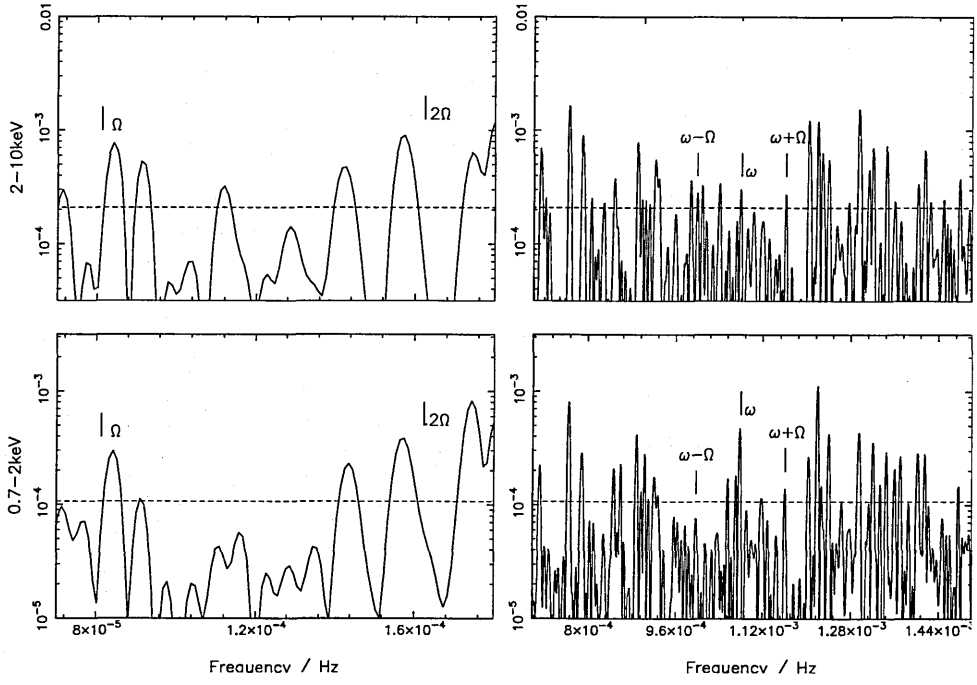

Figure 2.1: (d) V2400 Oph

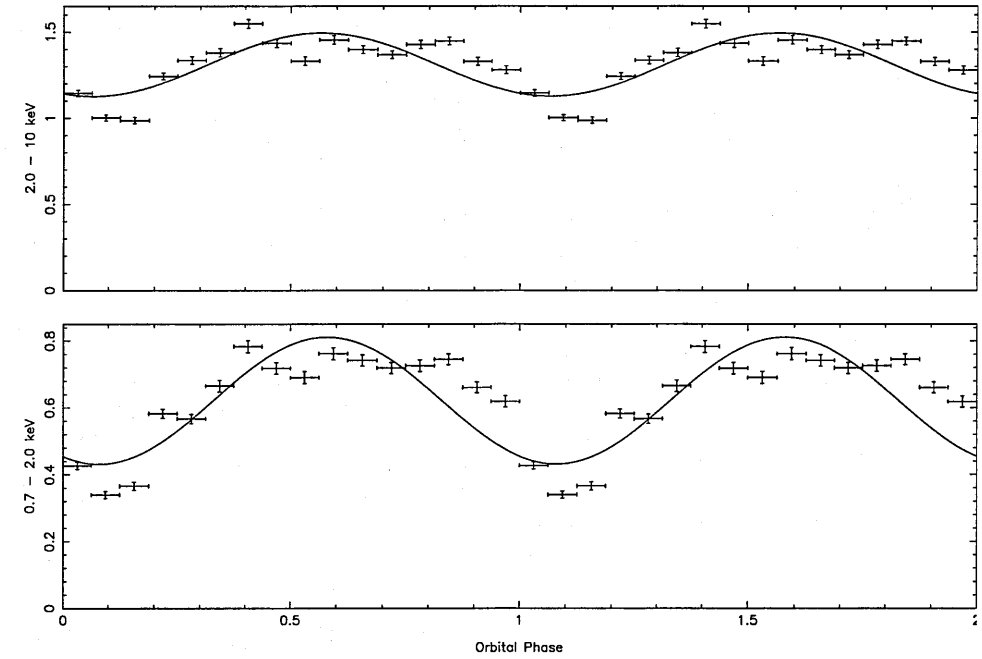

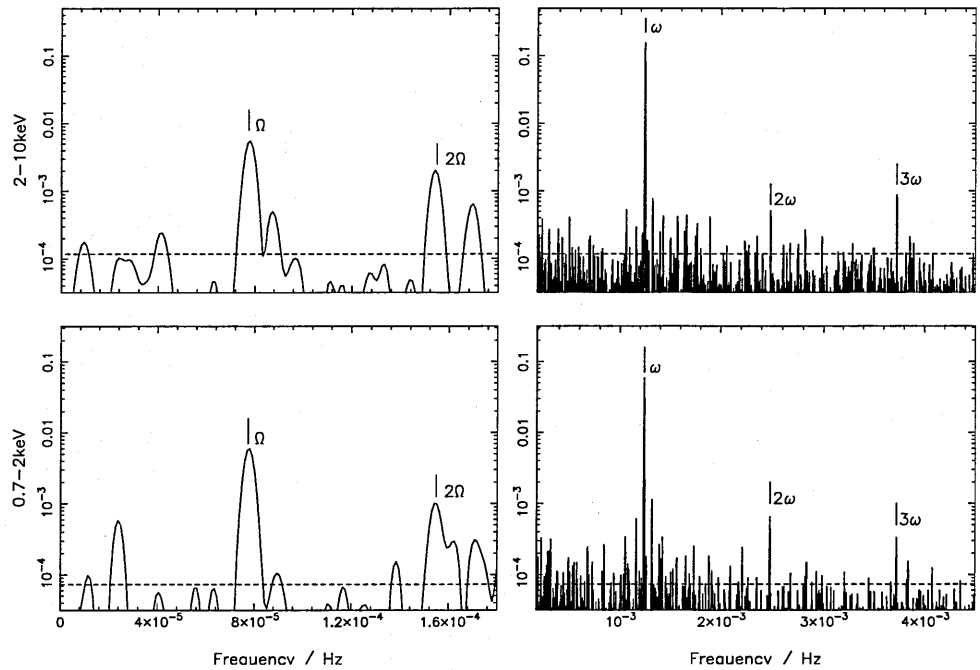

Figure 2.1: (e) AO Psc

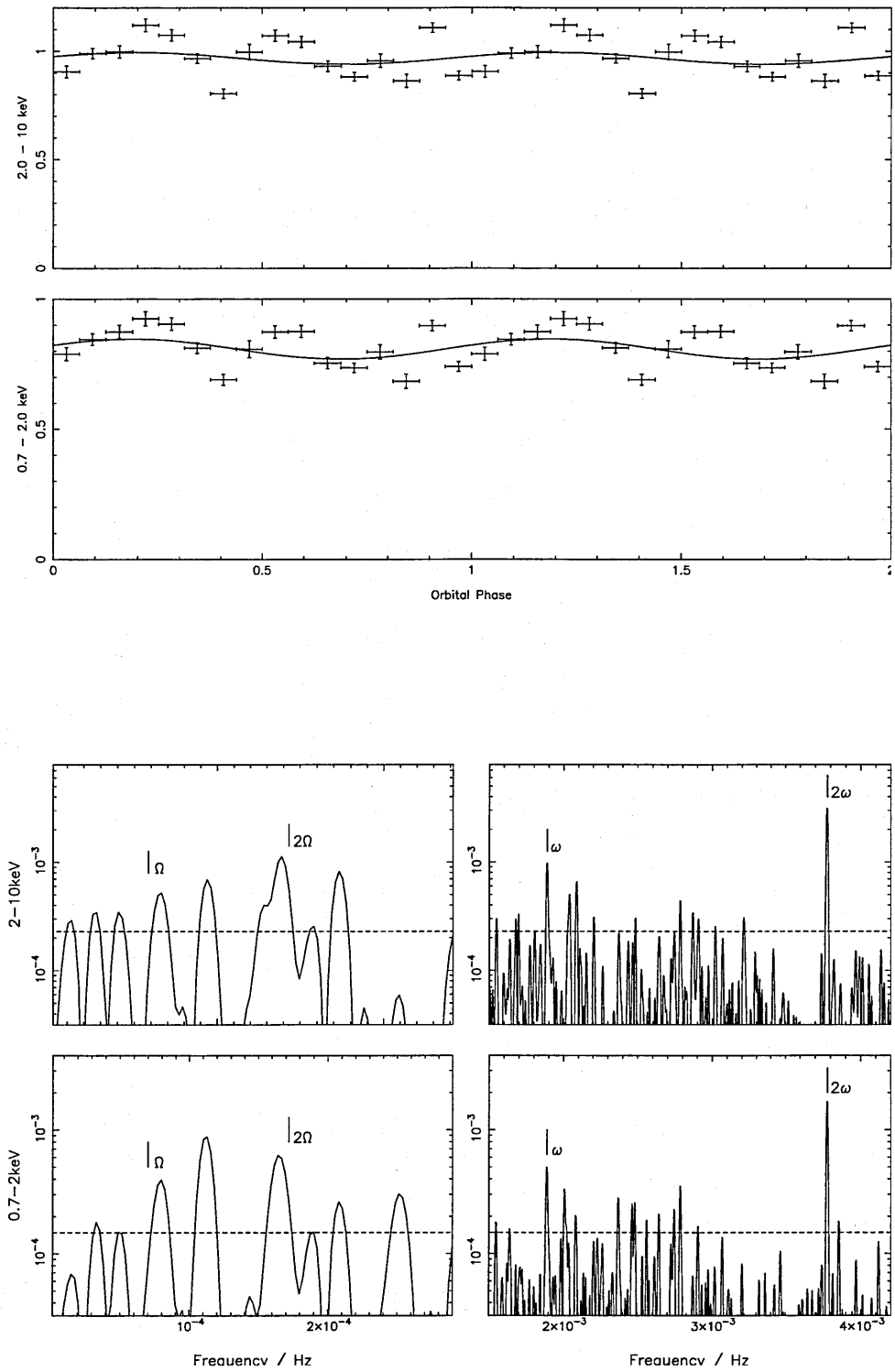

Figure 2.1: (f) YY Dra

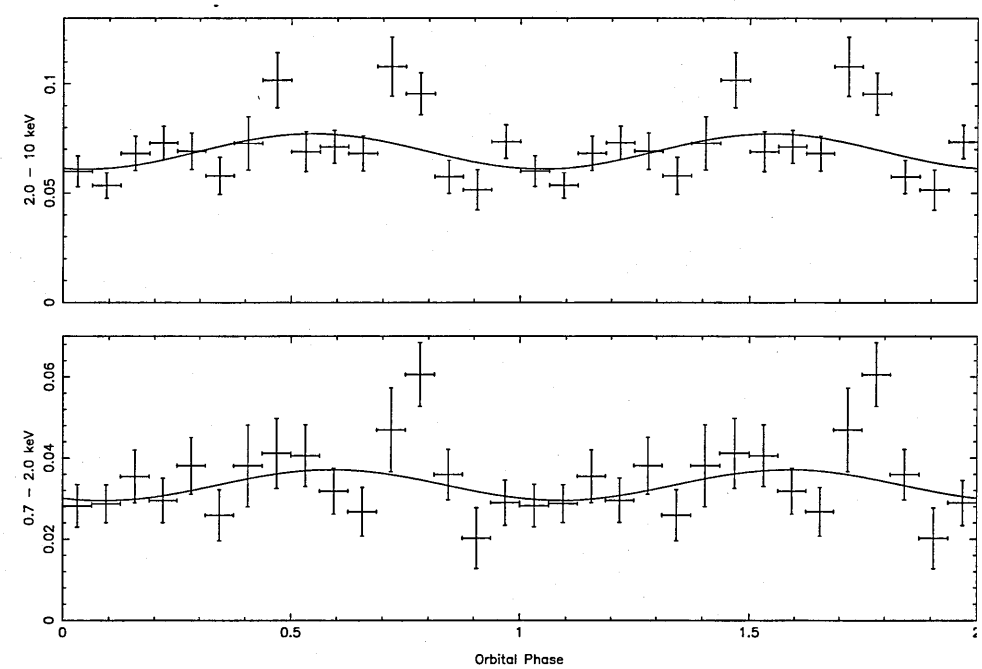

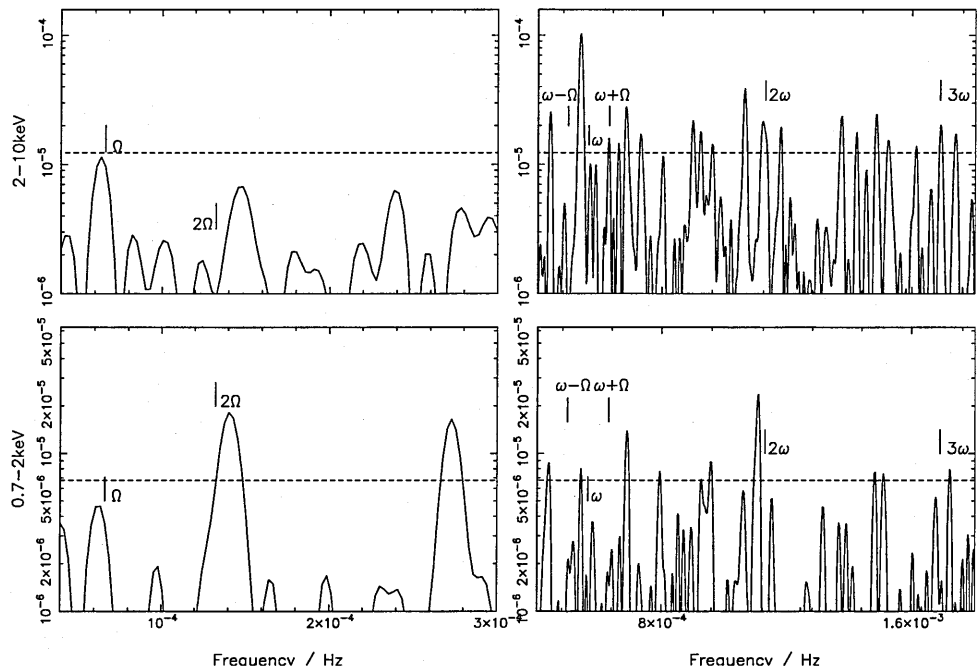

Figure 2.1: (g) LS Peg

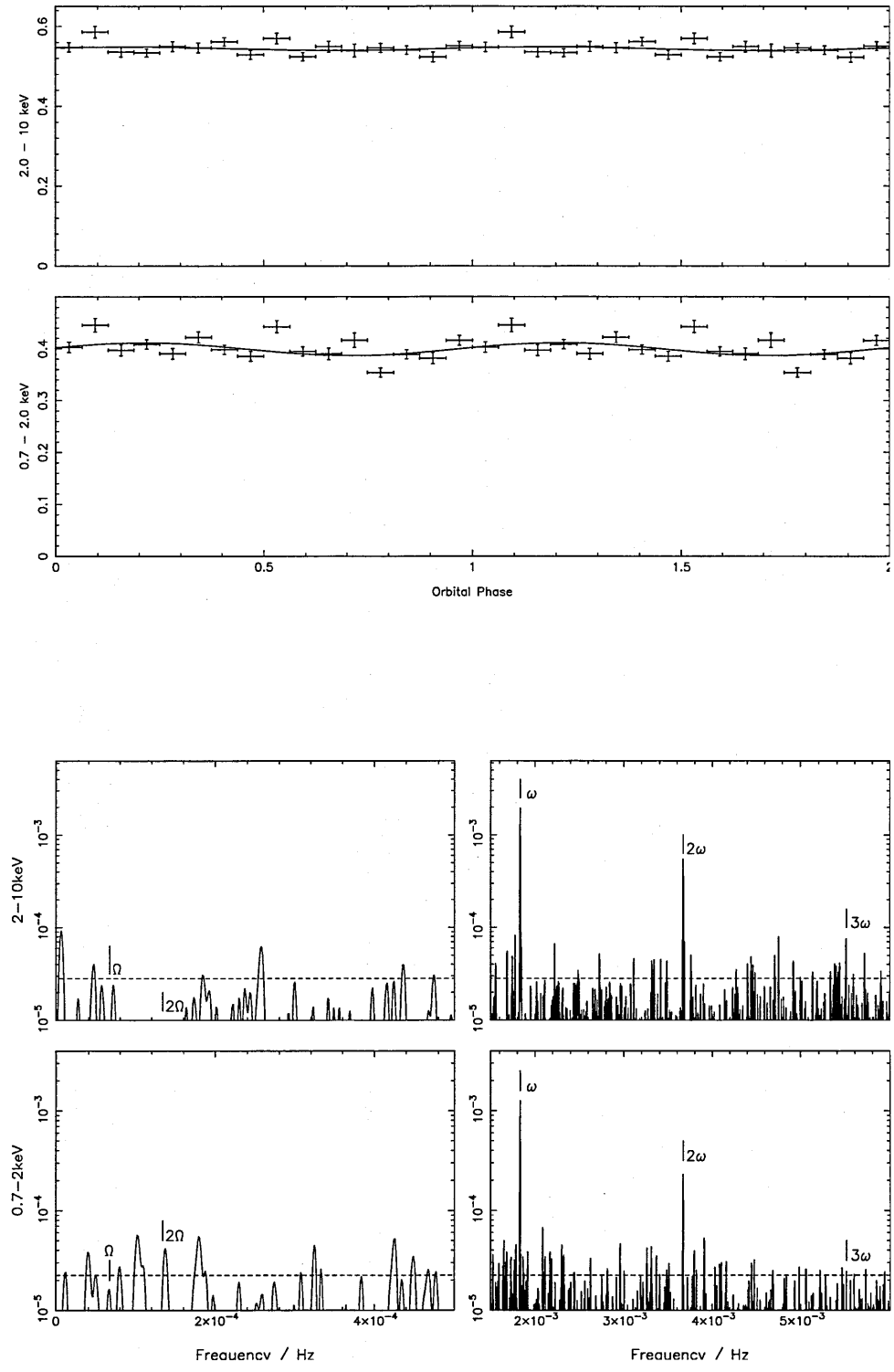

Figure 2.1: (h) V405 Aur (1)

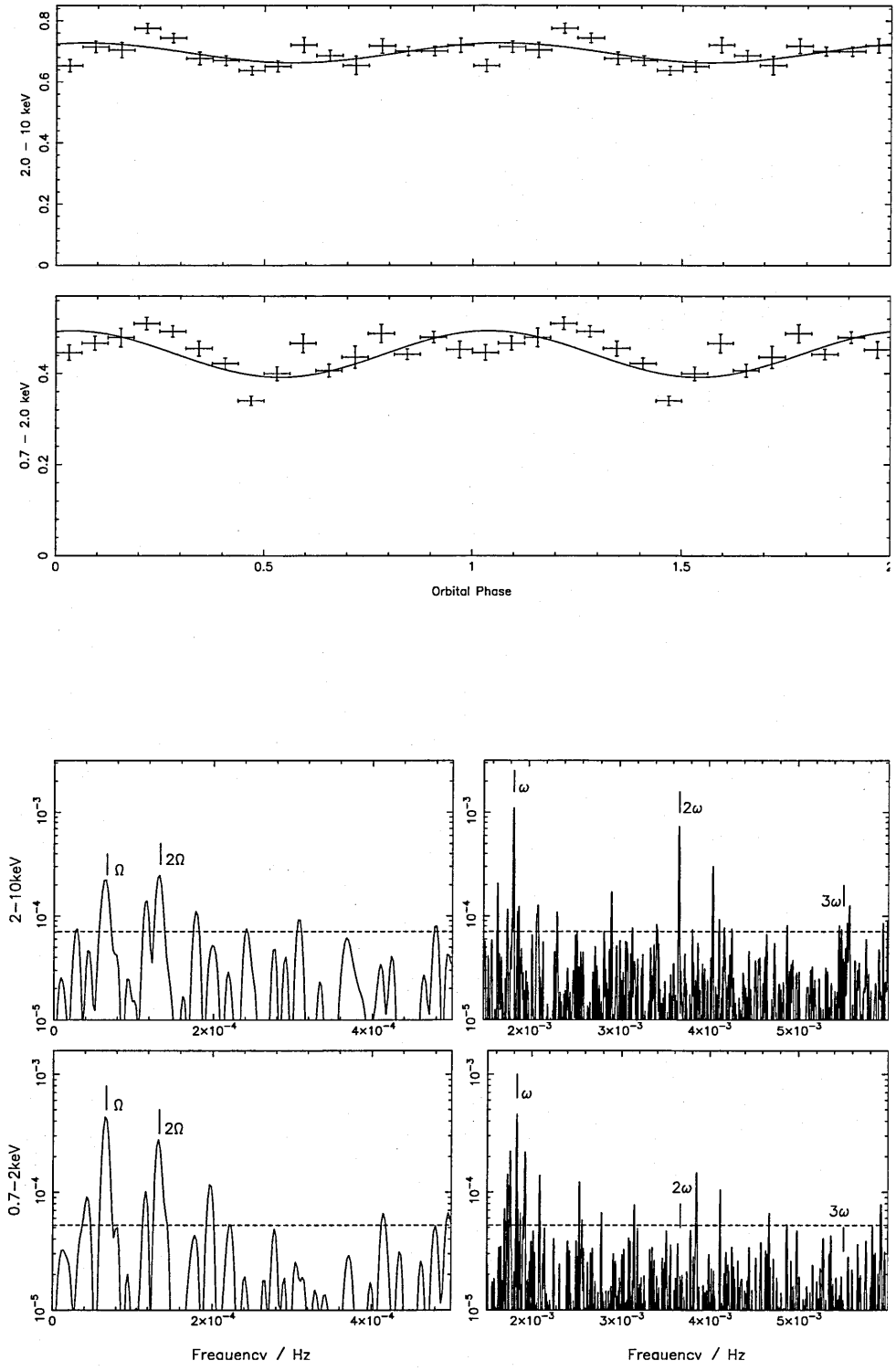

Figure 2.1: (i) V405 Aur (2)

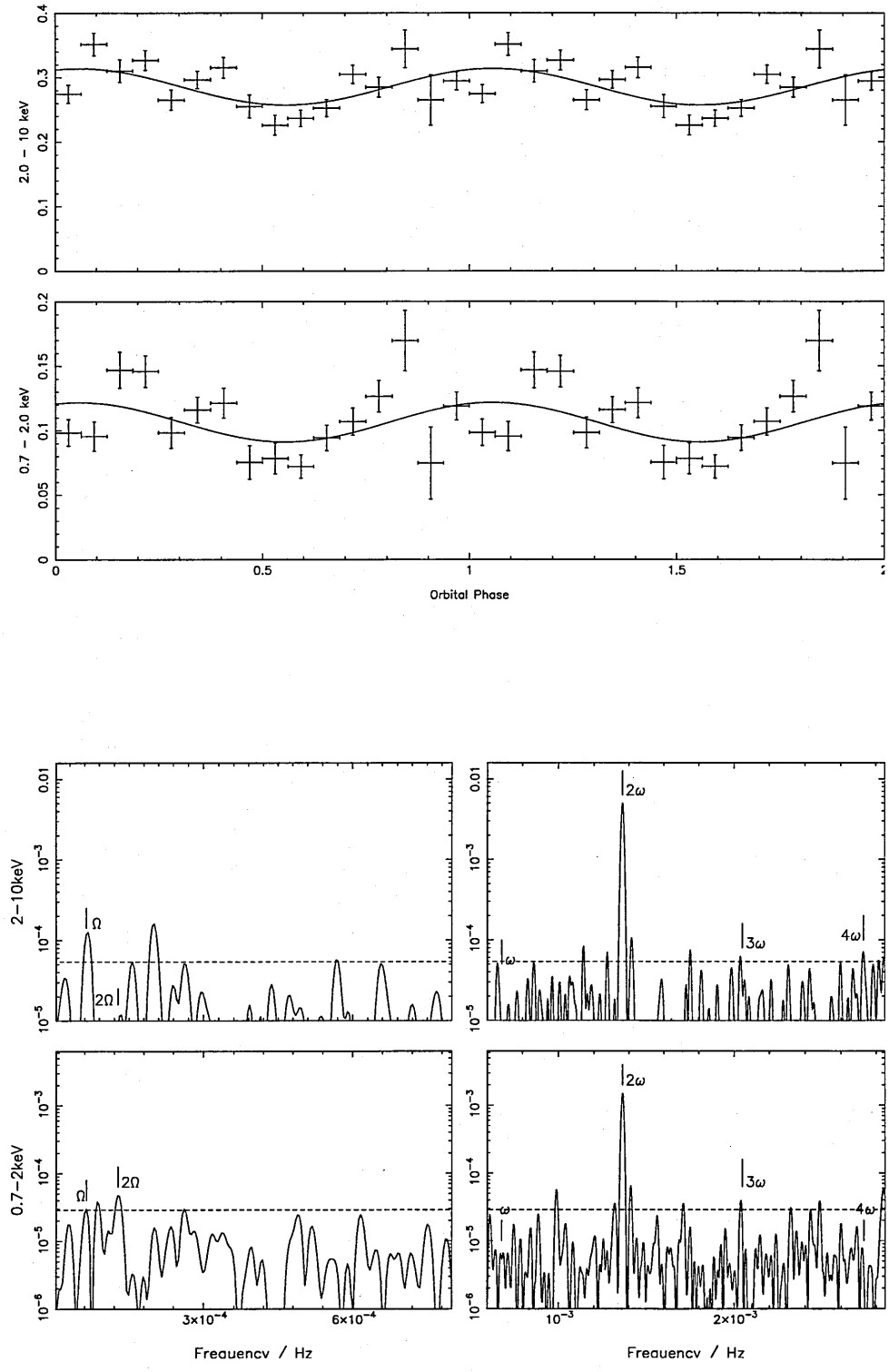

Figure 2.1: (j) V2306 Cyg

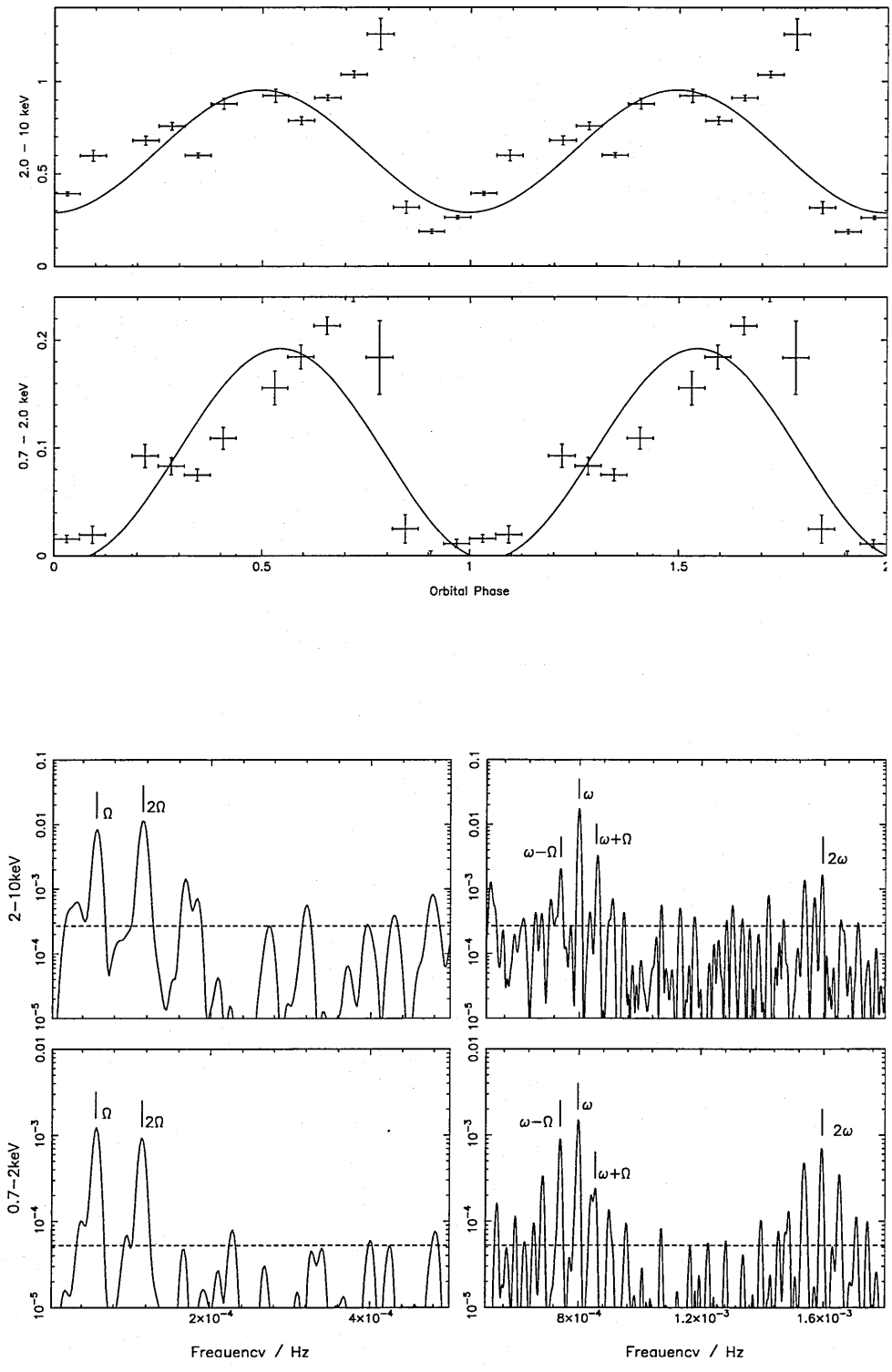

Figure 2.1: (k) FO Aqr

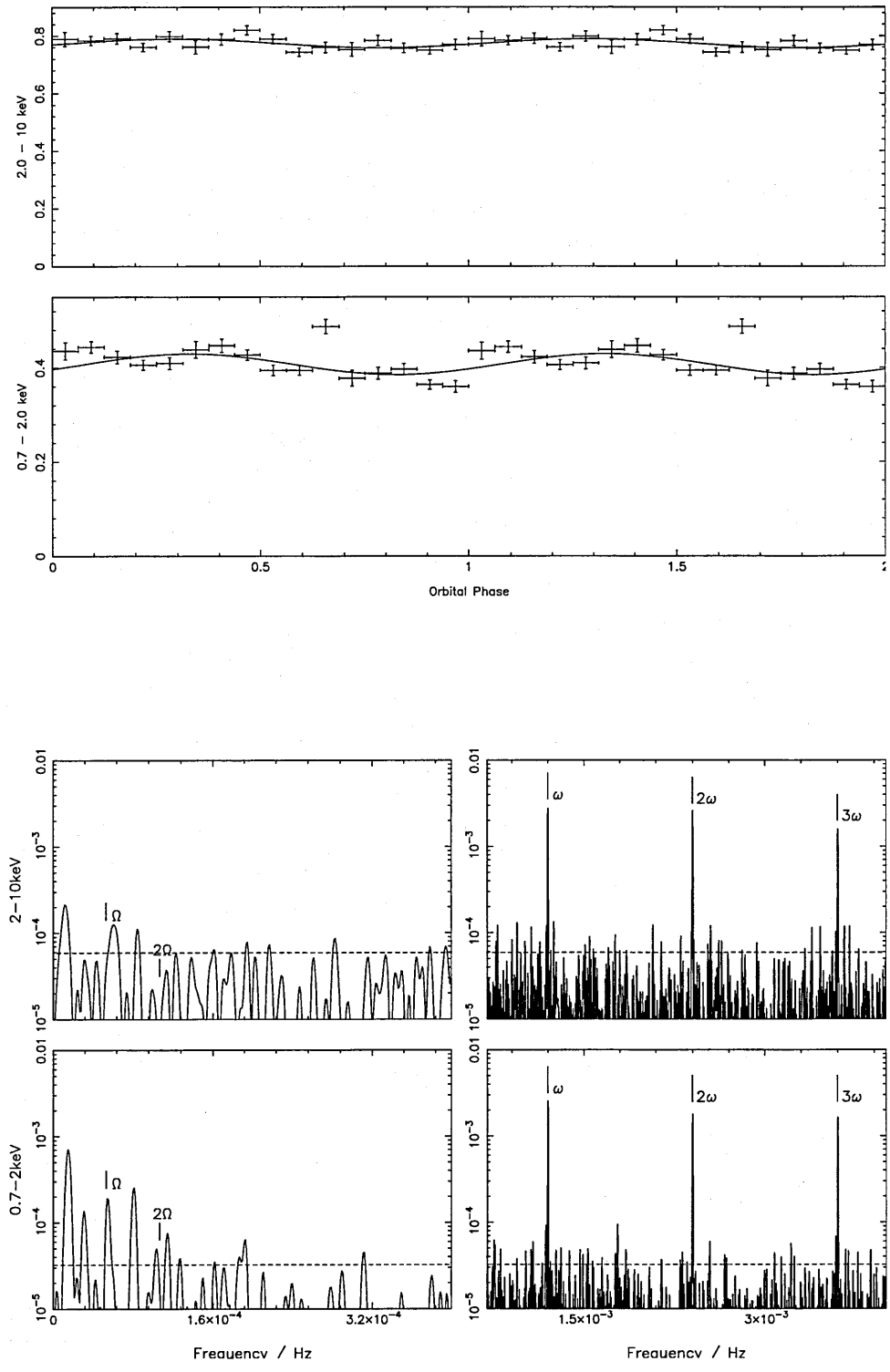

Figure 2.1: (l) PQ Gem (1)

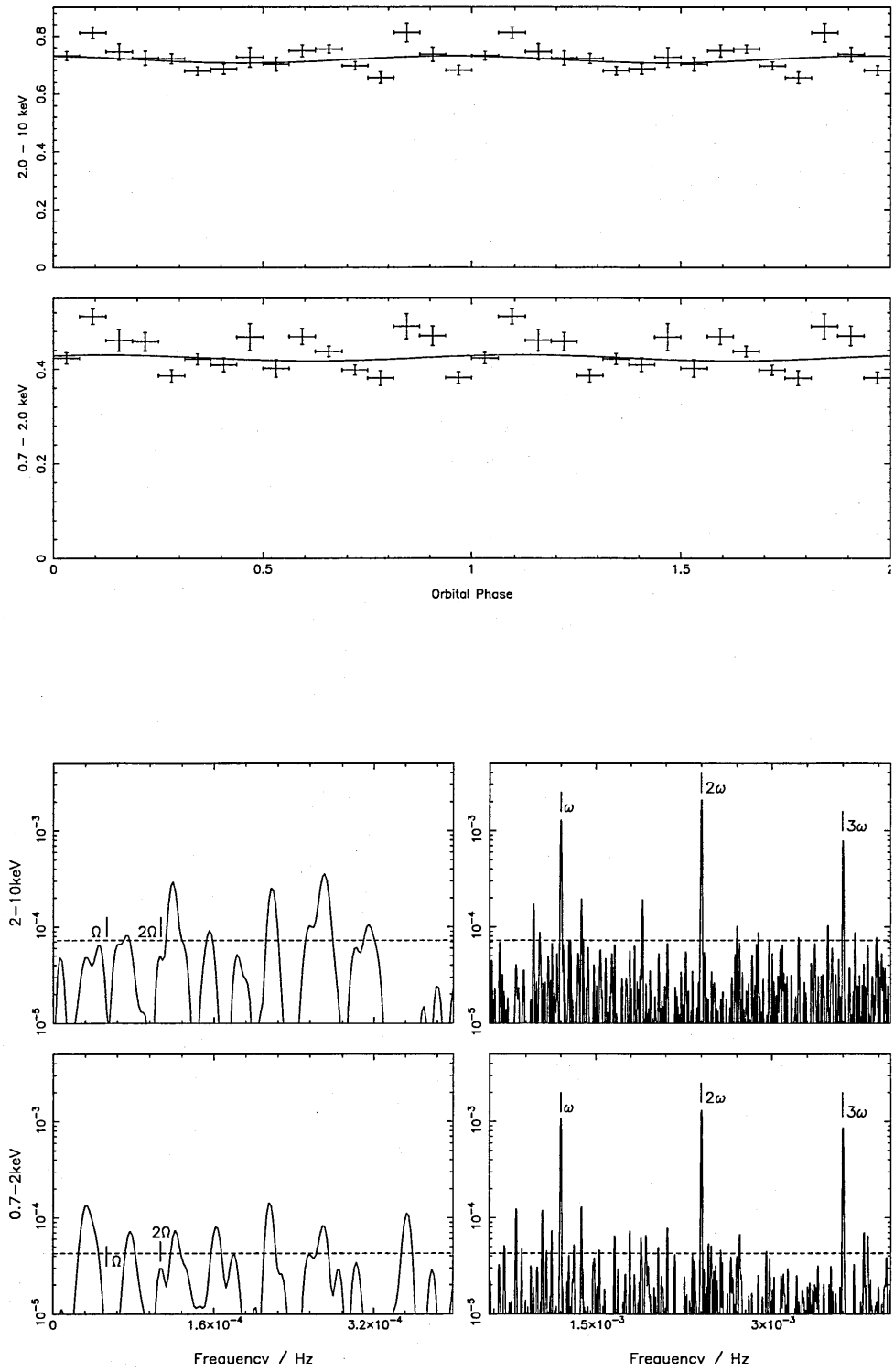

Figure 2.1: (m) PQ Gem (2)

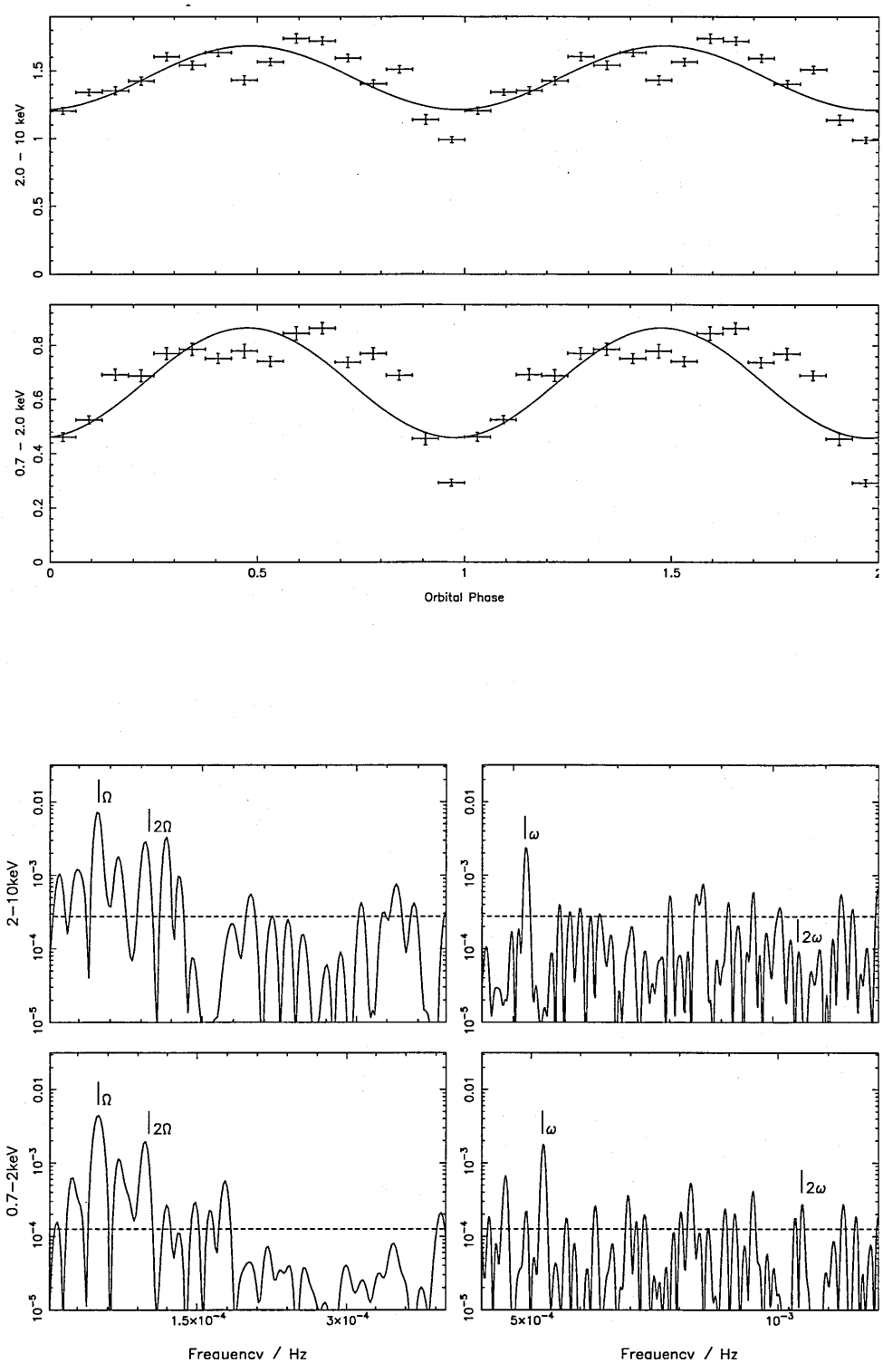

Figure 2.1: (n) TV Col

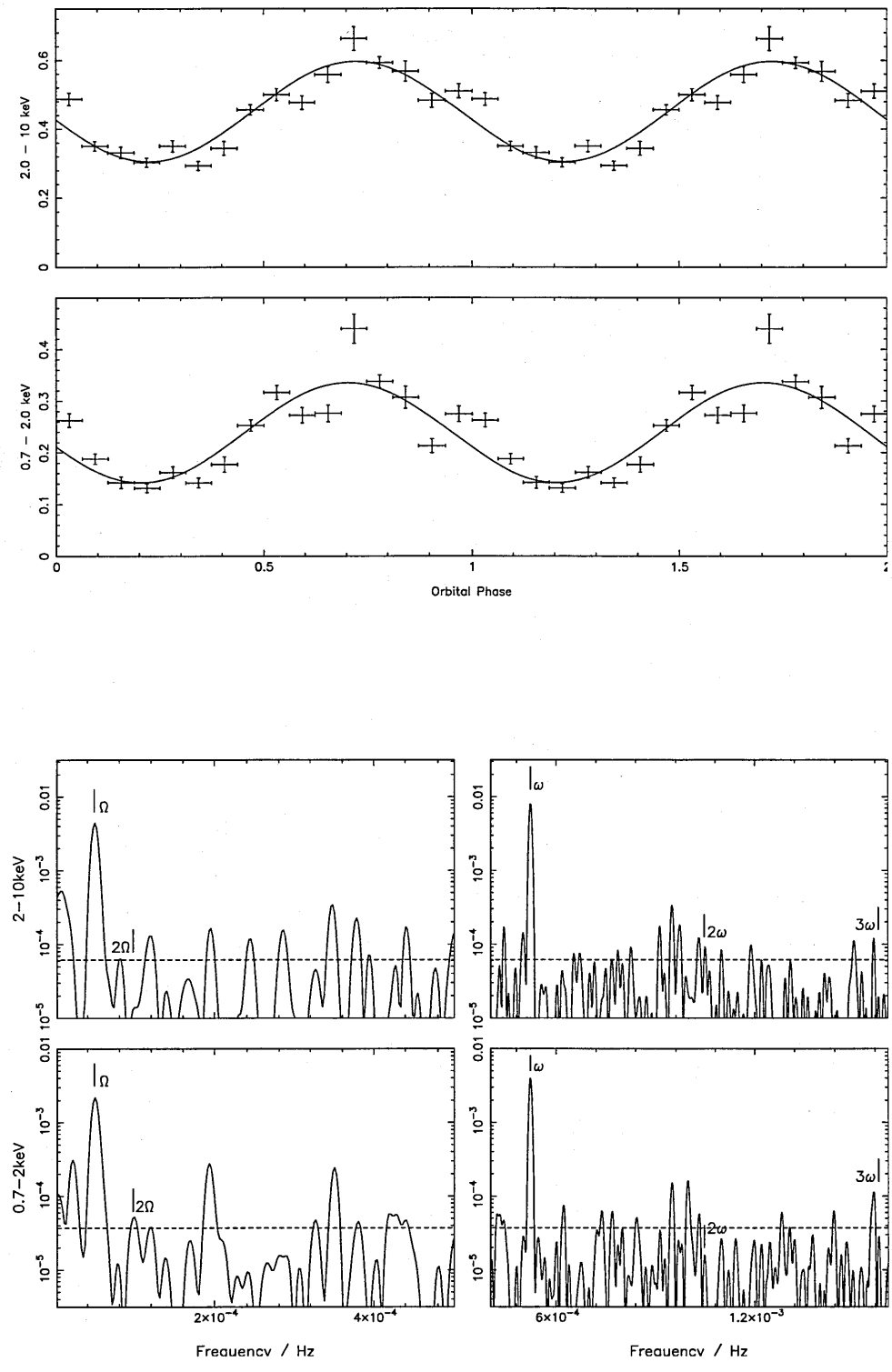

Figure 2.1: (o) TX Col

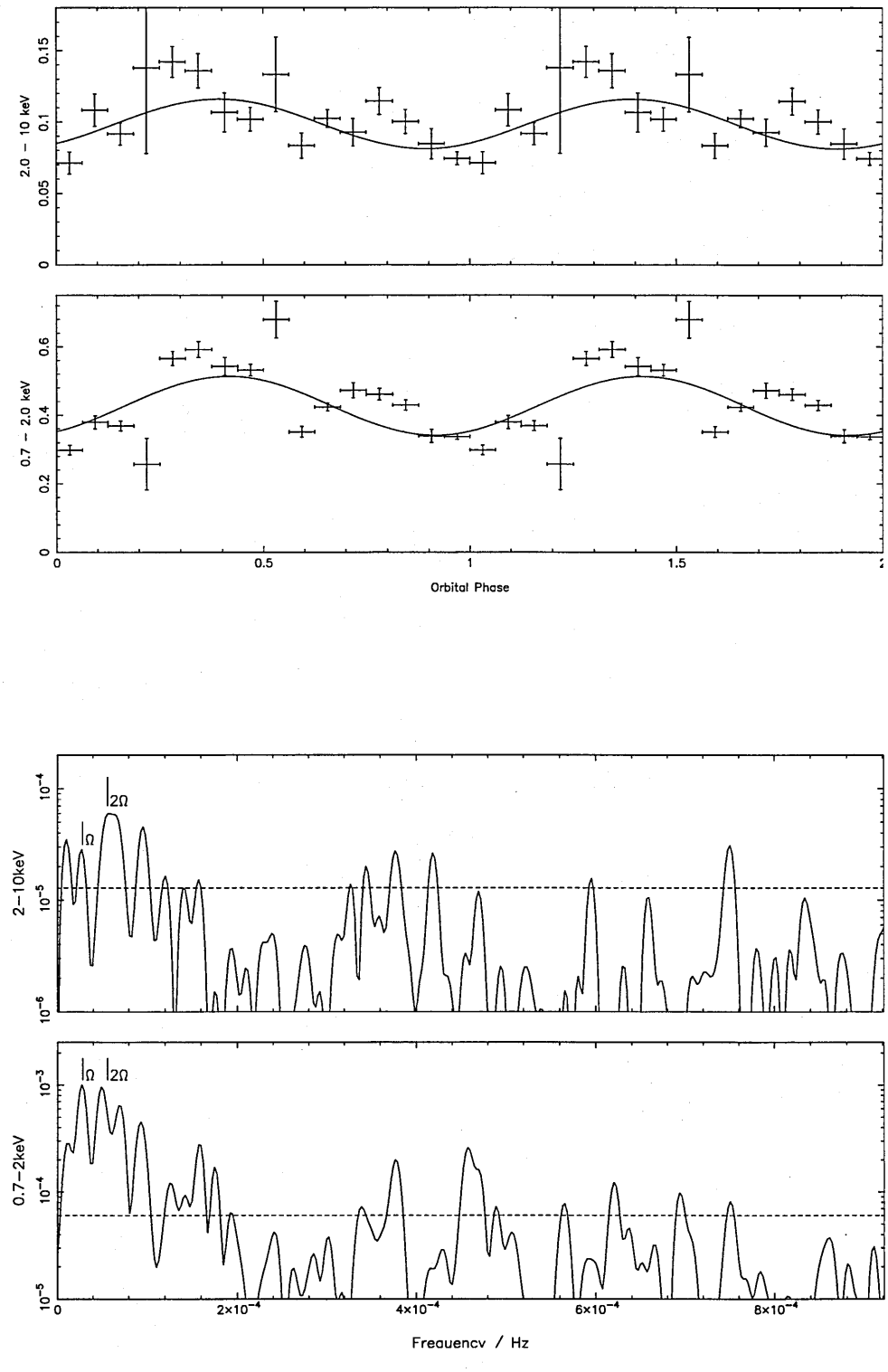

Figure 2.1: (p) AE Aqr

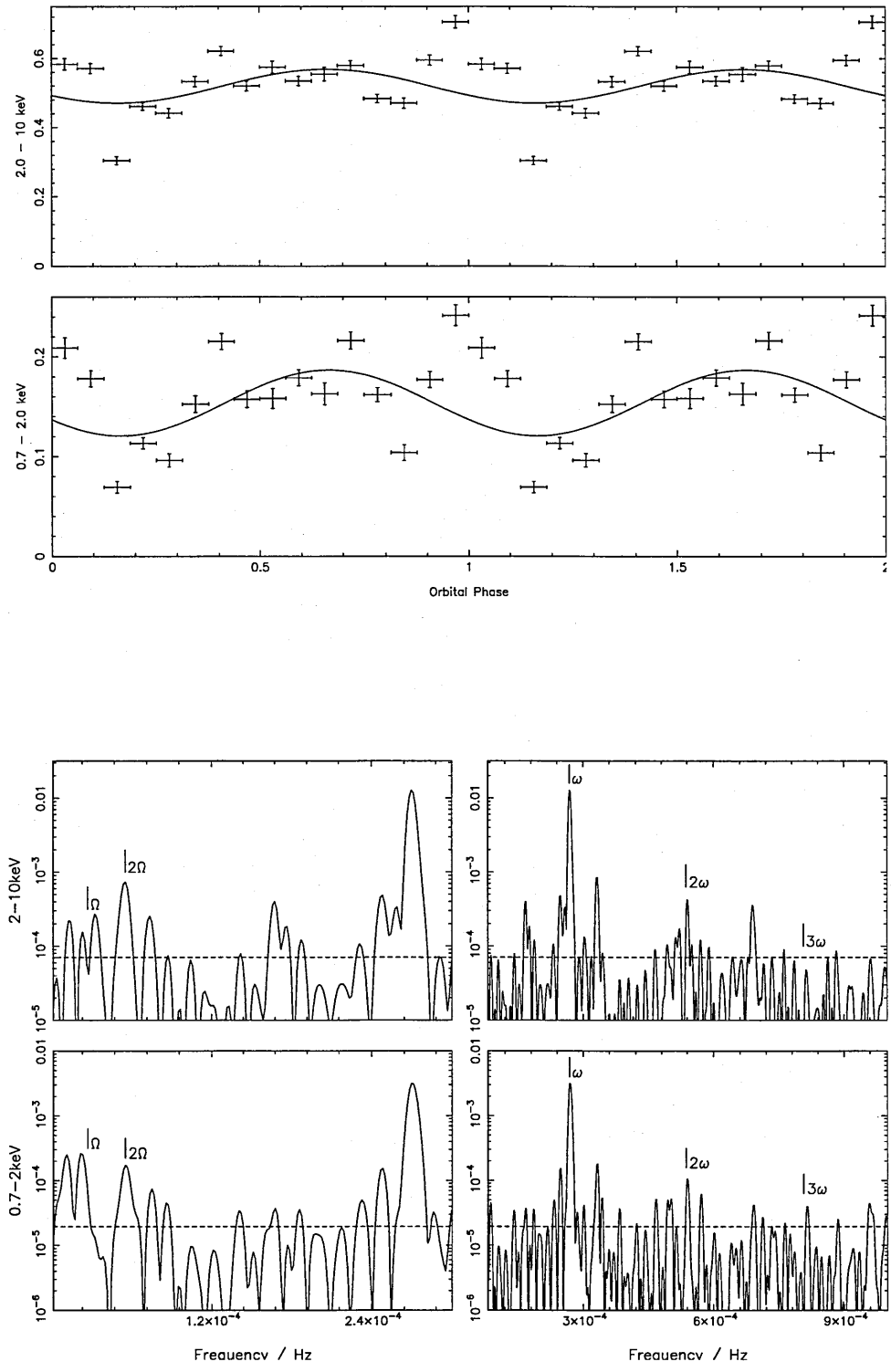

Figure 2.1: (q) V1062 Tau

Figure 2.2: Upper panels: Orbital phase folded *RXTE* lightcurves of each object with the best fit sinusoid overplotted in each case. Lower panels: power spectra of the *RXTE* lightcurves of each object. The low frequency range is shown on an expanded scale in each case to aid visibility of the orbital components; ω - indicates the spin frequency, Ω - indicates the orbital frequency and the horizontal dashed line indicates the noise level in the power spectra, for details see text.

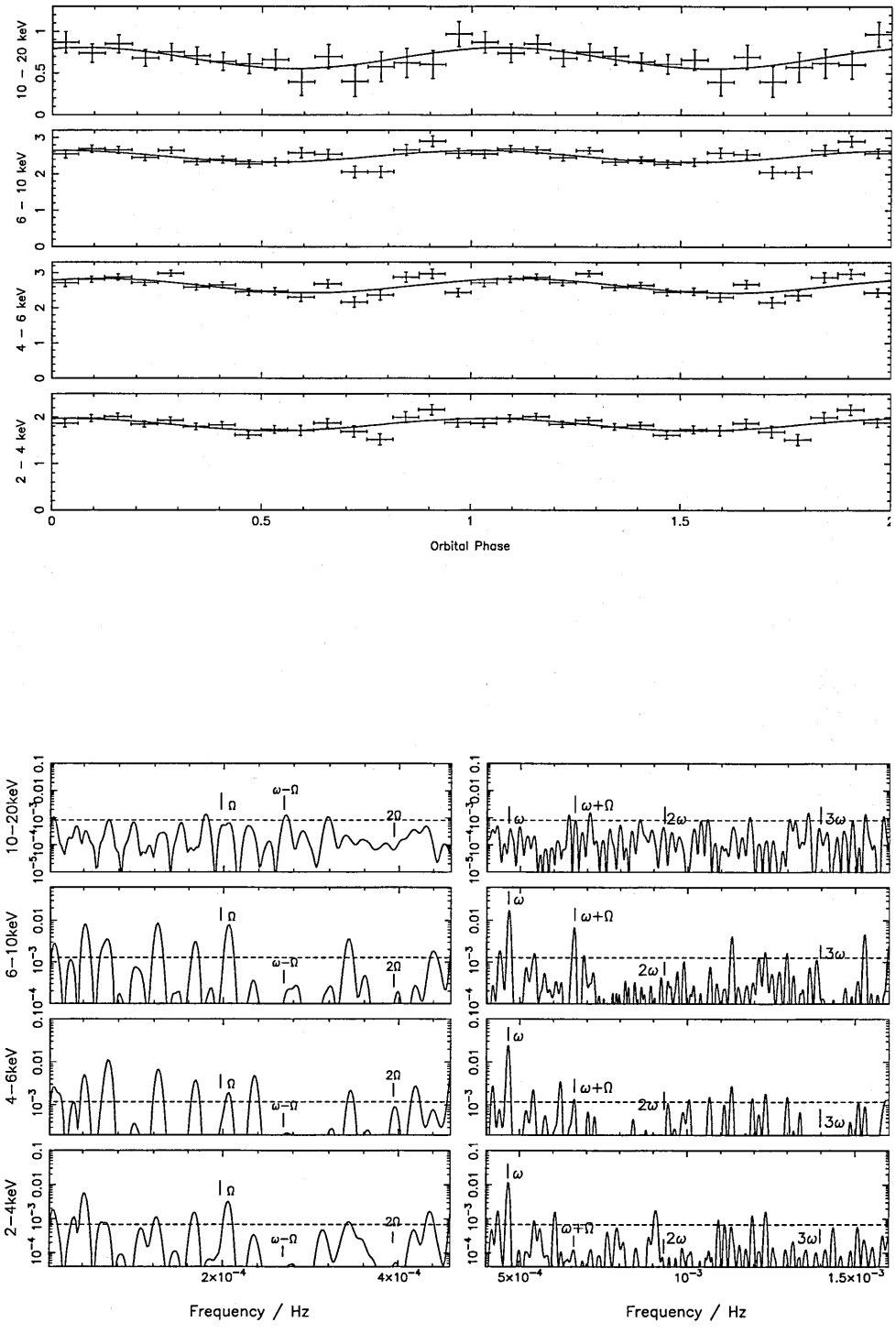

Figure 2.2: (a) V1025 Cen

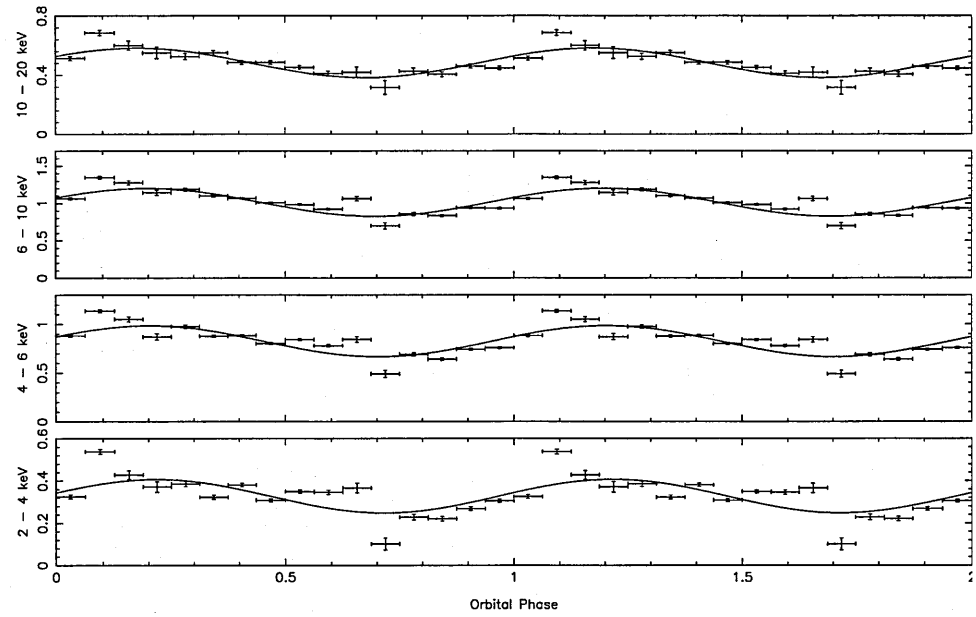

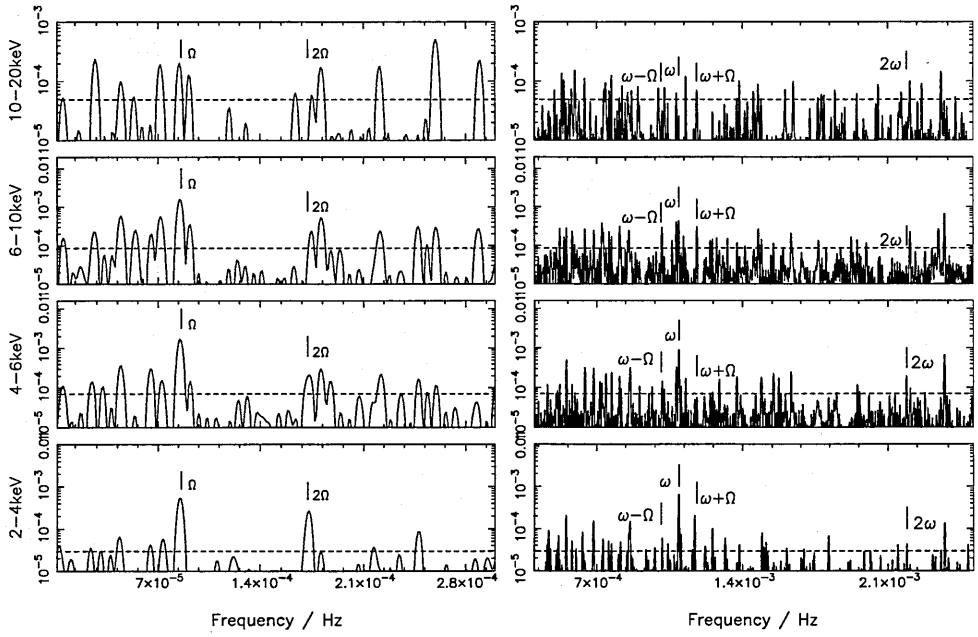

Figure 2.2: (b) BG CMi

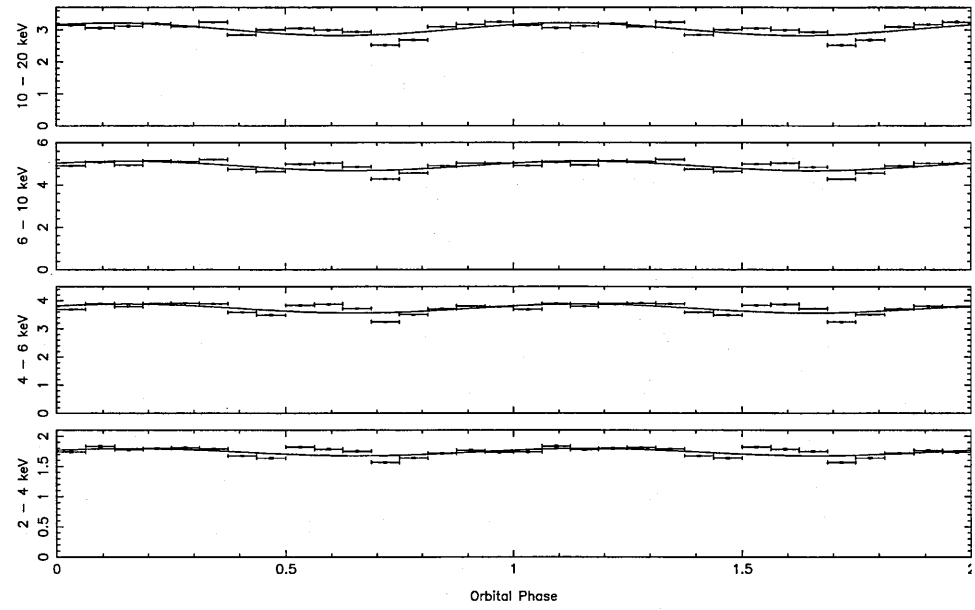

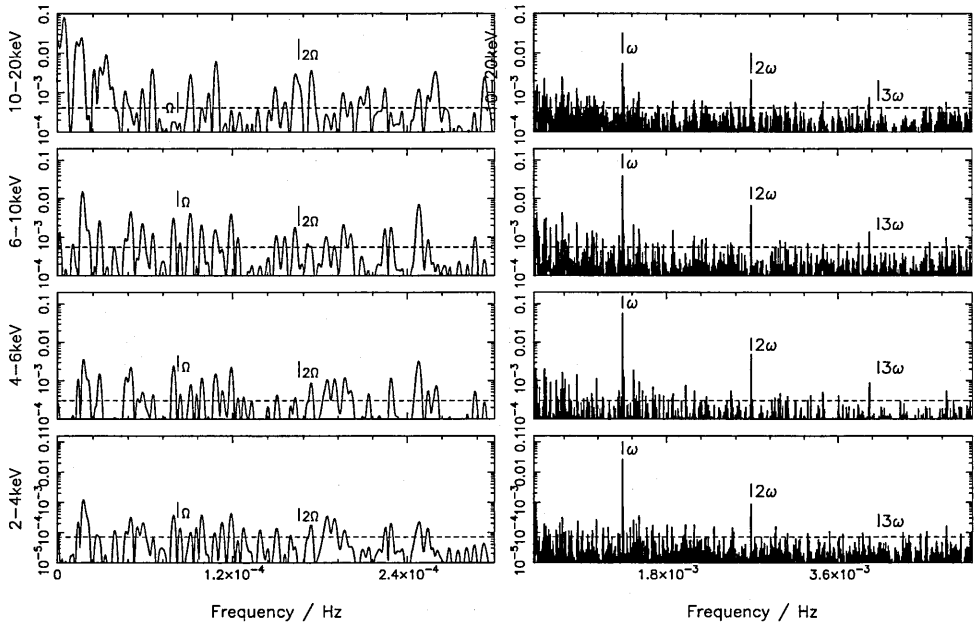

Figure 2.2: (c) V1223 Sgr

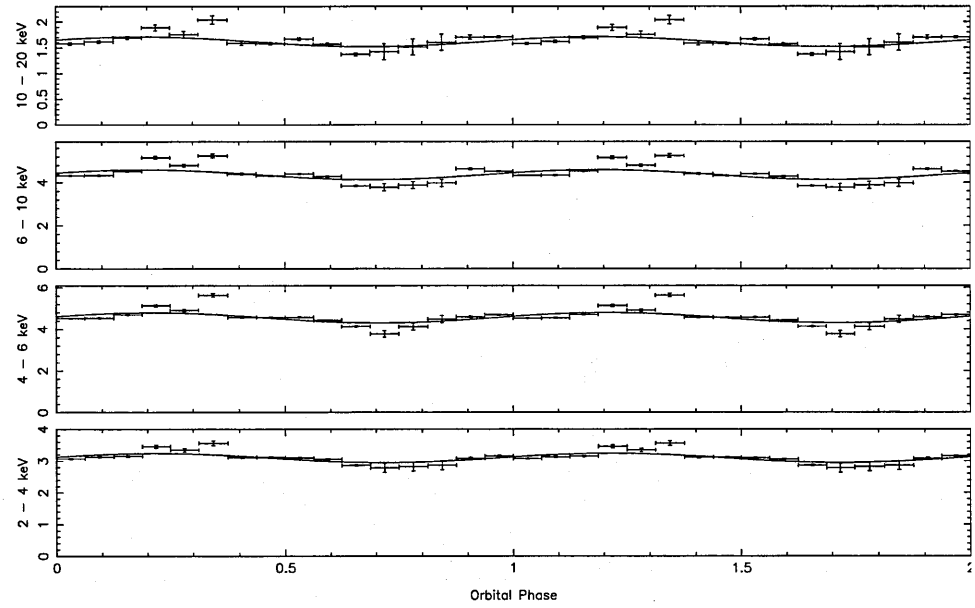

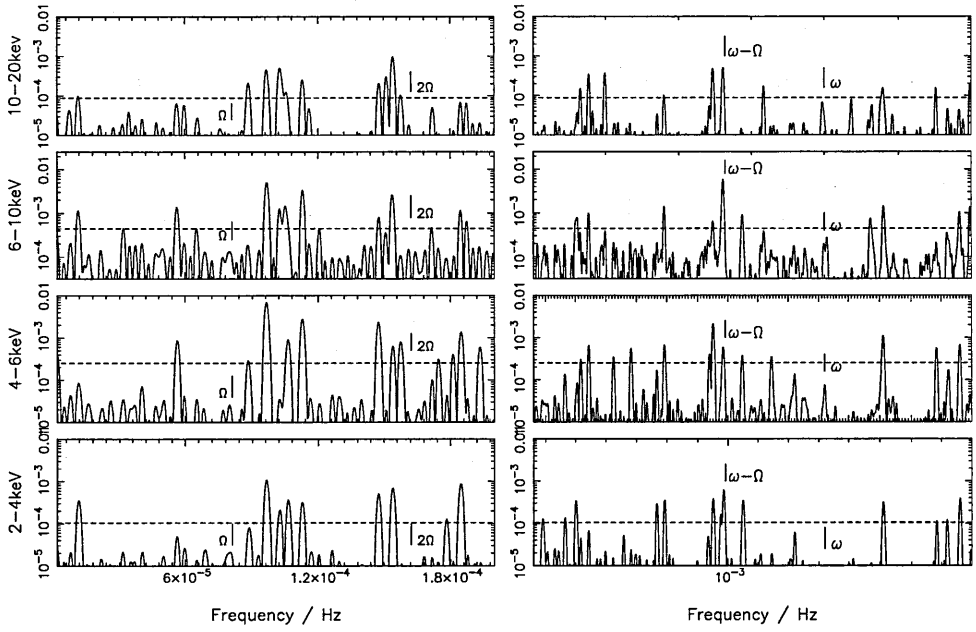

Figure 2.2: (d) V2400 Oph

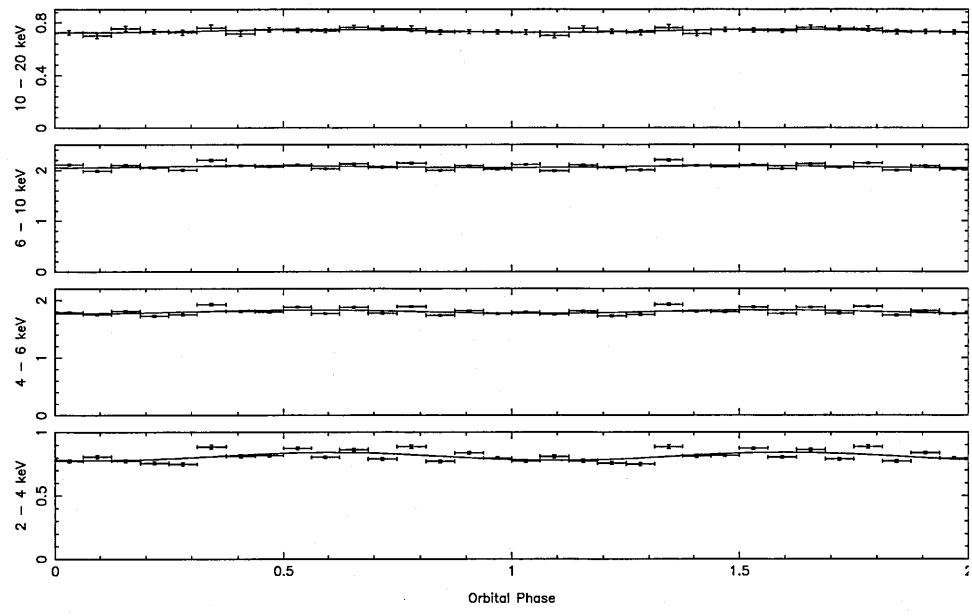

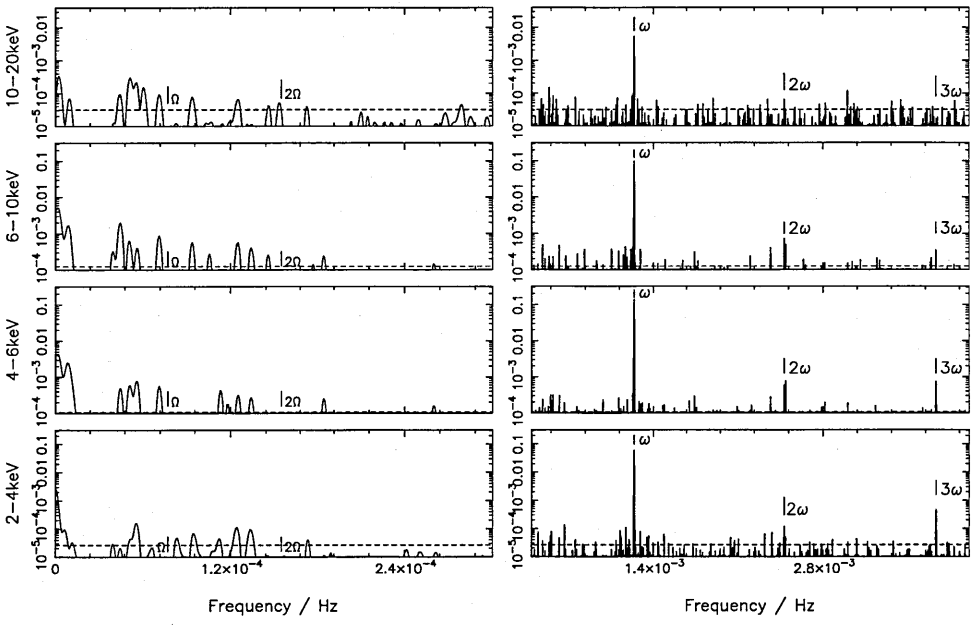

Figure 2.2: (e) AO Psc

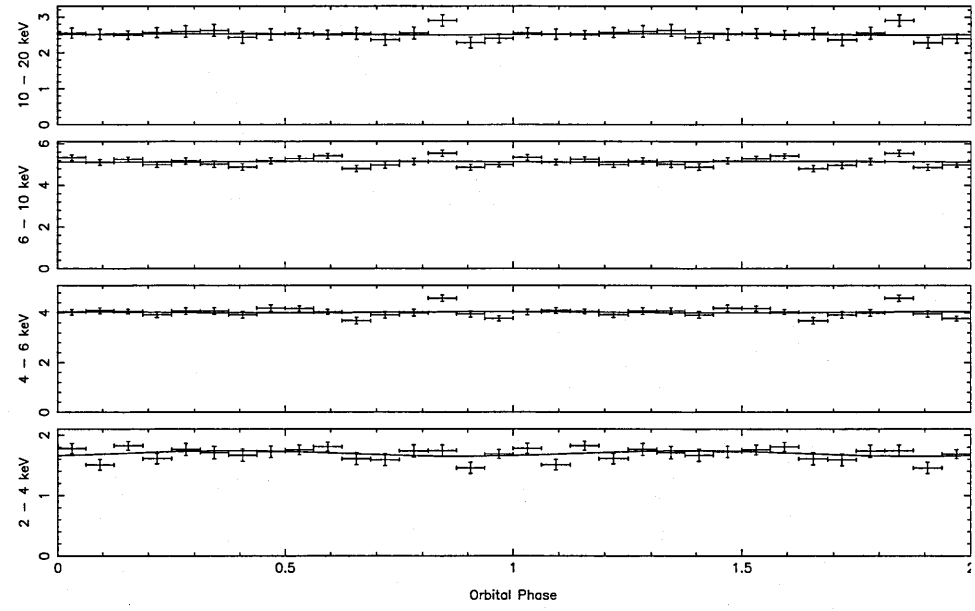

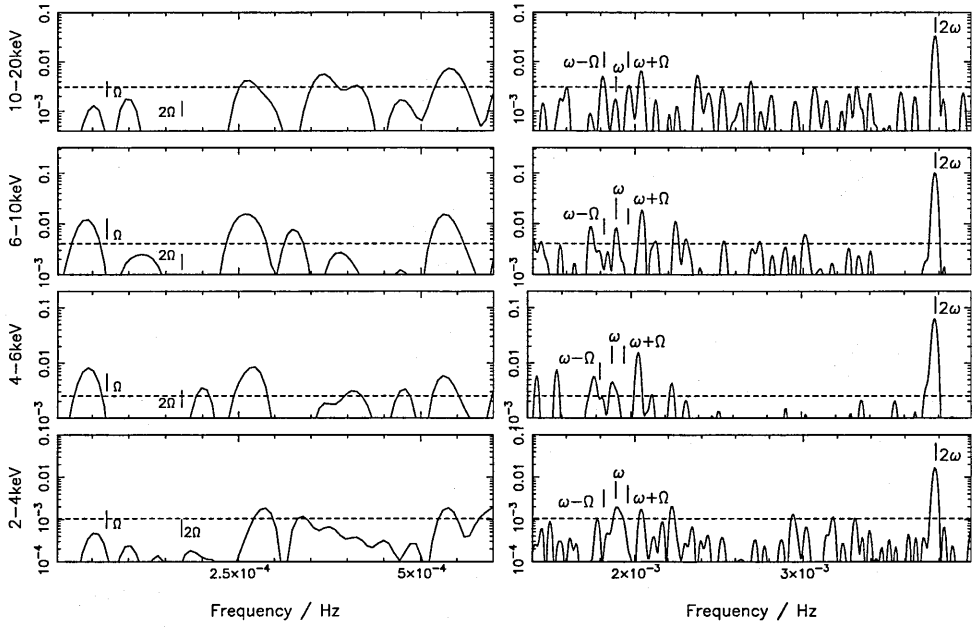

Figure 2.2: (f) YY Dra

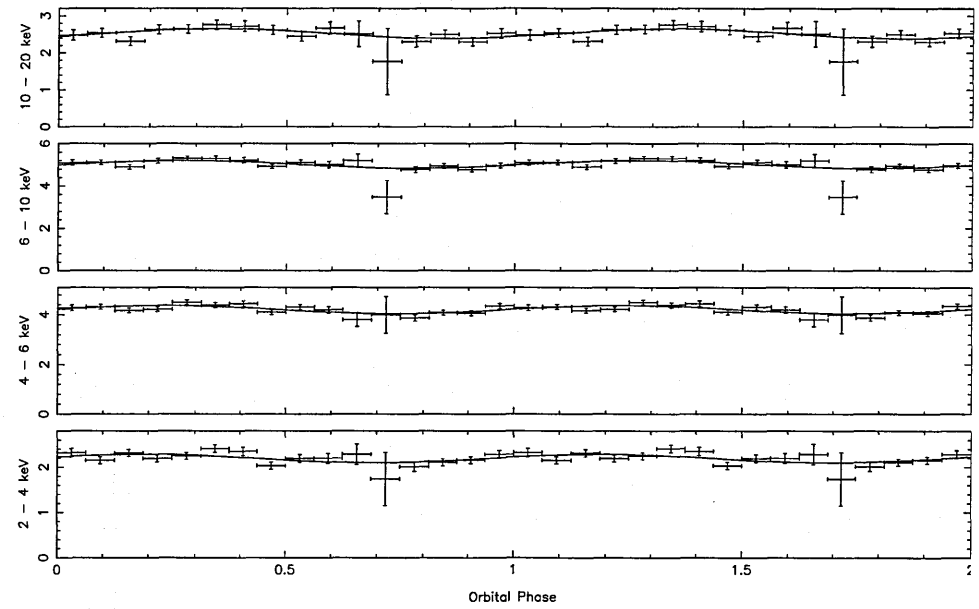

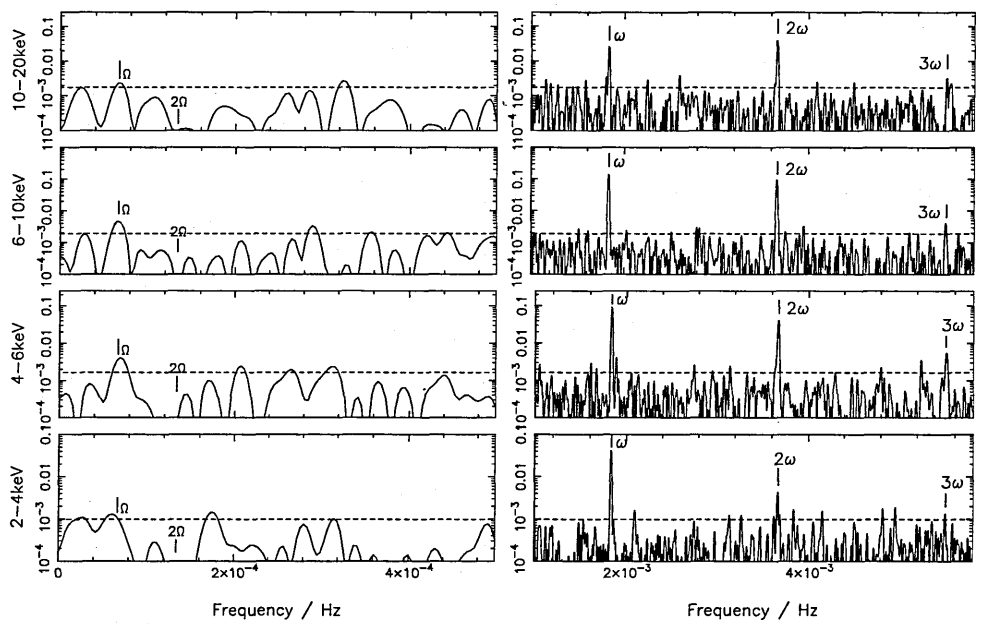

Figure 2.2: (g) V405 Aur

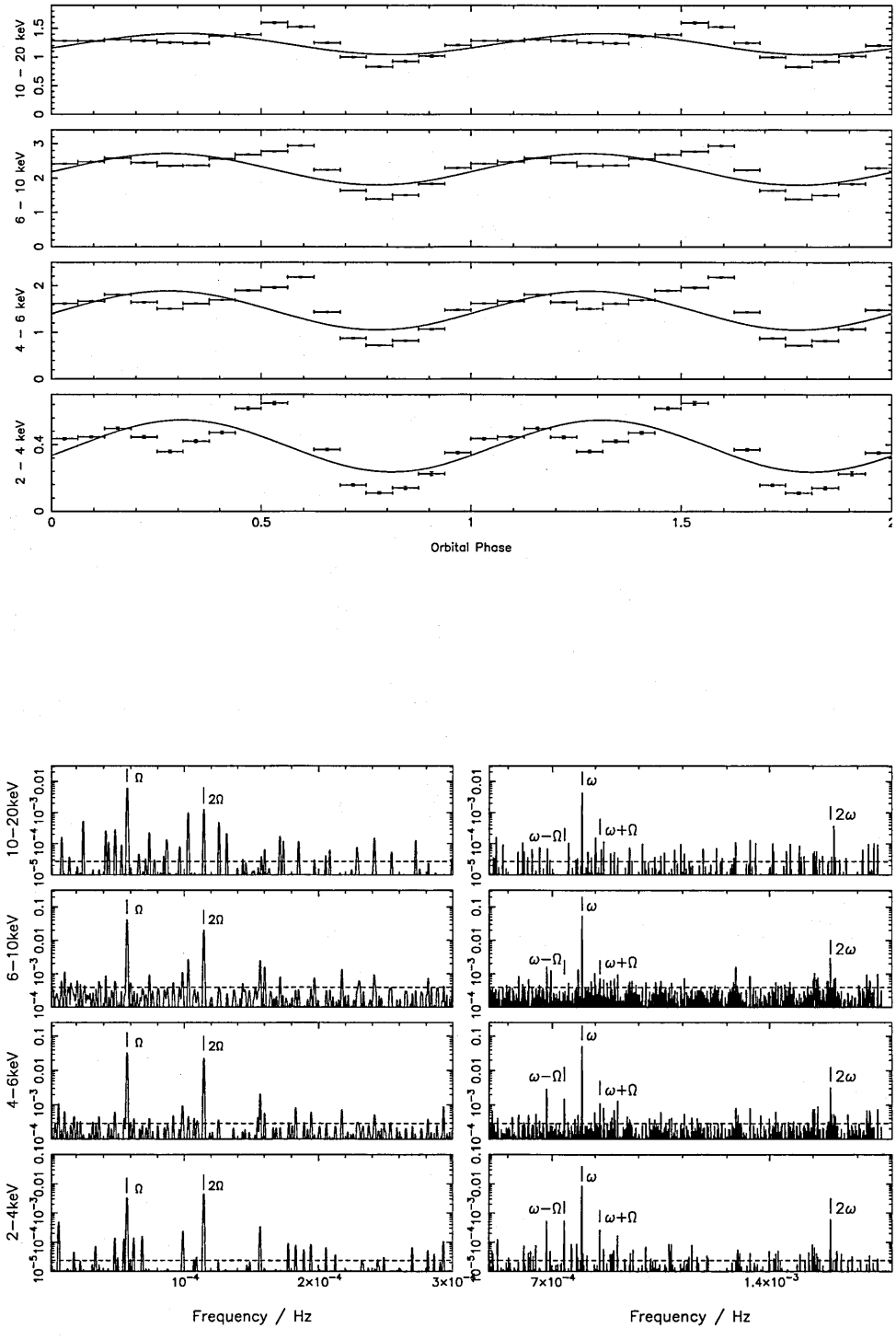

Figure 2.2: (h) FO Aqr

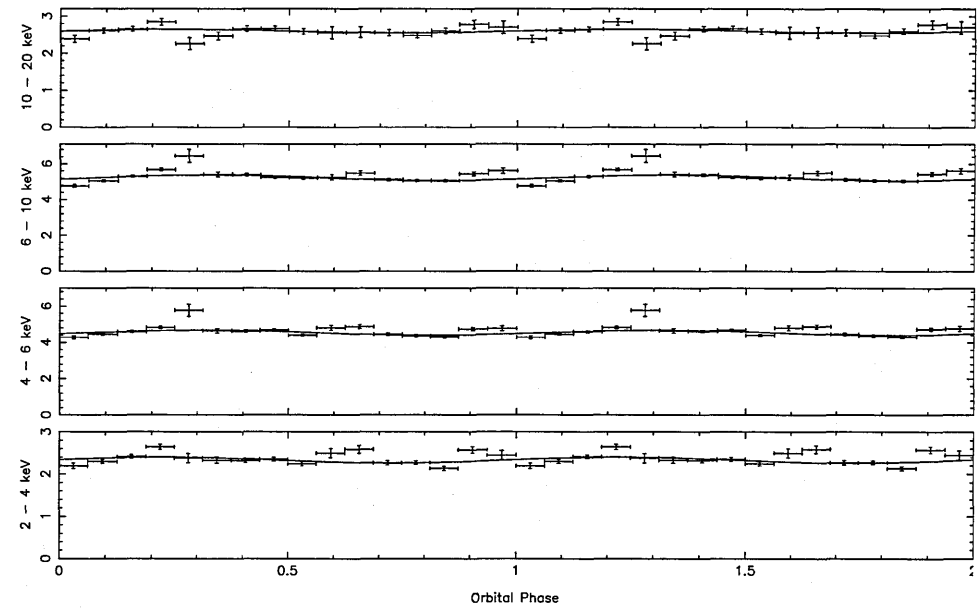

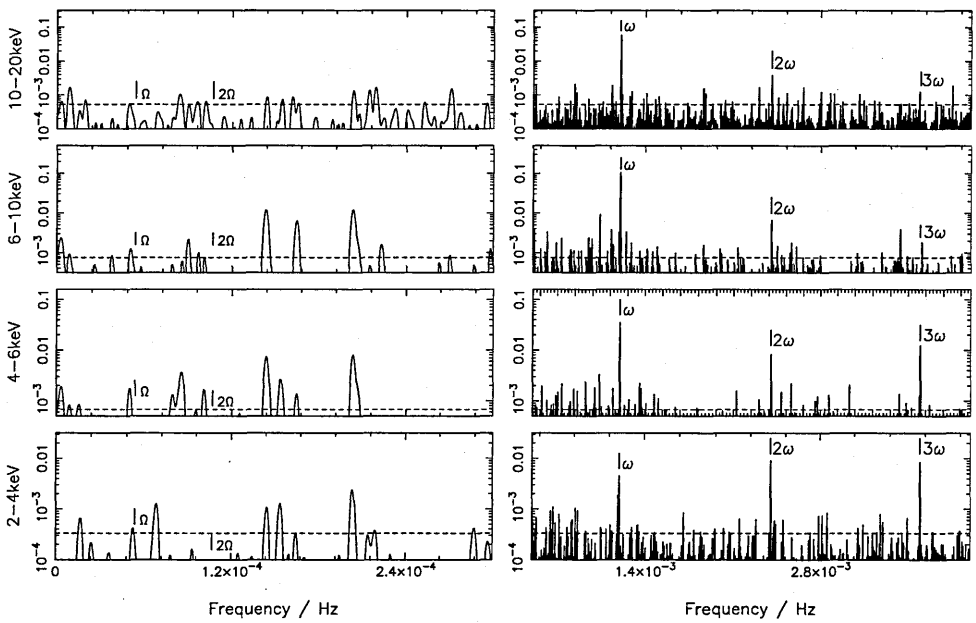

Figure 2.2: (i) PQ Gem

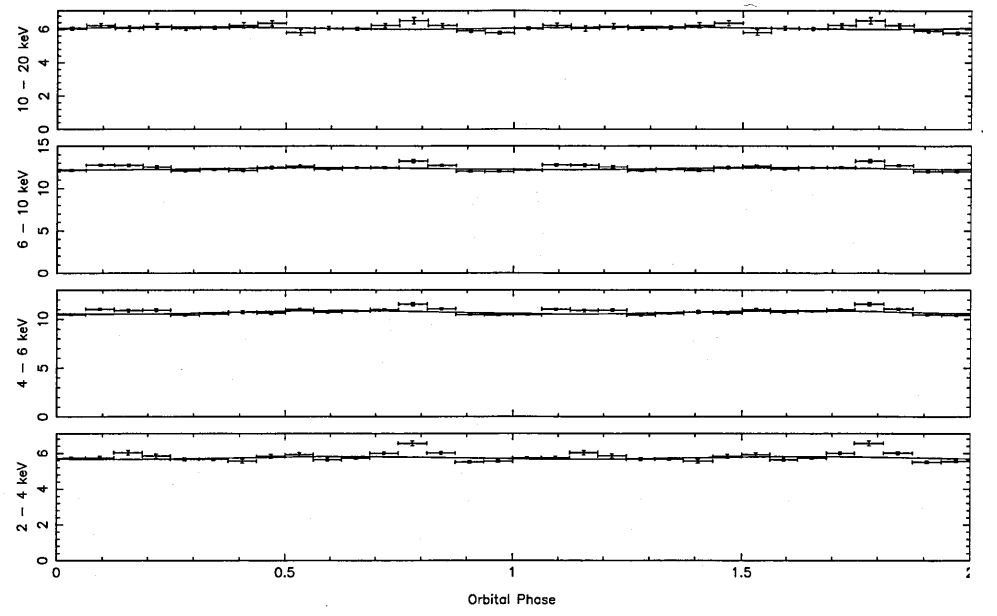

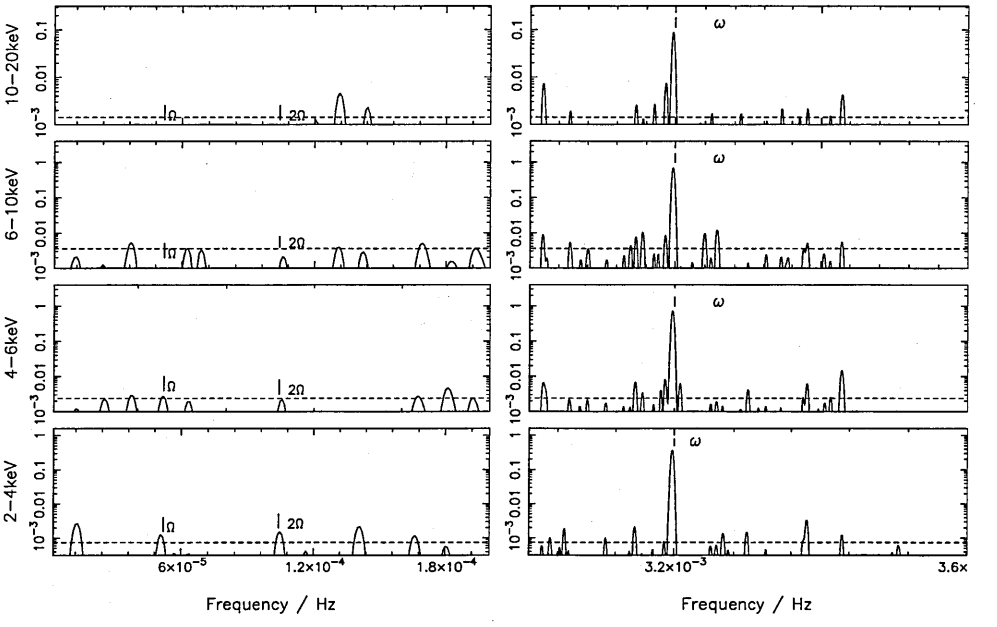

Figure 2.2: (j) V709 Cas

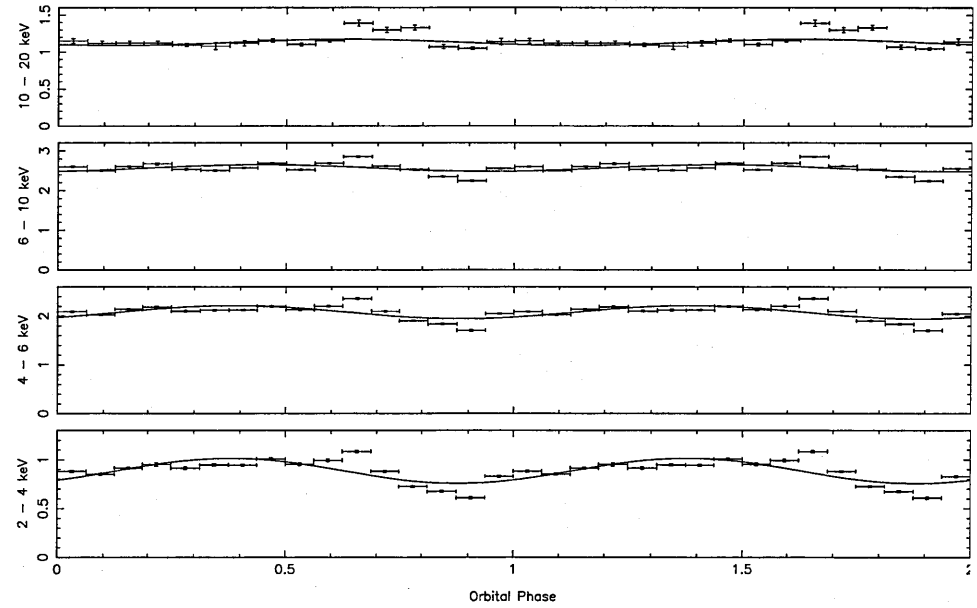

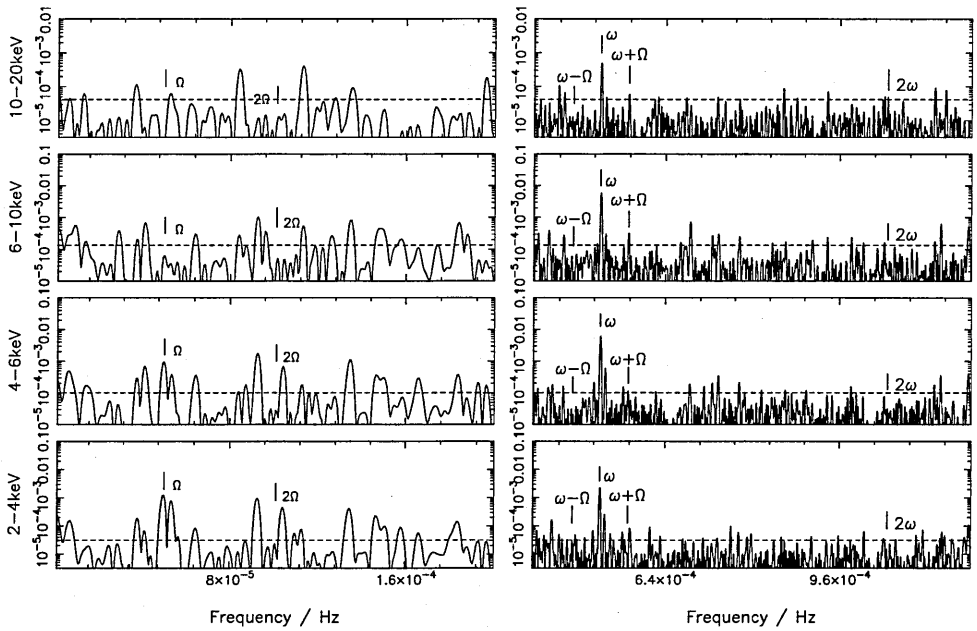

Figure 2.2: (k) TV Col

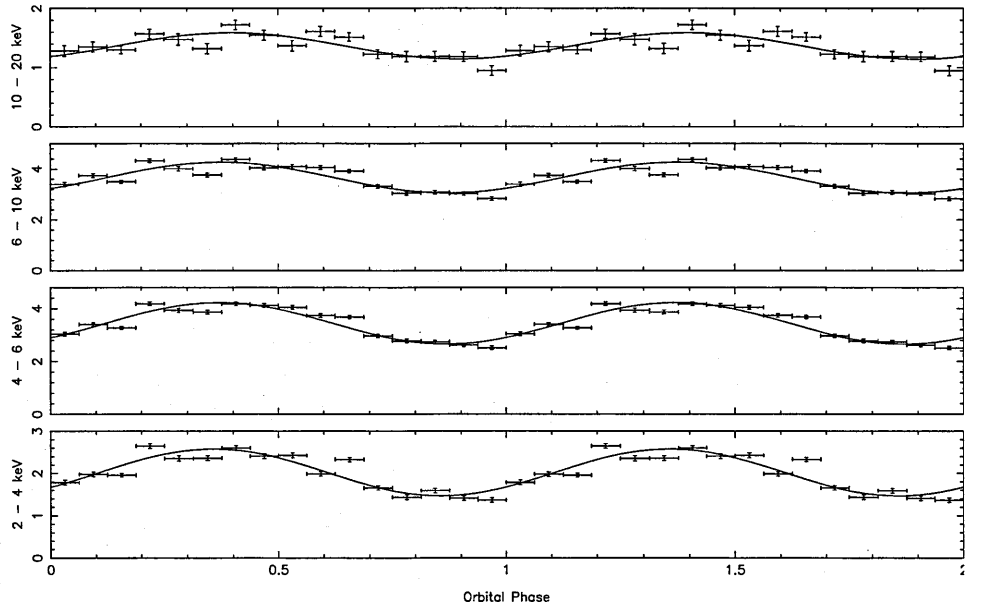

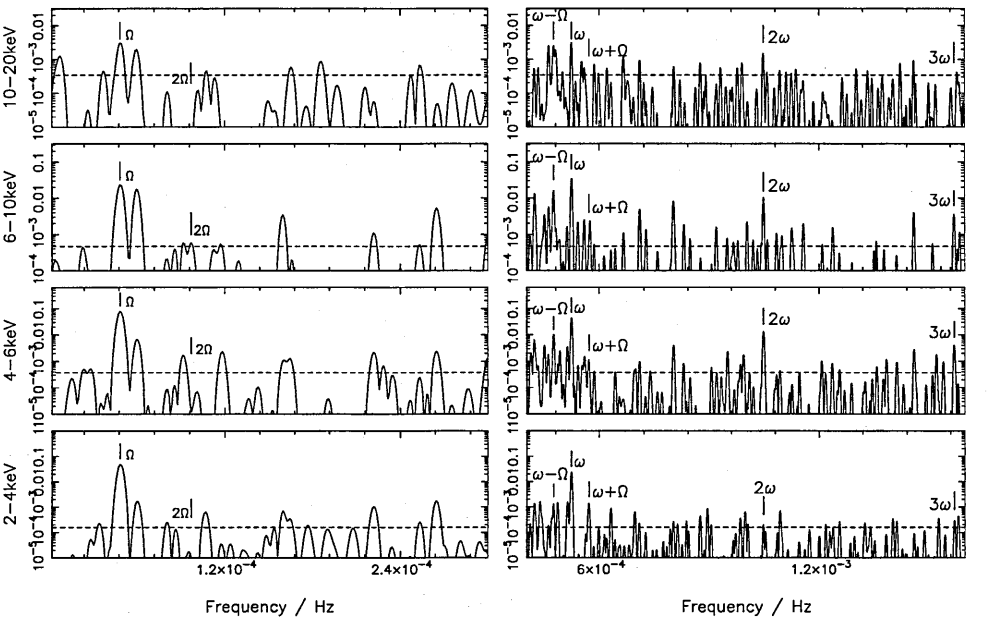

Figure 2.2: (l) TX Col

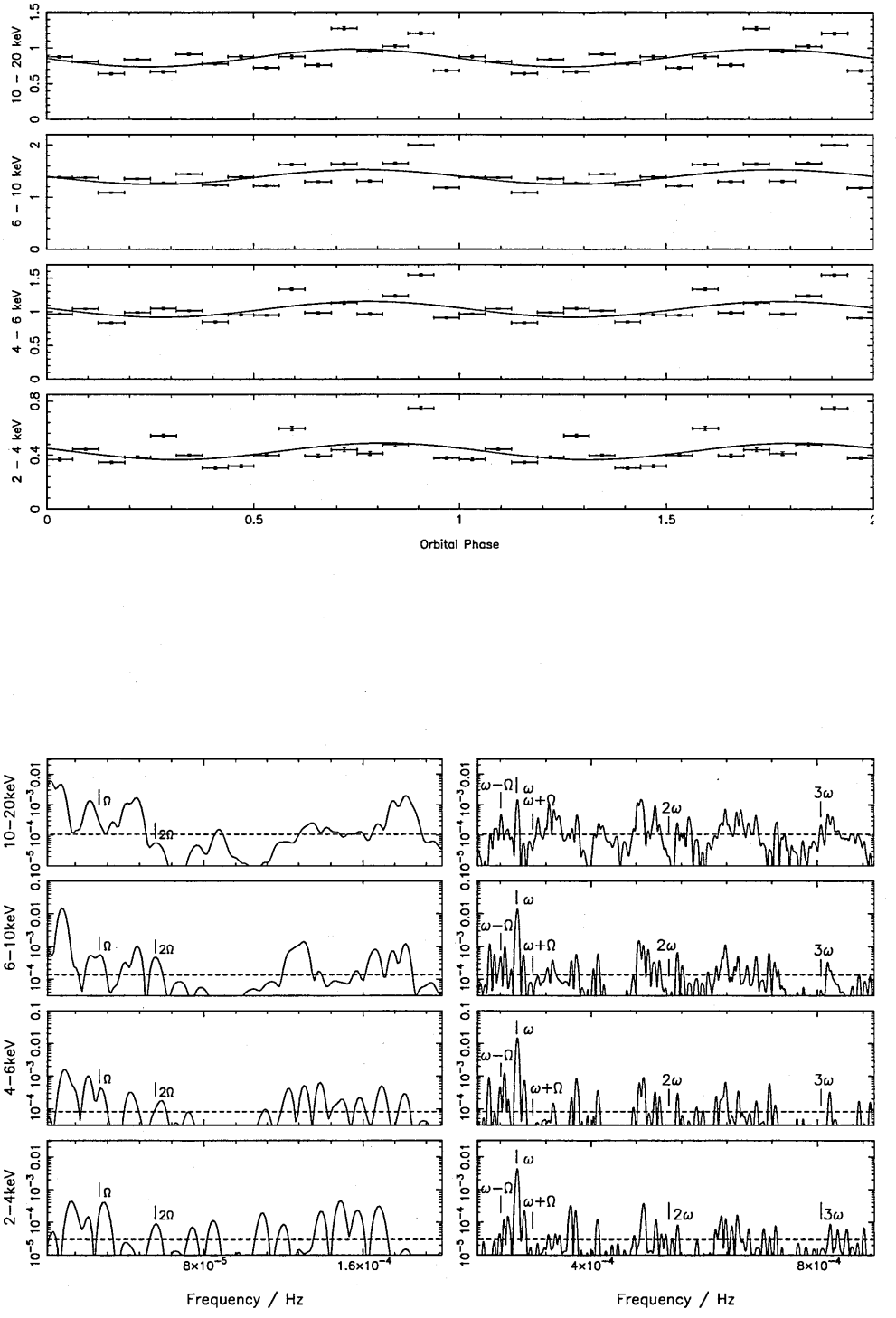

Figure 2.2: (m) V1062 Tau

Table 2.4: Orbital modulation depths for *ASCA* data

Source	0.7–2 keV depth $\pm 1\sigma$	phase of min. flux	χ^2_r	2–10 keV depth $\pm 1\sigma$	phase of min. flux	χ^2_r
V1025 Cen	3%±3%	0.73±0.17	5.8	2%±2%	0.76±0.16	4.7
BG CMi	82%±9%	0.73±0.02	11	43%±4%	0.70±0.01	9.8
V1223 Sgr	28%±3%	0.64±0.02	18	14%±2%	0.65±0.02	12
V2400 Oph	4%±2%	0.65±0.09	8.2	4%±2%	0.57±0.10	15
AO Psc	47%±5%	0.08±0.02	29	25%±4%	0.07±0.02	24
YY Dra	9%±4%	0.69±0.07	10	5%±5%	0.70±0.14	15
LS Peg	21%±10%	0.09±0.09	1.5	21%±8%	0.05±0.06	2.2
V405 Aur(1)	6%±2%	0.71±0.07	4.0	2%±1%	0.68±0.15	1.7
V405 Aur(2)	21%±4%	0.54±0.03	6.3	9%±3%	0.57±0.04	3.4
V2306 Cyg	25%±8%	0.56±0.06	3.3	18%±6%	0.56±0.04	3.2
FO Aqr	102%±13%	0.04±0.02	26	70%±10%	0.99±0.02	90
PQ Gem(1)	10%±3%	0.83±0.05	5.1	4%±1%	0.79±0.05	1.3
PQ Gem(2)	3%±4%	0.62±0.26	6.2	3%±3%	0.46±0.14	4.6
TV Col	47%±6%	0.98±0.02	32	28%±4%	0.98±0.02	22
TX Col	58%±6%	0.20±0.01	7.0	49%±3%	0.22±0.01	3.9
AE Aqr	34%±9%	0.92±0.03	14	30%±7%	0.89±0.04	3.1
V1062 Tau	35%±12%	0.16±0.06	32	17%±8%	0.16±0.08	40

Table 2.5: Orbital modulation depths for *RXTE* data

Source	2–4 keV depth $\pm 1\sigma$	phase of min. flux	χ^2_r	4–6 keV depth $\pm 1\sigma$	phase of min. flux	χ^2_r
V1025 Cen	13%±3%	0.53±0.03	1.5	14%±3%	0.61±0.03	2.7
BG CMi	39%±9%	0.72±0.02	29	32%±5%	0.70±0.02	31
V1223 Sgr	7%±2%	0.66±0.04	26	8%±2%	0.65±0.04	88
V2400 Oph	9%±2%	0.72±0.02	8.2	10%±2%	0.71±0.02	23
AO Psc	7%±2%	0.10±0.05	9.4	3%±1%	0.05±0.07	10
YY Dra	5%±3%	0.88±0.09	1.4	1%±2%	undefined	2.8
V405 Aur	8%±2%	0.69±0.04	1.2	7%±1%	0.74±0.03	1.3
FO Aqr	57%±14%	0.81±0.03	300	44%±8%	0.78±0.03	770
PQ Gem	6%±3%	0.73±0.07	4.5	6%±2%	0.81±0.05	5.0
V709 Cas	3%±2%	0.14±0.10	5.8	3% ±1%	0.13±0.06	5.5
TV Col	25%±4%	0.88±0.03	61	12%±3%	0.89±0.04	68
TX Col	43%±4%	0.86±0.01	12	37%±2%	0.87±0.01	8.9
V1062 Tau	25%±11%	0.31±0.06	80	20%±7%	0.28±0.05	120

Source	6–10 keV depth $\pm 1\sigma$	phase of min. flux	χ^2_r	10-20 keV depth $\pm 1\sigma$	phase of min. flux	χ^2_r
V1025 Cen	12%±3%	0.52±0.04	2.1	31%±6%	0.58±0.03	1.5
BG CMi	31%±4%	0.70±0.01	22	34%±4%	0.68±0.01	5.6
V1223 Sgr	9%±2%	0.65±0.03	110	12%±3%	0.62±0.03	70
V2400 Oph	10%±3%	0.69±0.03	39	11%±4%	0.69±0.04	9.2
AO Psc	2%±1%	0.98±0.13	9.1	3%±1%	0.08±0.05	0.7
YY Dra	1%±2%	undefined	2.2	2%±3%	undefined	0.8
V405 Aur	7%±1%	0.77±0.03	1.1	10%±2%	0.85±0.04	0.7
FO Aqr	34%±6%	0.78±0.03	650	26%±6%	0.81±0.03	130
PQ Gem	6%±2%	0.83±0.05	6.1	4%±2%	0.75±0.10	1.7
V709 Cas	2%±1%	0.09±0.10	6.3	2%±1%	0.94±0.10	2.4
TV Col	6%±2%	0.94±0.06	57	7%±3%	0.13±0.07	7.7
TX Col	28%±3%	0.87±0.02	11	28%±4%	0.90±0.02	5.2
V1062 Tau	18%±7%	0.26±0.05	160	25%±8%	0.24±0.04	71

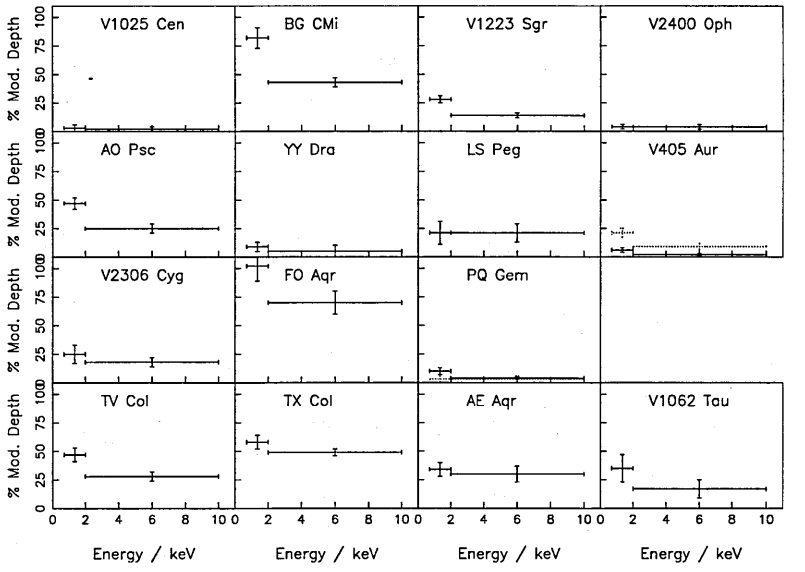

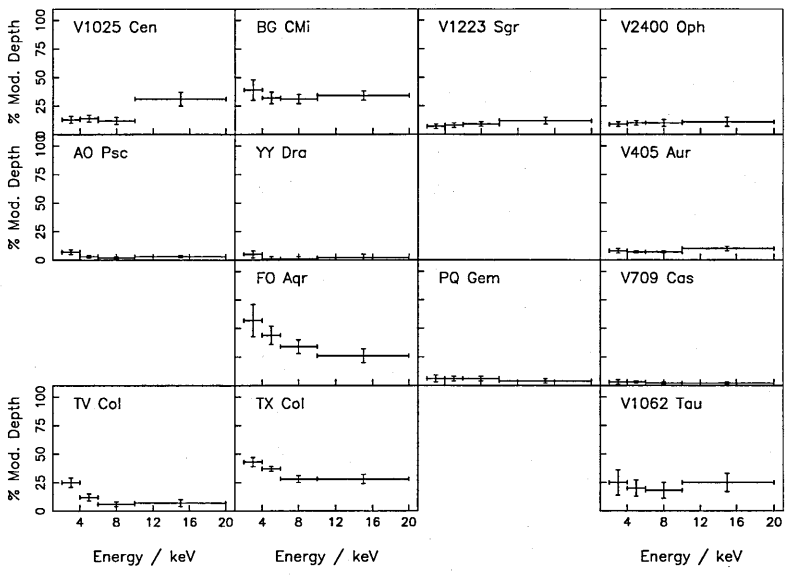

Figure 2.3: Orbital modulation depths measured from (a) the *ASCA* data and (b) the *RXTE* data. Vertical error bars represent the 1σ uncertainties in modulation depths, horizontal error bars indicate the energy range for each measurement. Where more than one observation of a source exists, the second observation is illustrated using dotted lines.

2.6 Discussion of Results

Below we discuss the detailed results for each of the systems, listed in order of increasing orbital period. We begin in each case by reminding the reader of the various periods in each system, whose discovery is discussed in the Appendix A.

2.6.1 V1025 Cen

V1025 Cen was discovered by Buckley et al. (1998a) and found to have a spin period of 2147s and a suggested orbital period of 1.41hr (Hellier et al. 1998). This object is little studied, with no published ephemeris and no determination of the binary inclination. From the *ASCA* data (Figure 2.1a) no significant orbital modulation is seen in the phase folded lightcurves though there is some variability. The power spectra show signals only at the WD spin frequency and its harmonics. From the sinusoid fits to the orbital folded data we see that the modulation depths are consistent with zero (Table 2.4) in both energy bands. The *RXTE* data (Figure 2.2a), like the *ASCA* data, show a variability in the folded lightcurves but the power spectra show nothing to indicate a clear orbital modulation. The sinusoid fits however, show evidence for a modulation depth that is just significant at the $\sim 3\sigma$ level at all energies (Table 2.5) and this is reinforced by the fitted phase of minimum flux being consistent with the same phase across the four energy bands.

2.6.2 BG CMi

BG CMi is a well-known IP with an orbital period of $\sim$ 3.25hr and a spin period of 913s. The published orbital ephemeris of Hellier (1997b) is referenced to a spectroscopic eclipse believed to coincide with inferior conjunction of the secondary. BG CMi has a moderate inclination angle, $\sim 55^\circ - 75^\circ$ inferred by de Martino et al. (1995b) from the orbital modulation. The *ASCA* observation of BG CMi comprised two separate visits,

separated by only a few days, in order to fully sample the orbital phase of the system whose period is close to twice the orbital period of the *ASCA* satellite. The resulting phase folded lightcurve (Figure 2.1b) shows a strong dip at phase 0.7 in both energy bands and the corresponding power spectra reveal the expected strong signals at the orbital frequency. Sinusoid fits to the modulation yield large modulation depths which decrease with increasing energy. The *RXTE* phase folded lightcurves (Figure 2.2b) also show a modulation dip at phase 0.7 in all energy bands, with corresponding power spectra peaks at both the orbital and twice the orbital frequency. From the sinusoid fitting, the modulation depths show a roughly constant amplitude at all energies.

2.6.3 V1223 Sgr

V1223 Sgr is amongst the brightest IPs in the 1–20 keV band, with an orbital period of 3.36hr (Jablonski & Steiner 1987), and a spin period of 745.63s (Osborne et al. 1985). The published orbital ephemeris of Jablonski & Steiner (1987) is referenced to photometric maximum. Watts et al. (1985), suggest that the inclination of this system is between 16° and 40°. For this system a clear modulation dip is seen in the phase folded lightcurve of the *ASCA* data (Figure 2.1c) at phase 0.65 and clearly seen in the power spectra with peaks at the orbital frequency and also at twice the orbital frequency. The sinusoid fits confirm a decreasing modulation depth with increasing energy. The *RXTE* data give a similar outcome (Figure 2.2c). Although only a slight variation is seen in the folded lightcurves, a shallow modulation dip is apparent at the same phase as seen by *ASCA*. A correspondingly small peak at the orbital frequency is seen in the power spectra, though a lot of noise is present. The sinusoid fits yield small modulation depths that are roughly constant in all energy bands, or possibly even increase slightly with energy, and are significant across all four energy bands.

2.6.4 V2400 Oph

The first diskless IP (Buckley et al. 1995 1997), has a spin period of 927s and an orbital period of 3.42hr, although no ephemeris has been published for V2400 Oph. It is believed to be at a low inclination of 10° (Hellier & Beardmore 2002). Observed with *ASCA* it shows little in the way of an orbital modulation in the phase folded lightcurve (Figure 2.1d). The power spectra and sinusoid fit reveal a similar result, with only a possible peak close to the orbital frequency and a modulation depth that is consistent with zero. A modulation is more apparent in the *RXTE* observation (Figure 2.2d). There is a clear variability in the phase folded lightcurves, with a shallow dip at (arbitrary) phase 0.7. Although no clear peaks are seen in the power spectra at the orbital frequency, the modulation depths from sinusoid fitting are small but just significant at the 3σ level and roughly constant across the energy bands, or possibly even increasing with energy as seen in V1223 Sgr.

2.6.5 AO Psc

AO Psc has a spin period of 805s and an orbital period at 3.59hr (White & Marshall 1981; Patterson & Price 1981). The orbital ephemeris of Kaluzny & Semeniuk (1988) is referenced to photometric maximum. AO Psc has features very similar to that of V1223 Sgr from photometric observations and the star's optical spectrum (Patterson & Price 1981). This similarity is also evident in the folded lightcurves and power spectra of the *ASCA* observation (Figure 2.1e). A strong modulation is clearly seen with a minimum close to phase 0.1, and clear peaks in the power spectra are seen at the orbital frequency. The fitted modulation depths decrease with increasing energy. With the *RXTE* observation, the situation is quite different (Figure 2.2e). There is no strong modulation in the phase folded lightcurve and hardly any variability, and no orbital peaks in the power spectra, which are essentially delta functions at the WD spin frequency. The fitted modulation

depths are not significant above the 3σ level. This system shows clear evidence that the orbital modulation in IPs can come and go on a timescale of a few years.

2.6.6 YY Dra

YY Dra is one of a small number of IPs that show outburst behaviour. Patterson et al. (1992) found the spin period to be 529s, while Mateo et al. (1991) found the orbital period at 3.96hr and derived the inclination to be $42° \pm 5°$. The orbital ephemeris of Haswell et al. (1997) is referenced to the inferior conjunction of the mass donor. YY Dra's phase folded lightcurve from the *ASCA* data does show some variability, and this is reflected in the power spectra with a peak at twice the orbital frequency (Figure 2.1f). However, the sinusoid fits reveal no significant modulation. The *RXTE* data too indicate only slight variability (Figure 2.2f). This is confirmed in the power spectra where no modulations are seen at either the orbital or twice the orbital frequency. The sinusoid fits are consistent with zero modulation depth in all bands.

2.6.7 LS Peg

LS Peg has an orbital period of 4.19hr (Martínez-Pais et al. 1999; Taylor et al. 1999), and a claimed spin period of 1776s (Rodríguez-Gil et al. 2001) deduced from polarimetry. Recent analysis of the *ASCA* data on this object by Baskill et al. (2005) has detected a modulation at 1854s which is probably a more accurate determination of the spin period, and confirms this object as a genuine IP. The orbital ephemeris of Taylor et al. (1999) is based on the blue-to-red crossing of the emission lines, which we interpret as inferior conjunction of the WD. Only observed with *ASCA*, this system shows a strong variability in its orbital phase folded lightcurve (Figure 2.1g). However, the modulation depths are not significant above the 3σ level. There are peaks close to the orbital frequency and twice the orbital frequency, particularly in the lower energy band power spectrum. Although

both power spectra are noisy, signals related to the recently-identified spin period are clearly seen in both bands.

2.6.8 V405 Aur

Haberl et al. (1994) found the orbital period of this system to be 4.15hr, and Skillman (1996a) discovered the WD spin period of 545.46s. The published orbital ephemeris, cited in Harlaftis & Horne (1999), is defined at inferior conjunction of the emission-line source (blue-to-red crossing) and a correction of 0.1 cycles anticlockwise is claimed to give the inferior conjunction of the secondary. The first of the two observations taken with *ASCA* shows a relatively unvarying phase folded lightcurve (Figure 2.1h) with no modulation significant above the 3σ level, although the apparent phase of minimum flux is consistent at 0.7 between the two energy bands. The power spectra show no evidence for an orbital signal either. However, the second *ASCA* observation (Figure 2.1i) shows a prominent dip in the folded lightcurves and the power spectra indicate significant power at both the orbital frequency and twice the orbital frequency. The sinusoid fits to these folded lightcurves struggle to fit the sharp dip in the low energy lightcurve near to phase 0.4 and instead find the sinusoidal minimum close to phase 0.55, in both energy bands. However, only the modulation depth in the low energy band is significant above the 3σ level. The *RXTE* data show something a little different (Figure 2.2g). The folded lightcurves have a very slight dip in each energy band around phase 0.7–0.8, with a significant modulation, whose depth is roughly constant with energy. The power spectra indicate a small peak close to the orbital frequency in each case.

2.6.9 V2306 Cyg

The orbital period of V2306 Cyg is 4.35hr (Zharikov et al. 2002) and its spin period is 1466.66s (Norton et al. 2002). The published orbital ephemeris is referenced to inferior

conjunction of the secondary from both photometry and spectroscopy (Zharikov et al. 2002). Another system to be observed only by *ASCA*, V2306 Cyg is the recently adopted name of 1WGA J1958.2+3232. The phase folded lightcurve of this system is an interesting one with a rather variable flux and an apparent modulation dip seen at phase 0.5 (Figure 2.1j). If we compare with the power spectra, in the low energy band a marginal peak at twice the orbital frequency is seen with also a small peak associated with the orbital frequency. If we move to the higher energy band, the orbital frequency peak becomes more visible. The sinusoid fits are consistent with a decreasing modulation depth with increasing energy but the modulation is not seen above 3σ significance in either band.

2.6.10 FO Aqr

Patterson et al. (1998) found the orbital and spin periods to be 4.85hr and 1254s respectively with the ephemeris referred to the optical photometric minimum. This system shows a very prominent dip in the phase folded lightcurve from the *ASCA* data (Figure 2.1k) in both energy bands. The power spectra show that the orbital frequency and its harmonic are detected strongly and the sinusoid fits confirm the decreasing modulation depth with increasing energy. The phase folded *RXTE* lightcurves also show a clear and prominent modulation in all four energy bands and the power spectra confirm this. The modulation depths determined from sinusoid fits also confirm what is shown in the figures, with a steadily decreasing modulation depth with increasing energy. The fitted phases of minimum flux suffer from the modulation profile being distinctly non-sinusoidal: in both observations, there is a deep minimum followed by a shallower minimum. In the *ASCA* data these minima occur at phases 0.9 and 0.3 respectively, whereas in the *RXTE* observation they have apparently shifted to phase 0.75 and 0.25. This apparent shift may be due to the shape of the modulation profile changing with energy, or alternatively it may

be evidence for a changing accretion structure on a four year timescale as the accumulated phase error from the ephemeris is less than 0.02 in phase.

2.6.11 PQ Gem

The ephemeris for PQ Gem (Hellier 1997b) is defined relative to red-to-blue crossing of the emission-lines. The system has an orbital period of 5.19hr and a spin period of 833.41s (Hellier 1997b). In the first observation of PQ Gem with *ASCA* (Figure 2.1l), the power spectra show a peak associated with the orbital frequency in the low energy band, but nothing is seen in the second observation (Figure 2.1m). The folded lightcurves of both observations are unconvincing and although the modulation depths from the first observation are just significant at the 3σ level, those from the second observation are not. Moving to the *RXTE* data (Figure 2.2i), there is again little evidence of orbital modulation in either the folded lighturves or power spectra, and the fitted modulation depths are once again consistent with zero at the 3σ level.

2.6.12 V709 Cas

Both the ephemeris and the orbital period for this system were determined by Bonnet-Bidaud et al. (2001b), the ephemeris being with respect to the blue-to-red crossing time of emission lines and the orbital period is 5.34hr. The spin period of the WD is known to be 312.8s (Haberl & Motch 1995a; Norton et al. 1999). V709 Cas has been observed by *RXTE* only (Figure 2.2j). It shows no evidence of an orbital modulation in either its folded lightcurves or power spectra, and the fitted modulation depths are all consistent with zero.

2.6.13 TV Col

TV Col has an orbital period of 5.486hr (Hutchings et al. 1981) and a spin period of 1911s (Schrijver et al. 1985) as well as a second photometric (superhump) period and a longer disk precession period. The orbital ephemeris (Hellier 1993) is referenced to a shallow photometric eclipse. TV Col shows very interesting features in both observations. The *ASCA* folded lightcurves (Figure 2.1n) give a very clear and strong modulation in both energy bands with a minimum close to phase 0.0. The *RXTE* data reveal a similar effect (Figure 2.2k) and although the modulation from the *RXTE* data is not as pronounced as that seen from *ASCA*, it is clearly present at low energies with a minimum around phase 0.9. The fitted modulation depths in both observations show the classic trend of decreasing depth with increasing energy. The power spectra of the *ASCA* data show strong peaks associated with the orbital frequency as do the *RXTE* power spectra, particularly at lower energies. As with FO Aqr, the apparent discrepancy between the phases of minimum flux in the two observations may be due to the changing shape of the modulation profile with energy and the inadequacy of a sinusoidal fit.

2.6.14 TX Col

TX Col is a supposedly a low inclination system $< 30°$ (Mouchet et al. 1991) with an orbital period of $\sim$5.72hr and a spin period of 1911s (Buckley & Tuohy 1989), but no ephemeris has been published for it. TX Col reveals a strong modulation in the phase folded lightcurves of both satellites' observations and in both the depth decreases with increasing energy. In the *ASCA* data (Figure 2.1o) the dip occurs at (arbitrary) phase 0.2 whilst in *RXTE* it occurs at (arbitrary) phase 0.9. The power spectra of the two observations confirm what is seen in the folded lightcurves, each showing a strong peak at the orbital frequency.

2.6.15 AE Aqr

The magnetic propeller system AE Aqr is a very unusual IP with a long orbital period of 9.88hr (Welsh et al. 1993) and a short spin period of 33s (de Jager et al. 1994). The spectroscopic orbital ephemeris is referenced to superior conjunction of the WD. Only observed by *ASCA*, the X-ray lightcurve exhibited strong flares during the observation. However, even after removing these sections, the phase folded lightcurve shows a large variation. The sinusoid fits imply a relatively large modulation depth in both bands with a consistent phase of minimum flux, but both are significant at only just above the 3σ level. The power spectra are very noisy at low frequencies although there are indications of peaks coincident with both twice the orbital frequency and the orbital frequency itself in each case.

2.6.16 V1062 Tau

This little studied system has no published ephemeris and no inclination angle is known. The spin period and orbital period are 3726s (Hellier et al. 2002a) and 9.95hr (Remillard et al. 1994) respectively. The *ASCA* and *RXTE* data both show strong variability (Figure 2.1q and 2.2m) and although sinusoid fits reveal modulation depths that either decrease with increasing energy or remain constant, these modulations are not significant above the 3σ level in any of the energy bands. No clear orbital modulation frequency is seen in any of the power spectra.

2.7 Summary of results

Of the sixteen IPs studied, seven systems show evidence for an X-ray orbital modulation whose amplitude decreases with increasing X-ray energy, in at least one observation. These are: BG CMi, FO Aqr, TV Col and TX Col in their observations with both *ASCA*

and *RXTE*, and V1223 Sgr, AO Psc and V405 Aur (second observation), each in only their *ASCA* observations but not their *RXTE* observations. Interestingly, six of these plus EX Hya comprise the seven objects studied by Hellier et al. (1993) in the original *EXOSAT* investigation of IP X-ray orbital modulation which found such modulation to be ubiquitous. This result also confirms the findings of the various *ROSAT* and *Ginga* studies of individual objects over the last decade.

A further six systems show X-ray orbital modulation that is just significant at the 3σ level or whose depth is apparently constant across the energy bands in one observation. These are the *RXTE* observations of V1025 Cen, V1223 Sgr, V2400 Oph and V405 Aur, and the *ASCA* observations of V2306 Cyg and AE Aqr. Given the noisy nature of some of these data and the large uncertainties on the measured modulation depths, many of these are also consistent with a slight decrease in modulation depth with increasing energy.

Finally, nine systems are consistent with zero X-ray orbital modulation, across the energy range, in at least one observation. These are: V1025 Cen, V2400 Oph, LS Peg and V405 Aur (first observation) in their *ASCA* observations; YY Dra, PQ Gem and V1062 Tau in both their *ASCA* and *RXTE* observations; and AO Psc and V709 Cas in their *RXTE* observations.

There is clearly a variety of orbital modulation depths seen in these systems. In the lowest energy range (0.7 – 2 keV, *ASCA*), the depths measured at greater than 3σ significance vary from 100% (FO Aqr) to 28% (V1223 Sgr). Similarly, in the highest energy range (10 – 20 keV, *RXTE*), the largest modulation depth significantly detected is 34% (BG CMi), whilst the smallest is 12% (V1223 Sgr). The uncertainty in the modulation depth is generally of order a few percent, although sometimes as small as 1%. Hence, the smallest modulation depth that can reliably be detected is typically around 10%, although in a few cases we would be sensitive to detecting modulation depths of less than 5%. How-

Table 2.6: Modulation depth comparison data

Energy Range	*ASCA* depth greater than *RXTE* value	*ASCA* depth less than *RXTE* value	*ASCA* depth approx. same as *RXTE* value
ASCA 2 – 10 keV /*RXTE* 2 – 4 keV	2	3	9
ASCA 2 – 10 keV /*RXTE* 4 – 6 keV	4	2	8

ever, in no instance here do we see a modulation depth as small as this detected with much more than 3σ significance. The average uncertainty in the measured modulation depths in each energy band for the ASCA satellite is: 6% for the 0.7 – 2 keV energy band and 4% for the 2 – 10 keV energy band. For the RXTE satiellite, the average uncertainty in the modulation depths in the four energy bands is: 5% for 2 – 4 keV; 3% for 4 – 6 keV; 3% for 6 – 10 keV and 4% for the 10 – 20 keV band. The smaller the typical uncertainty that is seen, the smaller the modulation depth that we are able to measure. Generally, RXTE has a smaller uncertainty as the satellite has a bigger collecting area and so has more sensitive detectors.

At first sight it may appear that the depth of the modulation measured by *RXTE* is systematically lower than that for *ASCA*. This may occur if the background flux in the *RXTE* observations is systematically under-estimated for instance. In order to ascertain whether this is the case, we look at systems which have been observed by both satellites and make a direct comparison. Although the energy ranges of the satellites are different we take the 2 – 4 keV and 4 – 6 keV energy ranges in *RXTE* and compare these to the 2 – 10 keV *ASCA* energy range. Most of the X-ray flux is below 6 keV so this comparison is appropriate. Table 2.6 indicates the number of modulation depths that are either greater than, less than or approximately equal to the *RXTE* modulation depth within errors when

compared to that of the *ASCA* modulation depths of the same systems.

Given the results in this table, we concluded that the depth of the *RXTE* modulation was not systematically lower than that for *ASCA* and therefore the background subtractions done for the *RXTE* observations is acceptable.

2.8 Overall Discussion

From these results we conclude that X-ray orbital modulation in IPs is indeed widespread, but not ubiquitous. The dominant behaviour seen in figure 2.3, is that of decreasing modulation depth with increasing X-ray energy, suggesting photoelectric absorption as the cause. The most likely site for this additional absorption is in material thrown up at the edge of the accretion disk, due to impact by the accretion stream. As noted earlier, this is similar to the situation envisaged to cause X-ray dips in low mass X-ray binaries. The effect has also been realised in three-dimensional SPH simulations of cataclysmic variables by Kunze et al. (2001), who show that dips will be caused around orbital phase 0.7 if the system inclination angle is at least 65°.

We note that an additional column density of $N_{\rm H} = 10^{22}$ cm^{-2} would produce modulation depths of $\sim$ 80% at 1keV, $\sim$ 10% at 3keV, $\sim$ 5% at 5keV and have negligible effect above 8keV. Increasing the additional column density at X-ray minimum to $N_{\rm H} = 10^{23}$ cm^{-2} would increase these modulation depths to $\sim$ 100%, $\sim$ 60% and $\sim$ 20% respectively, with significant modulation out to above 10keV (Norton & Watson 1989). A simple partial covering absorber can reduce the modulation depth at low energies significantly, whilst still maintaining the same effect above $\sim$ 4keV. The values in Tables 2.4 and 2.5 for those systems exhibiting a decreasing modulation depth with increasing energy suggest that additional column densities of this order may be present in many of these IPs, at least some of the time, at X-ray orbital minimum. A roughly constant modulation

depth across a wide energy range, as seen in some systems, would imply that some fraction of the X-ray emission is completely blocked for part of the orbit, akin to an occulation.

In total, 11 systems out of the 16 observed here exhibit a possible X-ray orbital modulation during at least one of the observations we have analysed. If we add in EX Hya and XY Ari which are known to have an X-ray eclipse, then the proportion of systems showing X-ray orbital modulation is 72%. Assuming the systems to be randomly distributed in inclination angle, and that X-ray modulation is preferentially seen at higher angles, implies that an X-ray orbital modulation is visible for all inclination angles greater than around 44°. If instead we only recognise the X-ray orbital modulation seen above a 3σ level throughout the energy range observed, namely that in BG CMi, V1223 Sgr, AO Psc, V405 Aur, FO Aqr, TV Col and TX Col (plus the two eclipsing systems), then the proportion of systems falls to 50% and the limiting inclination angle at which an orbital modulation is seen is increased to 60°, which is consistent with the predictions from the SPH simulations of Kunze et al. (2001).

The orbital phase at which minimum X-ray flux occurs in different systems is seen to be predominantly in range $\sim 0.7-1.0$. As noted above, stream impact with the outer edge of the disk is expected to occur around orbital phase 0.7, and this is indeed seen in BG CMi and V1223 Sgr (both observations of each), and FO Aqr (*RXTE* observation). Of the IPs with a well established orbital modulation and a previously published ephemeris, AO Psc stands out in having a minimum after phase zero instead of before. However, the accumulated phase error by the time of the *ASCA* observation is 0.1 (see Table 2.3), so this may not be significant. In some of the systems we have studied, we see evidence that may be interpreted as a variation in the orbital phase at which minimum X-ray flux occurs from one observation to the next, notably in FO Aqr and TV Col. This may indicate that the absorbing material is not fixed in its location at the edge of the disk. Alternatively,

both the lack of dips centred near phase 0.7 and the apparent variability in phase of X-ray minimum may simply reflect greater inaccuracies in the published orbital ephemerides than claimed, or uncertainties in assigning a particular system geometry to a given phase determined from a spectroscopic ephemeris.

We also note that the presence of X-ray orbital modulation in a given IP may come and go on a timescale of years or months. This is particularly apparent in two systems: for AO Psc a modulation was seen by *EXOSAT* (1983 and 1985), *Ginga* (1990), *ROSAT* (1994) and *ASCA* (1994), but not by *RXTE* (1997); whereas for V1223 Sgr, a modulation was possibly seen by *EXOSAT* (1983 and 1984), not seen by *Ginga* (1991) and *ROSAT* (1994), then seen by *ASCA* (1994) and *RXTE* (1998). We also note the significant differences displayed by the two *ASCA* observations of V405 Aur taken only two-and-a-half years apart. This indicates that the visibility or size of whatever structure is responsible for producing the photoelectric absorption also varies considerably on this timescale. A similar effect is seen in some LMXBs (Smale et al. 1988; Schmidtke 1988) and is ascribed to the presence of a precessing, tilted accretion disk. Such a disk has been suggested as the cause of negative superhumps in cataclysmic variables (Patterson 1999) although simulations vary in their success at reproducing the phenomenon (Larwood 1998; Murray & Armitage 1998; Wood et al. 2000; Murray et al. 2002). Nonetheless, if a tilted disk is present in an IP, a raised bulge at its outer edge caused by stream impact could move into and out of the line of sight to the X-ray source as its extent above the orbital plane varies with disk precession phase. In this way, a varying presence or depth of X-ray orbital modulation would naturally arise. The only IP with a confirmed tilted precessing disk is TV Col which has a 4d disk precession period (Barrett et al. 1988), but it is conceivable that such a phenomenon may also be present in other systems. It would be interesting to monitor the X-ray orbital modulation from TV Col throughout its 4-day disk precession period in order to test this

hypothesis.

Finally, we note that the apparently constant modulation depth as a function of energy seen in some IPs we have studied, at some epochs (i.e. *RXTE* observations of V1223 Sgr, V2400 Oph and V405 Aur), might indicate that an additional emission component is responsible for some or all of the variation in flux as a function of orbital phase. Alternatively, or additionally, it might imply that the absorbing region is highly structured or patchy and so the amount of absorption does not simply decrease with increasing energy. However, we see no constant or increasing modulation depth with increasing X-ray energy at a level much greater than 3σ significance so do not place too much weight on this interpretation.

In conclusion we note that to fully understand the 'hot spot' region we need to fully understand the accretion flow within intermediate polars. Furthermore it is essential to analyse the flow for all possible regimes of parameter space. As we cannot observe the flow directly, we need a theoretical model to compare with the real data that we can obtain. The following chapter describes one such model, a hydrodynamical computer model known as HyDisc used to investigate the types of accretion flow that occur through a variety of parameter space.

Chapter 3

Magnetic model

3.1 Introduction

In this chapter, we outline the computer model that we have used to obtain theoretical accretion flows for a certain parameter space. The code was originated by Rob Whitehurst (see Whitehurst (1988a)) and modified by Dr Graham Wynn at The University of Leicester. It has been used many time in many refereed publications. The version used in this thesis is the latest version of the code from Leicester and is the same as that used in the most recent publication by Norton et al. (2004b). For our use the model treats the accretion flow as a set of blobs and represents them by particles in a three-dimensional hydrodynamical code known as HyDisc. We start by giving a brief overview of HyDisc and then go through the equations the models implements and the assumptions we take into account. We discuss briefly the two types of model we used, how this model has already been used in other publications and finally how we have used it.

3.2 An overview of HyDisc

HyDisc is known as a sticky particle code, which refers to the way the viscosity works within the code, working in a similar way to smoothed particle hydrodynamics (SPH) applications. The main difference between SPH and HyDisc is the way in which the particles interact with each other. In HyDisc each particle only interacts with its nearest neighbour, whereas in SPH all particles within a certain radius are considered. Although HyDisc is less sophisticated than SPH it is computationally more efficient and gives widely similar answers. In particular when viscous and pressure forces are not dominant, HyDisc is very efficient and gives good results. As this is exactly the case for magnetic flows Hydisc produces viable results for the accretion flows within the parameters we are testing for IPs.

Within HyDisc, each particle is set up so as to carry mass and angular momentum. It then mimics the viscous and pressure forces in the gas by inelastic collisions between the particles. The particles move under the effects of gravity and any other external forces, such as the magnetic drag force, over a timestep by integrating the equation of motion of a plasma in a magnetic field. After each of these timesteps, the viscous and pressure forces are calculated by looking at nearest neighbour collisions. In this way the particles exert accelerations on one another and so exchange angular momentum. The loop then continues with the next gravity/magnetic field timestep and so on. The method used in HyDisc has been tested extensively by Whitehurst (1988a) and many times since and gives good agreement to SPH applications.

3.2.1 Basics

HyDisc works in the co-rotating reference frame to work out the Roche potential in terms of the masses of the two stars (assumed to be point-like masses) m_1 and m_2. It calculates

Figure 3.1: Forces acting on a particle 'P' in the co-rotating reference frame of a binary system. The particle feels the Coriolis force, centrifugal force and gravity due to the two masses m_1 and m_2. The distance of separation of the two masses is given by a and the distance from mass m_1 to the Lagrangian point L_1 is given by b.

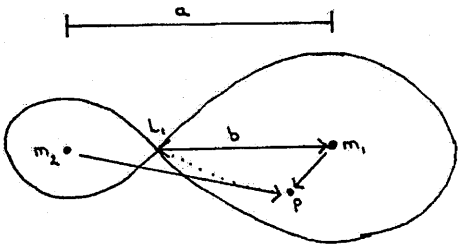

the distance of the L_1 point from the white dwarf (i.e. distance b in figure 3.1) and calculates the gravitational forces exerted on a particle due to each mass, as well as the fictitious forces of the Coriolis force, centrifugal.

The code uses certain scalings for time, length and mass. In code units the mass is 10^{17} g, length is the orbital separation and time is $1/\Omega$

3.2.2 Gas physics

Unlike an SPH code or a grid based code, HyDisc is something in between. It operates in a 3D grid of cells, whose length is 0.03 in code units (i.e. $0.03a$ in real units). It looks at each cell individually and assesses which two particles have the largest relative closing velocity u and then uses this to compute an acceleration for the gas particles in that cell.

The pressure force ∇P acting on the particle is assumed to be

$$P = c_s^2 \rho \tag{3.1}$$

for any given cell. Where the density ρ is the count of all the particles within one cell

divided by the volume of the cell and the sound speed c_s is assumed to be constant and appropriate for a temperature of $T \sim 3000$ K.

The two fundamental forces acting between the particles are due to pressure and viscosity. Pressure forces can be estimated by considering two adjacent elements of gas with density ρ, isothermal sound speed c_s, and sizes comparable to their separation r. Then they exert a pressure $P = c_s^2\rho$ over an interface area r^2, so the acceleration due to pressure is given by $a_p \approx c_s^2/r$. If the assumption is made that the whole flow is roughly isothermal then

$$a_r = \frac{C^2}{r} \tag{3.2}$$

where C is a constant of order the sound speed.

Viscous forces can be included by considering the impact of two particles separated by distance r_p and line-of-centres velocity u, (if particles are colliding then $u < 0$). If this velocity is supersonic, i.e. $u > c_s$, then a shock front will develop between them on time $\sim r/u$ and decelerate the particles by a velocity $\sim u$. This is achieved by an average repulsive acceleration of about u^2/r so the total acceleration between the particles is given as;

$$a_r = \frac{C^2}{r} + \frac{Qu^2}{r} \tag{3.3}$$

$$a_r = \frac{C^2}{r} \tag{3.4}$$

Where Q is a constant of order unity. Note that the forces between the particles always act along their line-of-centres, which ensures conservation of angular momentum.

3.2.3 When a magnetic field is involved

The volume of space of the Roche lobe around the mass m_1, is filled with a magnetic field. The gas flow within the Roche lobe feels the force of gravity, gas pressure, viscous forces and magnetic forces. Each force acts on a characteristic timescale:

The gravity force acts on a timescale $t_{\rm dyn}$ which is the dynamical timescale and is approximately equal to the orbital timescale of an element of gas.

The pressure and viscosity forces, combined as internal gas forces, are usually treated together and act on the viscous timescale t_{visc}.

The magnetic forces act on a timscale $t_{\rm mag}$ – this is the timescale to react to the local magnetic field.

If no magnetic field is present, as in the previous example, then

$$t_{\rm dyn} << t_{\rm visc} << t_{\rm mag}$$
$$t_{\rm dyn} << t_{\rm visc} << t$$

With a magnetic field present in a Polar system, we have the following

$$t_{\rm dyn} \sim t_{\rm mag} << t_{\rm visc}$$

and in IPs we have the range

$$t_{\rm dyn} << t_{\rm mag} \sim t_{\rm visc} \text{ to } t_{\rm dyn} \sim t_{\rm mag} << t_{\rm visc}$$

For magnetic forces on a unit mass in cgs units we have

$$\boldsymbol{F}_{\rm mag} = \frac{-\boldsymbol{\nabla}(\boldsymbol{B}\cdot\boldsymbol{B})}{8\pi} + \frac{(\boldsymbol{B}\cdot\boldsymbol{\nabla})\boldsymbol{B}}{4\pi} \tag{3.5}$$

The first term behaves like a pressure and we get:

$$P_{\rm mag} = \frac{B^2}{8\pi} \tag{3.6}$$

The second term behaves like a tension giving

$$T_{\rm mag} = \frac{B^2}{4\pi} \tag{3.7}$$

Thus the acceleration due to the magnetic tension may be expressed as

$$\rho \boldsymbol{a}_{\rm tension} = \frac{1}{R_{\rm c}} \frac{B^2}{4\pi} \hat{\boldsymbol{n}} \tag{3.8}$$

Figure 3.2: A schematic diagram for the local radius of curvature

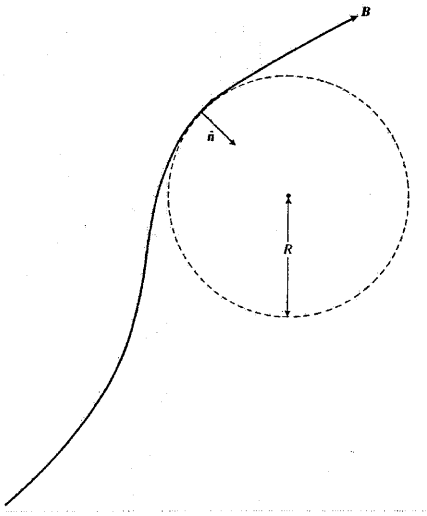

where $\hat{\boldsymbol{n}}$ is a unit vector that is perpendicular to the magnetic field at a given position and $R_{\rm c}$ is the local radius of curvature of the magnetic field lines. This term is such that it accelerates the gas flow along $\hat{\boldsymbol{n}}$ towards the centre of curvature of the field line. See Figure 3.2

There are two possibilities for the way the plasma behaves:

(i) If the field lines are frozen in to the plasma, then the field will be 'dragged' along by a 'packet' of plasma, and a drag force will act on the plasma (see Figure 3.3).

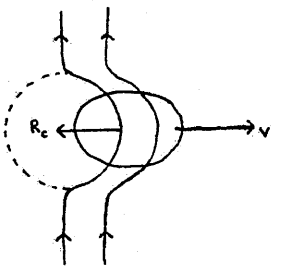

Figure 3.3: (i) Field lines frozen into a plasma blob. The fully threaded field lines and gas move together. The magnetic field is dragged by the plasma and the tension becomes dominant.

(ii) If the plasma 'packet' is diamagnetic and excludes the field lines, the field lines will be pushed ahead of the 'packet' of plasma (see Figure 3.4).

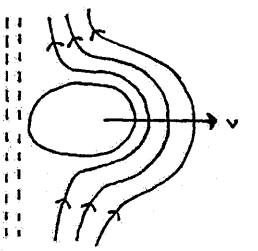

Figure 3.4: (ii) Diamagnetic plasma blob. The plasma scoops up the field lines infront of it. High relative velocities between flow and field mean a large tension is produced.

In both these cases, the local radius of curvature will become small as the gas flows at high velocity relative to the field lines. Therefore the magnetic tension will become large and dominate over the magnetic pressure term. The tension term dominates and will affect the velocity of the plasma significantly causing a change in the velocity of the plasma.

3.2.4 Introducing k

Each 'packet' of plasma has a component of its velocity perpendicular to the field lines, that is in the opposite direction to the unit vector $\hat{\boldsymbol{n}}$, along the radius of curvature. This relative velocity between the plasma and the field lines is referred to as $\boldsymbol{v}_\perp$. As this velocity is *relative* in this direction, it may be written as $\boldsymbol{v}_\perp = (\boldsymbol{v}_{\mathrm{gas},\perp} - \boldsymbol{v}_{\mathrm{mag},\perp})$.

So, the magnetic acceleration provided by the magnetic tension force can be written as

$$\boldsymbol{a}_{\mathrm{mag}} = \frac{1}{\rho(r,t)R_{\mathrm{c}}(r,t)} \frac{B^2(r,t)}{4\pi} \hat{\boldsymbol{n}} \tag{3.9}$$

This magnetic acceleration can be set equal to some parameter $k(r,t)$ multiplied by the relative velocity perpendicular to the field lines:

$$\boldsymbol{a}_{\mathrm{mag}} = \frac{1}{\rho(r,t)R_{\mathrm{c}}(r,t)} \frac{B^2(r,t)}{4\pi} \hat{\boldsymbol{n}} = k(r,t)\boldsymbol{v}_\perp \tag{3.10}$$

k is therefore equivalent to a "drag" coefficient. The conditions for the k parameter in magneto hydrodynamics (MHD) vary in both space and time. Thus the magnetic acceleration, induced by the magnetic tension, is therefore added on to the end of the original HyDisc prescription of gravitational force, gas force and viscosity force.

Dimensionally, $k(r,t)$ has the dimensions of time^{-1}, so we can write

$$k \sim \frac{1}{t_{\mathrm{mag}}} \text{ (in code units)} \tag{3.11}$$

or

$$t_{\mathrm{mag}} \sim \frac{1}{k} \frac{P_{\mathrm{orb}}}{2\pi} \text{ (in seconds)} \tag{3.12}$$

We further assume that k is not explicitly time dependent, so we have

$$\boldsymbol{a}_{\mathrm{mag}} = k(r)\boldsymbol{v}_\perp \tag{3.13}$$

where

$$\boldsymbol{a}_{\rm mag} = \frac{1}{\rho(r)R_{\rm c}(r)}\frac{B^2(r)}{4\pi}\hat{\boldsymbol{n}} \tag{3.14}$$

Therefore equating the two gives

$$k(r)\boldsymbol{v}_{\perp} = \frac{1}{\rho(r)R_{\rm c}(r)}\frac{B^2(r)}{4\pi}\hat{\boldsymbol{n}} \tag{3.15}$$

The k parameter is therefore input to HyDisc and used as a measure of the magnetic field strength. To interpret k, we go back to basic equations.

3.2.5 Estimating Parameters

We specify local conditions by 3 parameters ρ, R_c and B. We estimate the density of the gas (ρ_{gas}) as being approximately equal to the density of the material at the L_1 point (ρ_{L_1}). To estimate this we follow Pringle and Wade (1985, p10). Suppose that the width of the nozzle at the L_1 point is w, and the velocity of the flow through the nozzle is of the order of the local sound speed $c_{\rm s}$. The width of the nozzle may be estimated by asking how far to the side of the L_1 point can a particle with this velocity be and still escape from the Roche lobe of the secondary star? Equating the potential energy difference at this point to the specific kinetic energy of the particle, we get $\Delta\Phi = c_{\rm s}^2$, but the potential energy $\Delta\Phi \sim \Omega^2 w^2$. Hence

$$w = \frac{c_{\rm s}}{\Omega} = \frac{c_{\rm s}P_{\rm orb}}{2\pi} \tag{3.16}$$

To estimate the mass transfer rate, we assume that the mass flux $\dot{M}$ is given by the size of the nozzle (w^2) multiplied by the speed of the stream ($c_{\rm s}$) and the density of the stream (ρ) at the L_1 point. So

$$\dot{M} = w^2 c_{\rm s}\rho = \frac{\rho c_{\rm s}^3 P_{\rm orb}^2}{(2\pi)^2} \tag{3.17}$$

and therefore the gas density is:

$$\rho_{\rm gas} \sim \frac{\dot{M} 4\pi^2}{P_{\rm orb}^2 c_{\rm s}^3} \tag{3.18}$$

We assume that the local radius of curvature R_c is similar to the gas length scale l_{gas} which in turn is similar to the width of the nozzle at the L_1 point ω so:

$$l_{\rm gas} \sim w \sim \frac{c_{\rm s} P_{\rm orb}}{2\pi} \tag{3.19}$$

3.2.6 Scaling k – constant density and size scale

The equations above for ρ_{gas} and l_{gas} give the value for the density and length scale at the L_1 point. If we assume that the gas density and length scale are constant throughout the system, then we have:

$$k(r)\boldsymbol{v}_\perp = \text{constant} \times B^2(r)\hat{\boldsymbol{n}} \tag{3.20}$$

or for a constant velocity,

$$k(r) \propto B^2(r) \tag{3.21}$$

If we scale this in terms of the magnetic field at the surface of the WD then we have:

$$k(r) = k_0 \left(\frac{B(r)}{B_{\rm wd}}\right)^2 \tag{3.22}$$

where $B_{\rm wd}$ is the surface magnetic field strength of the white dwarf.

In the case for a dipole model where $B(r)$ is scaled as r^{-3} we have

$$k(r) \propto r^{-6} \tag{3.23}$$

$$k(r) = k_0 \left(\frac{r}{r_{\rm wd}}\right)^{-6} \tag{3.24}$$

This is referred to as the 'n^6' model in our HyDisc runs.

So, given an input k_0 value, $k(r)$ may be calculated at a range of various radii, such as

$$\text{at } 10^9 \text{ cm } (r_{\rm wd}) \qquad k \sim k_0 \tag{3.25}$$

$$\text{at } 10^{10} \text{ cm } (r_{\rm circ}) \quad k \sim k_0 \times 10^{-6} \tag{3.26}$$

$$\text{at } 10^{11} \text{ cm } (r_{\rm L1}) \quad k \sim k_0 \times 10^{-12} \tag{3.27}$$

Since k_0 is input in code units, in each case the appropriate magnetic timescale is given by

$$t_{\rm mag}(r) = k(r)\frac{P_{\rm orb}}{2\pi} \tag{3.28}$$

3.2.7 Scaling k – non-constant density and size scale

Clearly the assumption of constant density and length scale troughtout the system is unlikely. So, following on from King (1993), we also look at the case for non constant gas density and size scale. In practice, the gas density will increase at small r as it gets closer to the white dwarf (due to the effects of magnetic pressure) and the length scale will also increase at small r, as the gas is squeezed by the field lines. So we might expect $\rho(r) \propto r^{-x}$ and $l(r) \propto r^{-y}$ (x, y > 0). As an approximation to the unknown scaling we suppose that:

$$\rho(r)l(r) \propto r^{-3} \tag{3.29}$$

Hence, since we have

$$k(r)\boldsymbol{v}_\perp = \frac{1}{\rho(r)R_{\rm c}(r)}\frac{B^2(r)}{4\pi}\hat{\boldsymbol{n}} \tag{3.30}$$

then for a dipole field with $B(r) \propto r^{-3}$,

$$k(r) \propto \frac{1}{r^{-3}} \left(r^{-3}\right)^2 \propto r^{-3} \tag{3.31}$$

and we can write

$$k(r) = k_0 \left(\frac{r}{r_{\rm wd}}\right)^{-3} \tag{3.32}$$

This is referred to as the 'n^3' model in HyDisc terms; and is the "usual" way of modelling the dipole magnetic field in HyDisc.

So, as in the previous section, given an input k_0 value, $k(r)$ may be calculated at various radii. Notice that the timescales are therefore different for a given k_0 between the two models.

3.2.8 Calculating B from k

If we now assume that the blobs are diamagnetic, we can approximate the perpendicular relative velocity between the gas and field lines by the Alfvén speed, $c_{\rm A}$. So we can write

$$\frac{1}{\rho(r) R_{\rm c}(r)} \frac{B^2(r)}{4\pi} \hat{\boldsymbol{n}} = k(r) c_{\rm A} \hat{\boldsymbol{v}}_{\perp} \tag{3.33}$$

we substitute for ρ and $R_{\rm c}$ with:

$$\rho_{\rm gas} \sim \frac{\dot{M} 4\pi^2}{P_{\rm orb}^2 c_{\rm s}^3} \tag{3.34}$$

$$R_{\rm c} \sim l_{\rm gas} \sim w \sim \frac{c_{\rm s} P_{\rm orb}}{2\pi} \tag{3.35}$$

substituting in gives:

$$\frac{P_{\rm orb} B^2(r) c_{\rm s}^2}{8\pi^2 \dot{M}} = k_0 \left(\frac{r}{r_{\rm wd}}\right)^{-n} c_{\rm A} \tag{3.36}$$

So, rearranging the above for B^2 gives us

$$B^2(r) = \frac{8\pi^2 \dot{M}}{P_{\rm orb} c_{\rm s}^2} \left[k_0 \left(\frac{r}{r_{\rm wd}} \right)^{-n} \right] c_{\rm A} \tag{3.37}$$

In a dipole field, the magnetic field strength scales as

$$B(r) = B_{wd} \left(\frac{r}{r_{wd}} \right)^{-3} \tag{3.38}$$

If we then substitute for $B^2(r)$ from equation 3.40 we get:

$$B_{\rm wd}^2 \left(\frac{r}{r_{\rm wd}} \right)^{-6} = \frac{8\pi^2 \dot{M}}{P_{\rm orb} c_{\rm s}^2} \left[k_0 \left(\frac{r}{r_{\rm wd}} \right)^{-n} \right] c_{\rm A} \tag{3.39}$$

so

$$B_{\rm wd}^2 = \frac{8\pi^2 \dot{M}}{P_{\rm orb} c_{\rm s}^2} \left[k_0 \left(\frac{r}{r_{\rm wd}} \right)^{6-n} \right] c_{\rm A} \tag{3.40}$$

If we now substitute in a formula for the Alfven speed,

$$c_{\rm A} = \frac{B(r)}{(4\pi\rho)^{1/2}} \tag{3.41}$$

which may in turn be written as

$$c_{\rm A} = B_{\rm wd} \left(\frac{r}{r_{\rm wd}} \right)^{-3} \frac{1}{(4\pi)^{1/2}} \left(\frac{P_{\rm orb}^2 c_{\rm s}^3}{\dot{M} 4\pi^2} \right)^{1/2} \tag{3.42}$$

This can then be substituted into the equation for $B_{\rm wd}$ above to give:

$$B_{\rm wd} = \left(\frac{4\pi \dot{M}}{c_{\rm s}} \right)^{1/2} k_0 \left(\frac{r}{r_{\rm wd}} \right)^{3-n} \tag{3.43}$$

For a simple dipole with non-constant plasma density and scale length, $n = 3$, and so the dependence on r disappears. Note the above equation is also independent of $P_{\rm orb}$, but

remember that the value of k_0 input to the code is in code units, and so must be multiplied by $(2\pi/P_{\rm orb})$ before being used in the equation above.

3.3 Two Versions of HyDisc

For the investigation into the accretion flows within IPs we have run two models within HyDisc for a comparison between parameters. Both models within HyDisc are based on a dipole magnetic field structure. In the very simplest case we can assume that the density and size scale of the blobs are constant. As noted in the previous section, since this is a dipole, $B \propto 1/r^3$ and as $k \propto B^2$ so $k \propto 1/r^6$ and we call this the n^6 model.

More realistic (probably) is if the density and size scale of the blobs were not constant. It is still a dipole field so $B \propto 1/r^3$ but as noted above, now as $k \propto B^2 r^3$ we have $k \propto 1/r^3$ and we call this model the n^3 model.

In practice we should have something more realistic than the n^6 model as the size scale and gas density will not be the same at all WD radii. The n^3 model goes some way to achieving this. Although the n^6 model is probably less realistic than the n^3 model, we make the comparison as the n^6 uses simpler assumptions and so is less arbitrary.

3.4 Previous Uses of the Model

HyDisc has previously been used to investigate spin equilibria in IPs. When IPs reach their equilibrium state, the spin period of the white dwarf is equal to the co-rotation period (section 1.4.3) and becomes equal to the Keplerian orbital period of the material at the inner edge of the disk. The physical cause is that the spin up torque due to accretion is balanced by the magnetic torque, and the spin period then remains $\sim$ constant on long timescales. Using HyDisc, King & Wynn (1999) showed that the white dwarf spin period in EX Hydrae represents an equilibrium state in which the co-rotation radius is compara-

ble with the distance from the white dwarf to the inner Lagrangian point, which represents a new equilibrium spin state for magnetic CVs given by the approximation $R_{co} \sim b$. Previously most authors assumed that IPs are only in equilibrium when $P_{\rm spin}/P_{\rm orb} \approx 0.1$. However, King and Wynn show that a continuum of spin equilibria exists for which $P_{\rm spin}$ is significantly longer than $\sim 0.1 P_{\rm orb}$ and also observed that most systems that occupy these equilibrium states occur at short orbital periods, so occur below the period gap.

The typical $P_{\rm spin}/P_{\rm orb}$ ratio arises in the following way. We assume that the disk is truncated where $R_{co} \sim R_{circ}$. The circularisation radius can be quantified by assuming that the specific angular momentum at the circularisation radius is equal to that at the L_1 point. So we have:

$$(GM_1 R_{circ})^{1/2} \sim b^2 \left(\frac{2\pi}{P_{orb}}\right) \tag{3.44}$$

with b being the distance between the WD and the L_1 point, and a the semi major axis.

We know from Kepler's law that:

$$a^3 = GM_1(1+q)\frac{P_{orb}^2}{4\pi^2} \tag{3.45}$$

where q=M_2/M_1

Now we have

$$R_{co} = \left(\frac{GM_1}{\Omega^2}\right)^{1/3} \tag{3.46}$$

where

$$\Omega = \frac{2\pi}{P_{spin}} \tag{3.47}$$

so we get

$$R_{co} = \left(\frac{GM_1P_{spin}^2}{4\pi^2}\right)^{1/3} \tag{3.48}$$

We substitute equation 3.50 into equation 3.46 because of the condition $R_{co} \sim R_{circ}$ so we have:

$$\left[GM_1\left(\frac{GM_1P_{spin}^2}{4\pi^2}\right)^{1/3}\right]^{1/2} \sim b^2\left(\frac{2\pi}{P_o}\right) \tag{3.49}$$

If we then square both sides and substitute for the first GM_1 from rearranging equation 3.41 in terms of GM_1 we get the following:

$$\frac{a^3}{(1+q)}\frac{4\pi^2}{P_{orb}^2}\left(\frac{GM_1P_{spin}^2}{4\pi^2}\right)^{1/3} \sim b^4\left(\frac{2\pi}{P_{orb}}\right)^2 \tag{3.50}$$

Multiplying both sides by $\frac{P_{orb}^2}{4\pi^2}$ gives:

$$\frac{a^3}{(1+q)}\left(\frac{GM_1P_{spin}^2}{4\pi^2}\right)^{1/3} \sim b^4 \tag{3.51}$$

We now cube both sides and substitute again the expression for GM_1 from rearranging equation 3.41. Thus we then have:

$$\frac{a^9}{(1+q)^3}\frac{a^3}{(1+q)}\frac{4\pi^2}{P_{orb}^2}\frac{P_{spin}^2}{4\pi^2} \sim b^{12} \tag{3.52}$$

Cancelling the $4\pi^2$ and multiplying the first two terms gives us the simplified equation:

$$\frac{a^{12}}{(1+q)^4}\frac{P_{spin}^2}{P_{orb}^2} \sim b^{12} \tag{3.53}$$

Subsequently we get: :

$$\frac{P_{spin}}{P_{orb}} \sim \frac{b^6}{a^6}(1+q)^2 \tag{3.54}$$

Since the mass ratio is defined as $q = \frac{M_2}{M_1}$ so we substitute this into the above equation and get:

$$\frac{P_{spin}}{P_{orb}} \sim \left(\frac{b}{a}\right)^6 \left(1 + \frac{M_2}{M_1}\right)^2 \tag{3.55}$$

Finally we have the total binary mass as $M = M_1 + M_2$ which gives us our final expression:

$$\frac{P_{\rm spin}}{P_{\rm orb}} \sim \left(\frac{b}{a}\right)^6 \left(\frac{M}{M_1}\right)^2 \tag{3.56}$$

Since the distance to the L_1 point from the WD is b, where $b \sim$ (0.5 - 0.227 log q) a, then for a typical mass ratio of about ≈ 0.5, we do indeed have $P_{\rm spin}/P_{\rm orb} \approx 0.1$ as noted earlier.

Equation (3.52) reasonably describes the relation between $P_{\rm spin}$ and $P_{\rm orb}$ in most IPs. The corresponding accretion flow is sometimes referred to as 'diskless' but this is a rather misleading name, suggesting that the flow cannot surround the white dwarf, however simulations from the magnetic model show that this is possible. King & Wynn investigated the spin equilibrium of EX Hydrae and found that their spin-evolution calculations were in very good agreement with the observed period ratio of P_{spin}/P_{orb} ~0.68, for $t_{mag}(L_1)/t_{dyn}(L_1) \lesssim 1/3$ (Plavec & Kratochvil 1964)and concluded that this specifies a spin equilibrium state which EX Hya is very close to.

From running the model at this new spin equilibrium state, they suggested that the accretion of mass and angular momentum by the WD occurs only for a restricted range of spin phases, generally when the dipole axis points towards L_1. At other phases the model shows that matter which is trying to accrete along the field lines will be centrifugally ejected. Most of this material will accrete back onto the secondary, thus transferring angular momentum from the WD back to the binary orbit. It is the angular momentum

flows that balance over each orbit so holding the equilibrium state of the system. They state that strong evidence for this type of accretion has been seen from spectroscopic observation (Wynn, Wheatley & Maxted, in preparation). King & Wynn developed the same model further, with a greater spread in blob parameters (i.e. mass, size etc). The accretion flow it produced clearly showed 2 components, one similar to that described above, the other an azimuthally symmetric distribution of particles surrounding the WD. This type of system could show similar observational properties to that of accretion via a disk and via a stream, whilst still reaching an equilibrium ratio very close to the observed EX Hya system.

Following the work of King & Wynn (1999), Norton et al. (2004b) extended this work and used the model of magnetic accretion to investigate the rotational equilibria of magnetic CVs in general. Their results demonstrated that there is a range of parameter space in the $P_{\rm spin}/P_{\rm orb}$ versus μ_1 (magnetic moment) plane at which rotational equilibrium occurs. This led to the construction of a theoretical histogram which described the distribution of mCVs as a function of $P_{\rm spin}/P_{\rm orb}$ which agreed with the observed distribution as long as the assumption held that $N(\mu_1)d\mu_1 \propto \mu_1^{-1}d\mu_1$, where $N(\mu_1)$ is the number of systems as a function of the WD magnetic moment. This relationship implies that there are equal numbers of systems per decade of magnetic field strength, which is in rough agreement with observations of isolated WD (Schmidt et al. (2003)). The rotational equilibria allowed them to deduce approximate values for the magnetic moments of all known IPs. Norton et al. used the model to further show how the equilibrium spin periods relate to polar synchronisation and that the equilibrium situations they investigated produced a number of different types of accretion flow from disklike and streamlike, to accretion fed from a ring at the outer edge of the WD Roche lobe. In the next chapter I take this work further still, and present full data tables of the equilibrium spin periods and magnetic

moments, and the nature of the accretion flow when equilibrium is reached.

In another, rather different use of HyDisc in the paper by Ultchin et al. (2002), the structure of accretion disks around magnetic T Tauri stars (young solar like stars seen near many molecular clouds in our galaxy, pre-main sequence) is calculated numerically. In the paper, they set up the calculation so as to simulate the density structure of a quasi-steady disk in the equatorial plane of a T Tauri star and found that the central star's magnetic field typically produces a central hole in the disk and spreads out the surface density distribution and suggest that this is a promising mechanism for explaining the unusual flatness (IR excess, an unusually high emission in the infrared) of T Tauri accretion disk spectra.

Finally, in one more application of HyDisc, to magnetic CVs Hellier et al. (2002b) investigated the mode of accretion in the IP V1025 Centauri. Here the long white dwarf spin period implies that if the system possesses an accretion disk, then it could not possibly be in equilibrium as is the similar case for the IP EX Hydrae as mentioned above by King & Wynn (1999). As before it is suggested that instead of having a disk, the system is in fact a diskless accretor in which the spin-up torques resulting from accretion are balanced by the ejection of part of the accretion flow back towards the secondary. Hellier et al. (2002b) presented phase-resolved spectroscopy of V1025 Centauri aimed at deducing the nature of the accretion flow, and compared it with simulations from the magnetic model of a diskless accretor as well as producing trailed spectra and tomograms for further identification. They found that both the conventional disk-fed model and the diskless-accretor model had strengths and weaknesses, and that further work was needed before they could decide which applied to V1025 Centauri.

3.5 My Work

I have used the HyDisc model to investigate the accretion flow in IPs throughout parameter space for various orbital periods, spin periods, differing values of k, different magnetic co-latitudes, as well as how these would appear when viewed from different inclination angles. The model was in each case run for at least 2 orbital cycles as this was determined to be sufficient for the system to settle and stabilise its configuration. The time step was set to $0.01P_{\rm orb}$ implying that snapshots are produced after each 100th of the orbit, hence 200 time steps are produced. Further to this, the model can also be used to look at simulated Doppler tomograms of each system and this was carried out using the same criteria as above for the different parameters in the systems.

The next chapter shows the accretion flows corresponding to different regions of the parameter space explored. A variety of flows corresponding to streams, disks, propellers and rings are observed to arise.

Chapter 4

Accretion Flows from the Magnetic Model

4.1 Introduction

In this chapter we take the magnetic model that little bit further by producing an atlas of accretion flows corresponding to different regions of parameter space for the n^3 model and the n^6 model where the magnetic field follows a different dependence on the radial distance from the white dwarf. The model is run for 6 different orbital periods of 80m, 2h, 3h, 5h, 7h and 9h for each of 11 different values of k_0, i.e. the k parameter appropriate at the surface of the WD. 6 different spin periods of 50s, 100s, 200s, 1000s, 2000s and 4000s are used in the case of the magnetic field strength up to k_0=1×10^5 and 500s, 1000s, 2000s, 4000s, 8000s, 14000s and 18000s for the three magnetic field strengths above this value. The spin periods investigated at the higher magnetic fields strengths are increased in this way to allow us to cover the parameter space at which systems' spin equilibrium occur. A variety of accretion geometries arise corresponding to streams, discs and propellers as well as a new type of flow known as ring accretion. The scale in each figure illustrating the flows is normalised to the binary separation in each case. Following this we look in

detail at the equilibrium case and assess the types of flow that occur throughout parameter space when the systems are at their spin equilibrium. We also provide accretion flows at different dipole angle inclinations so as to fully understand the types of accretion flow that can be observed if the magnetic field is more tilted with respect to the spin axis. After each set of figures we discuss the findings individually and then give a brief conclusion to each set of model results. We compare and contrast the two different models and the different equilibrium flows they produce and then use this as the basis for the comparison with the dipole variations, giving an over-view of all the results at the end of the chapter.

4.2 n^3 model

In Figure 4.1 we present the accretion flow results of running HyDisc for the n^3 model with the range of $P_{\rm orb}$, $P_{\rm spin}$ and k_0 discussed above. Details are given in the caption. As noted in the last chapter, in the n^3 model we assume that the gas density and length scale of the blobs is **not** constant, but varies with distance from the WD, leading to the overall result that $k(r) \propto r^{-3}$. In all these simulations, the masses of the two stars are $0.6M_\odot$ and $0.3M_\odot$ and the dipole inclination angle is m$\sim 5°$. At longer orbital periods the mass of the donor star would be expected to be higher than that of the ones we use. For simplicity of the model however we choose to keep the mass of the stars fixed. If we did correct the donor star mass to coincide with the changing orbital period, then we predict that the only change that we would see would be a shift in the transition regions in the parameter space, from disk to propeller. That is to say, the same range of behaviour would be observed, but the changeover from one type of flow to another would occur at a different $P_{\rm spin}/P_{\rm orb}$ ratio for a given magnetic field strength.

Figure 4.1: Accretion flows for the n^3 model ($k(r) \propto r^{-3}$) for each k_0 value in parameter space. The red figures indicate propeller accretion, yellow figures indicate stream accretion, blue figures indicate disk accretion and green figures are ring structure accretion. A small magenta 'P' in the upper left of a figure indicates a polar system, i.e. the configuration where $P_{\rm spin}$=$P_{\rm orb}$ for the highest magnetic field strength. The scale is normalised to the binary separation in each case. The k value listed on each page of this figure is the value input to HyDisc, i.e. k_0 which is the value of $k(r)$ at the WD surface.

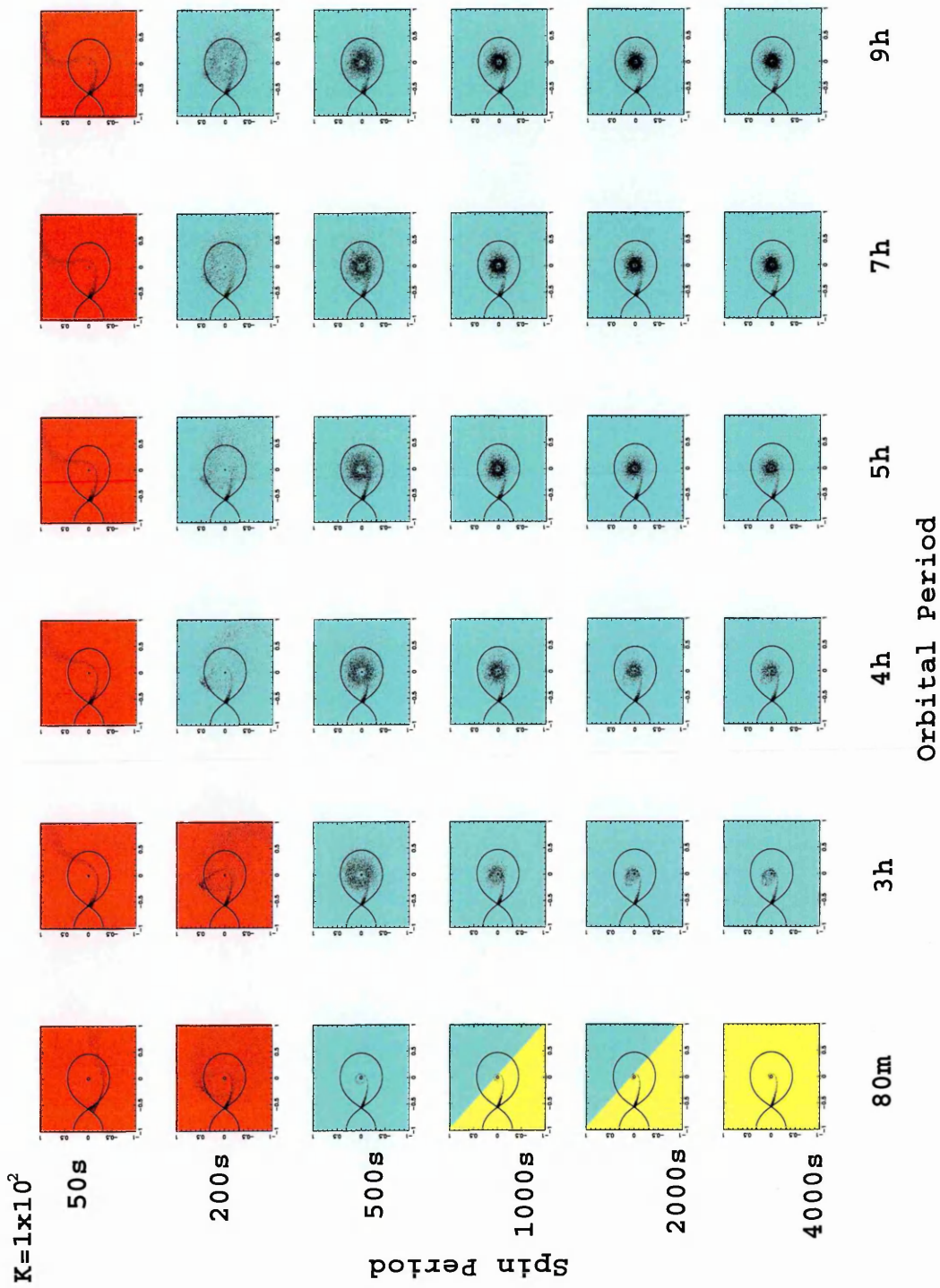
K=1x10^2
50s
200s
500s
1000s
2000s
4000s
Spin Period
80m
3h
4h
5h
7h
9h
Orbital Period

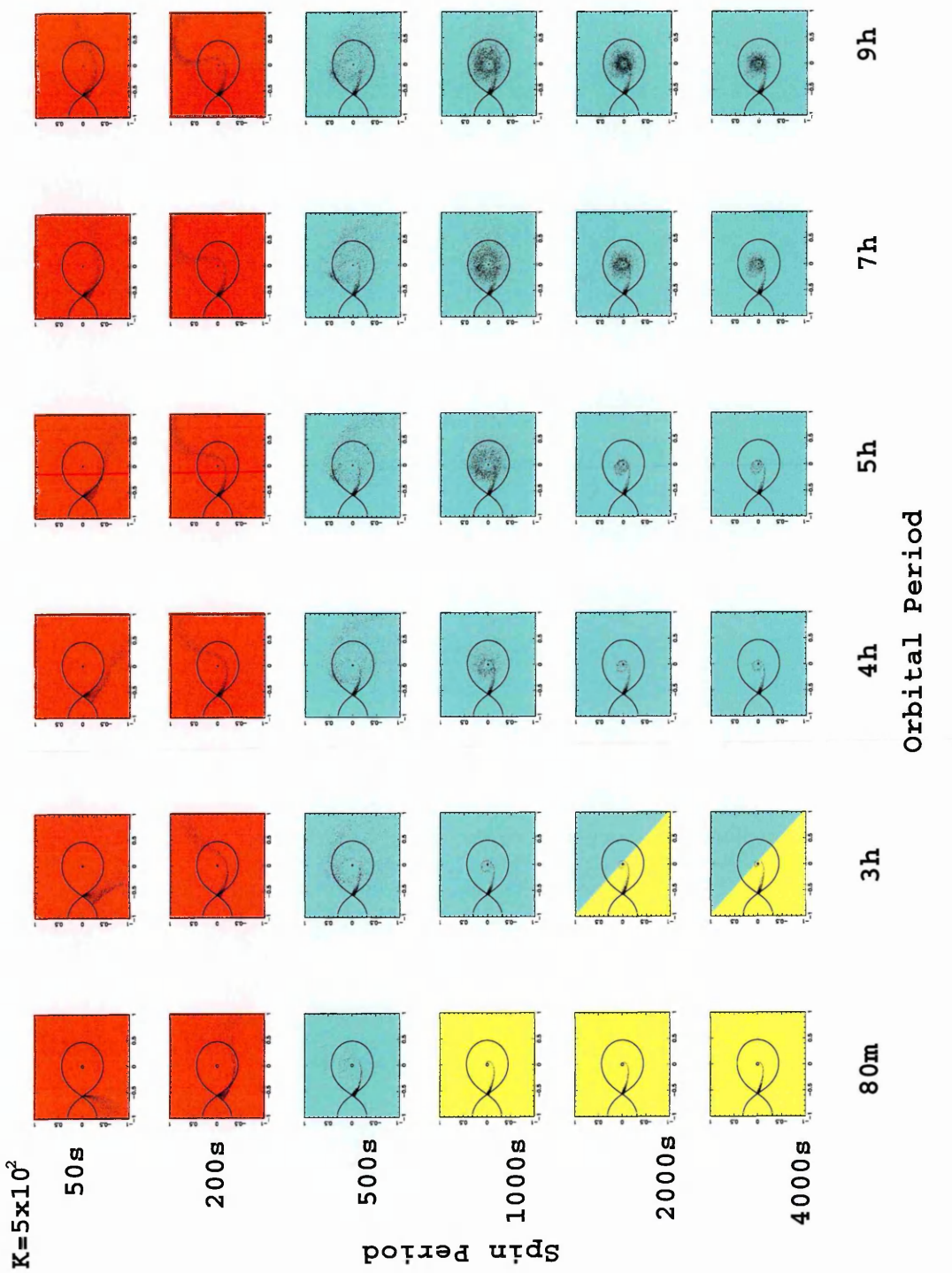
K=5x10^2
50s
200s
500s
1000s
2000s
4000s
Spin Period
80m
3h
4h
5h
7h
9h
Orbital Period

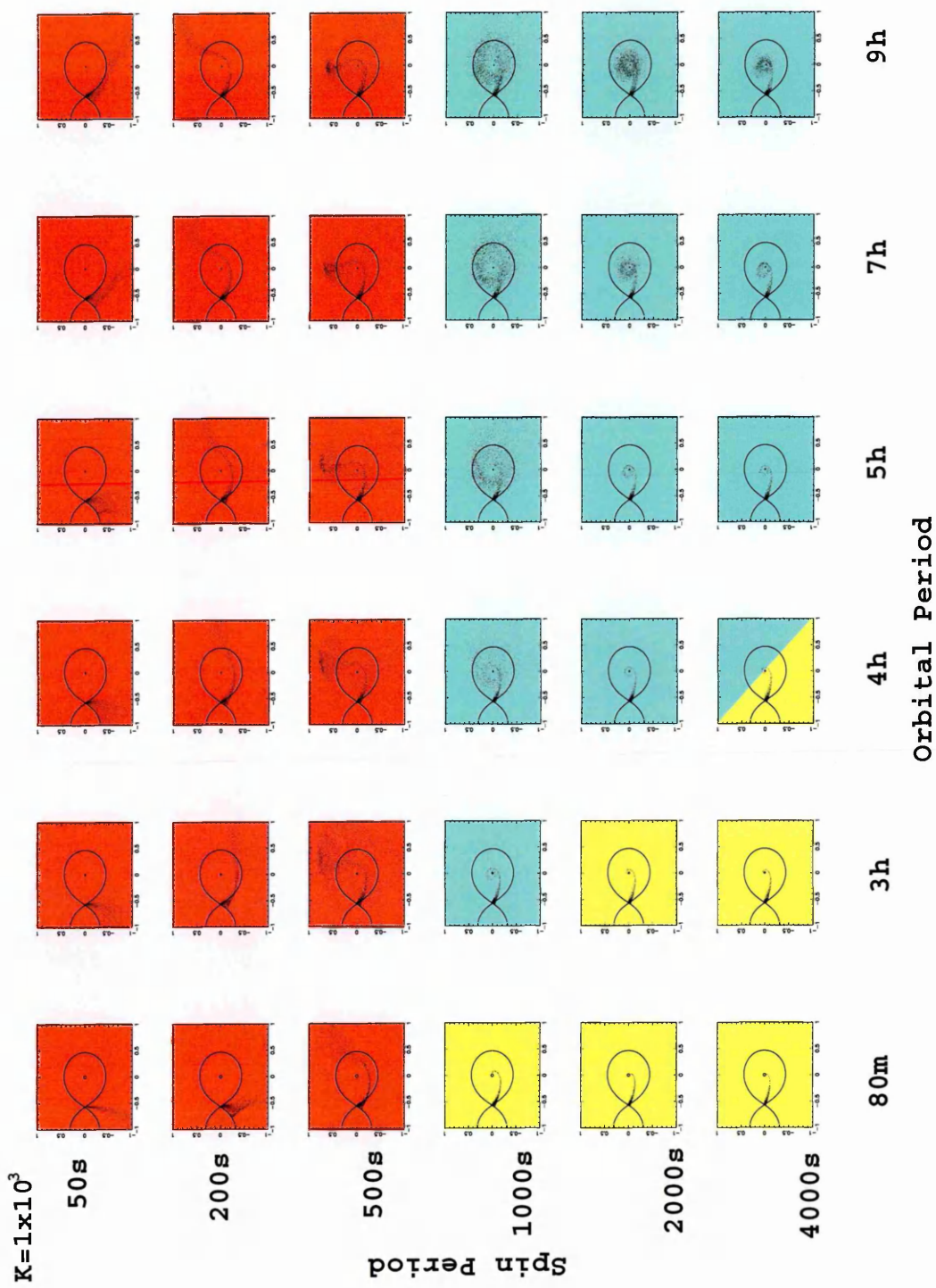
K=1x10^3
Spin Period
50s
200s
500s
1000s
2000s
4000s
80m
3h
4h
5h
7h
9h
Orbital Period

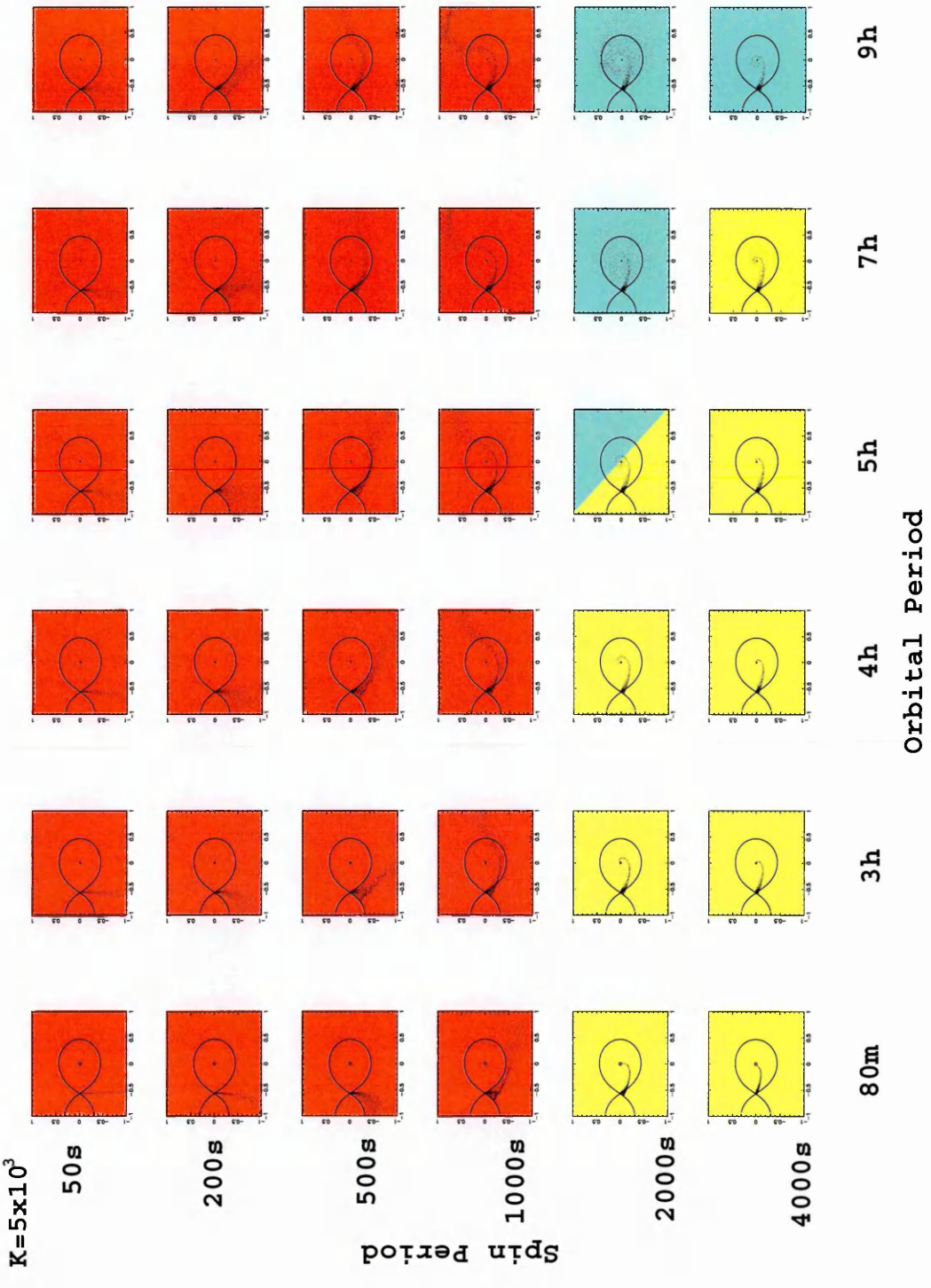
K=5x10^3
Spin Period
50s
200s
500s
1000s
2000s
4000s
80m
3h
4h
5h
7h
9h
Orbital Period

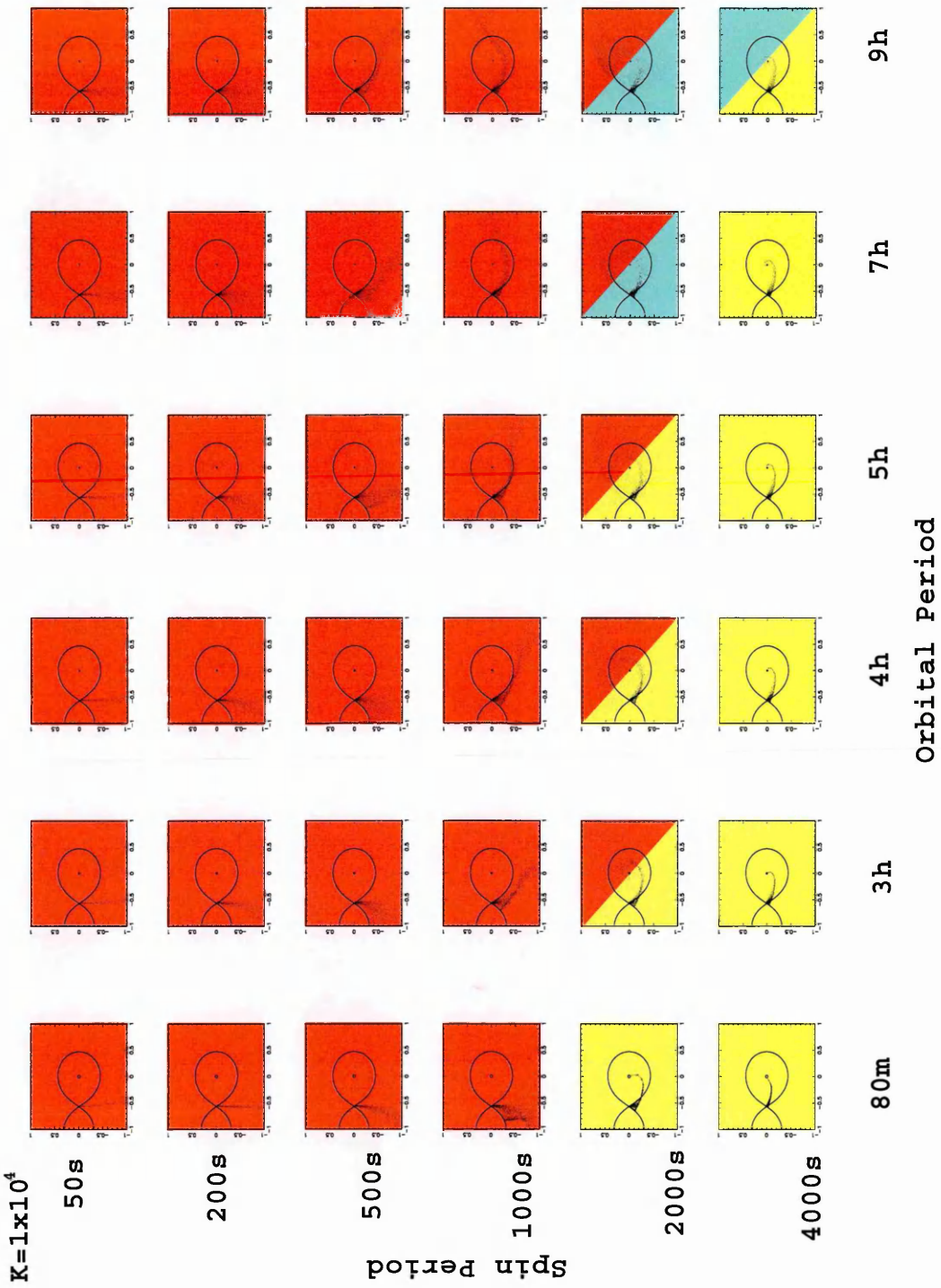
K=1x10^4
50s
200s
500s
1000s
2000s
4000s
Spin Period
80m
3h
4h
5h
7h
9h
Orbital Period

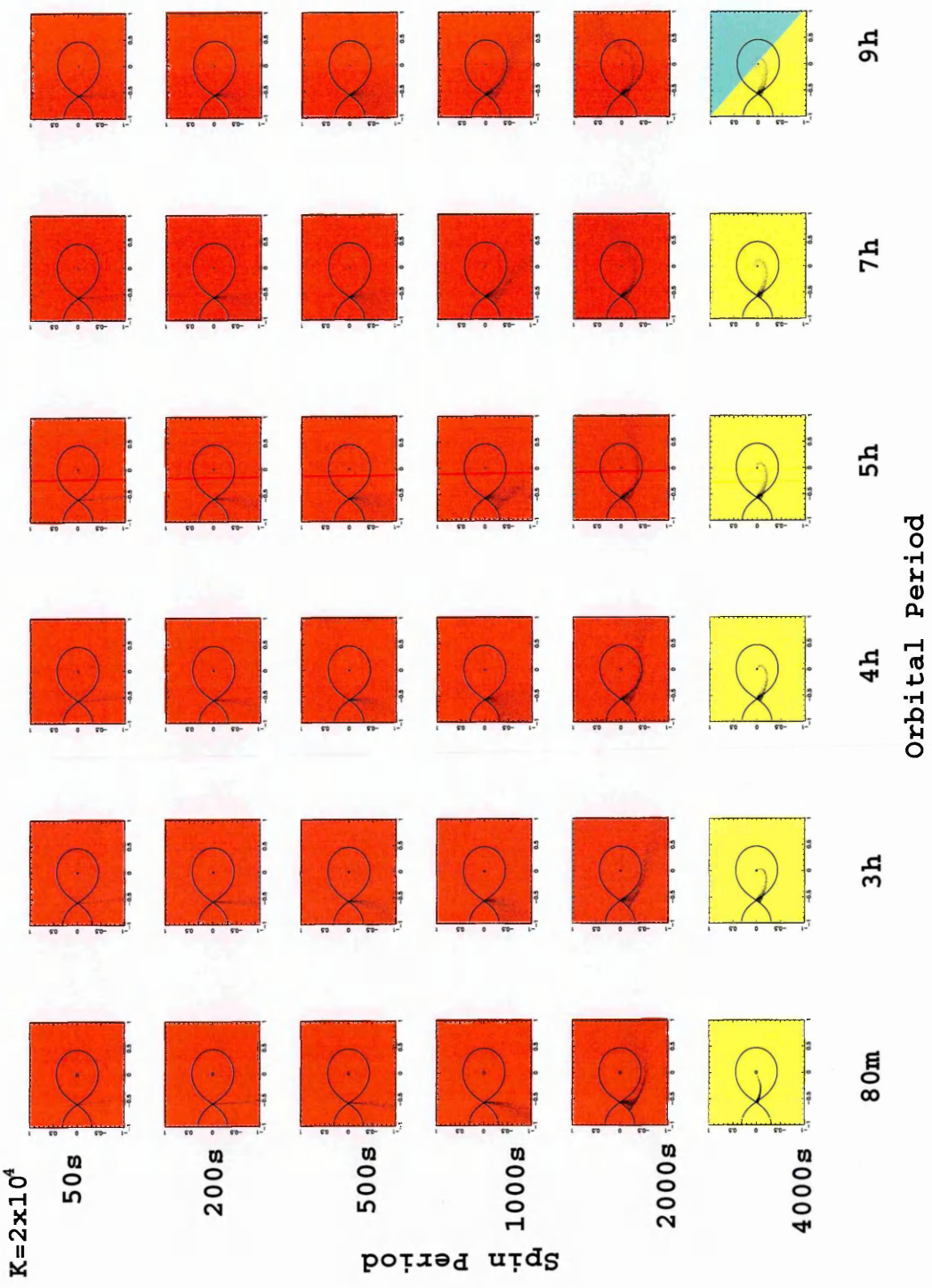
K=2x10^4
50s
200s
500s
1000s
2000s
4000s
Spin Period
80m
3h
4h
5h
7h
9h
Orbital Period

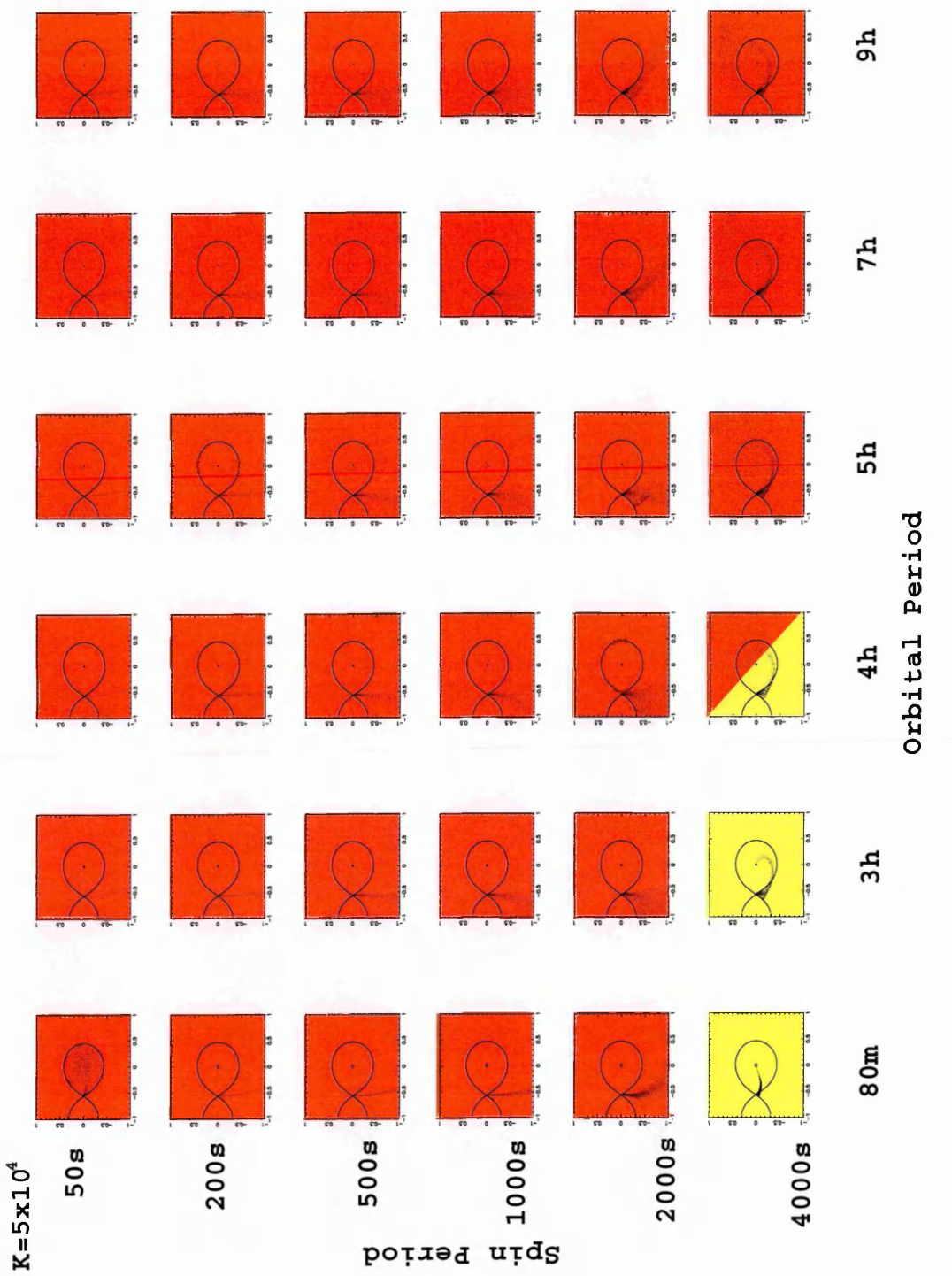
K=5x10^4
Spin Period
50s
200s
500s
1000s
2000s
4000s
80m
3h
4h
5h
7h
9h
Orbital Period

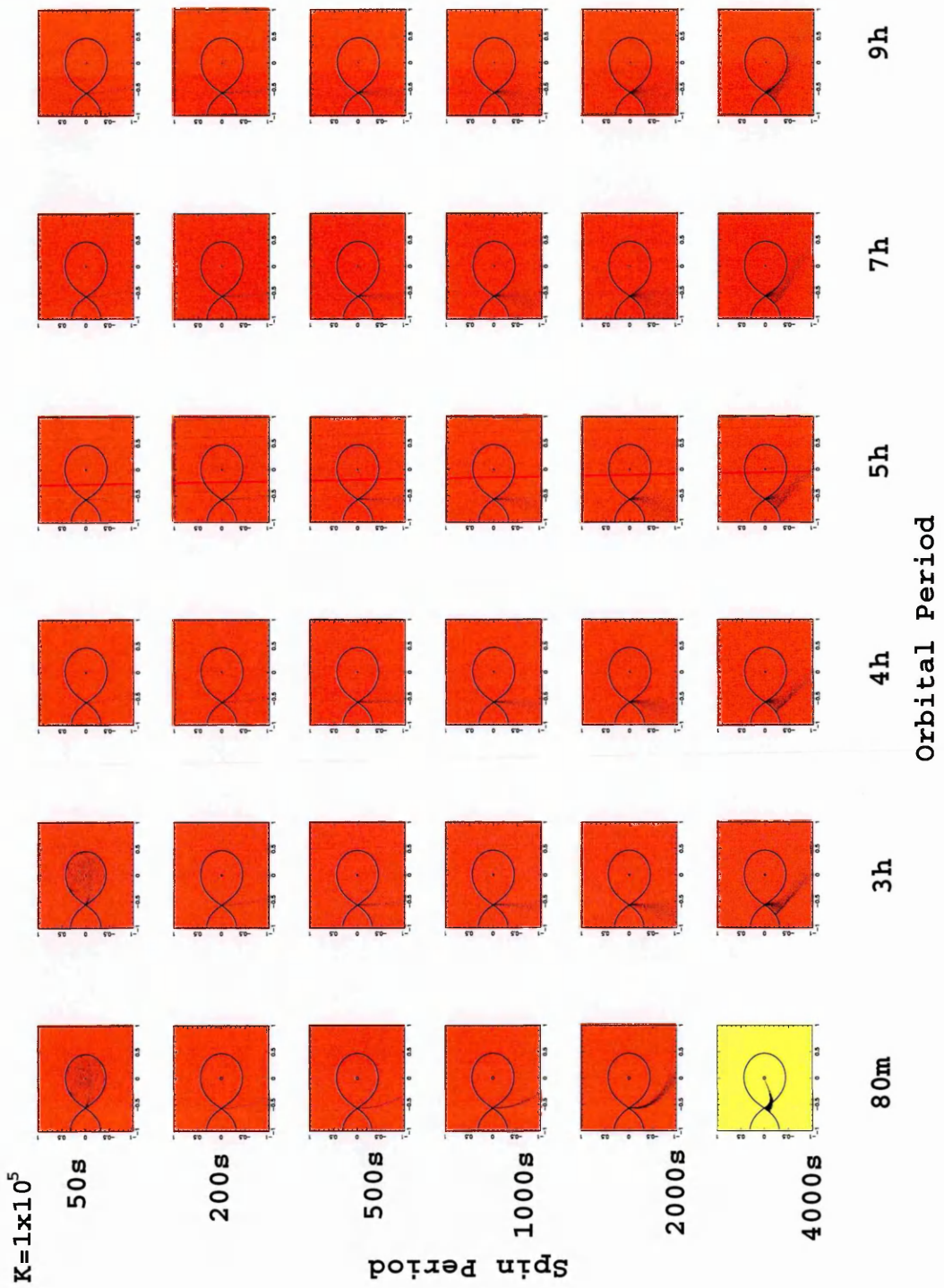
K=1x10^5
Spin Period
50s
200s
500s
1000s
2000s
4000s
Orbital Period
80m
3h
4h
5h
7h
9h

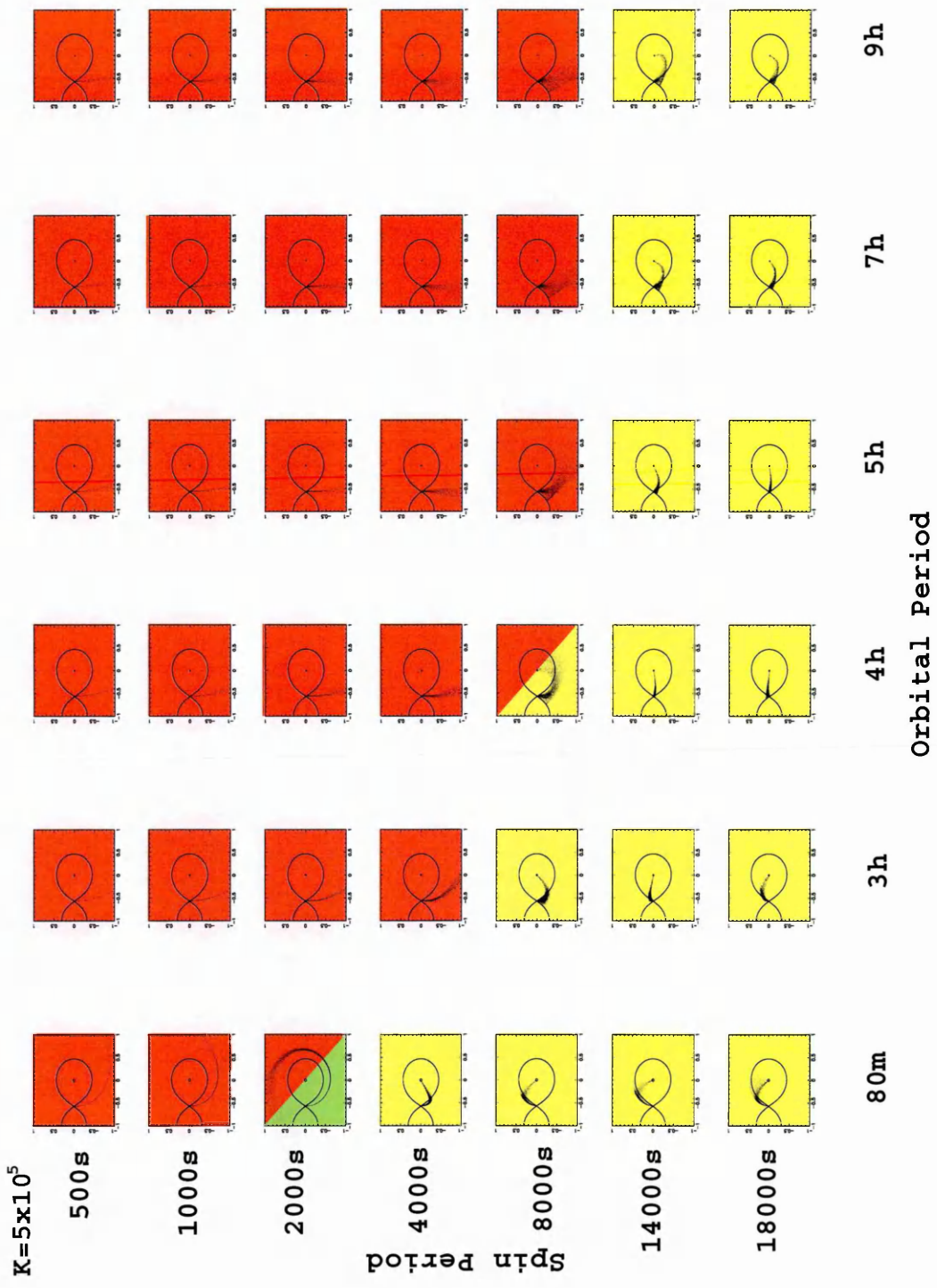
K=5x10^5
500s
1000s
2000s
4000s
8000s
14000s
18000s
Spin Period
80m
3h
4h
5h
7h
9h
Orbital Period

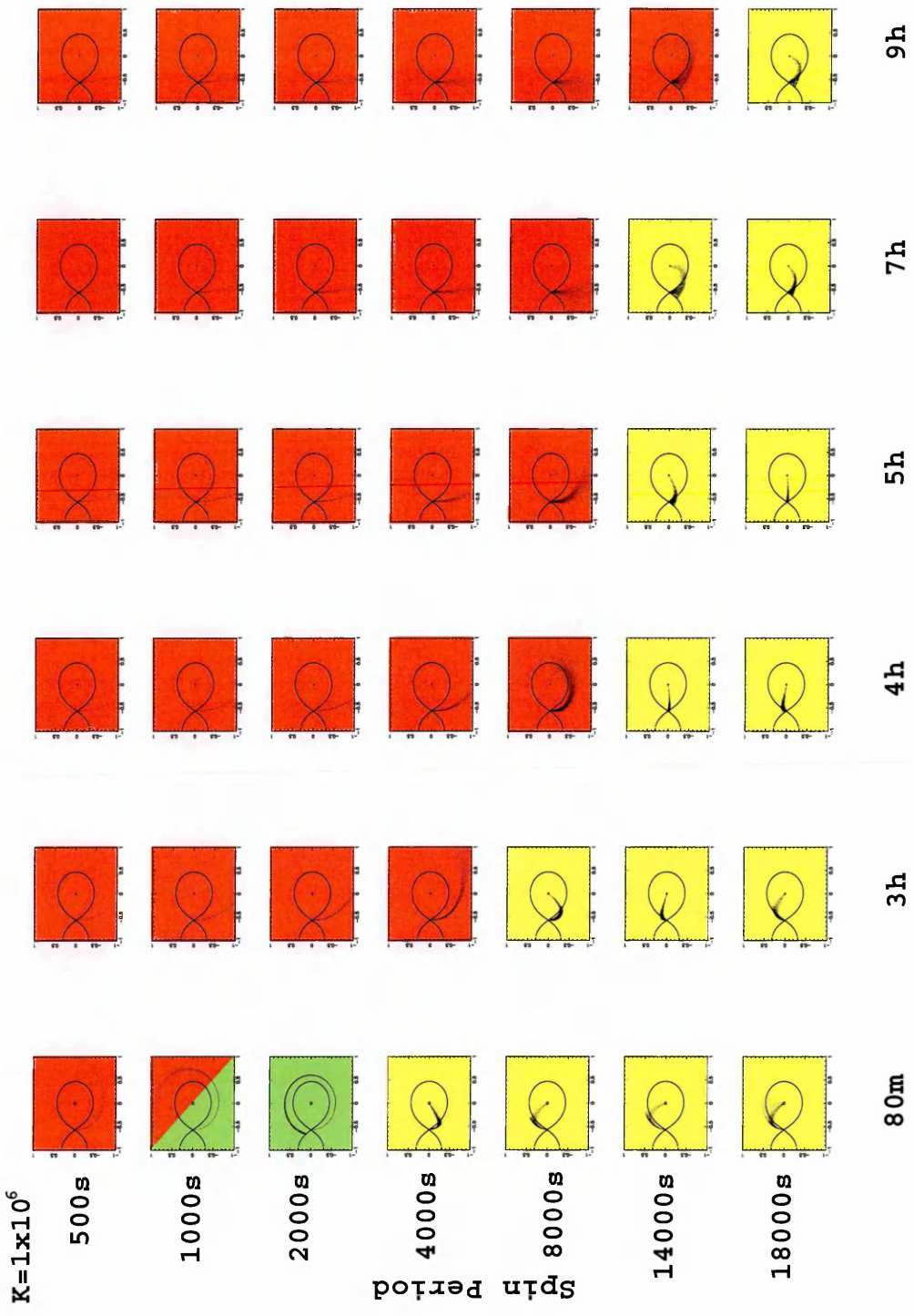
K=1x10^6
500s
1000s
2000s
4000s
8000s
14000s
18000s
Spin Period
80m
3h
4h
5h
7h
9h
Orbital Period


K=1x10^7
Spin Period
500s
1000s
2000s
4000s
8000s
14000s
18000s
Orbital Period
80m
3h
4h
5h
7h
9h
P

4.2.1 Discussion of accretion flows for the n^3 model

At low magnetic field strength we see that most of the IPs show disk accretion, with only the fast rotators at spin periods $\lesssim$ 200sec being propeller systems and the slow rotators with long orbital periods showing stream fed accretion.

As we progress to a slightly stronger field strength of k_0=5×10^2 we see more propellers coming into play with stream fed accretion also becoming more apparent at the longer spin periods and long orbital periods. The propeller systems are now seen at spin periods $\lesssim$ 500sec, still with disk accretion being dominant.

Strengthening the magnetic field further, we see a similar pattern to that of the previous figures but with the propellers taking over and becoming the dominant flow. Stream fed accretion becomes dominant over disk fed accretion at longer orbital periods with the increased field strength.

At a field strength of k_0=5×10^3, propeller flow is seen in all systems with spin periods $\lesssim$1000sec. The increase in the magnetic field strength means that even with a longer spin period material finds itself unable to form a stream onto the white dwarf and it is now propelled away. At this strength, for most of the orbital periods and long spin periods, stream-fed accretion is the result, with just a few disk fed accretion systems existing at the longest orbital periods of 7h and 9h at slow spin rates.

Propeller flow is now becoming the dominant flow at a field strength of k_0=1×10^4. The disk systems are hard to distinguish from the propellers and stream fed systems. Propeller flow is seen at spin periods $\lesssim$ 2000sec with stream fed accretion only seen for really slow rotators at 4000sec.

By k_0=2×10^4 propeller accretion governs almost all the IPs regardless of the spin or orbital period with disk fed systems becoming almost non existent. Stream fed accretion however is still seen at long spin periods for all the orbital period range.

In the scenario at k_0=5×10^4, stream fed accretion is now only seen for slow rotators at orbital periods $\lesssim$ 4h. The disk fed systems are now no longer formed at magnetic fields of this strength with almost all mass transfer from the secondary being propelled away no matter what the spin or orbital period. The magnetic field is strong enough to inhibit the accreting blobs from attaching to it and spiralling down to the white dwarf surface.

It seems by k_0=1×10^5 that no accretion can overcome the strength of the field as all but one system in the parameter space is now a propeller system. Only at a spin period of 4000sec and an orbital period of 80min does the right combination exist still to see stream fed accretion.

Moving to even higher field strengths, the accretion flows start to get interesting as we see a new type of flow emerging. A ring system forming outside the Roche lobe of the white dwarf but still likely to be bound to the system within the L_2 point and swept up by the secondary. With the material still being propelled away we see the accretion flow take a different direction with it almost coming back round on itself. We also see propeller accretion still dominant, for very slow rotators ($P_{\rm spin} \gtrsim$ 8000sec) stream fed accretion is seen.

Soon the ring accretion mode is becoming more apparent at k_0=1×10^6. At long spin periods and long orbital periods we can see clearly now the shape of the accretion flow in a ring around the outside of the Roche lobe of the white dwarf. The strength of the field is now causing more of the stream fed systems to become propellers at the longer orbital periods with spin periods $\lesssim$ 14000s.

In the final model at the highest magnetic field strength, we see a number of interesting features. The ring systems are clearly becoming very dominant in the parameter space at this high field strength. We see the polar systems also becoming apparent on this model with stream fed accretion being the characteristic accretion mechanism of these particular

systems. At still longer periods we see retrograde motion happening at the longest spin periods, i.e. when $P_{\rm spin} > P_{\rm orb}$

4.2.2 Overall Conclusions

We are seeing some interesting evolution in flow patterns as our systems evolve across parameter space. We see that at weak magnetic fields it was the short spin periods that gave us propeller effects and stream accretion was seen at the longer spin periods and longer orbital periods. But we see as the strength of the field increases, the propeller effect dominates. The field just gets too strong for material to attach to it regardless of the spin period of the white dwarf. At the very high end of the field strength we see new types of flow occurring, a 'ring' system forming outside the white dwarf. As $P_{\rm spin}$ approaches $P_{\rm orb}$ we see the IPs evolve across parameter space to polars and so take on the characteristic stream fed accretion seen in these systems. We then also even see retrograde motion taking place at the highest field strength with the slowest rotators. Table 4.1 shows this accretion distribution from the extensive coverage of $P_{\rm spin}$, $P_{\rm orb}$ and k_0 parameters.

Table 4.1: Accretion flow distribution that occurs for the n^3 model situation

Type	$P_{\rm spin}/P_{\rm orb}$	k_0
Propeller	< 0.01	$< 10^4$
	< 0.1	$10^4 - 10^5$
	< 0.5	$>10^5$
Disk	$0.01 - 0.2$	$< 10^4$
Stream	> 0.2	$< 10^4/10^4 - 10^5$
	> 0.5	$>10^5$
Ring	~ 0.6	$>10^5$
Stream (Polars)	~ 1	$>10^5$
Backward stream (retrograde)	> 1	$>10^5$

4.3 n^6 model

In Figure 4.2 we present the results of running HyDisc for the n^6 model where $k(r) \propto r^{-6}$, with the range of $P_{\rm orb}$, $P_{\rm spin}$ and k_0 discussed at the beginning of this chapter. As noted in Chapter 3, in the n^6 model we assume that the gas density and length scale are **constant** throughout the binary system. Details are given in the caption. In all these simulations, the same masses as in the n^3 version were used to keep consistency. The masses of the two stars are $0.6{\rm M}_\odot$ and $0.3{\rm M}_\odot$ and the dipole inclination angle is $m \sim 5°$.

Figure 4.2: Accretion flows for the n^6 model where $k(r) \propto r^{-6}$ for each k_0 value in parameter space. The red figures indicate propeller accretion, yellow figures indicate stream, blue figures indicate disk accretion and green figures are ring structure accretion. A small magenta 'P' in the upper left of a figure indicates a polar system, i.e. the configuration where $P_{\rm spin} = P_{\rm orb}$ for the highest magnetic field strength. The k value listed on each page of the figure is the value input to HyDisc, i.e. k_0 which is the value of $k(r)$ at the WD surface

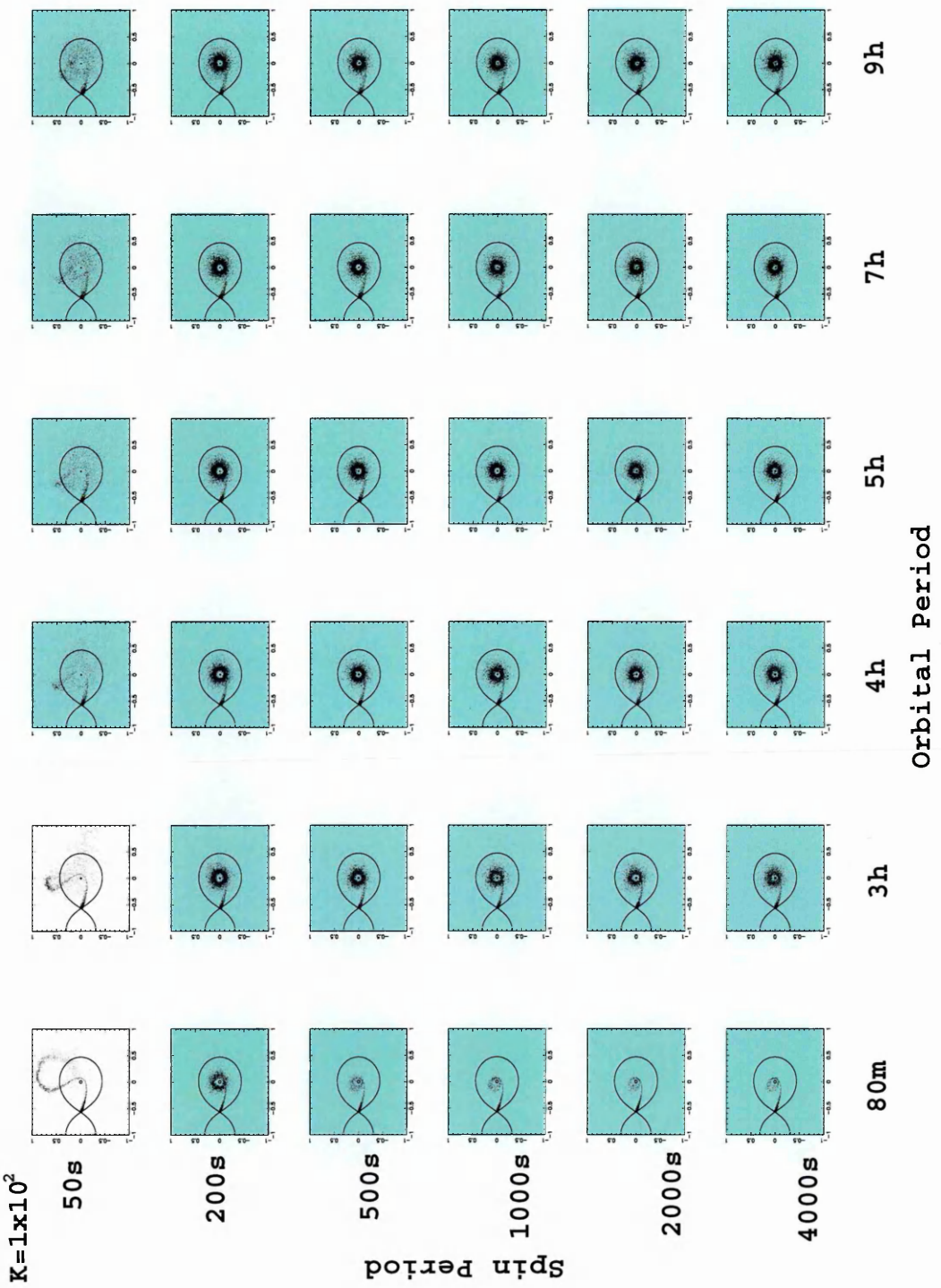
K=1x10^2
50s
200s
500s
1000s
2000s
4000s
Spin Period
80m
3h
4h
5h
7h
9h
Orbital Period

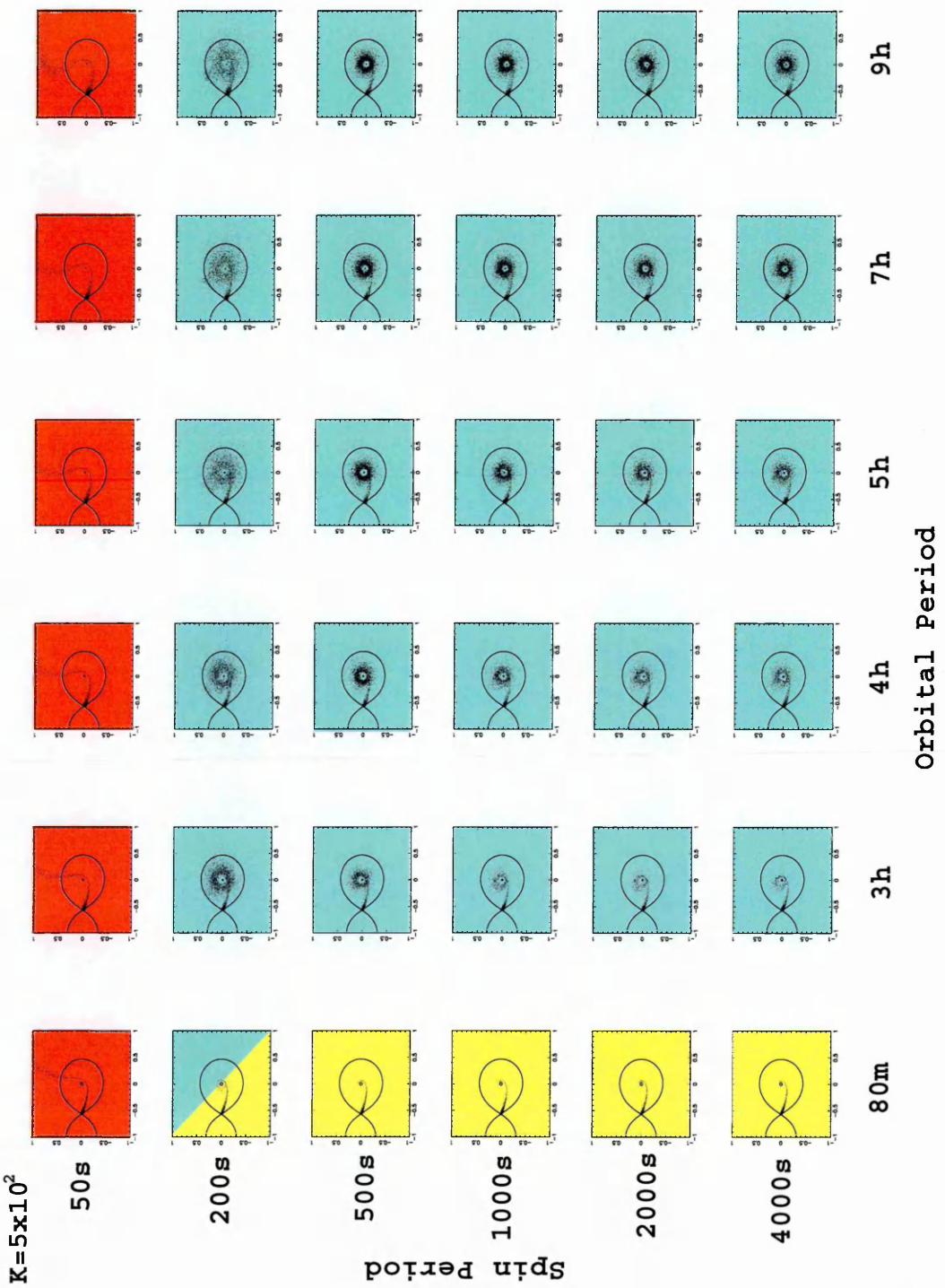
K=5x10^2
Spin Period
50s
200s
500s
1000s
2000s
4000s
Orbital Period
80m
3h
4h
5h
7h
9h

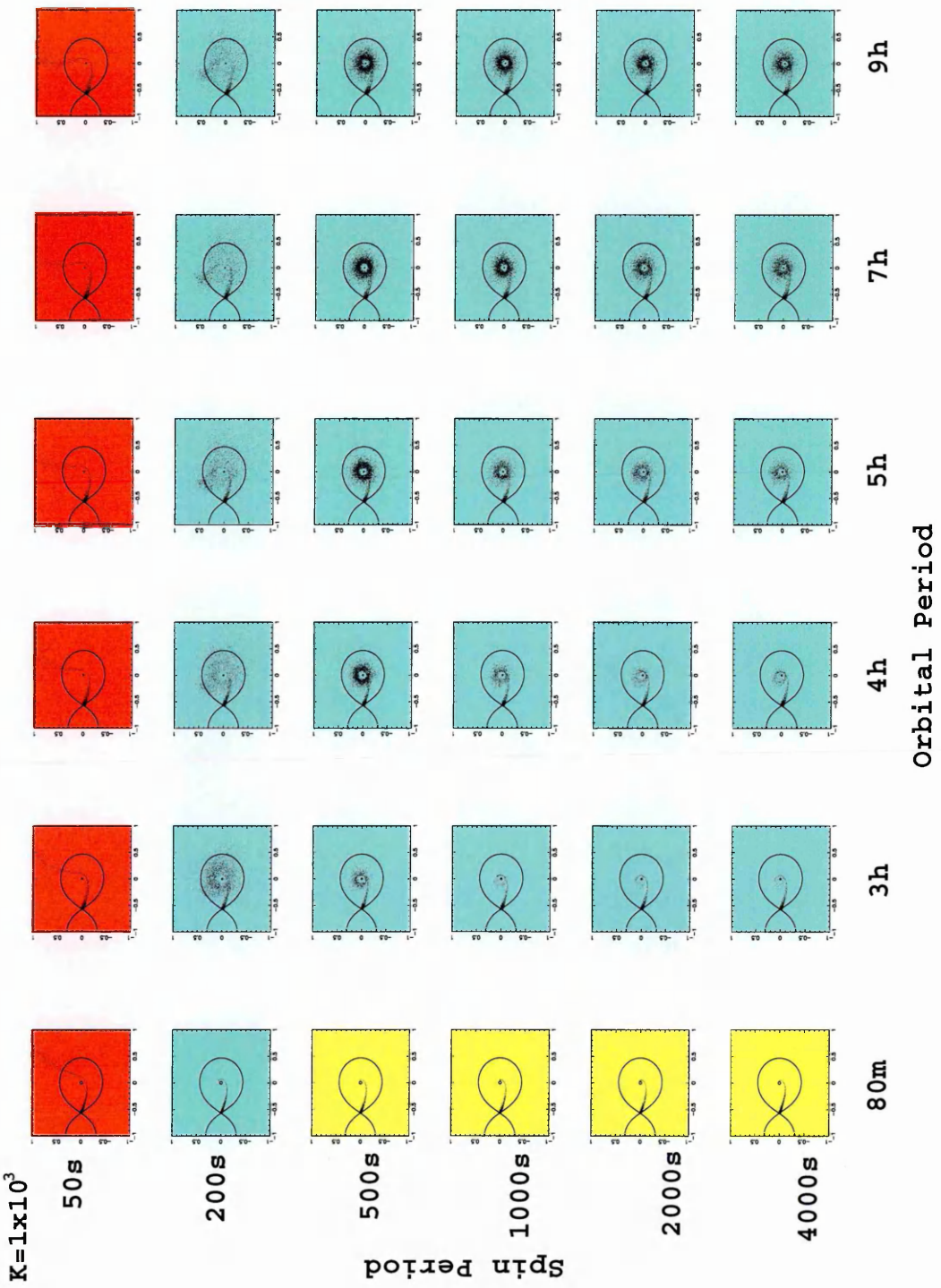
K=1x10^3
Spin Period
50s
200s
500s
1000s
2000s
4000s
80m
3h
4h
5h
7h
9h
Orbital Period

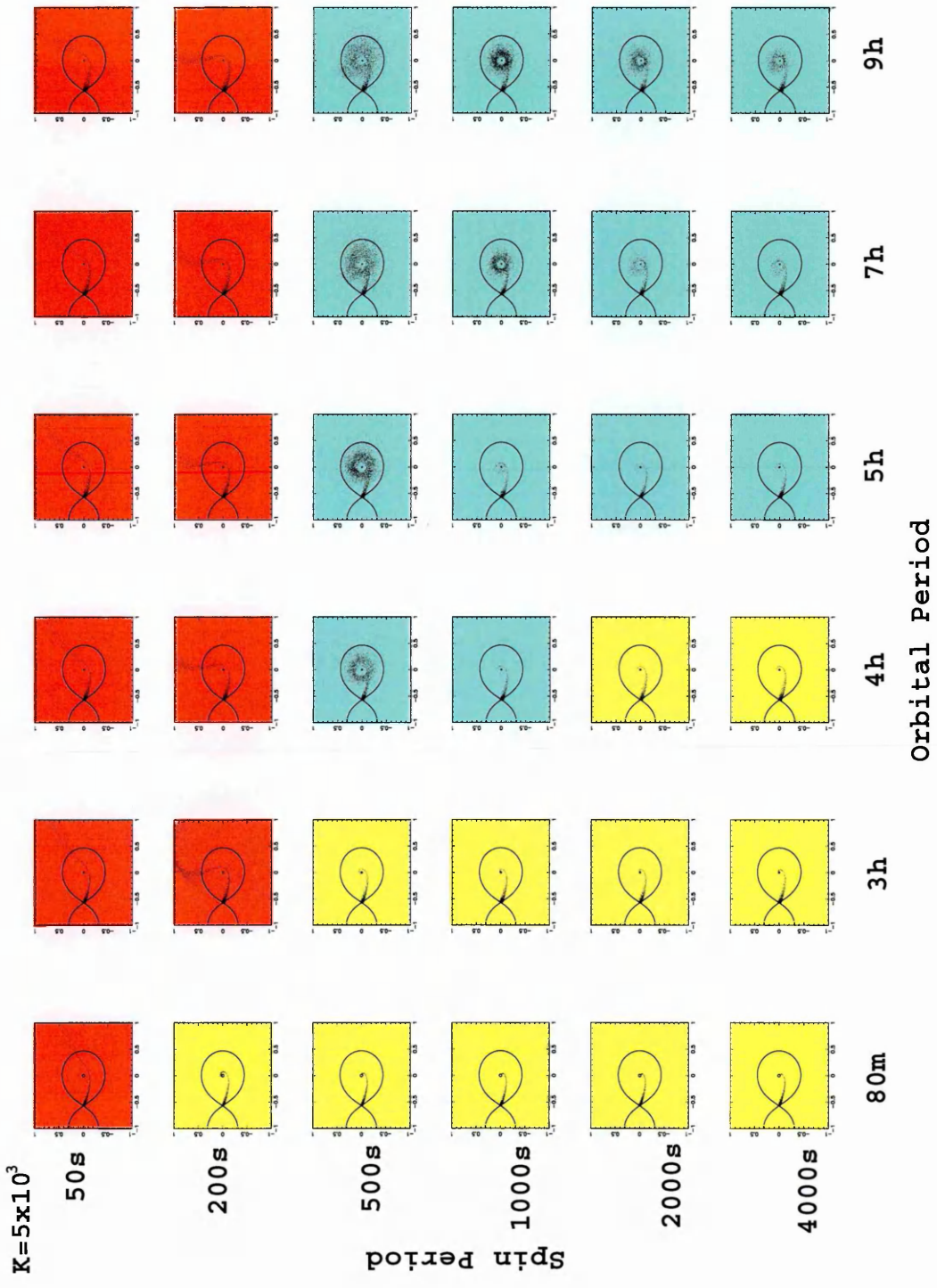
K=5x10^3
Spin Period
Orbital Period
50s
200s
500s
1000s
2000s
4000s
80m
3h
4h
5h
7h
9h

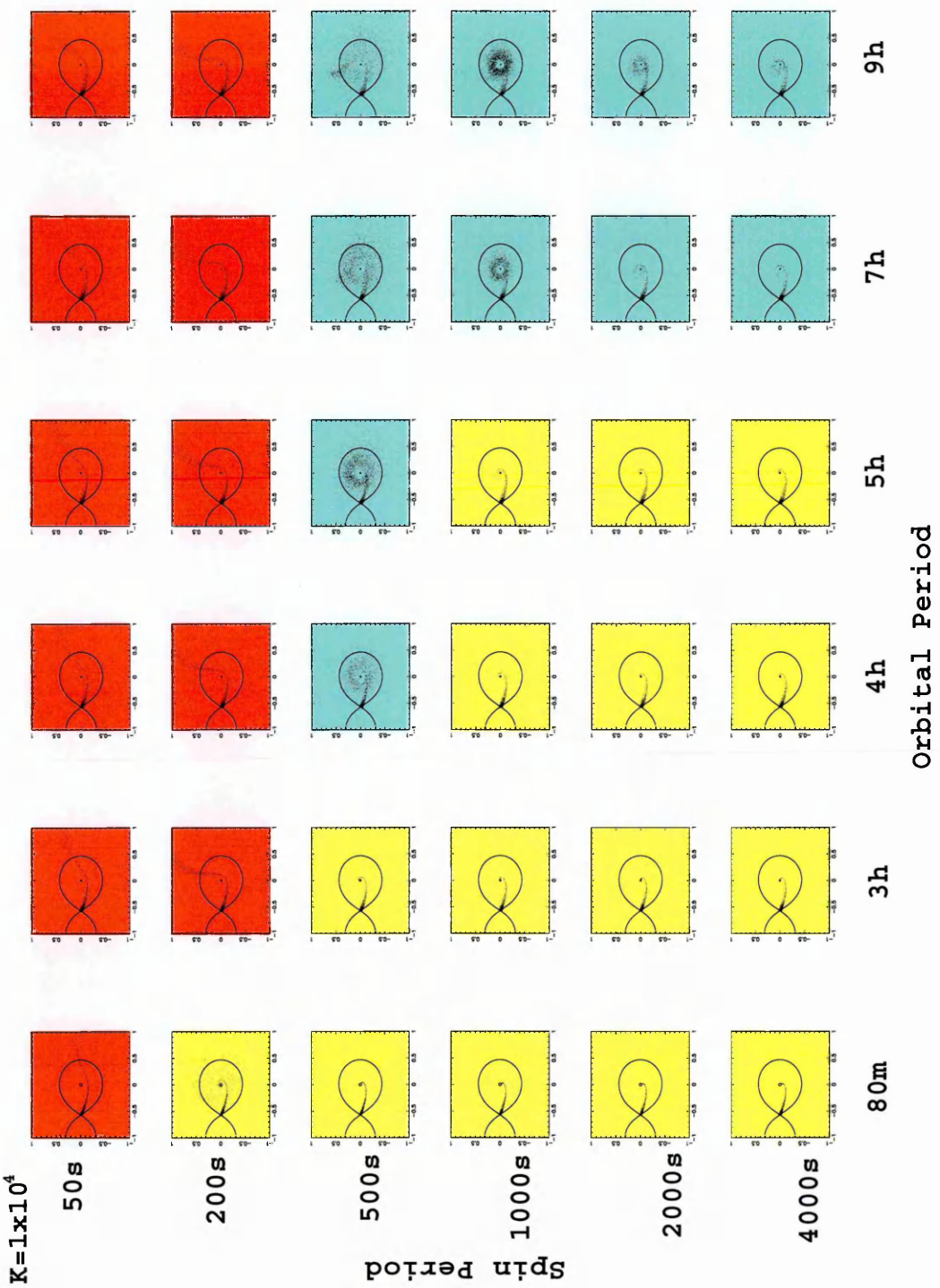
K=1x10^4
Spin Period
50s
200s
500s
1000s
2000s
4000s
80m
3h
4h
5h
7h
9h
Orbital Period

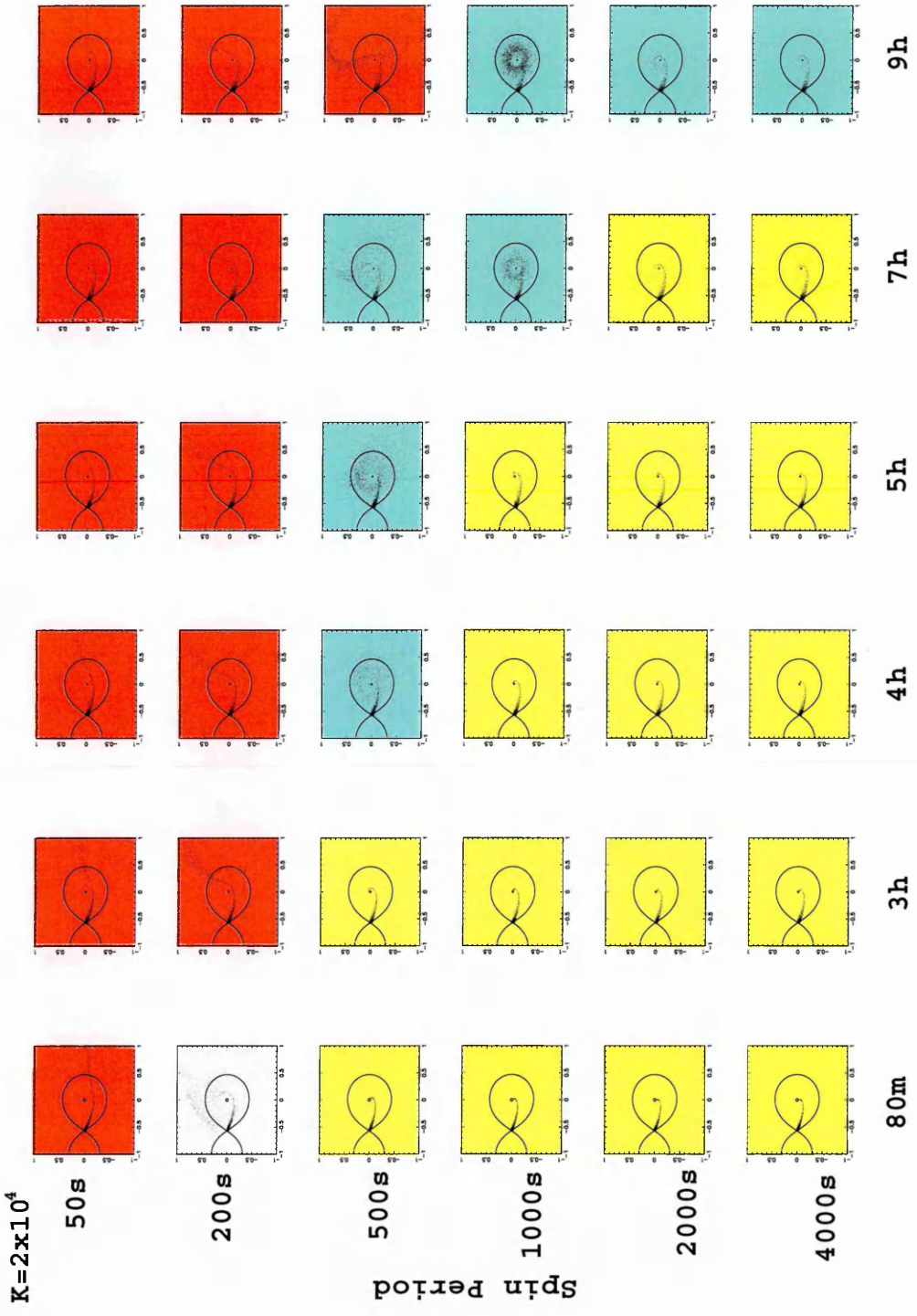
K=2x10^4
50s
200s
500s
1000s
2000s
4000s
Spin Period
80m
3h
4h
5h
7h
9h
Orbital Period

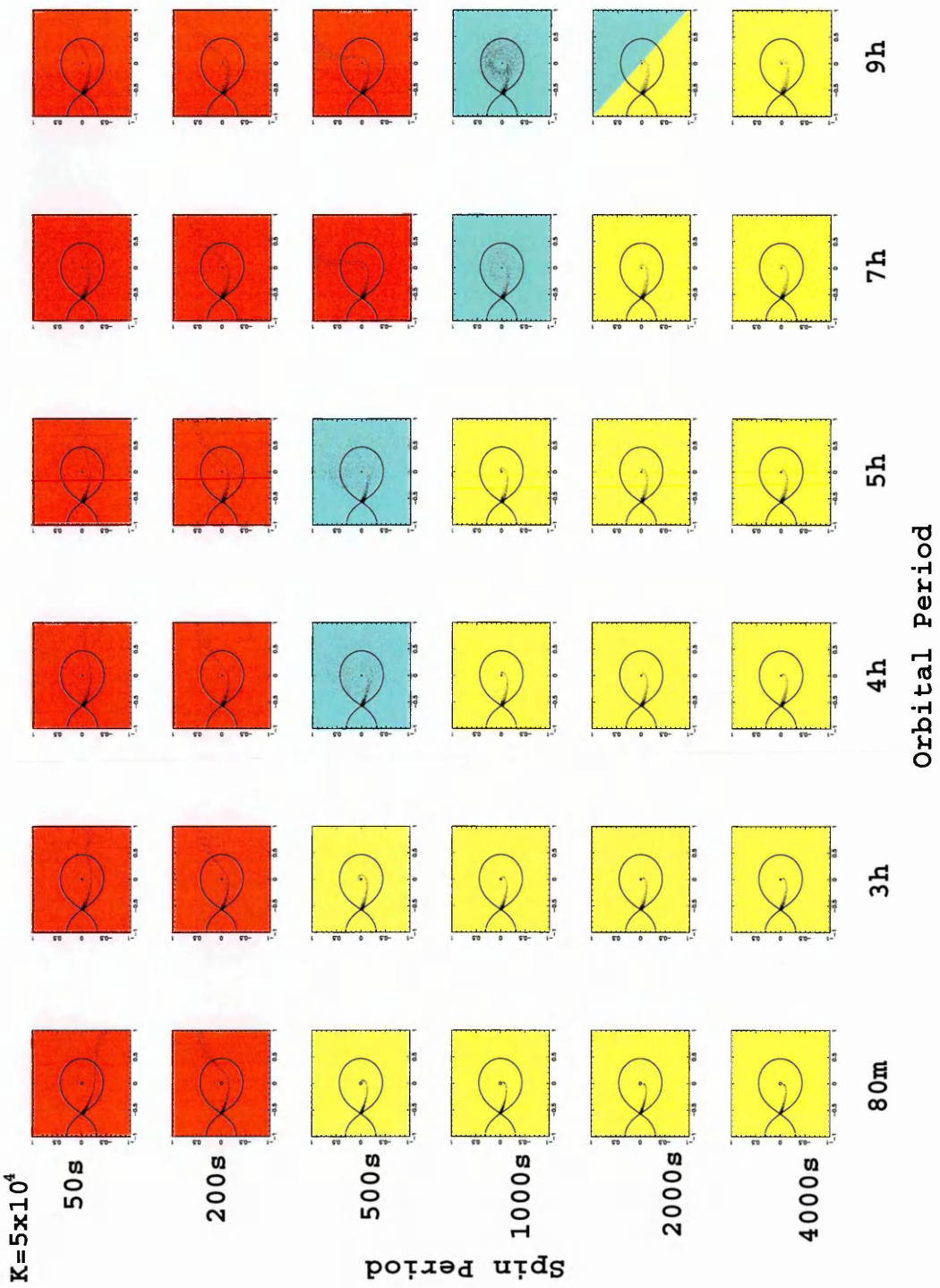
K=5x10^4
Spin Period
50s
200s
500s
1000s
2000s
4000s
80m
3h
4h
5h
7h
9h
Orbital Period

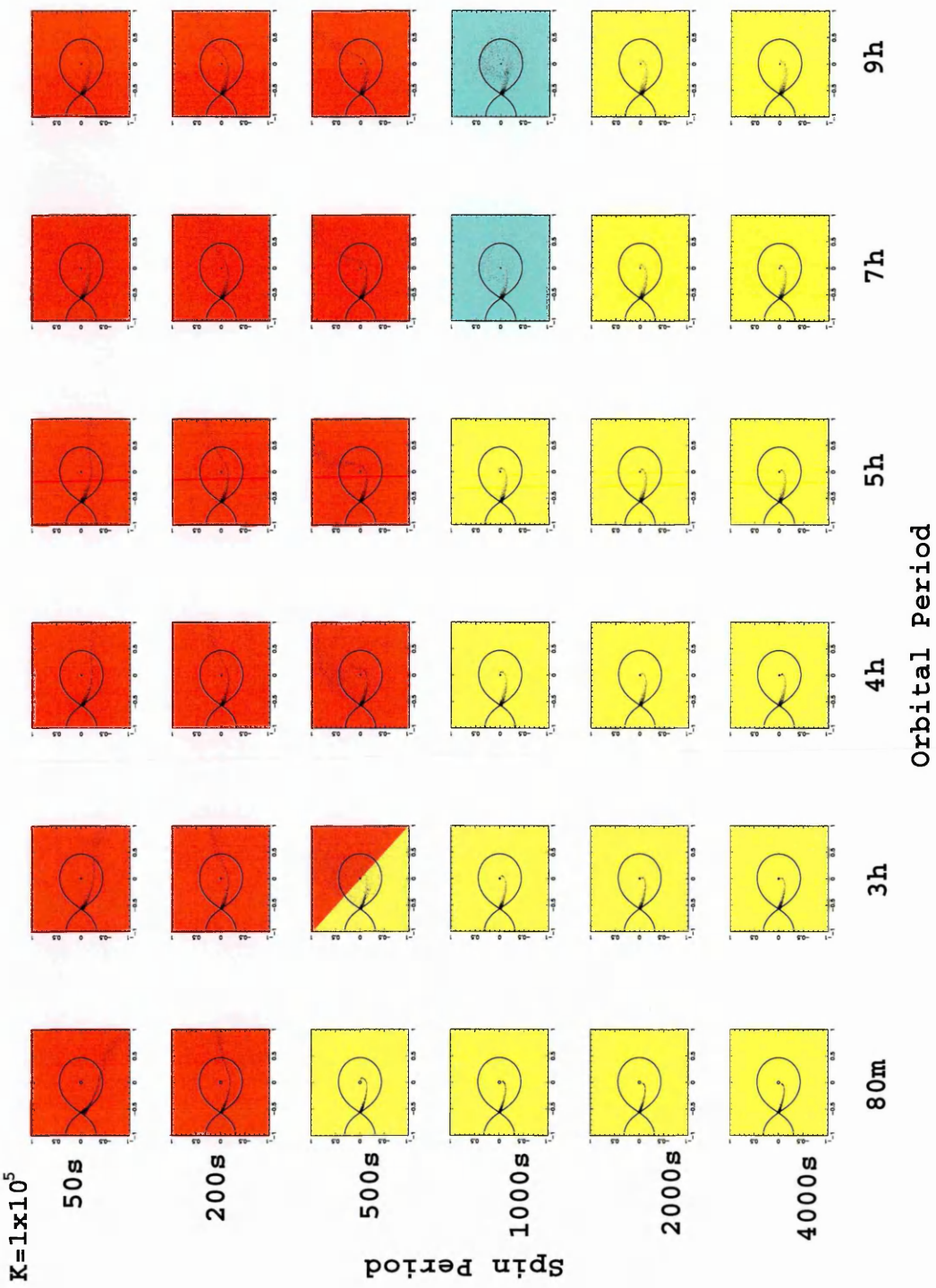
K=1x10^5
Spin Period
50s
200s
500s
1000s
2000s
4000s
80m
3h
4h
5h
7h
9h
Orbital Period

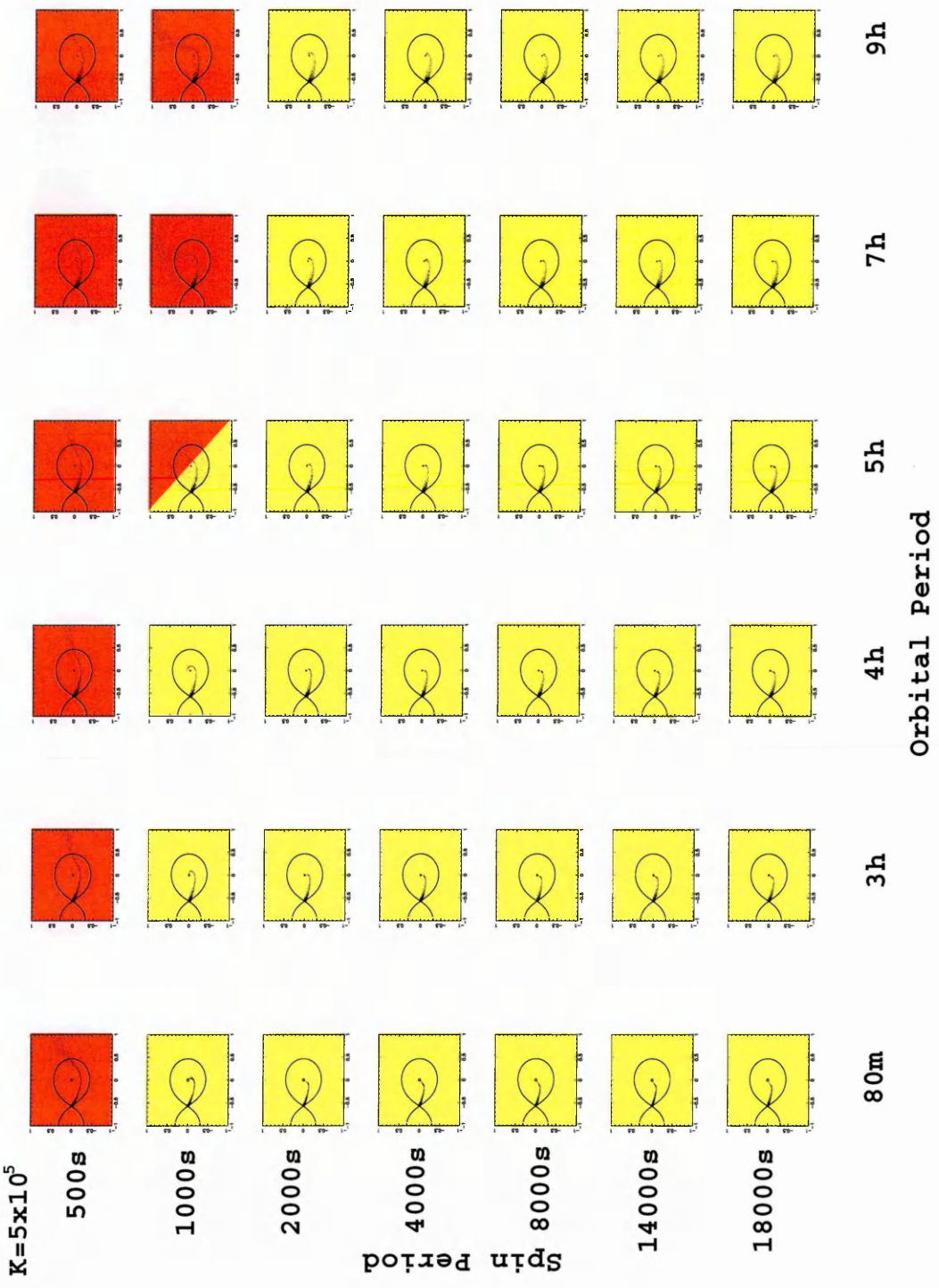
K=5x10^5
Spin Period
500s
1000s
2000s
4000s
8000s
14000s
18000s
Orbital Period
80m
3h
4h
5h
7h
9h

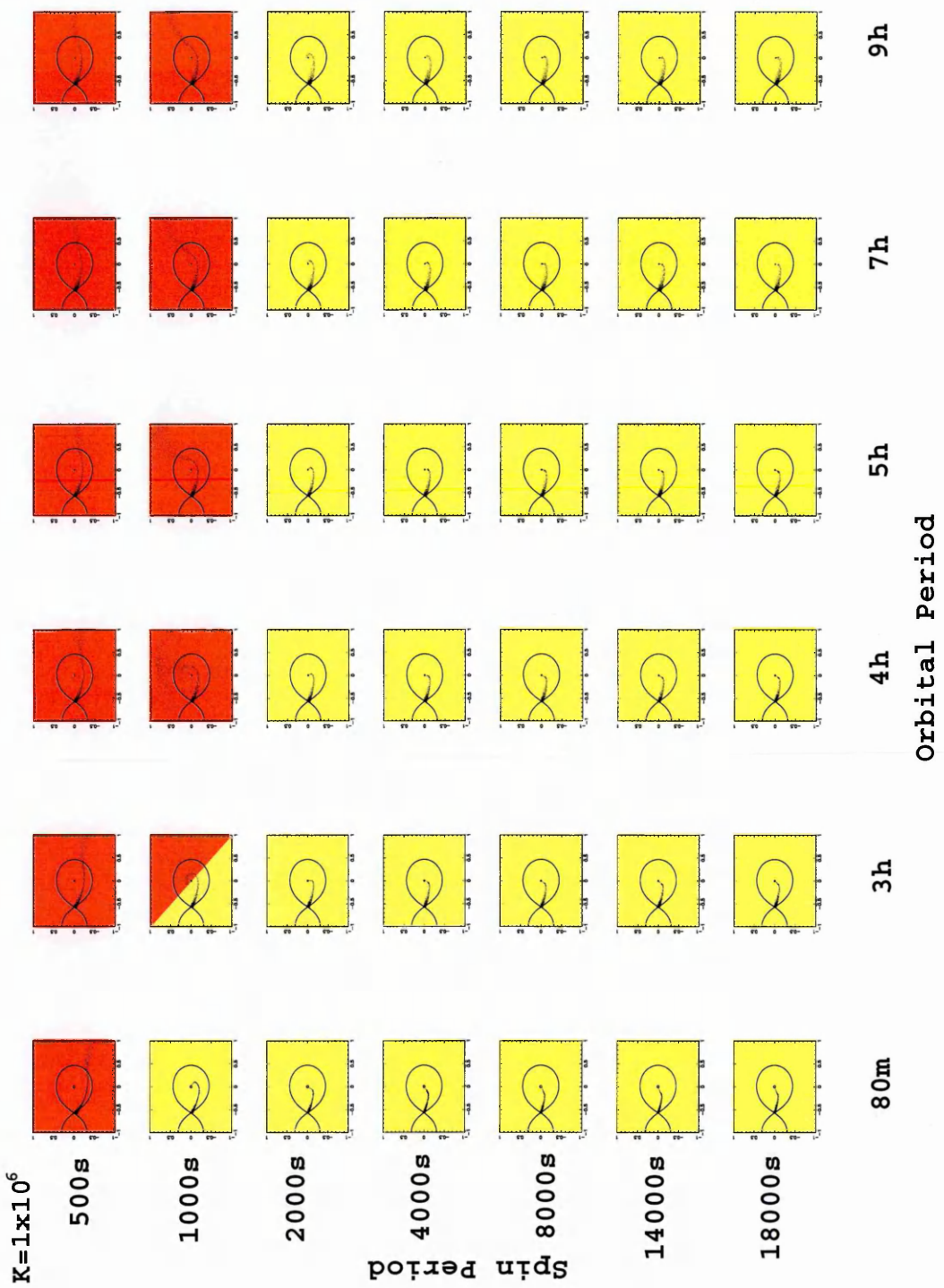
K=1x10^6
500s
1000s
2000s
4000s
8000s
14000s
18000s
Spin Period
80m
3h
4h
5h
7h
9h
Orbital Period

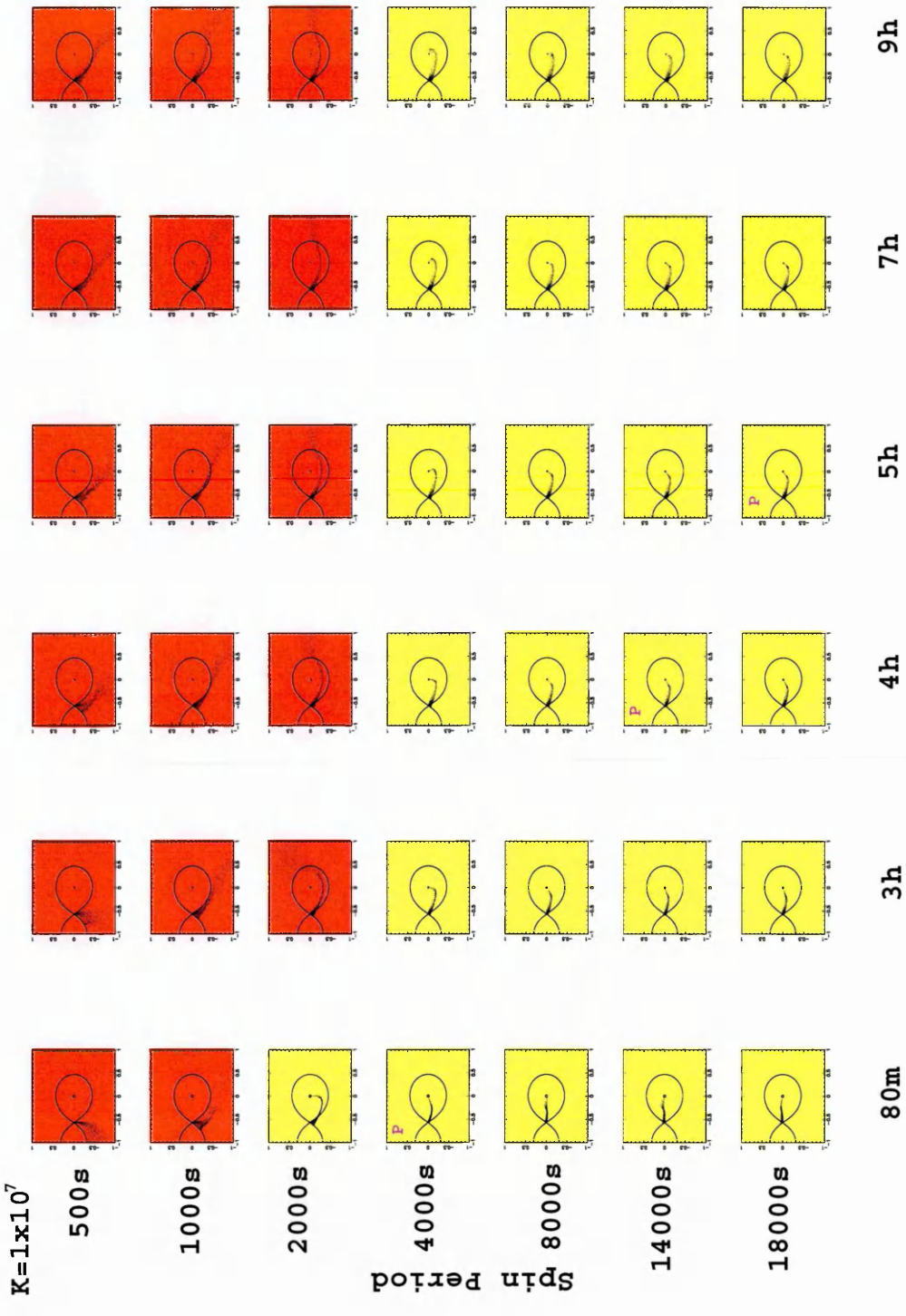
K=1x10^7
Spin Period
500s
1000s
2000s
4000s
8000s
14000s
18000s
Orbital Period
80m
3h
4h
5h
7h
9h

4.3.1 Discussion of accretion flows for the n^6 model

At the lowest magnetic field strength of k_0=1×10^2 we see that all the accretion flows are disk-like in nature with two systems at short orbital periods and short spin periods producing flows that are difficult to classify due to the unusual path of the flow.

As we progress further, we see that the combination of an increased magnetic field strength and a short spin period now leads to a propeller effect and we also see now that this stronger magnetic field has influenced the accretion flow more at the short orbital periods of 80min in that we are now starting to see stream fed accretion creeping in.

Increasing the magnetic field strength further from k_0=5×10^2 to k_0=1×10^3 does not seem to alter the type of flow in parameter space for any of the systems except on one where stream fed accretion becomes more observable than before.

If we keep increasing the field strength we start to see a bigger change in the accretion flow patterns. We see more propeller and stream fed systems emerging. The propellers emerge at the short spin periods, that is at $P_{\rm spin} \lesssim$ 200s for all orbital periods, whereas the streams appear at orbital periods of $P_{\rm orb} \lesssim$ 4h for spin periods of $\gtrsim$ 200s. The disk systems however are still the dominant accretion flows at this field strength for the parameters given.

At still higher magnetic field strength we see the stream fed systems progressing up the orbital period range and yet the propellers stay exactly where they are at the same parameters as was observed in the k_0=5×10^3 case. The disk systems though present are slowly being forced out of this flow scenario as the magnetic field is becoming more dominant over the material in these disks.

Progressing further in field strength, we see very little difference to what was observed previously at k_0=5×10^4. The slight increase in field strength does allow one more system to be controlled more by the magnetic field lines and shows stream fed accretion instead

of disk fed accretion. The increase in strength, along with the combination of fast rotator at $P_{\rm spin}$ = 500s and a long orbital period of 9h allows another system to become strong enough to propel the material out into space.

By k_0=5×10^4, the disk systems have almost gone with the stream flow now being the most dominant flow. The propeller systems with the aid of the stronger magnetic field are also advancing through the parameter space but only at the long orbital periods

At a magnetic field of k_0=1×10^5 the picture is much the same. The propeller systems and stream systems are about the same number. The propellers are seen at shorter orbital periods of $\lesssim$ 4h and still at the short spin periods. Stream fed accretion is taking over from disk fed accretion slowly, with two disk fed IPs left at long orbital periods and spin periods of 1000s.

Stream accretion and propeller accretion are now the governing flows at k_0=5×10^5. At this high field strength it is impossible for a disk system to form. At the short spin periods ($P_{\rm spin} \lesssim$ 1000s) and strong field the material just skips over the white dwarf as the magnetic torque of the field lines propels it away. At longer spin periods however, the material is still able to attach onto the field lines and spiral down to the surface.

The picture at k_0=1×10^6 is much the same as above, propeller and stream fed accretion being dominant. Propeller flows are seen at shorter orbital periods as has been seen through all the parameter space at the different strengths but still predominantly at the long spin periods.

At high magnetic field strengths, we can observe the evolution to polars and see their characteristic stream fed accretion. At k_0=1×10^7 again both stream fed and propeller accretion dominates. Propeller accretion is now seen at spin periods of P$_s$ $\lesssim$ 2000s and appearing now at all orbital periods. It seems that as the magnetic field strength gets stronger it can force material away from the white dwarf, even when the spin period gets

longer.

4.3.2 Overall Conclusions

Up to a k_0 value of 5×10^3 disk fed accretion is the dominant flow geometry. We see stream fed accretion taking influence of these disk systems quickly, progressing along the orbital periods from shortest $P_{\rm orb}$ (80min), to long $P_{\rm orb}$ (9h) and from really long spin periods up to spin periods of 200s. The propeller effect does start to come into play early on, but progresses at a slower rate than that of the stream fed scenarios. With the propeller systems seen only at $P_{\rm spin} \lesssim 500$s until very strong magnetic field strengths, it seems propeller accretion moves through parameter space slowly. It starts with the combination of a short spin period at all orbital periods but as we increase the magnetic field strength we see the propeller effect at slightly longer spin periods and longer orbital periods. Increasing the magnetic field strength further we start to get the propeller accretion at longer spin periods for all orbital periods again. At the really strong magnetic fields, stream fed accretion still dominates, with propellers only seen at $P_{\rm spin}$ <1000s increasing to 2000s at the strongest field strength. We see the cataclysmic variable group polars arise with their characteristic stream fed accretion. Table 4.2 shows this accretion distribution from the extensive coverage of $P_{\rm spin}$, $P_{\rm orb}$ and k_0 parameters.

4.3.3 n^3 model vs n^6 model

In both models we see that disk accretion is the dominant mode at very weak magnetic field strengths. At stronger fields however we see that for the n^3 model propeller accretion is dominant whilst stream fed accretion is dominant in the n^6 model.

In the n^3 situation, the systems evolve across parameter space to propeller accretion rapidly, becoming the dominant accretion flow as the magnetic field strength is increased. Propeller accretion starts with short spin period systems for all orbital periods at weak

Table 4.2: Accretion flow distribution that occurs for the n^6 model situation

Type	P_{spin}/P_{orb}	k_0
Propeller	< 0.1	10^4 - 10^5
	< 0.2	$>10^5$
Disk	< 0.5	$<10^4$
	$0.01 - 0.5$	10^4 - 10^5
Stream	> 0.5	10^4 - 10^5
Stream	> 0.2	$>10^5$
Stream (Polars)	~ 1	$>10^5$
Backward stream (retrograde)	> 1	$>10^5$

field strengths and progresses to longer spin periods at all orbital periods with increasing field strength.

By k_0=1×10^5 all systems bar one exhibit propeller accretion, no matter what the spin and orbital period combinations. In the n^6 model we see a very different situation. Disk fed accretion is the dominant accretion mechanism over most of the range of spin and orbital period parameters, up to a k_0 value of 5×10^3. At this magnetic field strength and stronger, stream fed accretion starts to replace the disk accretion systems seen at the same spin and orbital period combinations but lower magnetic field strength. Unlike the n^3 model where we saw propeller accretion becoming the dominant mechanism, it is stream fed accretion that becomes the dominant flow mechanism for most of the combinations of P_{spin} and P_{orb} at the higher magnetic field strength. Systems that were once able to form disks at lower magnetic field strengths can no longer do so with the stronger field present. The P_{spin}/P_{orb} combination is the same, but the stronger field forces stream accretion on the system.

In the n^6 model, many systems show propeller accretion but not as many as we see in

the n^3 version. The system parameters of the n^3 model and the combination of the strong magnetic field strength causes more of the systems to become propellers at $P_{\rm spin}/\ P_{\rm orb}$ combinations than their counterparts in the n^6 model.

Another interesting feature is the so called 'ring' systems. These are quite clearly present from k_0=1×10^6, particularly so at k_0=1×10^7 in the n^3 model, but no such system exists in the n^6 model. The ring system according to Norton et al. (2004b) which forms outside the white dwarf's Roche lobe keeps it's shape from exchanging angular momentum from the WD which is passed back to the accreting material in the ring. Some of this material is then lost from the outer edges of the ring to maintain equilibrium.

One other thing to note is that the white dwarf spin phase has no effect on the overall appearance of the accretion flow. After looking at 6 different snap shots throughout the orbit, we see no obvious differences in the case of disk, propeller and ring accretion (Figures 4.4 - 4.6), but we see a slight difference in the accretion onto the WD in the stream fed cases where the orientation varies, see figure 4.3 below.

Figure 4.3: Spin phase variations for stream accretion. The six snapshots represent views of a model at six different spin phases within a single orbit.

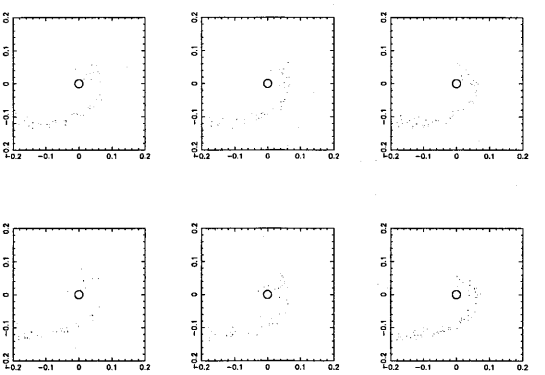

Figure 4.4: Spin phase variations for disk accretion

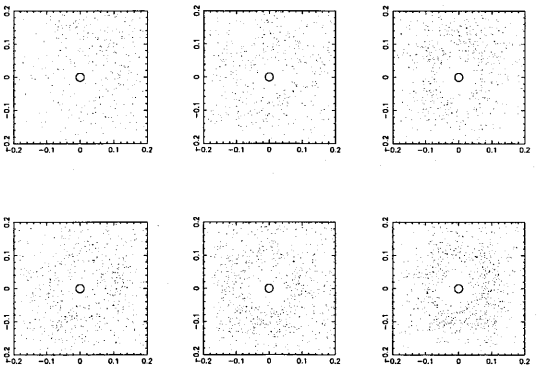

Figure 4.5: Spin phase variations for propeller accretion

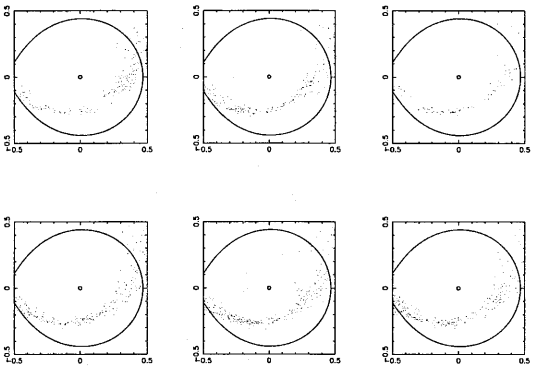

Figure 4.6: Spin phase variations for ring accretion

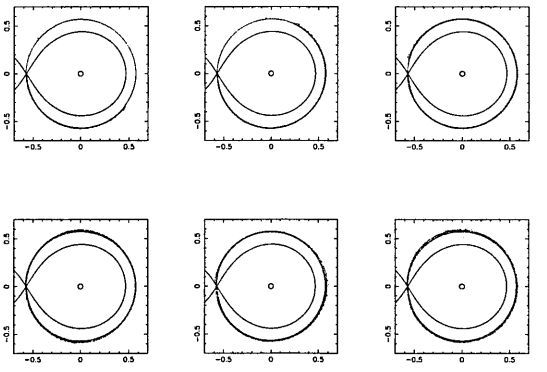

4.4 Equilibrium Flows

When IPs reach their equilibrium state, the spin period of the white dwarf is equal to the co-rotation period and becomes equal to the Keplerian orbital period of the material at the inner edge of the disk (if one exists). The physical consequence is that the spin up torque due to accretion is balanced by the magnetic torque, and the spin period then remains $\sim$ constant on long timescales. For these specific spin periods we wanted to see the type of flow that occurs. In Figure 4.3 we present the results of running HyDisc for the equilibrium situations with the range of $P_{\rm orb}$ and k_0 as discussed at the beginning of this chapter. Norton et al. (2004b) used an adapted version of HyDisc to allow the systems to evolve across parameter space in $P_{\rm spin}$ until a constant $P_{\rm spin}$ was reached. The adapted version of HyDisc set the moment of inertia of the WD to be artificially low, in order that it could spin up and spin down rapidly, so allowing equilibrium to be reached in a relatively short timescale. They evolved the model over about 100 orbits depending on how far away from equilibrium the systems were initially. $P_{\rm spin}$ was allowed to change according to the change of angular momentum. Plots of $P_{\rm spin}$ versus time were constructed, the point at which no change was observed was where equilibrium had been reached. These values are listed in the equilibrium data tables that follow the figures. Details are given in the caption. In all these simulations, the same masses as in the n^3 version and n^6 model were used to keep consistency. The masses of the two stars are $0.6M_\odot$ and $0.3M_\odot$ and the dipole inclination angle is $m \sim 5°$.

Figure 4.7: Accretion flows at equilibrium spin period for each k_0 value as a function of orbital period. The red figures indicate propeller accretion, yellow figures indicate stream, blue figures indicate disk accretion and green figures are ring structure accretion. The first two pages are for the n^3 model, and the second two pages for the n^6 model.

K=1x10^2
Equilibrium Spin Period = 339
K=5x10^2
Equilibrium Spin Period = 442
K=1x10^3
Equilibrium Spin Period = 551
K=5x10^3
Equilibrium Spin Period =1120
K=1x10^4
Equilibrium Spin Period =1420
K=2x10^4
Equilibrium Spin Period =1830
80m
690 340 270 250 330
770 1000 1170 770 770
790 1020 1270 1600 1130
1250 1390 1520 1870 2300
1660 1760 1890 2160 2500
2220 2350 2440 2680 3000
3h 4h 5h 7h 9h
Orbital Period

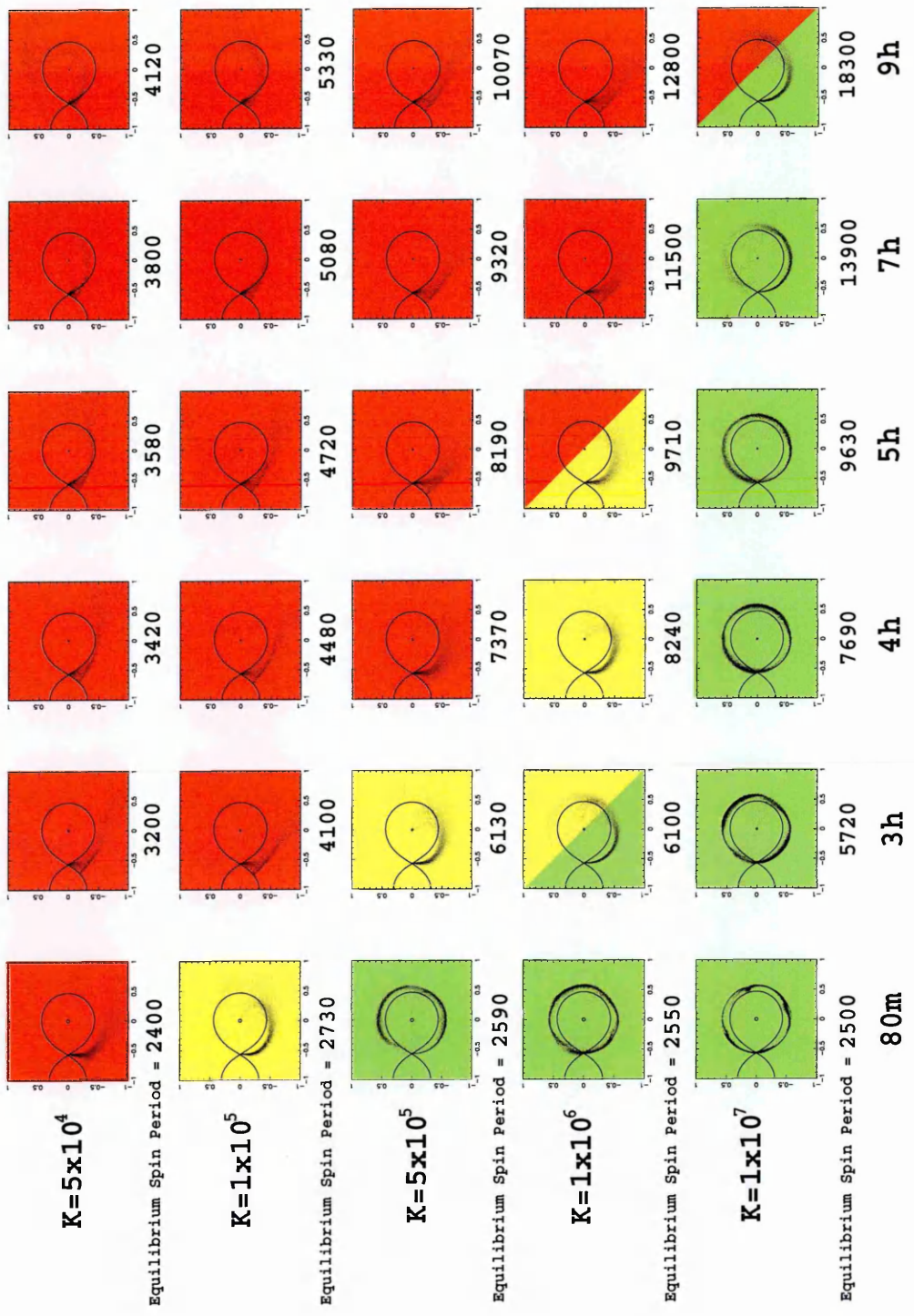
K=5x10^4
Equilibrium Spin Period = 2400
3200
3420
3580
3800
4120
K=1x10^5
Equilibrium Spin Period = 2730
4100
4480
4720
5080
5330
K=5x10^5
Equilibrium Spin Period = 2590
6130
7370
8190
9320
10070
K=1x10^6
Equilibrium Spin Period = 2550
6100
8240
9710
11500
12800
K=1x10^7
Equilibrium Spin Period = 2500
5720
7690
9630
13900
18300
80m
3h
4h
5h
7h
9h
Orbital Period

K=1x10^2
Equilibrium Spin Period = 339
690
340
270
250
330
K=5x10^2
Equilibrium Spin Period = 442
770
1000
1170
770
770
K=1x10^3
Equilibrium Spin Period = 551
790
1020
1270
1600
1130
K=5x10^3
Equilibrium Spin Period =1120
1250
1390
1520
1870
2300
K=1x10^4
Equilibrium Spin Period =1420
1660
1760
1890
2160
2500
K=2x10^4
Equilibrium Spin Period =1830
2220
2350
2440
2680
3000
80m
3h
4h
5h
7h
9h
Orbital Period

K=5x10^4
Equilibrium Spin Period = 2400
3200
3420
3580
3800
4120
K=1x10^5
Equilibrium Spin Period = 2730
4100
4480
4720
5080
5330
K=5x10^5
Equilibrium Spin Period = 2590
6130
7370
8190
9320
10070
K=1x10^6
Equilibrium Spin Period = 2550
6100
8240
9710
11500
12800
K=1x10^7
Equilibrium Spin Period = 2500
5720
7690
9630
13900
18300
80m
3h
4h
5h
7h
9h
Orbital Period

4.4.1 Data for equilibrium models

Table 4.3: Data tables of Equilibrium Spin Periods. The following tables give the values of where the equilibrium situations take place; see Norton et al. (2004b)

$P_{\rm orb} = 80$min

k_0	μ/Gcm^3	$P_{\rm spin}/P_{\rm orb}$	Equilibrium $P_{\rm s}/sec$
1x10^2	0.97x10^{32}	0.0707	339.
5x10^2	0.22x10^{33}	0.0920	442.
1x10^3	0.31x10^{33}	0.115	551.
5x10^3	0.69x10^{33}	0.233	1120
1x10^4	0.97x10^{33}	0.295	1420
2x10^4	0.14x10^{34}	0.380	1830
5x10^4	0.22x10^{34}	0.501	2400
1x10^5	0.31x10^{34}	0.568	2730
5x10^5	0.69x10^{34}	0.540	2590
1x10^6	0.97x10^{34}	0.531	2550
1x10^7	0.31x10^{35}	0.520	2500

$P_{\rm orb}$ = 3hrs

k_0	$\mu/{\rm Gcm}^3$	$P_{\rm spin}/P_{\rm orb}$	Equilibrium $P_{\rm s}/sec$
$1\text{x}10^2$	$0.26\text{x}10^{33}$	0.0638	690.
$5\text{x}10^2$	$0.58\text{x}10^{33}$	0.0710	770.
$1\text{x}10^3$	$0.82\text{x}10^{33}$	0.0733	790.
$5\text{x}10^3$	$0.18\text{x}10^{34}$	0.116	1250
$1\text{x}10^4$	$0.26\text{x}10^{34}$	0.154	1660
$2\text{x}10^4$	$0.37\text{x}10^{34}$	0.206	2220
$5\text{x}10^4$	$0.58\text{x}10^{34}$	0.297	3200
$1\text{x}10^5$	$0.82\text{x}10^{34}$	0.380	4100
$5\text{x}10^5$	$0.18\text{x}10^{35}$	0.568	6130
$1\text{x}10^6$	$0.26\text{x}10^{35}$	0.565	6100
$1\text{x}10^7$	$0.82\text{x}10^{35}$	0.530	5720

$P_{\rm orb}$ = 4hrs

k_0	$\mu/{\rm Gcm}^3$	$P_{\rm spin}/P_{\rm orb}$	Equilibrium $P_{\rm s}/sec$
$1\text{x}10^2$	$0.33\text{x}10^{33}$	0.0237	340.
$5\text{x}10^2$	$0.74\text{x}10^{33}$	0.0693	1000
$1\text{x}10^3$	$0.11\text{x}10^{34}$	0.0706	1020
$5\text{x}10^3$	$0.23\text{x}10^{34}$	0.0968	1390
$1\text{x}10^4$	$0.33\text{x}10^{34}$	0.122	1760
$2\text{x}10^4$	$0.47\text{x}10^{34}$	0.163	2350
$5\text{x}10^4$	$0.74\text{x}10^{34}$	0.238	3420
$1\text{x}10^5$	$0.11\text{x}10^{35}$	0.311	4480
$5\text{x}10^5$	$0.23\text{x}10^{35}$	0.512	7370
$1\text{x}10^6$	$0.33\text{x}10^{35}$	0.572	8240
$1\text{x}10^7$	$0.11\text{x}10^{36}$	0.534	7690

$P_{\rm orb}$ = 5hrs

k_0	μ/Gcm^3	$P_{\rm spin}/P_{\rm orb}$	Equilibrium $P_{\rm s}/sec$
1x10^2	0.40x10^{33}	0.0150	270.
5x10^2	0.90x10^{33}	0.0648	1170
1x10^3	0.13x10^{34}	0.0708	1270
5x10^3	0.28x10^{34}	0.0844	1520
1x10^4	0.40x10^{34}	0.105	1890
2x10^4	0.57x10^{34}	0.135	2440
5x10^4	0.90x10^{34}	0.199	3580
1x10^5	0.13x10^{35}	0.262	4720
5x10^5	0.28x10^{35}	0.455	8190
1x10^6	0.40x10^{35}	0.540	9710
1x10^7	0.13x10^{36}	0.535	9630

$P_{\rm orb}$ = 7hrs

k_0	μ/Gcm^3	$P_{\rm spin}/P_{\rm orb}$	Equilibrium $P_{\rm s}/sec$
1x10^2	0.53x10^{33}	0.0100	250.
5x10^2	0.12x10^{34}	0.0305	770.
1x10^3	0.17x10^{34}	0.0634	1600
5x10^3	0.38x10^{34}	0.0740	1870
1x10^4	0.53x10^{34}	0.0856	2160
2x10^4	0.76x10^{34}	0.106	2680
5x10^4	0.12x10^{35}	0.151	3800
1x10^5	0.17x10^{35}	0.201	5080
5x10^5	0.38x10^{35}	0.370	9320
1x10^6	0.53x10^{35}	0.457	11500
1x10^7	0.17x10^{36}	0.552	13900

$P_{\rm orb}$ = 9hrs

k_0	μ/Gcm^3	$P_{\rm spin}/P_{\rm orb}$	Equilibrium P_s/sec
1x10^2	0.66x10^{33}	0.0102	330.
5x10^2	0.15x10^{34}	0.0238	770.
1x10^3	0.21x10^{34}	0.0348	1130
5x10^3	0.47x10^{34}	0.0711	2300
1x10^4	0.66x10^{34}	0.0770	2500
2x10^4	0.93x10^{34}	0.0927	3000
5x10^4	0.15x10^{35}	0.127	4120
1x10^5	0.21x10^{35}	0.164	5330
5x10^5	0.47x10^{35}	0.311	10070
1x10^6	0.66x10^{35}	0.394	12800
1x10^7	0.21x10^{36}	0.566	18300

4.4.2 Discussion

The equilibrium situations are expected to be the **only** configurations that real IPs can exist in at least when averaged over long timescales. They do however have excursions to faster and slower spin periods, which is why the previous parameter space values were investigated. The timescales for reaching equilibrium are about $10^6 \sim 10^7$ years, so at a given instant a particular system may be far from equilibrium.

For the n^3 model, the exploration of parameter space shows broadly that if the ratio of the spin to orbital period in equilibrium is:

$$\frac{P_{\rm spin}}{P_{\rm orb}} \lesssim 0.1$$

then a truncated accretion disk will form.

and if the ratio is:

$$0.1 \lesssim \frac{P_{\rm spin}}{P_{\rm orb}} \lesssim 0.5$$

then a propeller will form. For the highest equilibrium period ratios of

$$\frac{P_{\rm spin}}{P_{\rm orb}} \sim 0.55$$

a ring system is seen, or in a few cases a stream is observed.

As all these flows are in equilibrium, including those which appear to be propellers, the angular momentum accreted and ejected must be balanced. If the system behaved as a true propeller the WD would spin down, losing angular momentum. As this is not the case we must have accretion taking place onto the WD as well as material being ejected, to be able to maintain the balance and keep the system in equilibrium. In fact detailed examination of the HyDisc output shows that in the apparent propellers, a small proportion of the material is indeed accreted in these models to maintain angular momentum balance. Hence, we refer to these systems as **weak propellers** (see King & Wynn (1999) for more on the weak propeller effect, also see Ikhsanov (2001) and Meintjes (2002) for other ideas of accretion on to the WD in propeller systems). A weak propeller therefore signifies a combination of propeller and stream accretion.

For the n^6 model we see a rather different situation.

At equilibrium, if the ratio is:

$$\frac{P_{\rm spin}}{P_{\rm orb}} \lesssim 0.1$$

then a truncated accretion disk will form.

Whereas, if the ratio is

$$\frac{P_{\rm spin}}{P_{\rm orb}} \gtrsim 0.1$$

then stream fed accretion is seen. No propellers or ring systems are seen at equilibrium in the n^6 case.

For each of the equilibrium runs, 5000 particles were entered into the HyDisc model per orbit. As 100 snapshots were output during each orbit of each run, this meant that

50 particles would enter each model per snapshot. In order to quantitatively define the accretion mechanisms taking place we looked at 5 of these different snapshots over the 100 snapshot range for all 66 of the equilibrium runs. We noted how many particles in each system either escaped from the system or were accreted by the system. The results of this are shown as averaged percentages in Table 4.4 for the n^3 model and Table 4.5 for the n^6 model. The remaining particles, not escaped or accreted, are either swept back up by the secondary star, or remain within the accretion flow itself.

Table 4.4: Average percentage of material that either escapes the model or is accreted onto the WD for the various accretion mechanisms seen for the equilibrium n^3 runs

Type	% Escaped	% Accreted
Disk	22	10
Stream	10	33
Propeller	55	2
Ring	<1	33

Table 4.5: Average percentage of material that either escapes the model or is accreted onto the WD for the various accretion mechanisms seen for the equilibrium n^6 runs

Type	% Escaped	% Accreted
Disk	2	31
Stream	<1	44

In equilibrium both accretion and ejection are seen in all accretion modes as the angular

momentum balance has to be conserved. Notice though that what is important is the amount of angular momentum carried by each of the accreted or ejected particles. The simple numbers of particles accreted or ejected may not reflect the angular momentum balance. For disk systems we have a contribution from both escaped and accreted material to maintain this balance. In propeller systems we see that more particles escape than are accreted and for stream and ring accretion it is the opposite, with more particles being accreted than escaping. Thus we have:

$$E > A \qquad \text{propeller} \tag{4.1}$$

$$E < A \quad \text{stream and ring} \tag{4.2}$$

$$\text{E and A} \qquad \text{disk} \tag{4.3}$$

In order to assess the types of flow that may occur in real magnetic CVs, we first show in Figures 4.4 and 4.5 for the n^3 and n^6 model respectively, a summary of the $P_{\rm spin}/P_{\rm orb}$ value at equilibrium as a function of μ_1, colour coded to indicate the type of flow that corresponds to each parameter combination.

Then, in Figures 4.6 and 4.7, we show a plot of all known IPs in the $P_{\rm spin}$ vs $P_{\rm orb}$ plane. This shows which systems are likely to exhibit the various accretion flows, assuming they are in equilibrium. As can be seen from the plots we can clearly see which classification of accretion flow the various real IPs might belong to. The results in Chapter two tell us that BG CMi; FO Aqr; TV Col; TX Col; V1223 Sgr; AO Psc and V405 Aur must all contain a disk, due to their observed X-ray orbital modulation. If we look at where these systems lie in the areas on the graph, we see that BG CMi; FO Aqr; V1223 Sgr; AO Psc and V405 Aur are all in good agreement for containing accretion disks, TV Col and TX Col are border line cases, appearing just on the edge of the border between weak propeller flow and disk accretion. The position of TX Col on the edge of the border is interesting

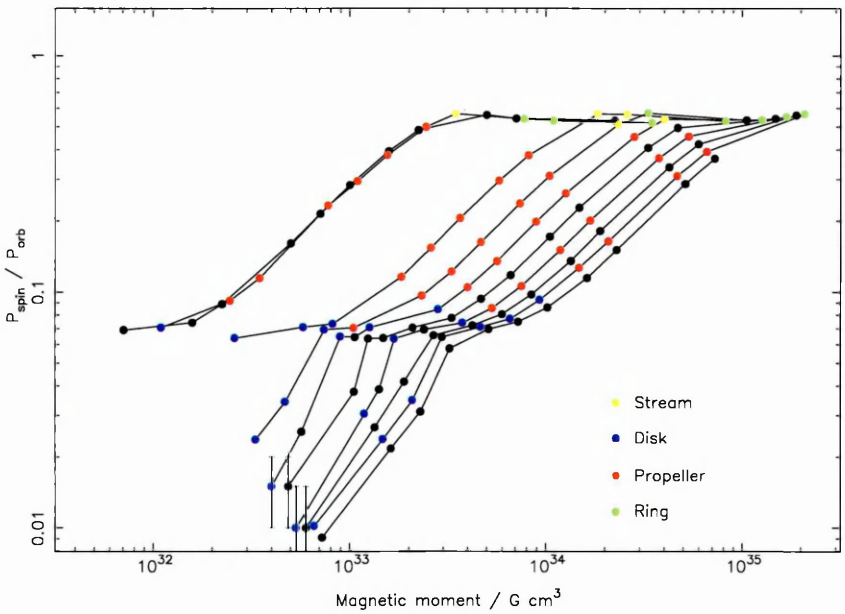

Figure 4.8: Plot of equilibrium spin periods of intermediate polars obtained from running HyDisc for the n^3 model, (adapted from Norton et al. (2004b)) with indication as to the types of accretion flows that take place at each parameter space value. Each line connects a set of data points corresponding to different k values and represents the equilibrium spin period at a given orbital period. The 9 lines correspond to orbital periods of 80m, 2h, 3h ... 10h. In general the uncertainty in each equilibrium spin period is smaller than the size of the plotted point, except for a few of the points at the lower extreme of the lines, where indicative error bars are shown. The blue circles corresponds to disk accretion, the red circles to weak propeller accretion, the yellow circles correspond to stream fed accretion and the green circles to ring accretion.

as Norton et al. (1997) found that this system varied in its accretion mechanism. The system went from being a pure disk accretor to accreting via both a stream and a disk on a timescale of a year. Does this mean that both TV Col and WX Pyx may also behave in a similar way? As Schlegel (2005) pointed out, these three objects lie very close to each

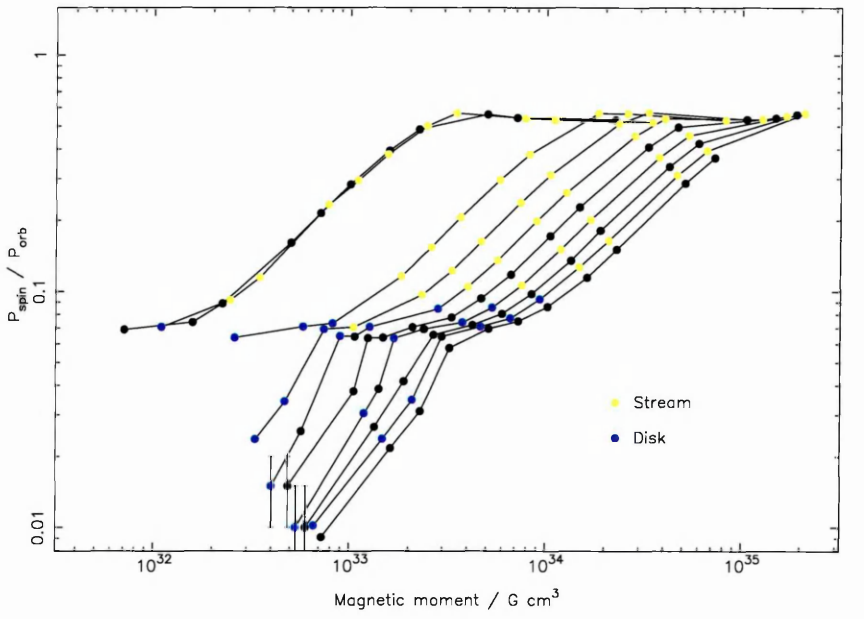

Figure 4.9: Plot of equilibrium spin periods of intermediate polars obtained from running HyDisc for the n^6, (adapted from Norton et al. (2004b)) with indication as to the types of accretion flows that take place at each parameter space value. Each line connects a set of data points corresponding to different k values and represents the equilibrium spin period at a given orbital period. The 9 lines correspond to orbital periods of 80m, 2h, 3h ... 10h. In general the uncertainty in each equilibrium spin period is smaller than the size of the plotted point, except for a few of the points at the lower extreme of the lines, where indicative error bars are shown. The blue circles corresponds to disk accretion and the yellow circles correspond to stream fed accretion.

other in the $P_{\rm spin}$ - $P_{\rm orb}$ plane and yet show varied parameters. There must therefore be an additional parameter that dictates the different behaviour from the three IPs which have nearly identical $P_{\rm spin}/P_{\rm orb}$ ratios. By comparing these real systems to our simulated data and seeing that they agree means that the simulated data is a good approximation to what the accretion mechanism is in real IPs. However there are limitations to the model

Figure 4.10: A plot of the spin and orbital periods of mCVs (adapted from Norton et al. (2004b)) with indication as to the types of accretion flows as predicted by the simulated flows with a n^3 model. The blue area corresponds to disk accretion, the red area to weak propeller accretion and the green area to stream or ring accretion. Some individual systems, referred to in the text, are identified by the key.

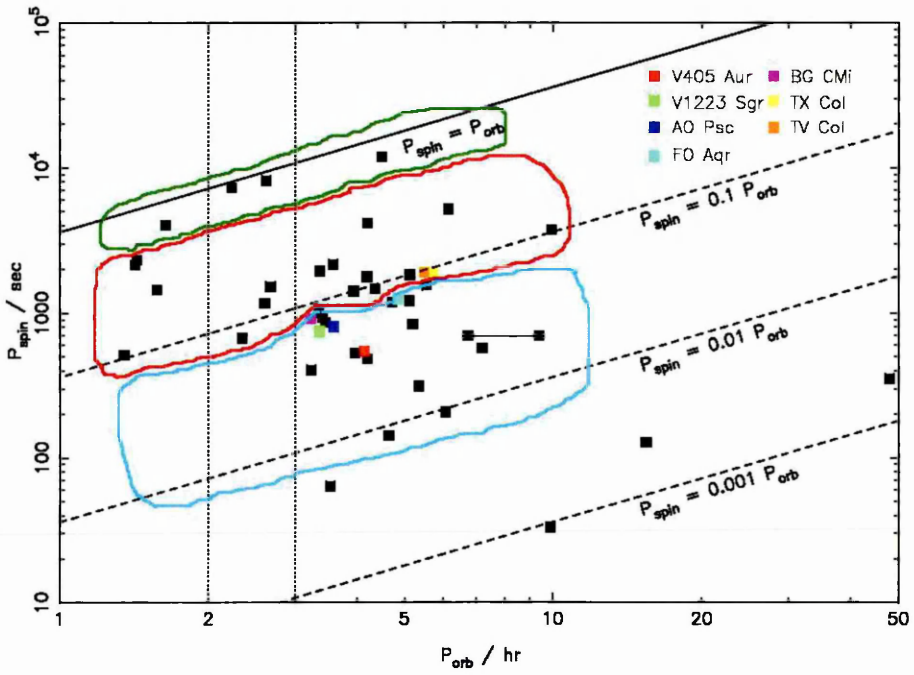

that need to be addressed first, as discussed at the end of this chapter.

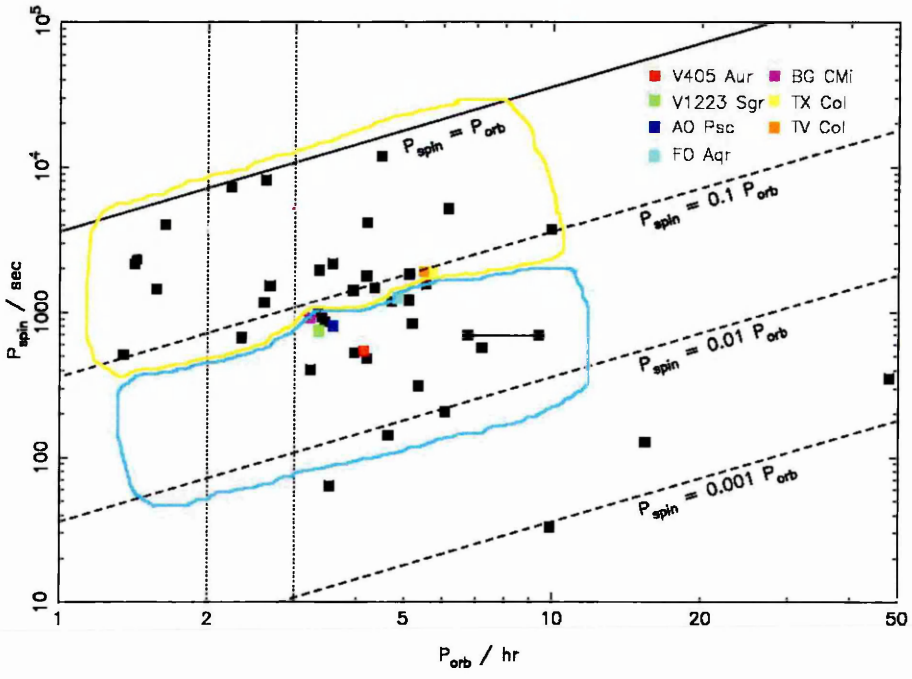

Figure 4.11: A plot of the spin and orbital periods of mCVs (adapted from Norton et al. (2004b)) with indication as to the types of accretion flows as predicted by the simulated flows with a n^6 model. The blue area corresponds to disk accretion and the yellow area to stream fed accretion. Some individual systems, referred to in the text, are identified by the key.

4.5 Dipole angle variations

The magnetic co-latitude of a star, also called the complement to the latitude, is the angle between the spin axis and the magnetic axis. To investigate the effect of changing the magnetic co-latitude, we decided to run the n^3 version of the magnetic model at the equilibrium situation for four different orbital periods of 2h, 3h, 5h and 7h, at five different k_0 values for 3 angles of magnetic co-latitude of 10°, 40° and 70° The results of this are shown in Figure 4.8.

Figure 4.12: Accretion flows for increasing magnetic co-latitude for each k_0 value in parameter space calculated at equilibrium parameters for m. The red figures indicate propeller accretion, yellow figures indicate stream, blue figures indicate disk accretion and green figures are ring structure accretion.The first page is for m=10°, the second page for m=40° and the third page for m=70°

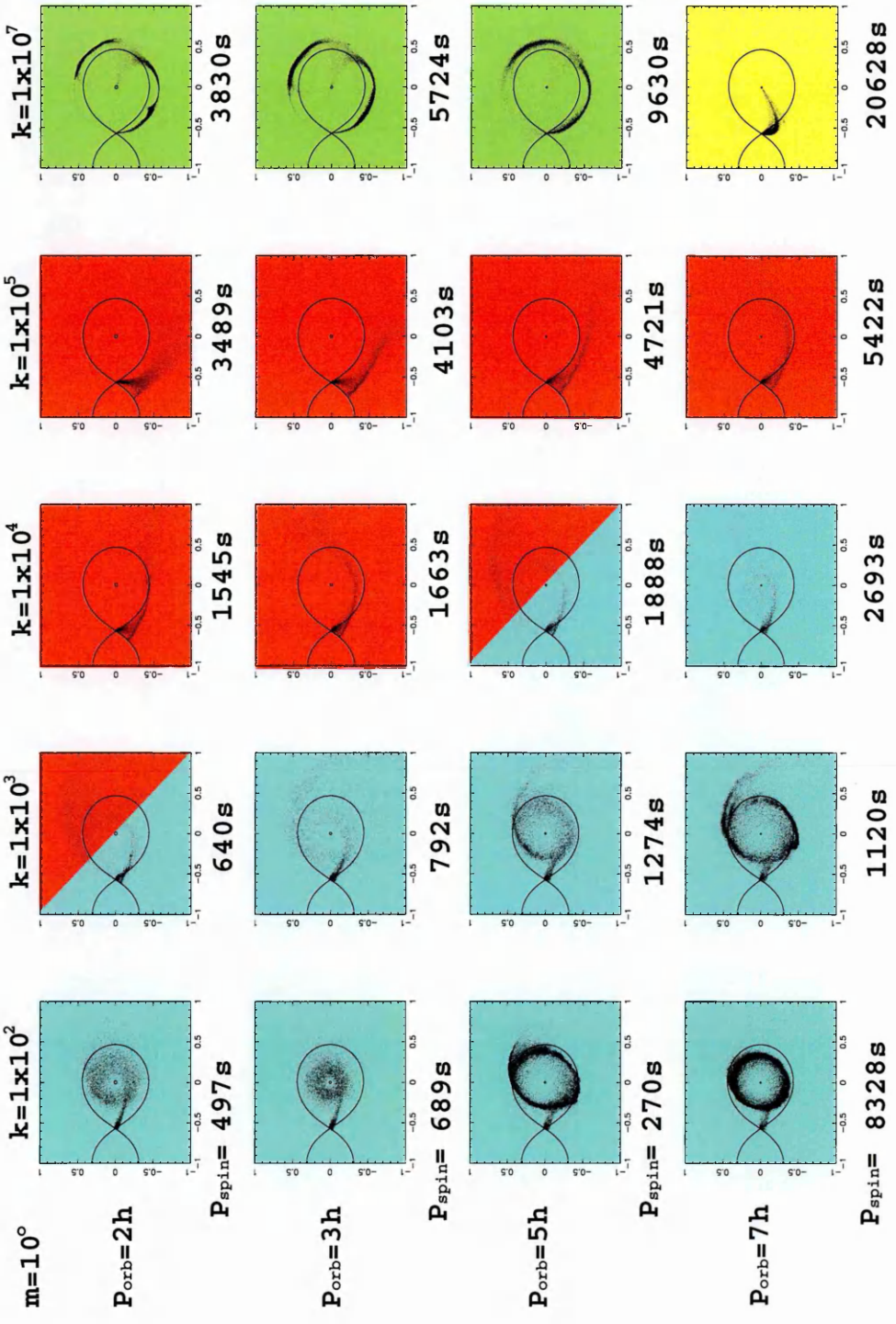
m=10°
k=1x10^2
k=1x10^3
k=1x10^4
k=1x10^5
k=1x10^7
Porb=2h
Porb=3h
Porb=5h
Porb=7h
Pspin= 497s
640s
1545s
3489s
3830s
Pspin= 689s
792s
1663s
4103s
5724s
Pspin= 270s
1274s
1888s
4721s
9630s
Pspin= 8328s
1120s
2693s
5422s
20628s

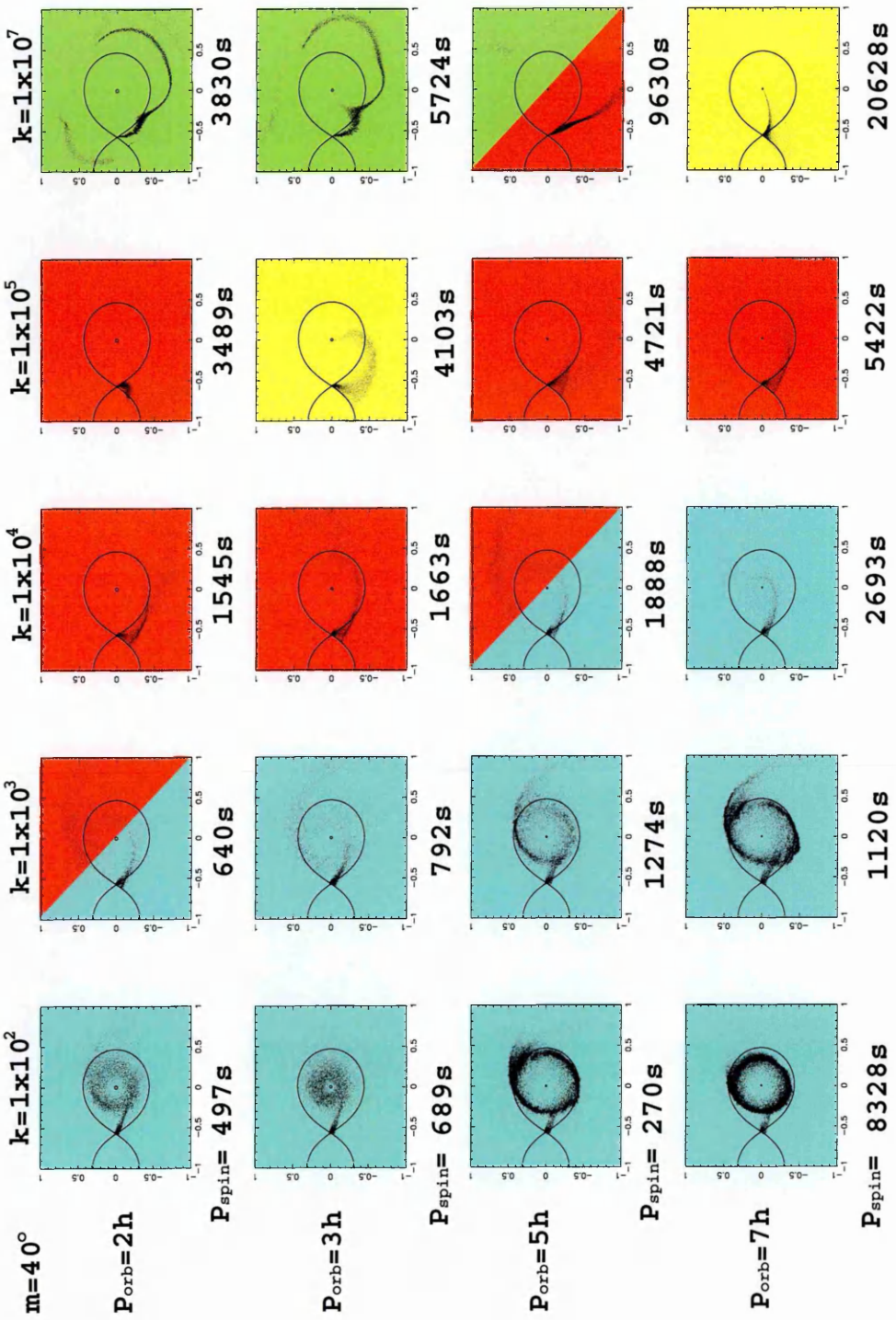
m=40°
k=1x10^2
k=1x10^3
k=1x10^4
k=1x10^5
k=1x10^7
Porb=2h
Porb=3h
Porb=5h
Porb=7h
Pspin= 497s
Pspin= 689s
Pspin= 270s
Pspin= 8328s
640s
792s
1274s
1120s
1545s
1663s
1888s
2693s
3489s
4103s
4721s
5422s
3830s
5724s
9630s
20628s

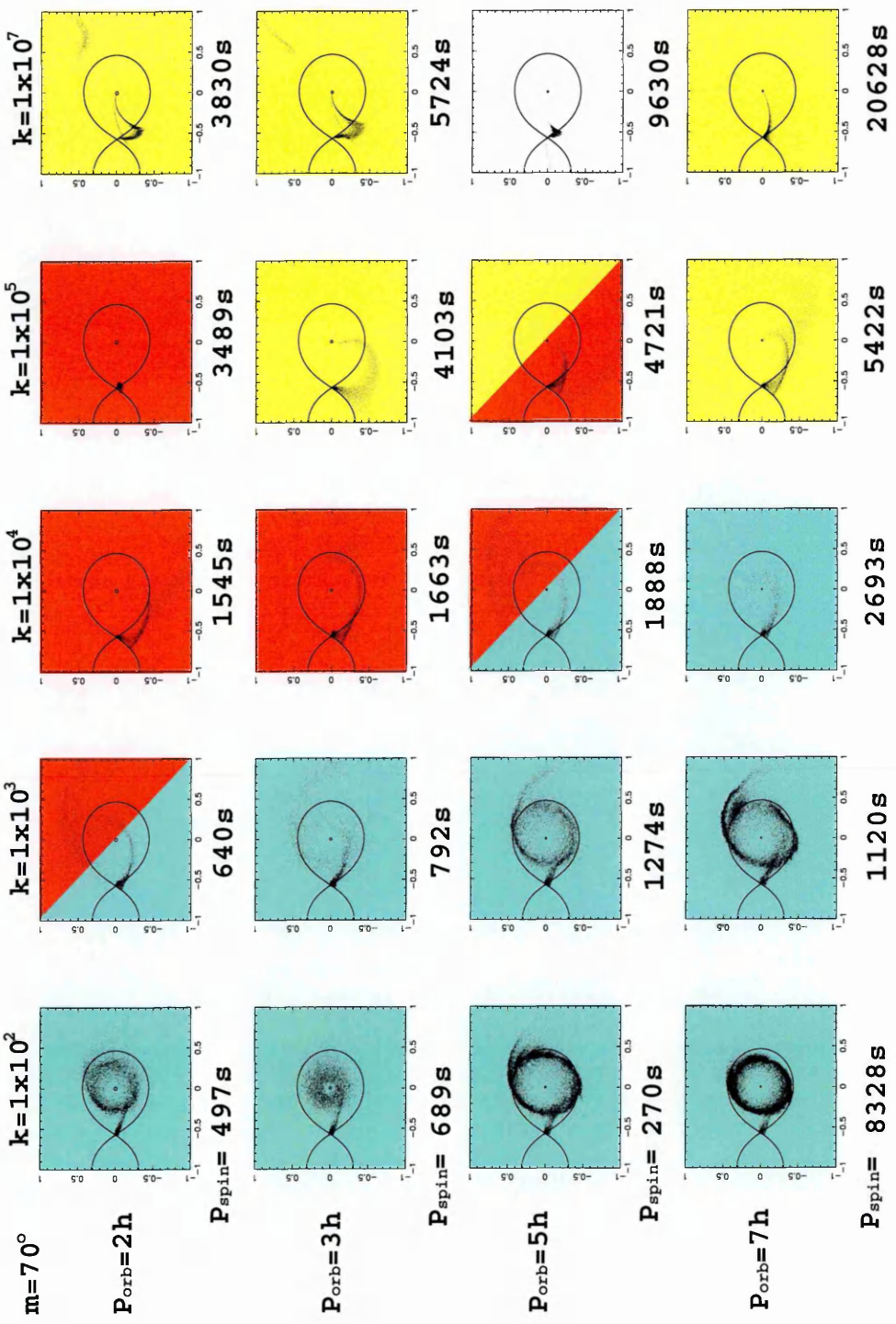
m=70°
k=1x10^2
k=1x10^3
k=1x10^4
k=1x10^5
k=1x10^7
Porb=2h
Porb=3h
Porb=5h
Porb=7h
Pspin= 497s
Pspin= 640s
Pspin= 1545s
Pspin= 3489s
Pspin= 3830s
Pspin= 689s
Pspin= 792s
Pspin= 1663s
Pspin= 4103s
Pspin= 5724s
Pspin= 270s
Pspin= 1274s
Pspin= 1888s
Pspin= 4721s
Pspin= 9630s
Pspin= 8328s
Pspin= 1120s
Pspin= 2693s
Pspin= 5422s
Pspin= 20628s

If we observe the m=10° figure first we see that all accretion scenarios are present as before, disk, stream, propeller and ring. If we then turn our attention to m=40° we see that some of the systems have either completely changed their accretion flow or are changed slightly. The interest lies in the propeller, stream and ring systems all of which depend very largely on the strength of the magnetic field and also its angle with respect to the spin axis of the WD.

At m=40°, the few remaining propellers are just barely seen as propellers, one system at k_0=1×10^5, 3h and a spin period of 4103s has managed to alter the flow from propeller to stream even though before at m=10° the combination was such that the material was unable to latch onto the field lines. We also see the ring structure undergoing some change. With the change in the magnetic co-latitude the material finds itself unable to attach to the field lines and continue round the WD, instead it is propelled away.

By m=70° the picture is very different to that which we started out with. All the disk systems have remained and some propellers are still observed but they are hard to identify as propellers. What is very interesting is how more of these propellers have succumbed to the magnetic field and more interesting still is that we no longer see any ring structures. They have also turned into stream fed accretion or the start of stream fed as indicated by the colourless figure.

4.6 Conclusions

What we are seeing is that not only does the spin period, orbital period and magnetic field strength have an effect on the accretion mechanism, it seems that so too does the angle of the magnetic field to that of the spin axis. From the varying results that both the magnetic models produce, we can also see that IPs are very sensitive to the field model.

However there are limitations to the model:

- The structure in the model is based on a dipole field as explained in Chapter 3. In practice the magnetic field might be a lot more complex pattern than what we consider here. We already see the large difference in accretion flows throughout the parameter space that the two models produce.

- The determination of the k_0 parameter relating to the magnetic field strength is based on certain approximations. To make the model more appropriate to real systems, these approximations would have to be dealt with and made to fit in more with what the real systems would produce. The best situation to obtain this would be to investigate several different fields and compare the simulated flows and tomograms with real tomograms to tell us observationally what the field in these systems is likely to be (see next chapter).

- We have only carried out the simulations for a single value of mass ratio. As noted earlier, varying this will alter the regions of parameter space in which different types of flow are seen. In order to accurately match a given system to a predicted type of flow, its actual mass ratio should also be taken into account.

However we cannot just rely on a model to tell us the answers, we need to compare what we have seen to observational data of these different types of systems in the parameter space that we have explored. As we cannot observe the accretion flows directly, we need another technique to help us distinguish the flow patterns that happen in these systems. A technique known as Doppler Tomography can help with this, which is what we have concentrated on in the next chapter. In this chapter we consider how the magnetic model can help aid in understanding observational tomograms in order to determine the nature of accretion flow in IPs.

Chapter 5

Doppler Tomography of Intermediate Polars

5.1 Introduction

In this chapter we investigate the geometry of the accretion flows further by using the magnetic model to produce Doppler tomograms for all the accretion flows produced in the previous chapter. The tomograms correspond to the same regions of parameter space as they did for the flows, and are produced for both the n^3 model and the n^6 situation. We look at the defining characteristics that each tomogram produces for the specific accretion flows corresponding to stream, disc, propeller and ring accretion. Following this we look at the tomograms in the equilibrium case and assess the velocity maps in those specific cases too. We also provide Doppler tomograms at different inclination angles for the systems to see if this affects how the velocity map is perceived and hence if the accretion flow might show some variation depending on what the inclination of the system is with respect to our line of sight. After each set of figures we discuss the findings individually and then give a brief conclusion to each set of tomogram results. We compare and contrast the velocity maps that are produced from the accretion flows in the two different models and

of those produced for the different equilibrium flows and then compare all the maps with the inclination variations, giving an over-view of all the results at the end. Finally we compare our results to published observations that have used the Doppler tomography technique in studying the accretion flows in intermediate polars.

5.2 Background to the technique of Doppler tomography

Doppler tomography of CVs was first introduced by Marsh & Horne (1988). It maps the emission-line profile variations arising from an accretion region as a function of the orbital phase and reconstructs this region into a velocity space map making use of the Doppler effect. It is an indirect imaging technique that allows us to spatially resolve accretion flows in interacting binaries even though they are point sources.

If we consider a disc structure, then the side that is rotating away from us will produce a redshift in the emission line components and the side that is rotating towards us will produce blue-shifted emission components half an orbit later, see Figure 5.1.

If we consider the motion of a point-like source of emission fixed in the binary frame, that moves parallel to the orbital plane of the binary, then the line emission from the source will produce a sinusoid around the mean velocity of the system (see Marsh (2001)). This sinusoid in the spectral lines is referred to as an "s-wave". Since the Doppler shift gives us information about the motions of the gas, the wavelength shifts can be converted into velocity shifts which are then used to produce an image of the disc gas in dimensions of velocity in the tomograms. By observing the sinusoid we can then associate it with particular velocity vectors in the binary, depending on its phase and amplitude. Thus each component s-wave can be mapped onto a particular x,y location on the velocity map.

A given point in the binary system can be defined by its spatial position, but more importantly by its velocity (V_x, V_y) (see Figure 5.2) where this velocity is relative to the

Figure 5.1: Areas with similar radial velocities, for an observer located at the bottom of the figure, form a dipolar pattern on the surface of the disc if we assume the velocity is Keplerian at each radius. Each velocity bin in the emission profiles can be mapped to an area on the Keplerian accretion disc (Horne & Marsh (1986))

.

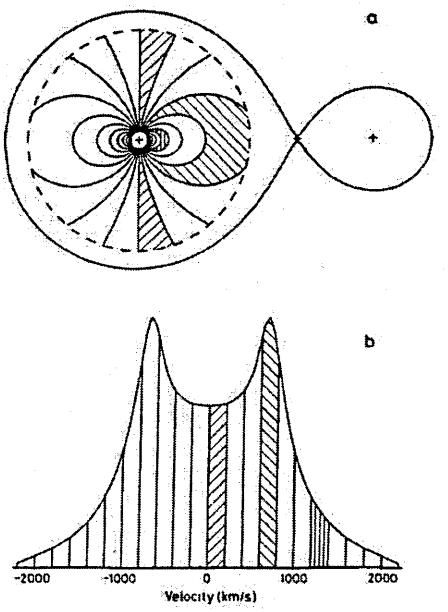

inertial frame.

As inertial frame velocities are always changing as the binary rotates, we define the values of V_x and V_y by measuring them at particular orbital phases. This is usually taken to be when the inertial frame lines up with the rotating frame. The X-axis is usually defined as pointing from the white dwarf to the mass donor and the positive Y-axis points in the direction of the secondary star's motion. This coordinate system then rotates with the stars. Any velocity vector ($V_x V_y$) stationary in this coordinate system will have a corresponding sine curve in trailed spectra given by:

$$V(\phi) = -V_x cos(\phi) + V_y sin(\phi) \tag{5.1}$$

where ϕ is the orbital phase. At the same time this vector will be represented by a point in the $V_x - V_y$ plane on the Doppler map (Kaitchuck et al. (1994)).

So to sum up, CVs and mCVs emit emission lines of mainly Hydrogen and Helium. These emission lines show a certain line profile, depending on the type of source (e.g. polar, dwarf nova) or the inclination angle. During an orbit the line profile, which is

Figure 5.2: Schematic view of a cataclysmic variable star including the Roche lobe filling companion star, the mass transfer stream, and the accretion disk around the WD, shown in both spatial coordinates (X,Y), and in the corresponding Doppler coordinates (V_x,V_y), Steeghs (1996)

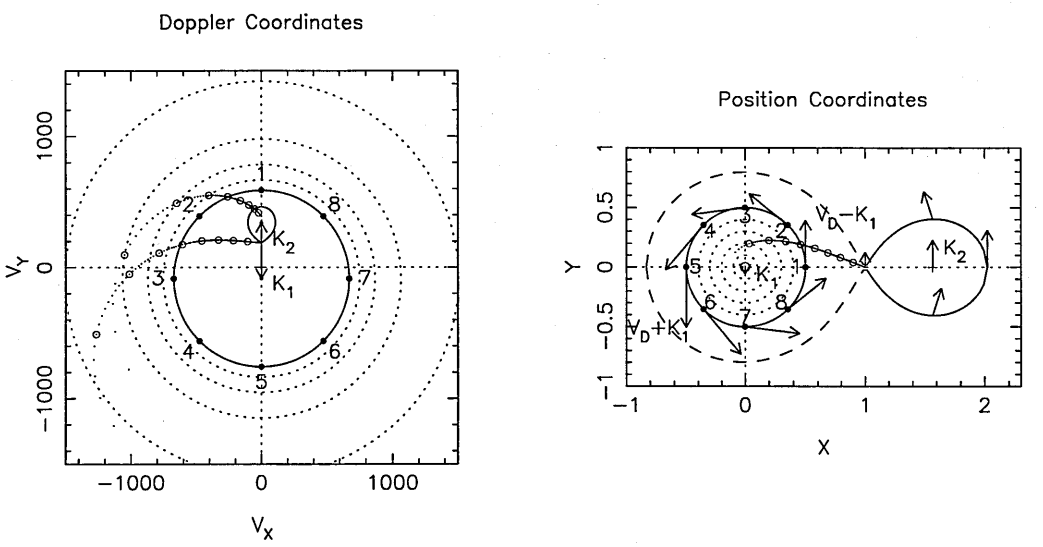

a super-position of various emission sources in the system, varies periodically. Doppler Tomography uses the information in the line profile in order to reconstruct the location of the various emission sources. Figure 5.3 shows how these line profiles work, with the explanation from Marsh (2001):

Figure 5.3: A model image and the equivalent profiles formed by projection at an angle for the orbital phases of 0.25 (right-most profile) and 0.5 (lower-profile)

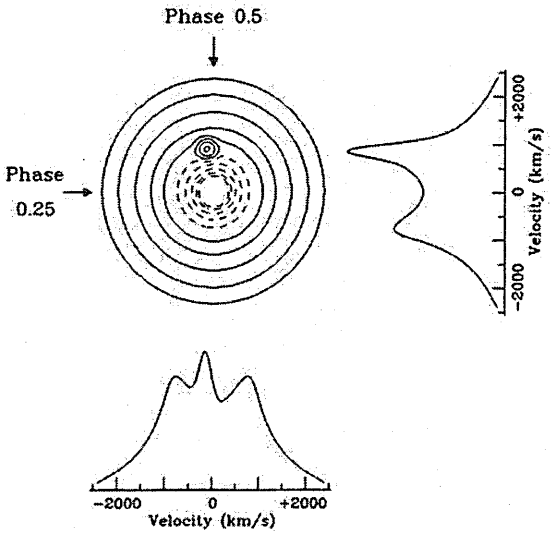

"...The artificial image has been created with a spot which can be seen to project into different parts of the profile at different phases. Tracing back from the peaks along the projections leads to the position of the original spot. This is in essence how line profile information can be used to reconstruct an image of the system.

A series of line profiles at different orbital phases is therefore nothing more than a set of projections of the image at different angles. The inversion of projections to reconstruct the image is known as "tomography"..."

5.3 Assumptions that must be considered for mCV Doppler Tomography

Doppler tomography of the orbital cycle in cataclysmic variables has become very common, the situation for intermediate polars however is very different.

Doppler tomography rest on the following assumptions: Marsh (2005)

1. The visibility of all elements remains constant.
2. The flux of each element is constant.
3. All motion is parallel to the orbital plane.
4. All velocity vectors rotate with the binary.
5. The intrinsic width (e.g.thermal) of the profile is negligible.

IPs however violate some of these assumptions. The first, 'motion parallel to the orbital plane' is violated by the fact that IPs contain accretion curtains that clearly take material out of the plane. This makes the analysis more complex and means that interpretations of observational tomograms will be flawed as they are based on false assumptions. The second is that Doppler tomography assumes that the accretion flow is constant throughout the orbital period, that is the structure of the flow does not change at different orbital phases. Intermediate polars violate this assumption too, which further complicates the interpretation of their observational tomograms. This is why we must generate simulated tomograms from simulated accretion flows so we can compare them with real tomograms from observed data and begin to interpret them better. In this way we can discover the nature of the accretion flows in real systems and thus use this to determine the effects of motion out of the orbital plane.

The tomograms we produce from the HyDisc simulations are, however, subject to

some limiting assumptions of their own. The main one of these is that we do **not** model specific emission components or fluxes from different parts of the accretion flow. We simply construct tomograms based on the velocity components of all the particles present in the simulated accretion flow at a given instant. This is equivalent to assuming that all parts of the accretion flow have a uniform temperature and level of flux emission. These tomograms cannot therefore be directly compared with (say) those of observed Hydrogen lines or Helium lines, but they can at least give a first idea of how those observational tomograms may be interpreted.

5.4 n^3 model Doppler Tomograms

In Figure 5.5 we present the tomogram results of running HyDisc for the n^3 model with the range of $P_{\rm orb}$, $P_{\rm spin}$ and k_o discussed earlier. Details are given in the caption. In all these simulations, the masses of the two stars are 0.6 $M_\odot$ for the WD and 0.3 $M_\odot$ for the secondary and the dipole inclination angle is m$\sim$ 5°. All tomograms assume a system inclination angle of 90°, i.e. edge on.

The following Figure (5.4) from Kaitchuck et al. (1994) shows a schematic Doppler map. The origin of the map is at the center of mass of the system. As the motion of the secondary star is in the +V$_y$ direction with no V$_x$ component the star is located along the +V$_y$ axis. As the motion of the WD is in the opposite direction moving in the -V$_y$ direction with no V$_x$ component its position is located along the -V$_y$ axis. The position of each star is determined by its radial velocity amplitude with the shapes of the Roche lobe staying the same in the Doppler map as they would be in positional coordinates. The Figure shows a "typical" stream trajectory from the L$_1$ point and a circle representing a disk feature.

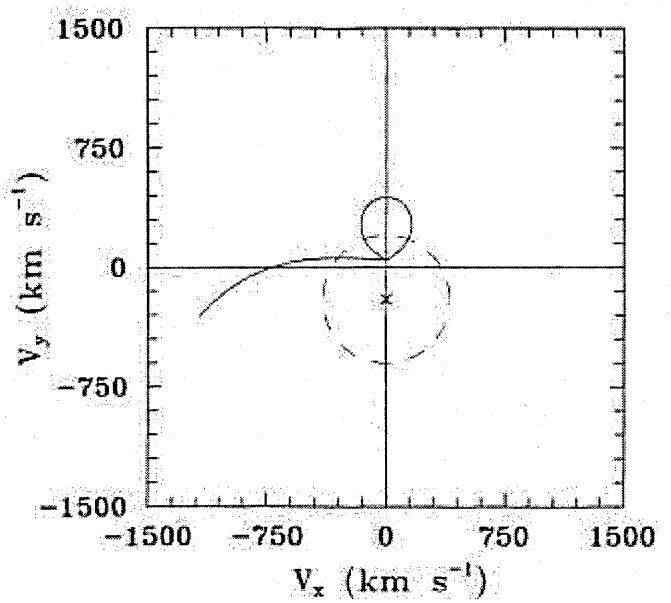

Figure 5.4: A schematic layout of a Doppler tomogram. The main features are the Roche lobe of the secondary star, the mass-transfer stream, and the circular emission from an accretion disk. The stream appears as an arc and the disk emission, which is a diffuse ring in tomograms, is indicated by a circle in this figure. The small 'x' is the position of the WD. (Figure taken from Kaitchuck et al. (1994))

Figure 5.5: (overleaf) Tomograms for the n^3 model ($k(r) \propto r^{-3}$) for each k_o value in parameter space. The red figures indicate propeller accretion, yellow figures indicate stream accretion, blue figures indicate disk accretion and green figures are ring structure accretion. A small magenta 'P' in the upper left of a Figure indicates a polar system, i.e. the configuration where $P_{\rm spin}$=$P_{\rm orb}$. All figures are in grey scale, however with the colour coding the contour lines show up clearest so the edges of the features are easier to see. All angles are quoted from an imaginary horizontal line between the L_1 point and the WD, and the v axis in each figure is in units of kms^{-1}. The k value listed on each page of this figure is the value input to HyDisc, i.e. k_0 which is the value of $k(r)$ at the WD surface.

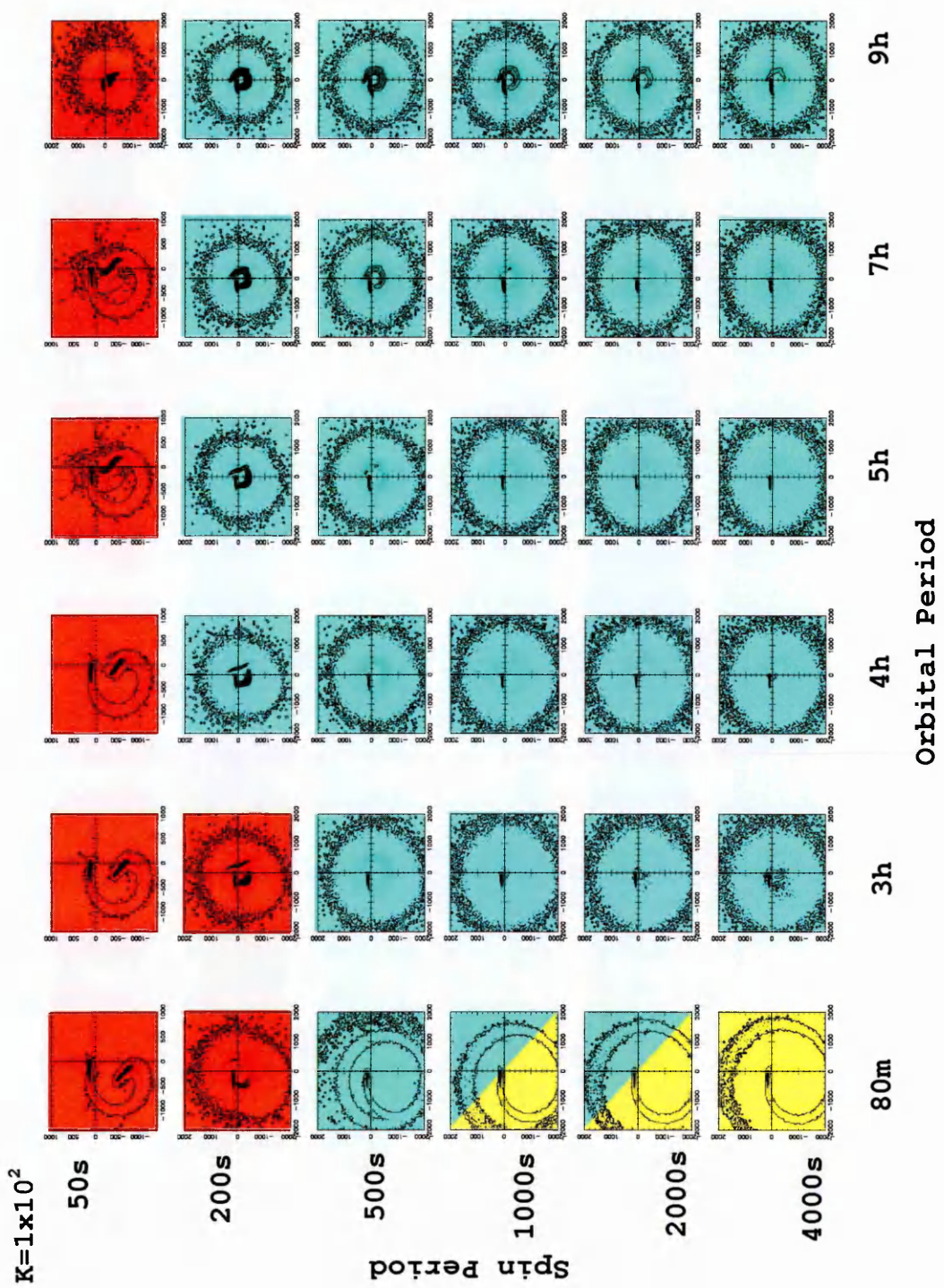
K=1x10^2
Spin Period
50s
200s
500s
1000s
2000s
4000s
Orbital Period
80m
3h
4h
5h
7h
9h

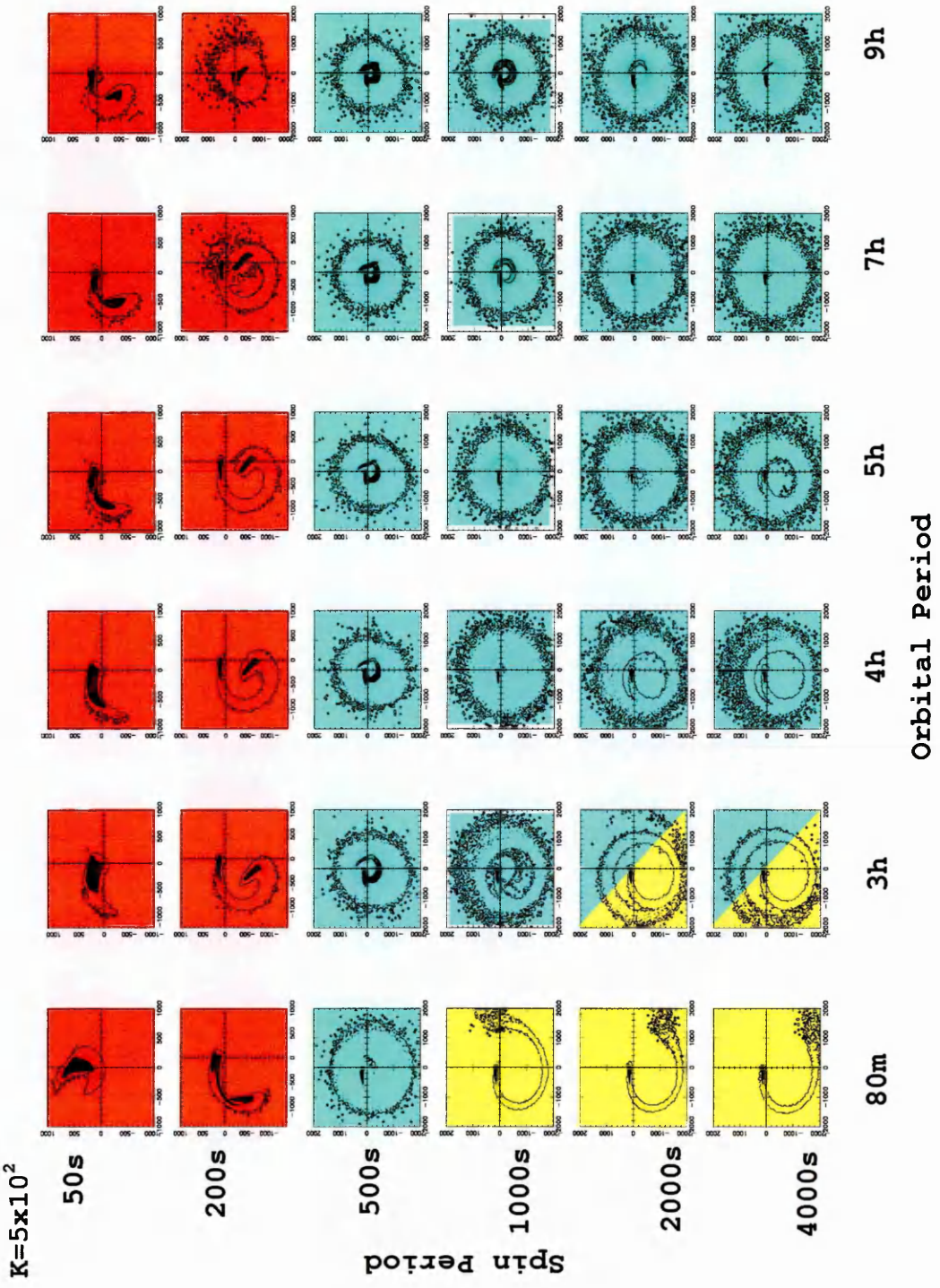
K=5x10^2
Spin Period
50s
200s
500s
1000s
2000s
4000s
80m
3h
4h
5h
7h
9h
Orbital Period

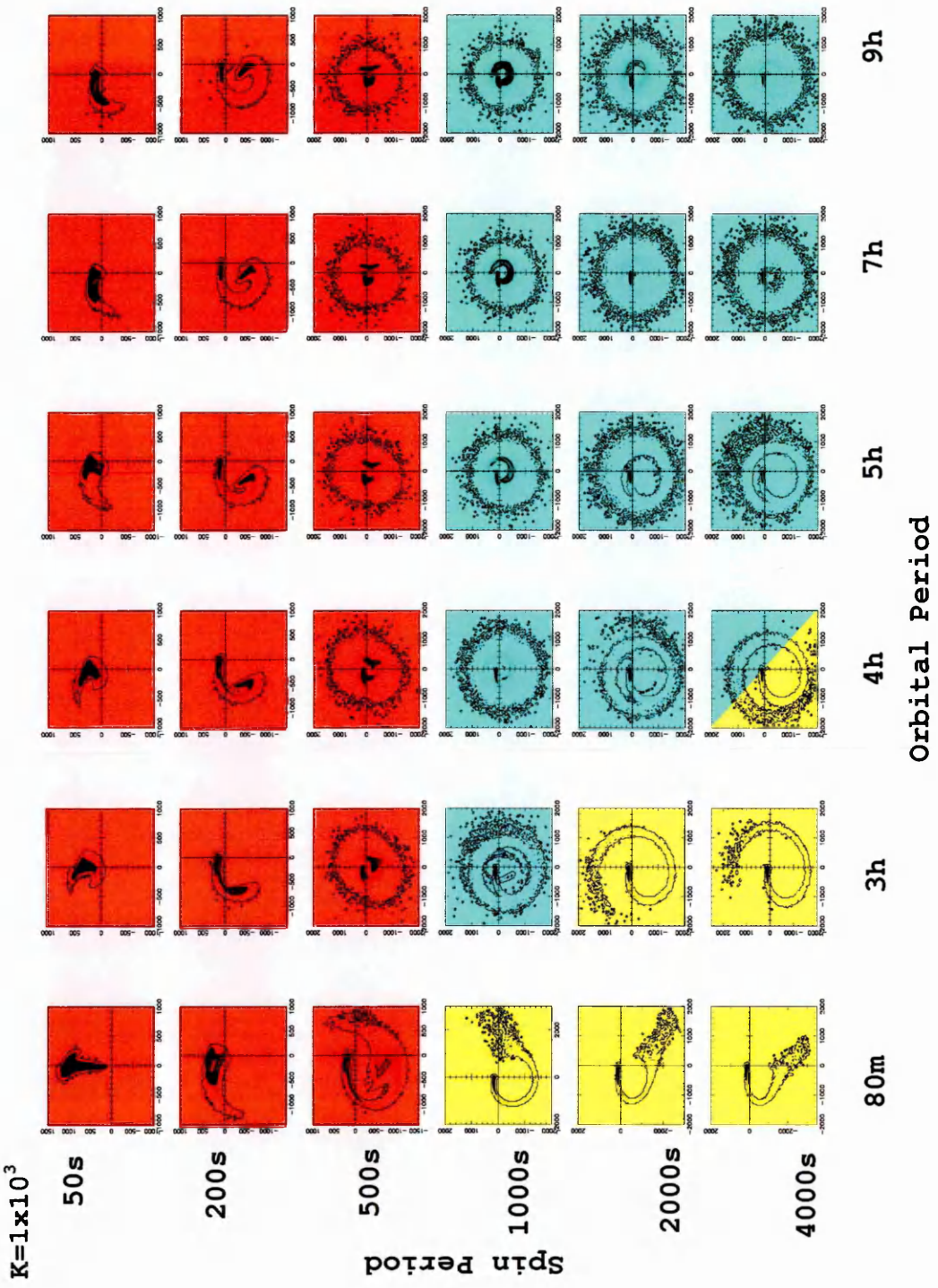
K=1x10^3
50s
200s
500s
1000s
2000s
4000s
Spin Period
80m
3h
4h
5h
7h
9h
Orbital Period

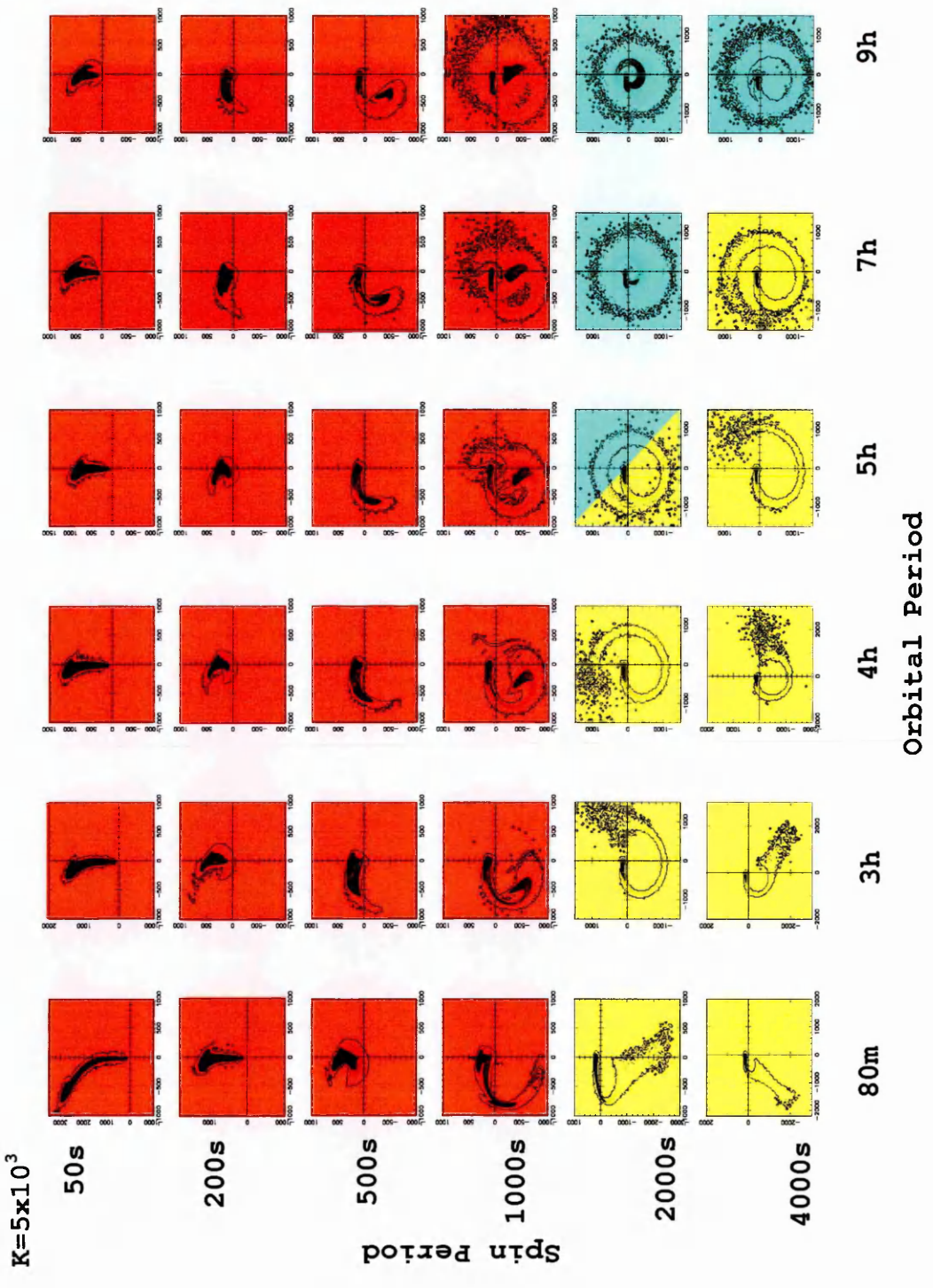
K=5x10^3
Spin Period
50s
200s
500s
1000s
2000s
4000s
Orbital Period
80m
3h
4h
5h
7h
9h

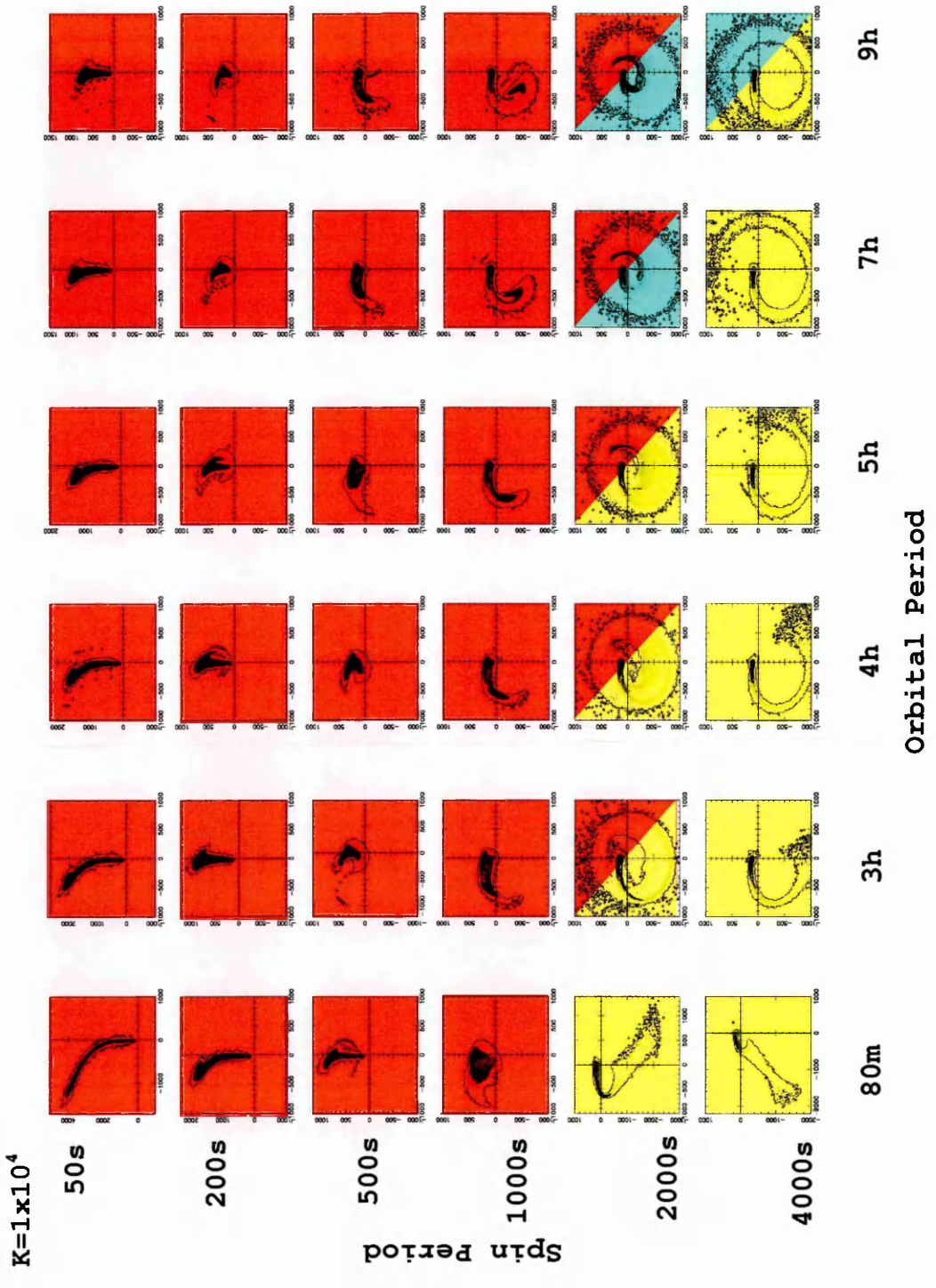
K=1x10^4
Spin Period
50s
200s
500s
1000s
2000s
4000s
Orbital Period
80m
3h
4h
5h
7h
9h

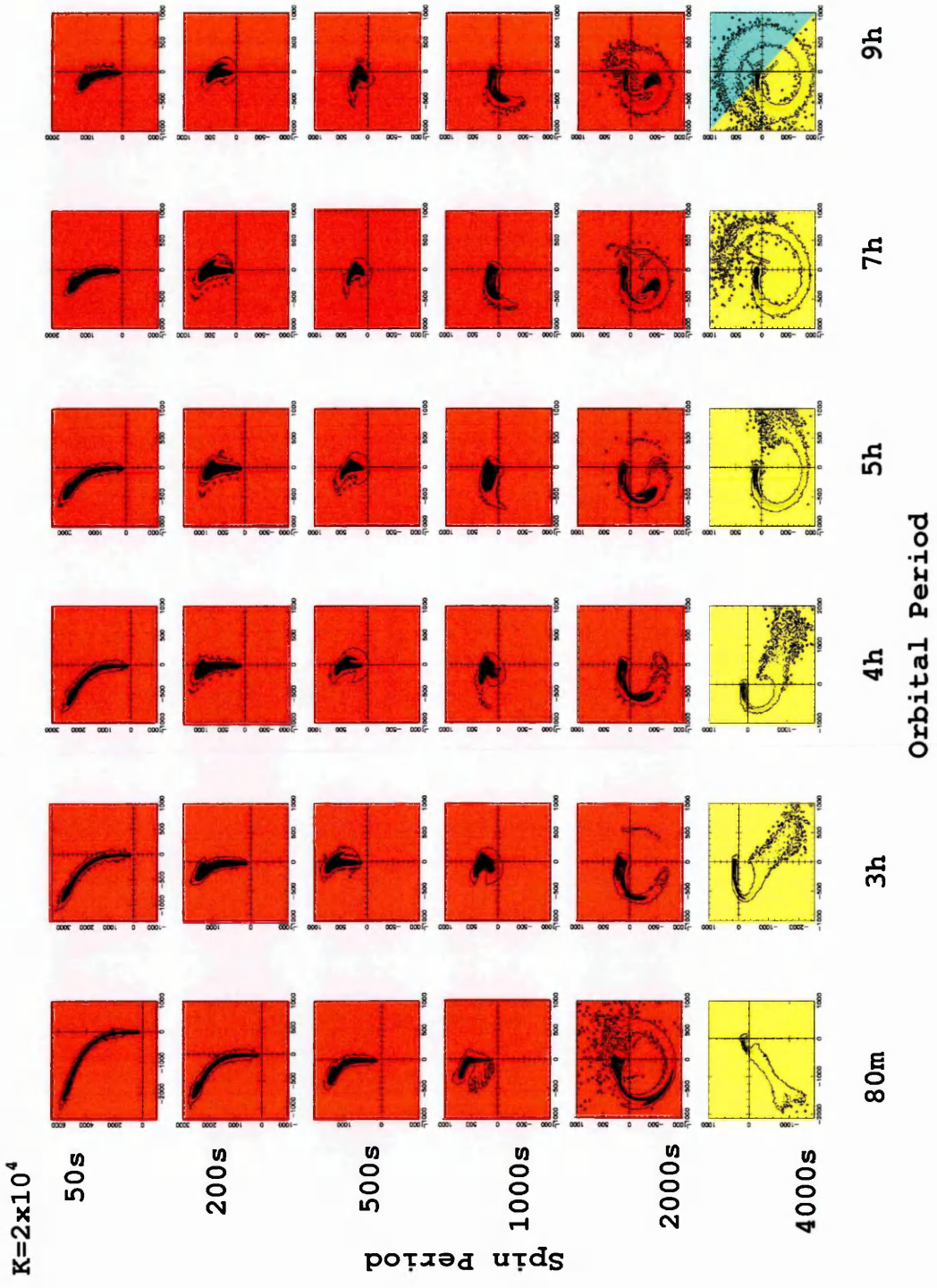
K=2x10^4
50s
200s
500s
1000s
2000s
4000s
Spin Period
80m
3h
4h
5h
7h
9h
Orbital Period

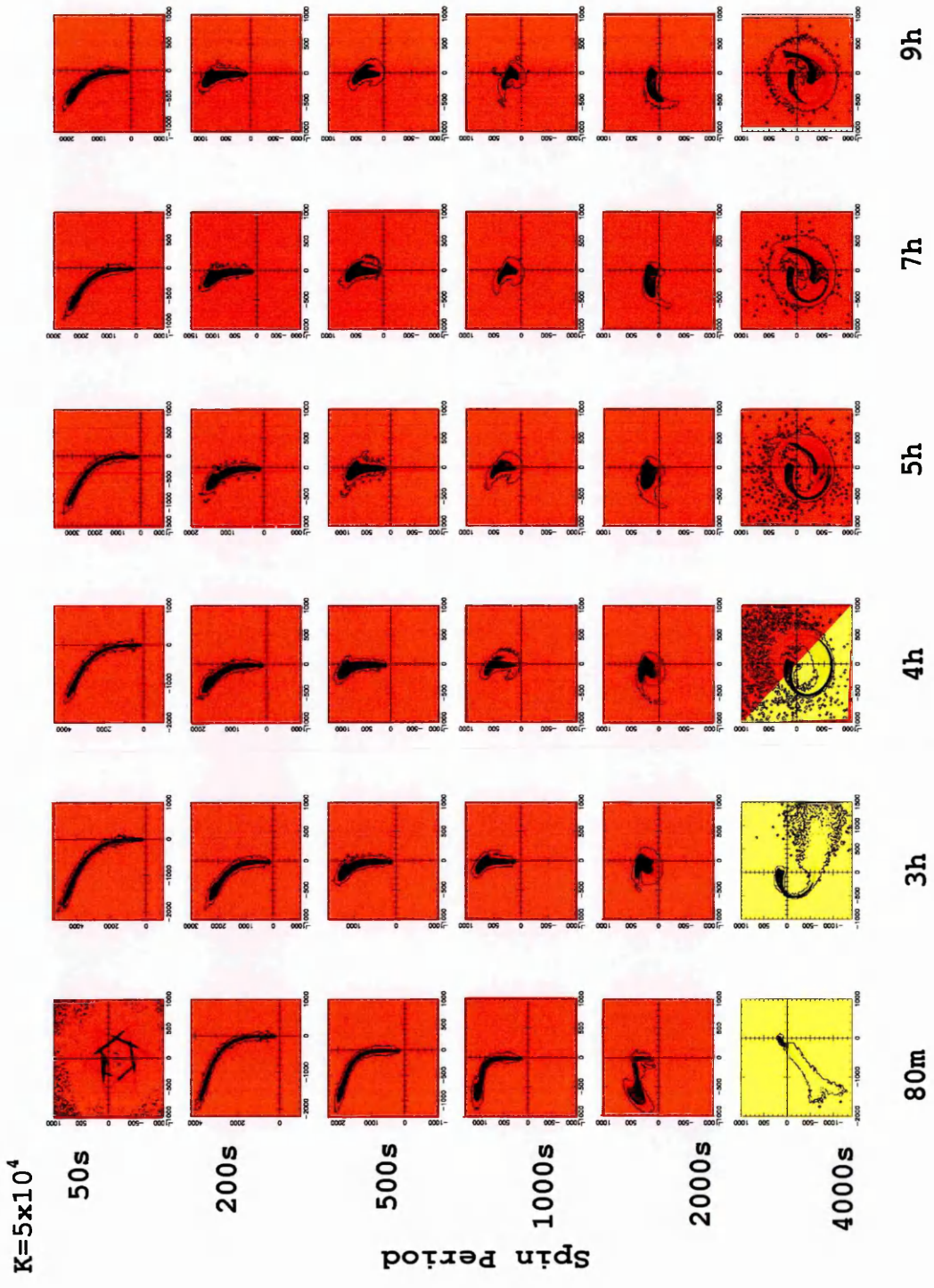
K=5x10^4
Spin Period
50s
200s
500s
1000s
2000s
4000s
80m
3h
4h
5h
7h
9h

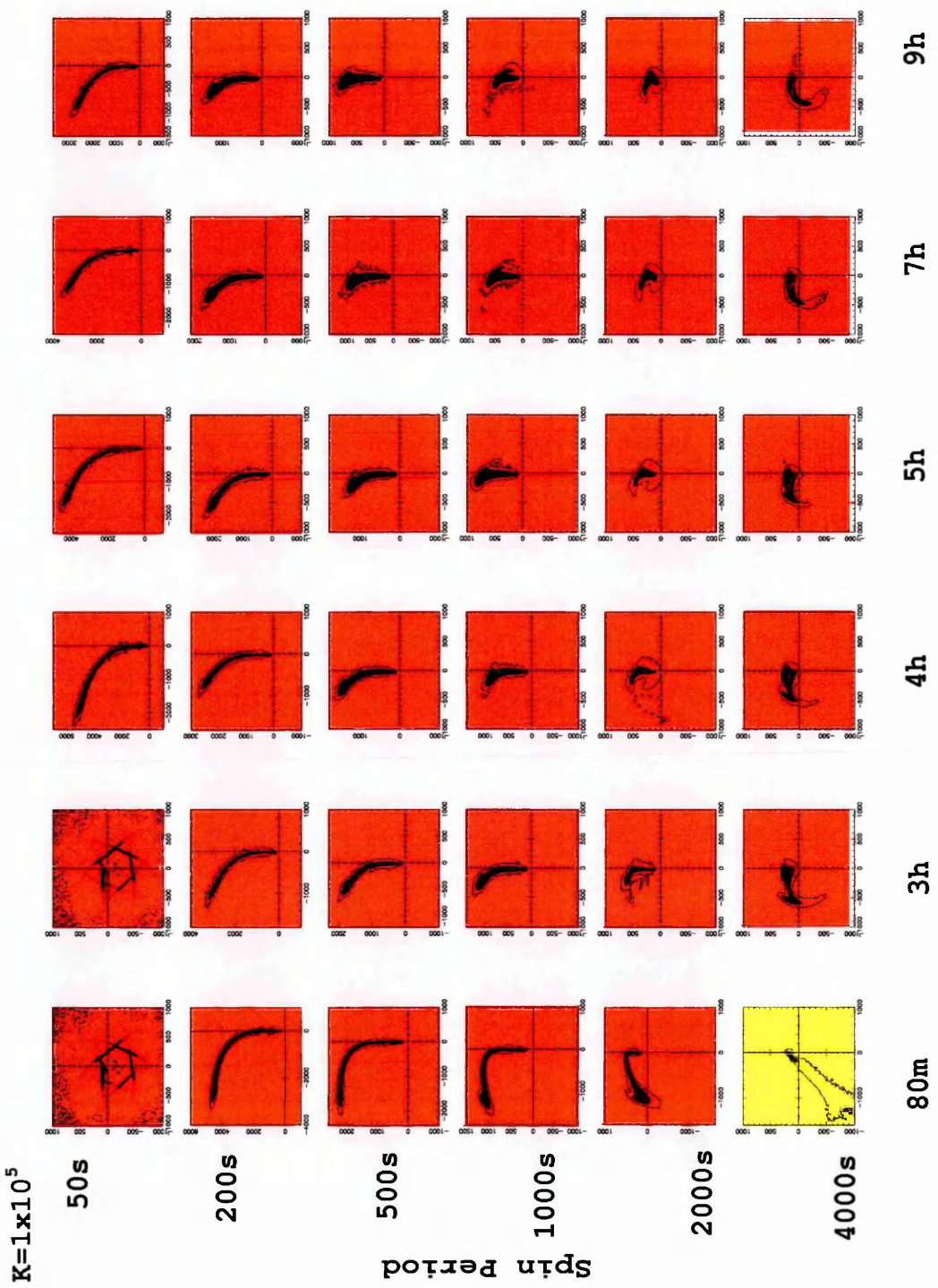
K=1x10^5
50s
200s
500s
1000s
2000s
4000s
Spin Period
80m
3h
4h
5h
7h
9h

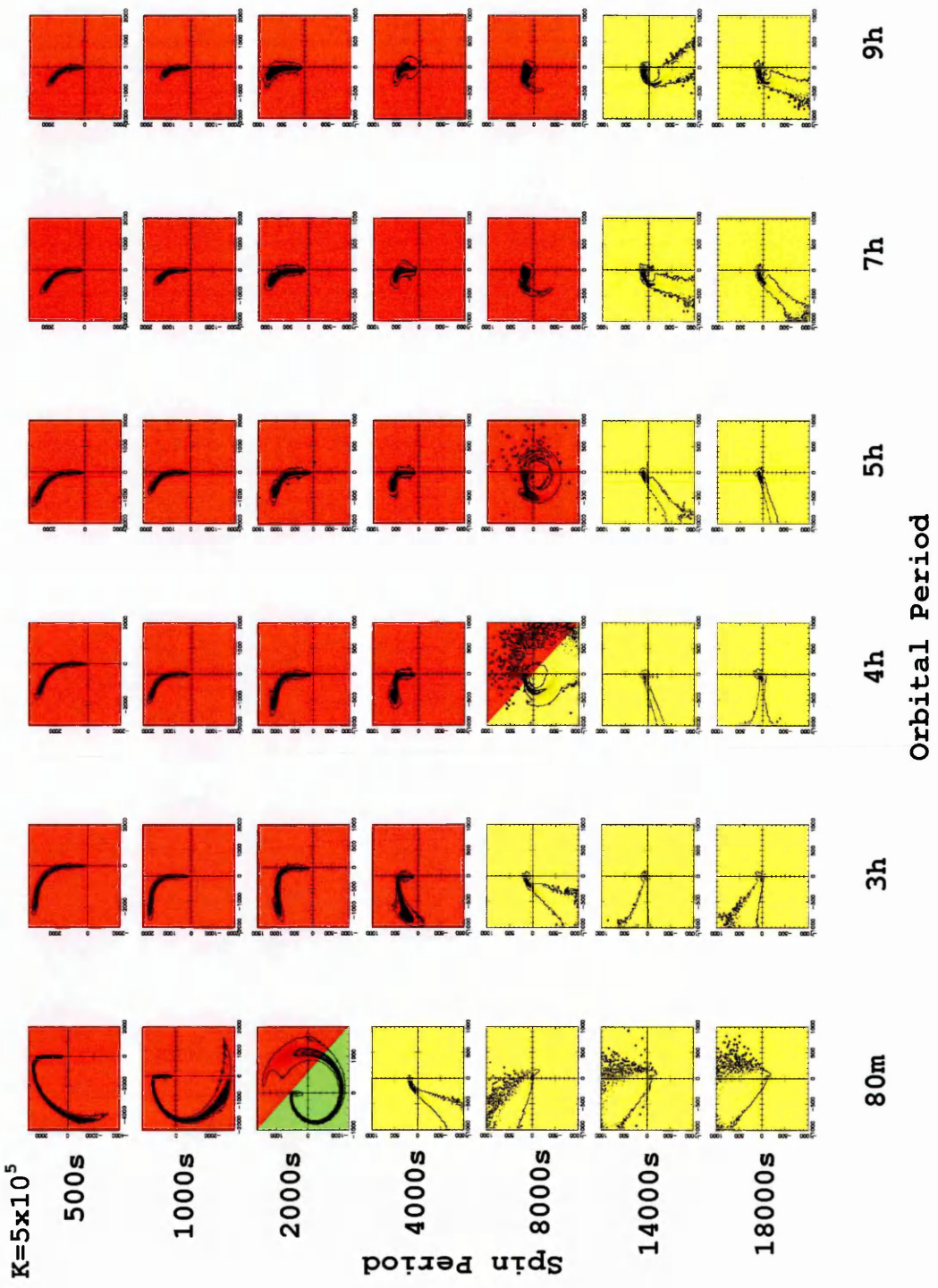
K=5x10^5
500s
1000s
2000s
4000s
8000s
14000s
18000s
Spin Period
80m
3h
4h
5h
7h
9h
Orbital Period

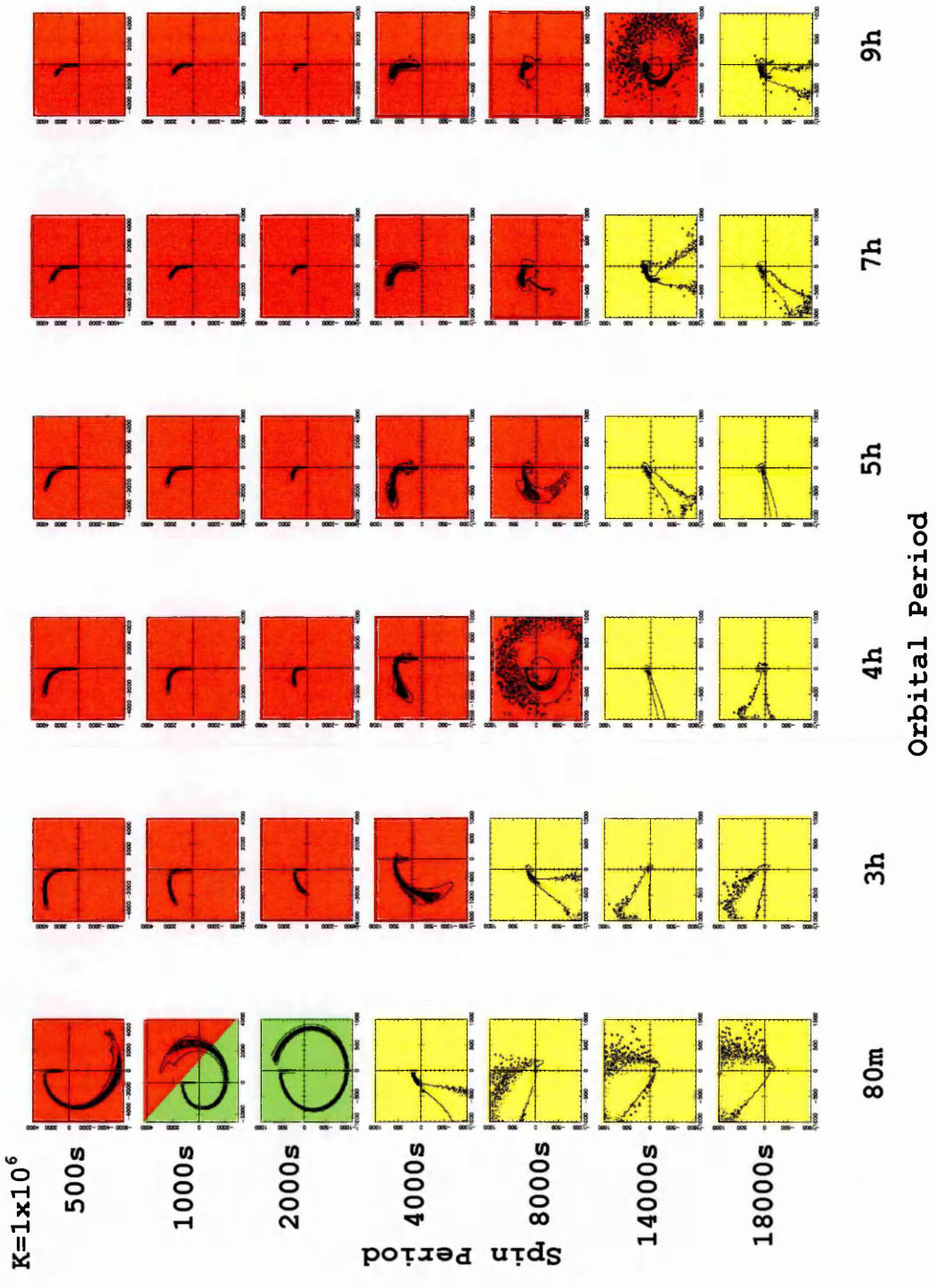
K=1x10^6
500s
1000s
2000s
4000s
8000s
14000s
18000s
Spin Period
80m
3h
4h
5h
7h
9h
Orbital Period

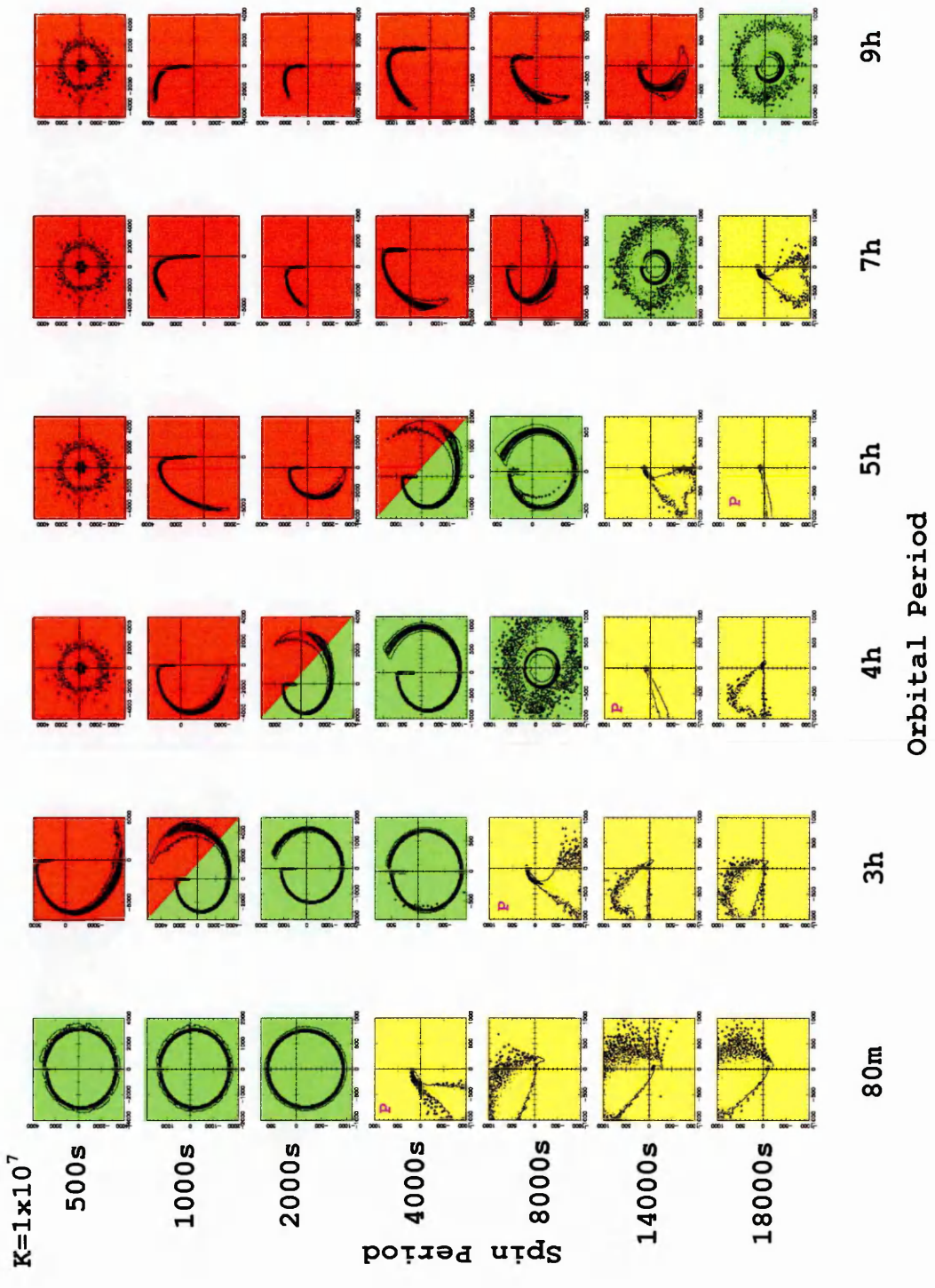
K=1x10^7
500s
1000s
2000s
4000s
8000s
14000s
18000s
Spin Period
80m
3h
4h
5h
7h
9h
Orbital Period

5.4.1 Discussion of the Doppler tomograms for the n^3 model

In the following, the reader may find it useful to glance at the flows from each page of Figure 4.1 as they consider each page of the tomograms in Figure 5.4.

- k_o=1×10^2

  At k_o=1×10^2 the simulated accretion flows produce three of the four known accretion mechanisms in IPs, propeller, disk and stream. If we look at the first three tomograms for the propeller systems at a 50s spin period we see a 'hook' feature that curls anticlockwise from the emission at the L_1 point; this is a dark region as blob density is high. The structure then loops round with low density where the blobs interact with the magnetic field as they come close to the magnetospheric radius. It then loops back leftwards to slower velocity corresponding to the blobs being ejected and decelerate as they leave the system in the simulated flows. A dense feature is also seen here as the ejected material is highly collimated. Notice that the tail of the loop in the tomograms moves to lower velocity as the trajectory angle of the simulated flows increases from $\sim 20°$ to $\sim 50°$. As the orbital period gets longer the hook feature becomes a ring of material. There is more emission at low velocity as well as the densely populated regions, the collimated flow is becoming more dispersed. The remaining propeller tomograms show material being propelled and also forming a disk. The ring structure at high velocities indicates this scenario. This ring appears very diffuse as the blobs are scattered within the Roche lobe of the WD, hence it is a not very dense region. The majority of the blobs are still being ejected from the propeller effect, seen by the presence of the dense emission regions around the centre, being captured back to circulate close to the WD.

  The disk tomograms all show an obvious ring structure at high velocity corresponding to material circulating close to the WD at the magnetospheric radius. Nine of the

tomograms show also a circular region at low velocity, produced from the blobs in the simulated flows that are near the outer edge of the Roche lobe circling at lower velocity. As the orbital period gets longer at $P_{\rm spin}$=200s this area in the tomogram gets increasingly denser with the blobs in the accretion flow staying in the Roche lobe instead of being ejected. As the spin period gets longer, the blobs move closer to the WD, are captured and forced to rotate further in, gaining velocity. At $P_{\rm spin}$=500s, $P_{\rm orb}$=80m we still see disk accretion in the simulated flows, a small disk close to the WD. In the tomograms we see a ring structure of low density and fairly high velocity. We also see a stream of low density from the L_1 point in the tomogram so the magnetosphere must be small in this binary system and unable to capture the material until it loses some angular momentum and moves further into the Roche lobe of the WD, eventually captured and forced to rotate round it.

As the spin period is increased at an 80m orbital period we see less disk structure and more stream in the simulated flows. The magnetosphere is small in these systems, the blobs in the accretion flow must still be captured and forced to rotate round the WD being magnetically controlled. In the tomograms we see the ring structure slowly uncurling but staying at high velocities.

- k_o=5×10^2

For this parameter space at k_o=5×10^2 we see propeller trajectories at $P_{\rm spin}$=50s at an angle of -90° out of the binary, slowly moving back towards the Roche lobe of the WD as the orbital period gets longer. The same is true for $P_{\rm spin}$=200s, the trajectory increases in angle moving back towards the WD from about ∼10° to ≳90°. If we compare this scenario to the tomograms we see a large region of very dense emission from the L_1 point that increases in the $+V_y$ direction, due to the accretion flow now moving away from the system. We see a very dense region next to and just leaving the

L_1 point that disperses quickly in the flows so we get a large dark region surrounded by the lower density one. As the trajectory moves back round to the Roche lobe we see both the high and low density regions move round and down into the lower-left quadrant. The blobs stay very closely packed throughout as we see very little low density. As the orbital period gets longer the lower density material increases in velocity as it moves into the binary system. As the magnetic field interacts with it, it affects it slightly, propelling it away and we see the 'hook' feature seen previously with slower less dense material being ejected as well as staying around the outer edge of the Roche lobe to produce the ring of the material at low velocity.

As before in the disk systems we see the slow velocity dense material in the centre as the magnetosphere is still close to the WD so does not have a strong interaction with the material in the outer edge, we see the high velocity ring of less dense material for the blobs that have been captured (see the previous section for more detail).

As before, we also see stream systems evolving to disks. The tomograms show the dense emission leaving the secondary and the high-velocity emission region where it is controlled by the magnetic field. How far round the stream moves before impacting the WD is indicated by the position of the tail in the upper-right quadrant moving further down into the lower-right one. As the orbital period increases the magnetosphere increases, having a greater affect on the stream curling it round the WD evolving into a disk. The tomograms indicate this by the tail curling round more till it rejoins the original stream continuing on to form a disk.

- k_o=1×10^3

The propeller systems at this magnetic field strength show the same features as before in paragraph one of the previous section. Trajectories of -90° out of the binary produce dense emission regions moving from $V_y \sim 100 \mathrm{kms}^{-1}$ to $V_y \sim 1200 \mathrm{kms}^{-1}$.

As the trajectory moves closer towards the Roche lobe of the WD the feature in the tomogram moves further down into the lower-left quadrant eventually looping round with a dense region of emission from the ejected blobs at slower velocity. The one major difference is the tomogram at $P_{\rm spin}$=500s, $P_{\rm orb}$=80m which shows a feature unlike that seen before. We have a long dense emission region from the L_1 point so the trajectory is very collimated here and entering the Roche lobe, we then get a whole mass of less dense material that continues to curl anticlockwise to the upper-right quadrant. The trajectory of the propeller expels and scatters material very early on within the Roche lobe so we see many blobs at low density scattered about.

The disk systems produce all the characteristics seen in the preceding sections. There is a high velocity, low emission, ring with a dense low velocity ring at the centre. These correspond to a very disperse disk ranging from close to the WD at high velocity to further out at lower velocities. The same evolution from stream to disk is seen, the curl for the stream moving further anticlockwise round the four quadrants till it merges in on itself at the beginning to form a ring. In the stream flow, we see it evolve further round the WD producing a small disk as well as a stream.

The stream systems also show similar features to that of before however at $P_{\rm orb}$=80m we see more clearly how the tomograms may be used to interpret the position of the stream impact onto the WD. The positioning of this affects the tomogram result by how far round the curl moves in the anticlockwise direction. The further round the WD from the L_1 point, the further round anticlockwise the tail curls.

- k_o=5×10^3

At k_o=5×10^3 we see the propeller systems are dominant, the trajectory angle being the criteria for what particular feature is seen in the tomogram. Twelve systems show trajectories out to the side of the binary system indicated in the tomogram by the

dense emission regions bordering V_x=0 and increasing in velocity in the V_y direction. We also see the dense emission region decrease in size as we increase the orbital period, this feature relating to how collimated the flow is. As the orbital period increases we see the flows getting more scattered as they leave the L_1 point so reducing the dense region. The tomogram also indicates that the material gets slower with increasing orbital period from a top speed of $V_y \sim 3000 \mathrm{kms}^{-1}$ to $V_y \sim 700 \mathrm{kms}^{-1}$. This region curls round anticlockwise into the lower left quadrant as the trajectory approaches and enters the Roche lobe of the WD. At P_{spin}=1000s, $P_{\mathrm{orb}} \gtrsim$ 5h we see the two dense regions of the L_1 point and the decelerating blobs as they leave the binary system. We see more low density material at slower velocity as well, the result of the ejected blobs being scattered more at different angles as well as the blobs that still leave at the same collimated angle.

Of the disk systems, we see one with a very strong magnetosphere at P_{spin}=2000s, P_{orb}=7h, seen in the tomograms by dense emission from the L_1 point with high velocity material surrounding it from the disk. There is also one at P_{spin}=2000s, P_{orb}=9h which still has a lot of blob material circling the outer area of the Roche lobe so we get a dense ring at the center of the high velocity ring. Finally there is one at P_{spin}=4000s, P_{orb}=9h showing evolution from stream to disk, where we see the less dense part of the stream before it is captured by the magnetosphere as well as the material already in the disk close to the WD so at high velocity in the tomogram.

The stream tomograms tell us again how far round the WD the material has gone before it impacts. The further it curls round, the more curled the tomogram is. The more collimated the stream from the L_1 point to the WD surface, the less scattered the tail of the curl in the tomogram.

- k_o=1×10^4

At this magnetic field strength, 17 of the 24 simulated propeller systems show a trajectory of -90° out of the binary system, with dense emission in the $+V_y$ direction in the tomograms. The greater the magnetic field strength the greater the speed at which the blobs are expelled, reaching $V_y \sim 4000 kms^{-1}$. The more collimated the accretion flow is in the simulated data, the greater the length of the emission region in the tomogram. Increasing the orbital period at constant spin decreases the blob density and overall speed so we see short, slightly wide, emission in the tomogram. Increasing the spin at constant orbital period decreases the density of the blobs in the flow and their speed. For P_{spin} of 500s and 1000s increasing the orbital period also decreases the angle of the trajectory moving closer to the Roche lobe of the WD. This is depicted in the tomogram feature by it curling round into the lower-left quadrant and back on itself as it approaches the WD where the magnetic field has a great affect on it, the blobs move quicker initially then slow down as they leave the binary.

The pure stream systems show the same characteristics as before in the tomograms (see paragraph 3 of section k_o=5×10^2 for a detailed explanation) but we also see the evolution of stream to propeller, disk systems with propelled material, and stream to disk accretion as well. If we look at the first of these stream to propeller tomograms (P_{spin}=2000s, P_{orb}=3h), it shows a stream like flow in the simulated accretion figures curling found at a fair distance from the WD as well as material being ejected away out of the Roche lobe. In the tomogram we see the stream feature curl round in a medium velocity ring characteristic of disk accretion, so some of the material must also be kept in the Roche lobe near the WD and forced to rotate around it so forming a weak disk. The disk/propeller at P_{spin}=2000s, P_{orb}=7h are a similar scenario. We see a high velocity ring in the tomograms but also a fairly dense region circling at

low velocity indicative of material circling further out in the Roche lobe from the WD. The simulated accretion flow shows quite clearly that a lot of the material is being ejected so adding to the density of blobs at slow velocity. The stream/disk tomogram at $P_{\rm spin}$=2000s, $P_{\rm orb}$=9h shows clearly the stream feature curling round at high velocity and back on itself as it streams from the L_1 point and curls around the WD as it is captured by the magnetic field.

- k_o=2×10^4

At a k_o value of 2×10^4 we see that the accretion flows are predominantly propeller systems with just a few at long spin periods being stream fed. The first 21 of these propeller systems are all ejected at -90° with the 22nd starting to move in towards the Roche lobe of the WD. This is indicated by dense emission regions in the $+V_y$ direction in each of the tomograms. In the other tomograms, the feature curls further round corresponding to the direction of the trajectory of the flow (see paragraph 1 of the previous section). However both $P_{\rm spin}$=2000s, $P_{\rm orb}$=80m and $P_{\rm spin}$=2000s, $P_{\rm orb}$=9h show a bigger region of less dense material at low velocity than the others. In the first case we see that a lot of the flow is still collimated from the large dense emission region, but we see a lot also getting scattered as the curl moves round into the upper-right quadrant. So the material must also be moving slightly round the Roche lobe before being ejected at low velocity.

In the 9h case we see a different picture. We have the emission from the L_1 point, the loop as the material in the accretion flow gets close to the WD and interacts with the magnetic field and also both a high density region as well as a low density one surrounding it. This suggests that not only do we get a large number of blobs following the same path out of the system we must also get a large number scattered out of the system.

The stream systems give us very collimated flows becoming more dispersed moving further round the WD in the tomograms. This corresponds to the straight flows with not much scatter at the end moving to very curled flows at high velocity with a large scatter at the end, evolving into a disk to give a ring like tomogram at high $P_{\rm spin}$, high $P_{\rm orb}$.

- k_o=5×10^4

  At k_o=5×10^4, the first 27 systems of the 33 propellers all have trajectories of -90° from the WD indicated by vertical emission in the tomograms. The more elongated the emission region the more collimated the flow. The faster the spin period the greater the velocity that is reached, the shorter the orbital period the greater the maximum velocity. As this emission curls round into the lower left quadrant, the closer the trajectory gets to the Roche lobe of the WD and the WD itself.

  At $P_{\rm spin}$=4000s we see the evolution from stream to propeller. First there is a highly collimated flow so giving rise to a straight feature in the tomogram. Increasing the orbital period causes the stream flow to move further round the WD and the tomogram feature gets more curled. Increasing the orbital period further gives two emission regions as well as the stream feature in the tomograms, indicating emission from the L_1 point and material leaving the binary system over a large area of the Roche lobe. By $P_{\rm orb}$=9h we see quite clearly in the simulated flow that it is propeller accretion. The tomogram tells us this by the two emission regions. It is also surrounded by a fairly low density ring indicating that some of the material must be circling the WD at quite large distances in the outer edge of the Roche lobe. This is near the expelled material region, so the magnetic field must have a weak affect on some of this material and draw it in to rotate.

- k_o=1×10^5

The flows here are all propeller systems, bar one at this field strength, and we see a lot of familiar features coming through in the tomograms. At this high k_o value almost all the propeller trajectories are at -90° indicated in the tomograms by the emission in the $+V_y$ direction. Those at an orbital period of 80m, $P_{\rm spin} \lesssim$2000s where the flow appears to be moving round towards the Roche lobe of the WD show their feature in the tomogram curling more into the lower-left quadrant. It appears that as the magnetic field strength increases, it causes the material to be expelled at higher velocities reaching $V_y \sim 5500 {\rm kms}^{-1}$ at one point.

At $P_{\rm spin}$=4000s, $P_{\rm orb}$=80m we see the only stream fed accretion in this set, a highly collimated stream that hits the WD almost straight on, so we see a straight stream in the tomogram moving from low velocity as it leaves the L_1 point to high velocity in the lower-left quadrant, the magnetically controlled section of the stream.

- k_o=5×10^5

At k_o=5×10^5 we see that propeller accretion is still the dominant flow. However, the flow is stream fed at slow spin rates of $\gtrsim$8000s and ring accretion is now also seen. From a brief glance at the tomograms of the propeller systems and a comparison to their simulated accretion flows we see that most of the trajectories are at -90°, so giving emission in the $+V_y$ direction in the tomograms. There are however a few different features that we see in the tomograms. The first at $P_{\rm spin}$=500s, $P_{\rm orb}$=80m is a very long, very dense, slightly curled emission region corresponding to a highly collimated propeller flow travelling close to the WD. As the spin period increases to 1000s the flow is still very collimated to a point then material is expelled and scattered out slightly away from the previous course. Hence the larger dense region is seen in the tomogram and the curl is carried on by less dense material. By 2000s we see ring accretion starting to form. In this propeller system the material moves

round the Roche lobe of the WD and is expelled back towards the secondary rather than away from it. In the tomogram we see a large curl of emission almost into the upper-right quadrant corresponding to the highly collimated flow. We then see a large curl increasing into the upper-right quadrant which reflects the large amount of blobs that are scattered back towards the secondary. An interesting thing to note is that as the orbital period is increased, the trajectory appears to move away from the Roche lobe of the WD. The increase in orbital period also slows down the ejected material.

For the stream systems we see the characteristics in the tomograms much more clearly now. We have streams that flow first out in the +y direction before travelling to the WD, streams that flow in the -y direction first then onto the WD, and streams where the flow almost appears straight from the L_1 point to the WD, each of these is depicted differently in the tomograms. If the stream travels in the +y direction first, the stream in the tomogram is in the top quadrants. The higher the accretion stream moves in the +y direction and fans out for material to fall onto the WD, the more we see the material spreads in the tomogram. The straighter the flow trajectory, the straighter the tail in the tomogram. The further down the stream moves in the -y direction, the more it moves down into the lower-left quadrant.

- k_o=1×10^6

If we compare this section of parameter space to that at k_o=5×10^5 we see a similar picture of accretion flows except we have a full ring system and a stream fed system that has now become a very dispersed propeller system. The whole ring structure is highly collimated, slightly less so as it approaches the surface of the secondary in the simulated flow, so we see a slight region of lower density material circling alongside the denser region. It is interesting to note that the material in the ring

in the tomogram travels faster in the two bottom quadrants than it does in the top two. If we look at the accretion flow we see the distance the ring is from the Roche lobe of the WD increases slightly as it gets further round the Roche lobe and hits the secondary star some distance from the original emission at the L_1 point.

We also see two systems in which the propeller is very dispersed at P_{spin}=8000s, P_{orb}=4h and at P_{spin}=14000s, P_{orb}=9h. However it is dispersed close to the Roche lobe of the WD, so some of it still streams onto the WD as well as circling it. So we get stream features, a large blob density region around the centre and a slight ring of material around it for the blobs circling at the outer edge. For information on the other propeller and stream tomograms refer to the last section.

- k_o=1×10^7

At k_o=1×10^7 there is now a plethora of ring accretion systems. Propeller accretion is still dominant and within the stream accretion systems we see Polar systems and retrograde motion also.

At P_{orb}=80m, P_{spin}=500s, 1000s and 2000s we see very clear ring structures that meet almost exactly back at the start on the V_x axis. Where the rings are more collimated in the simulated flows, we get a greater dense emission region curling round the tomograms. The more dispersed they are at the end, the more we see lower density material circulating. The distance they are from the original emission at the L_1 point in the tomograms indicates just where they re-impact the secondary star Roche lobe. We also see three different features for ring systems at P_{spin}=8000s, P_{orb}=4h at P_{spin}=14000s, P_{orb}=7h and at P_{spin}=18000s, P_{orb}=9h. All show either a full or partial ring at their centres at low velocity. The rings in the accretion flows are collimated in parts and scattered in others so we see a thick ring of dense material but also less dense material circling on the inside. The scattered material in a ring

at medium velocity circling the ring in the middle is due to scattered material from the propeller flow also entering into the Roche lobe so the magnetic field must have some affect and get the material to rotate causing this feature. Notice again that in all these ring systems the material travels faster in the two lower quadrants than the two upper ones. The rings rotate slower with increasing spin period and get faster with longer orbital periods.

In the stream systems we see that the direction of the initial stream from the L_1 point in the simulated flows before it is on a path to the WD determines the direction of the feature in the tomogram, and the more spread out this material is before it heads towards the WD the more spread the feature is in the tomogram (see k_o=5×10^5 for a full explanation).

The propeller systems show long dense emission regions corresponding to highly collimated flows with the length and shape of the curl determined by the trajectory of the propelled flow (see k_o=5×10^5 for a full explanation).

5.4.2 Overall Conclusions

We see some interesting features showing up in the tomograms, with very diverse characteristics for each of the typical accretion mechanisms: propellers, streams, disks and rings.

The tomogram features for the propeller systems depend largely on the trajectories of the propeller flow which range from an ejection angle of +90° through to $\gtrsim -90°$ quoted from an imaginary horizontal line between the L_1 point and the WD. At trajectories with high angular ejection of ∼+90°, we see a 'hook' like feature formed in the tomograms. We see a dense emission region in the tomograms at the L_1 point surrounded by lower density material that loops round from this point anticlockwise into the lower-left quadrant at

high velocities. In the accretion geometry, this is the collimated flow leaving the L_1 point and then interacting with the magnetic field. The tomogram loop then curls back on itself at low V_x velocity and -V_y velocity, decreasing towards zero, as the material in the flow moves to slower velocities as it is expelled. Here we also see a second very dense region corresponding to the collimated blobs leaving the system at the same angle. At an ejection angle of -90° we see very dense emission in the +V_y direction that moves anticlockwise into the lower-left quadrant as the trajectory angle decreases to 0 and then increases again up to +90° and the 'hook' feature is re-formed. We see that the greater the magnetic field strength the greater the speed at which the blobs are expelled. The more collimated the flow is, the greater the length of the emission region and the more elongated it is. We also see a high velocity ring, form in the tomogram around the two dense emission regions when the ejected material is very dispersed and ejected early on. The material stays within the Roche lobe and the magnetic field has a slight effect on it forcing it to rotate in a diffuse disk. These main features are depicted in Figure 5.6, where we see the propeller trajectory at $\sim$ +90° with the corresponding 'hook' feature, the opposite at -90°, with the vertical emission feature and finally a flow trajectory that lies in between the two, where we see the feature curling round further than that of the vertical, but not enough to form a 'hook' feature.

The propeller flows that are observed at $\sim$+90° to the system are seen at the turning point of disk accretion to propeller accretion. To begin with this type of propeller flow is seen at all orbital periods for very fast spin periods and then seen at increasingly slower spin periods as the magnetic field strength is increased up to a value of k_o=2×10^4 where disk accretion just barely exists at $P_{\rm orb}$=9h, $P_{\rm spin}$=4000s.

The -90° propeller accretion flows are seen just materialising at a magnetic field strength of k_o=5×10^2 for fast spin periods and short orbital periods. Increasing the magnetic field

strength allows more of this type of propeller accretion to form at slightly slower $P_{\rm spin}$ and slightly longer orbital periods. This type of propeller accretion then becomes dominant for all orbital periods and $P_{\rm spin}$ of 50s $\sim$ 2000s. Above k_o=1$\times$10^5 we see the flow at orbital periods $\geq$3h for intermediate spin periods and then $\geq$5h for spin periods between 2000s and 8000s at the highest magnetic field strength, being the precursor to ring like accretion.

Finally the intermediate case is just that. It lies between the latter two extremes, the border of disk like accretion and the border to ring accretion. It occurs across the range of orbital periods and mainly at the fast spin periods at low magnetic field strengths increasing to intermediate $P_{\rm spin}$ as the field strength increases.

For the disk systems we see two main types of tomograms also depicted in Figure 5.6, a diffuse disk and a concentrated disk. In the diffuse case, we see in the tomograms a large ring of high velocity corresponding to the material circling close to the WD as well as a small very dense ring at low velocity corresponding to the material circulating further out from the WD. In the tomogram for the concentrated case we still see a ring of high velocity but we see just a small dense region from the L_1 point. Soon after the material leaves the L_1 point it interacts with the large magnetosphere and is forced to rotate at high velocities, hence we see only the one dense emission region in the centre of the tomogram.

These disk accretion systems exist more at the lower magnetic field strengths, just able to form at a k value of 2×10^4 for a spin period of 4000s at an orbital period of 9h. Before this field strength we see the more concentrated disks forming at longer and longer orbital periods as the magnetic field strength increases at $P_{\rm spin}$ above 200s. The diffuse disks we see near the border line propellers at the faster spin periods as the magnetic field strength increases. At the slowest $P_{\rm spin}$ and short orbital periods we see small disk structures that are on the edge of becoming stream like flows at the same parameters but stronger field strength.

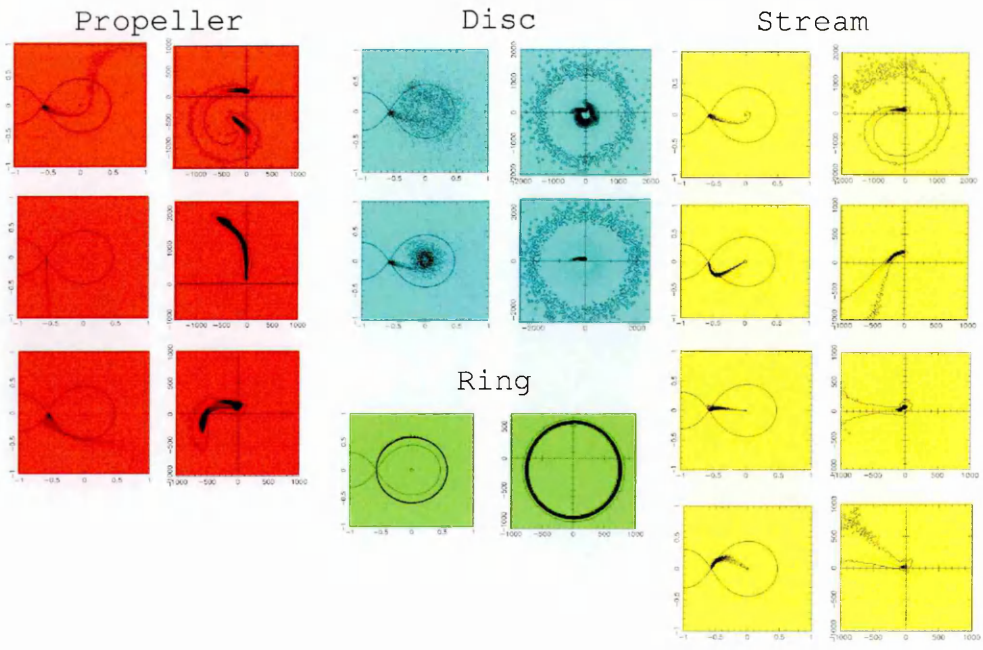

Figure 5.6: Overall result features from the n^3 field tomograms. Each pair of panels shows the simulated flow on the left and its corresponding tomogram on the right.

The features in the tomograms corresponding to streams, like the propellers, are determined by their direction of flow: mainly in the direction at which it leaves the L_1 point, either in the +y, -y direction or straight to the WD. For stream tomograms we see dense emission from the L_1 point, the stream interaction with the magnetic field curling round in the tomogram and the ballistic trajectory, with a scattered end to the curl. Three main features exist with interpreting the stream tomograms: 1) The further round the stream impacts the WD in the accretion flow, the further round we see the stream curl in the tomograms. If the stream rotates all the way round the WD then we will see the curl merge with itself at the beginning in the tomograms and we start to see a comparison with the disk tomograms. 2) As the spin period is increased, we see the curl in the tomogram moving further round anticlockwise, hence in the simulated flow the stream is moving further round the WD. 3) As the orbital period is increased, we see the curl feature in the

tomogram moving further back round clockwise, the stream in the flow moving further back round the WD towards the L_1 point. All these situations are depicted in the Figure 5.6.

These stream features are seen only at the slowest spin periods of 1000s and greater for low magnetic field strengths and short orbital periods. As the magnetic field strength increases, they emerge at slower and slower spin periods at increasingly longer orbital periods. The first of the stream accretion scenarios is seen to occur at the border between stream and disk accretion. The second scenario where the stream accretion is seen coming further out from the Roche lobe before its approach to the WD is seen at magnetic field strengths of k_o=1×10^4 and stronger for $P_{\rm spin}$ of 2000s and slower, short $P_{\rm orb}$ to increasingly longer orbital periods at k_o=5×10^4, where the stream borders propeller accretion. We only see the stream accretion that is almost straight from the L_1 point to the WD at magnetic field strengths of k_o=5×10^5 and stronger, at very short spin periods of 14000s and 18000s and intermediate orbital periods. They are seen lying in between the retrograde stream and the opposite case of the stream moving out in the other direction, out of the Roche lobe before heading to the WD. The final stream accretion 'retrograde' is seen only at very slow $P_{\rm spin}$ of 8000s and slower, for very short $P_{\rm orb}$ of less than 4h at magnetic field strengths of k_o=5×10^5 and stronger.

Like the disk tomograms, ring accretion is also evident by a ring structure in their tomograms. It is a much denser ring and more concentrated than a disk feature and we see very little low density emission in the tomograms. We also see that the ring moves at a higher velocity in the two lower-quadrants than it does in the upper two.

Ring accretion is seen at only the highest magnetic field strength of k_o=1×10^7 at spin to orbit combinations ranging from fast spin/short orbital period to slow spin/long orbital period.

5.5 n^6 model Doppler Tomograms

In Figure 5.7 we present the tomogram results of running HyDisc for the n^6 model with the range of $P_{\rm orb}$, $P_{\rm spin}$ and k_o discussed above. Details are given in the caption. In all these simulations, the masses of the two stars are 0.6 $M_\odot$ for the WD and 0.3 $M_\odot$ for the secondary and the dipole inclination angle is m$\sim$ 5°. All tomograms assume a system inclination angle of 90°, i.e. edge on.

Figure 5.7: Tomograms for the n^6 model ($k(r) \propto r^{-6}$) for each k_o value in parameter space. The red figures indicate propeller accretion, yellow figures indicate stream accretion and blue figures indicate disk accretion. A small magenta 'P' in the upper left of a Figure indicates a polar system, i.e. the configuration where $P_{\rm spin}$=$P_{\rm orb}$. The k value listed on each page of this figure is the value input to HyDisc, i.e. k_0 which is the value of $k(r)$ at the WD surface.

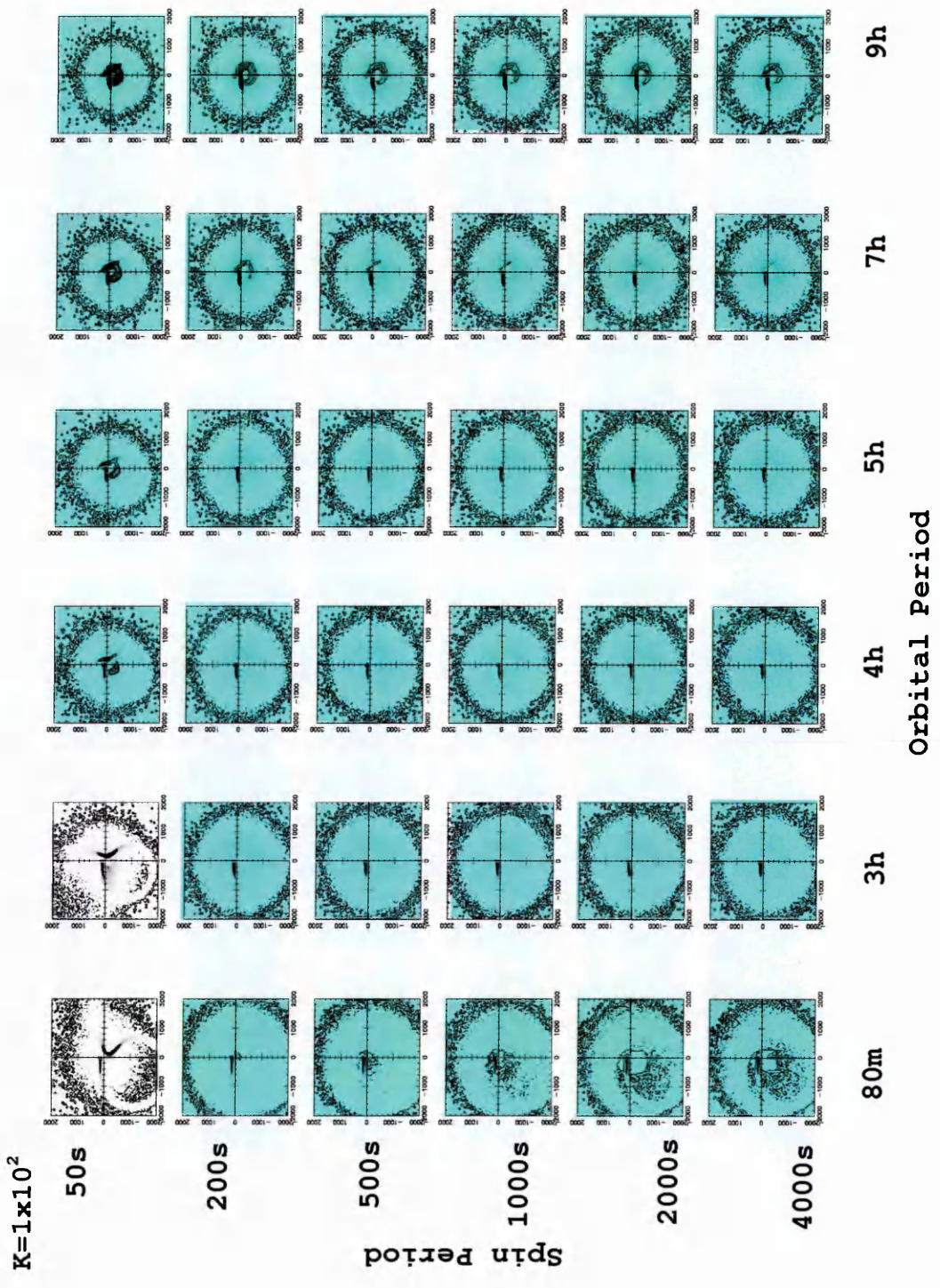
K=1x10^2
Spin Period
50s
200s
500s
1000s
2000s
4000s
Orbital Period
80m
3h
4h
5h
7h
9h

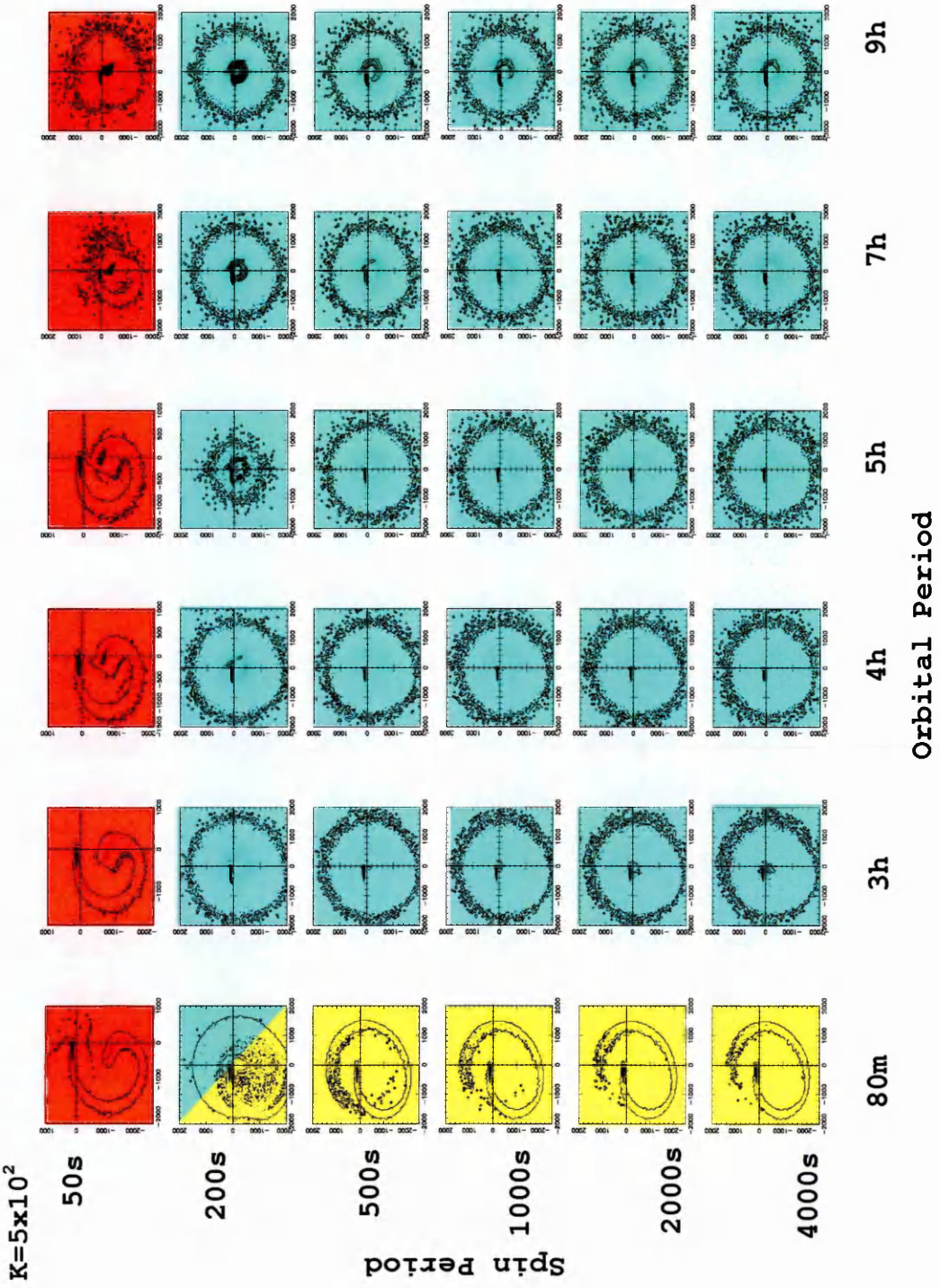
K=5x10²
Spin Period
50s
200s
500s
1000s
2000s
4000s
Orbital Period
80m
3h
4h
5h
7h
9h

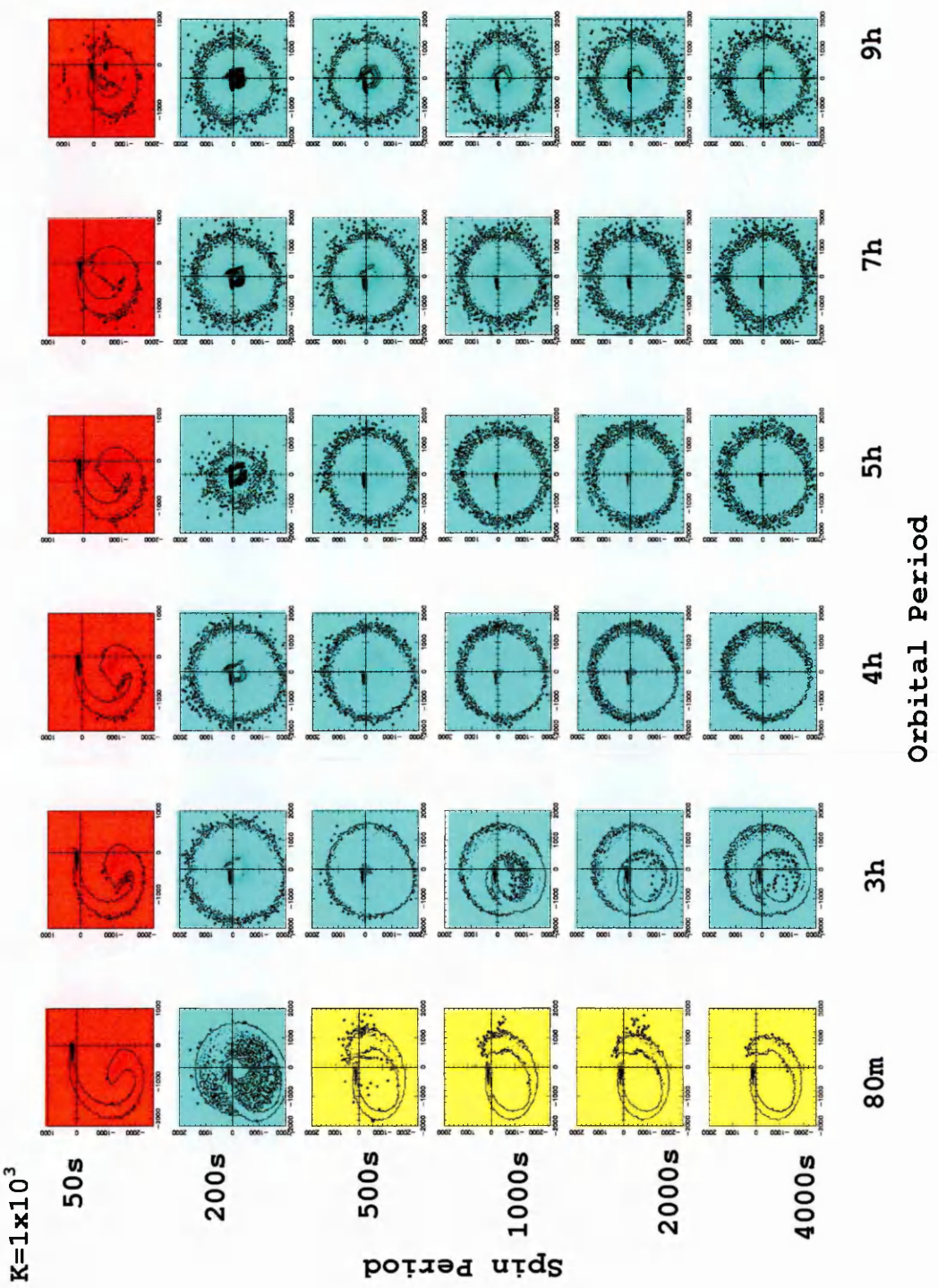
K=1x10^3
Spin Period
50s
200s
500s
1000s
2000s
4000s
80m
3h
4h
5h
7h
9h
Orbital Period

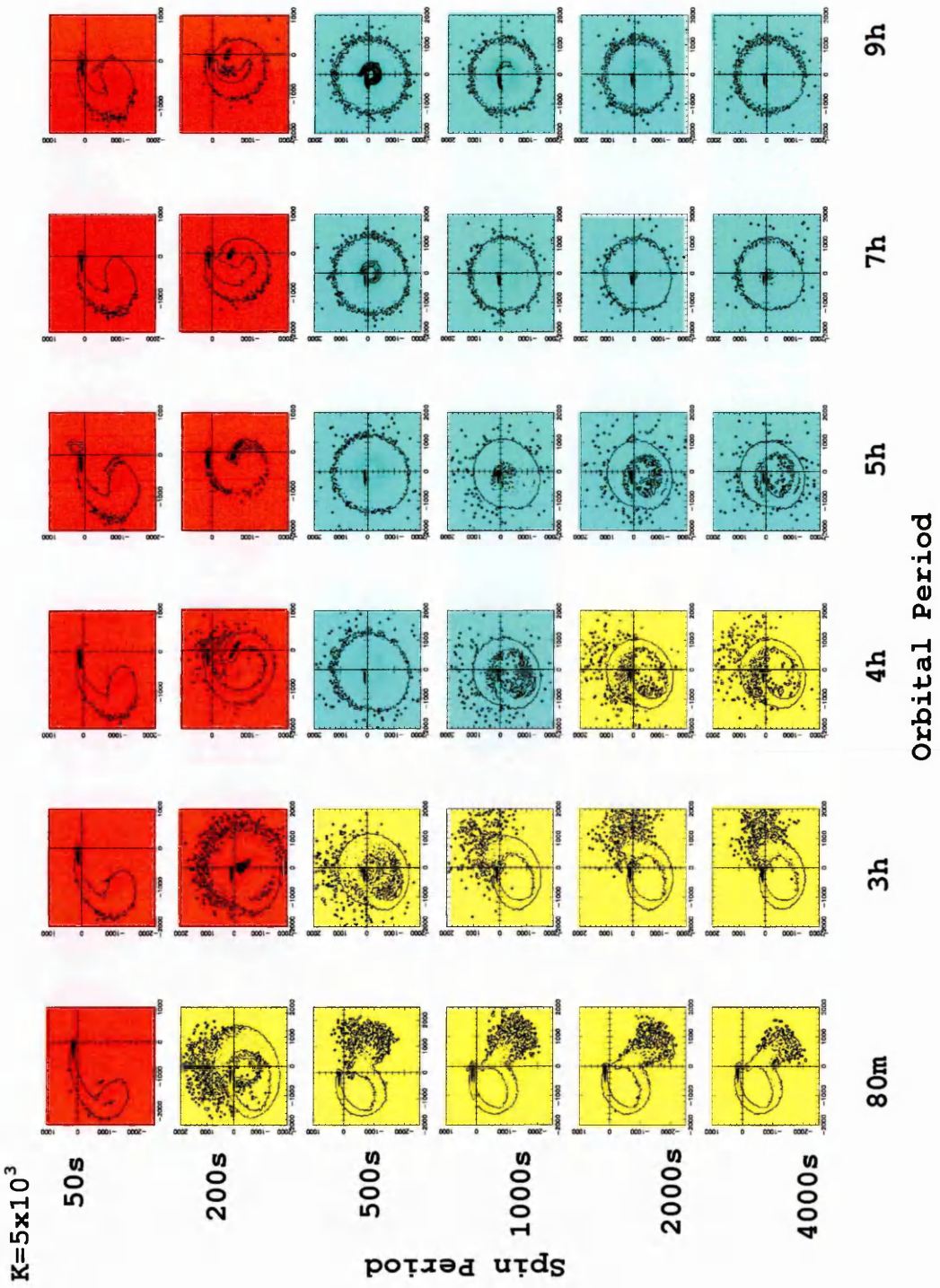
K=5x10^3
Spin Period
50s
200s
500s
1000s
2000s
4000s
Orbital Period
80m
3h
4h
5h
7h
9h

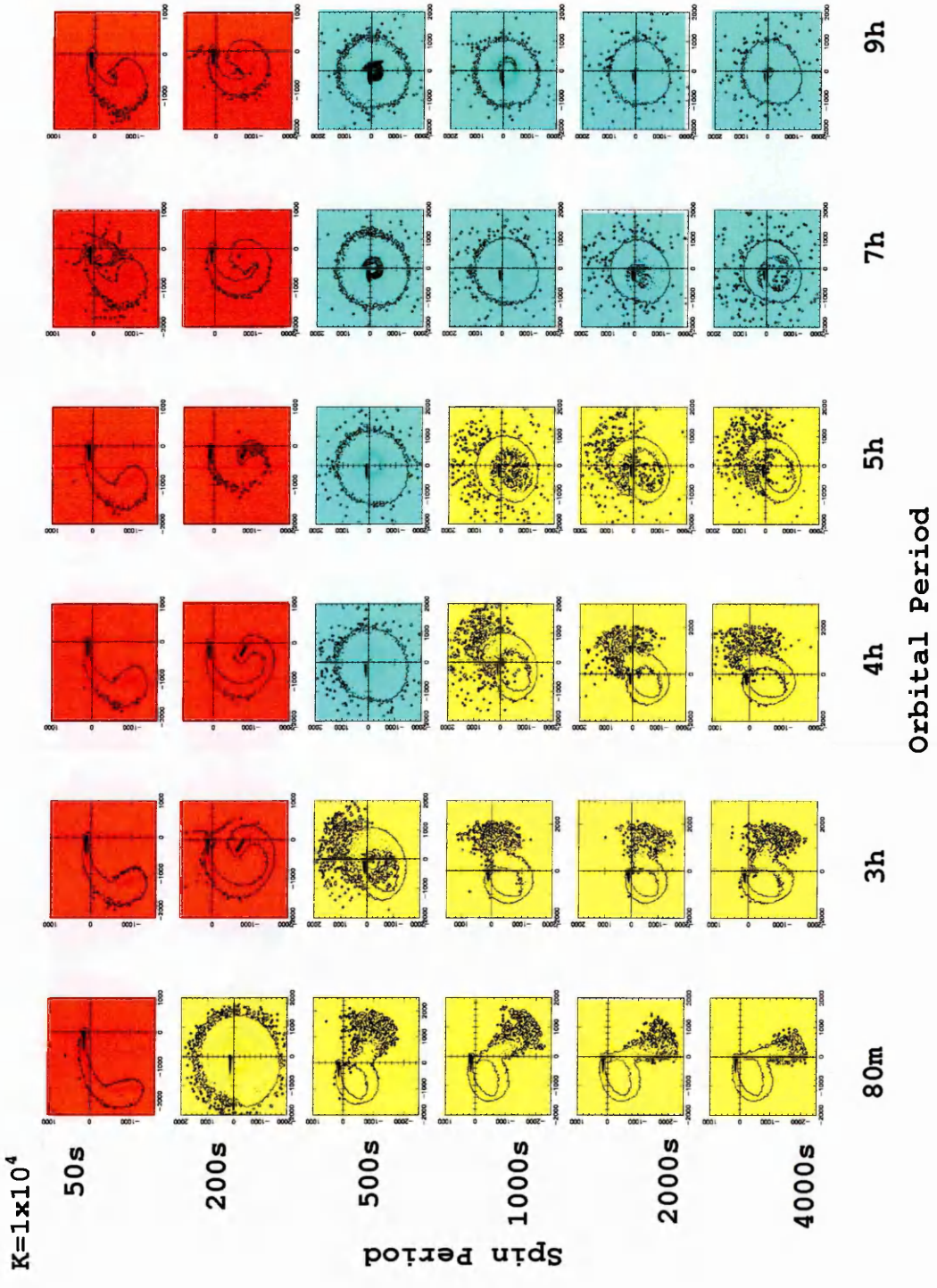
K=1x10^4
50s
200s
500s
1000s
2000s
4000s
Spin Period
80m
3h
4h
5h
7h
9h
Orbital Period

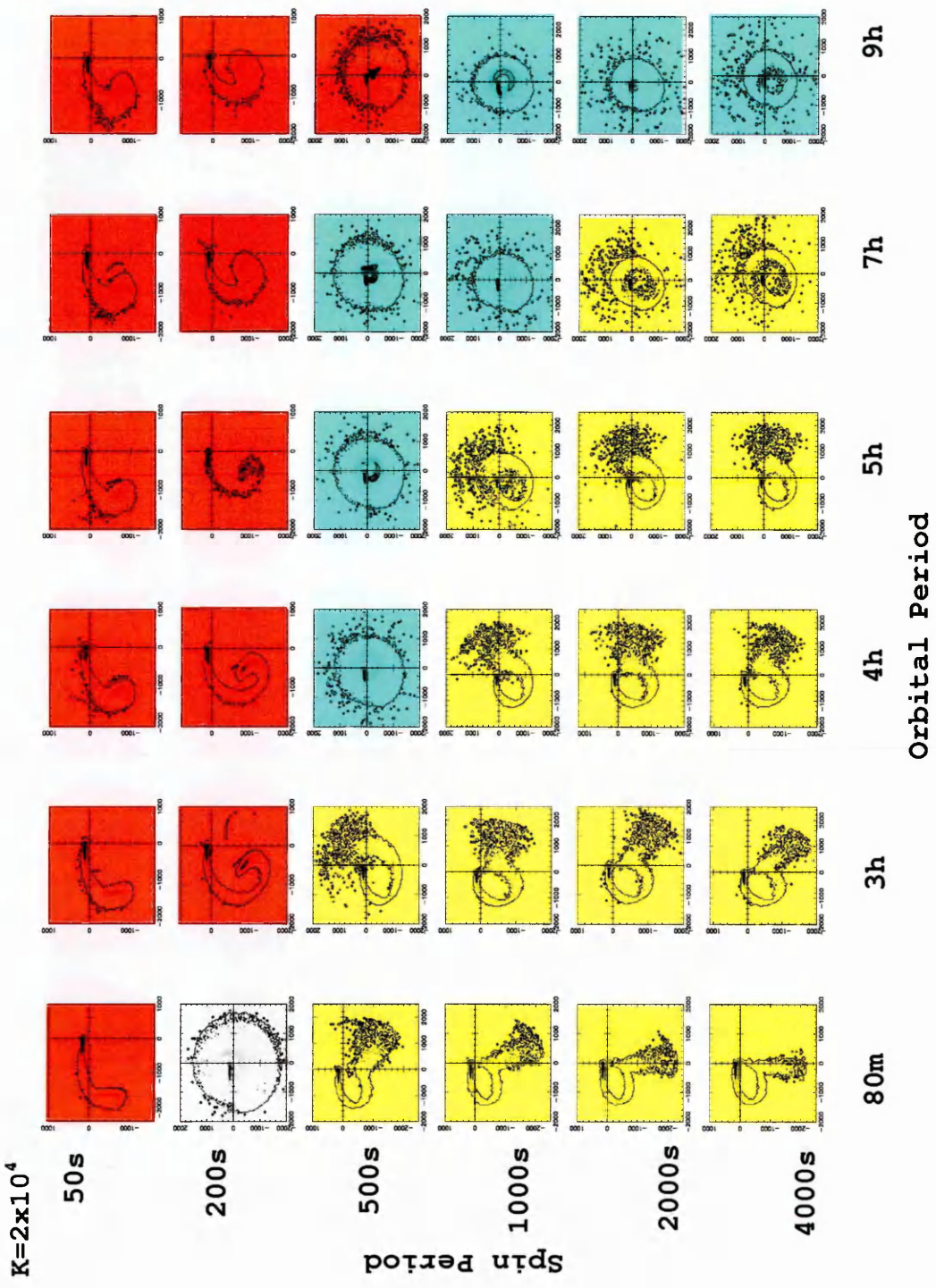
K=2x10^4
Spin Period
50s
200s
500s
1000s
2000s
4000s
Orbital Period
80m
3h
4h
5h
7h
9h

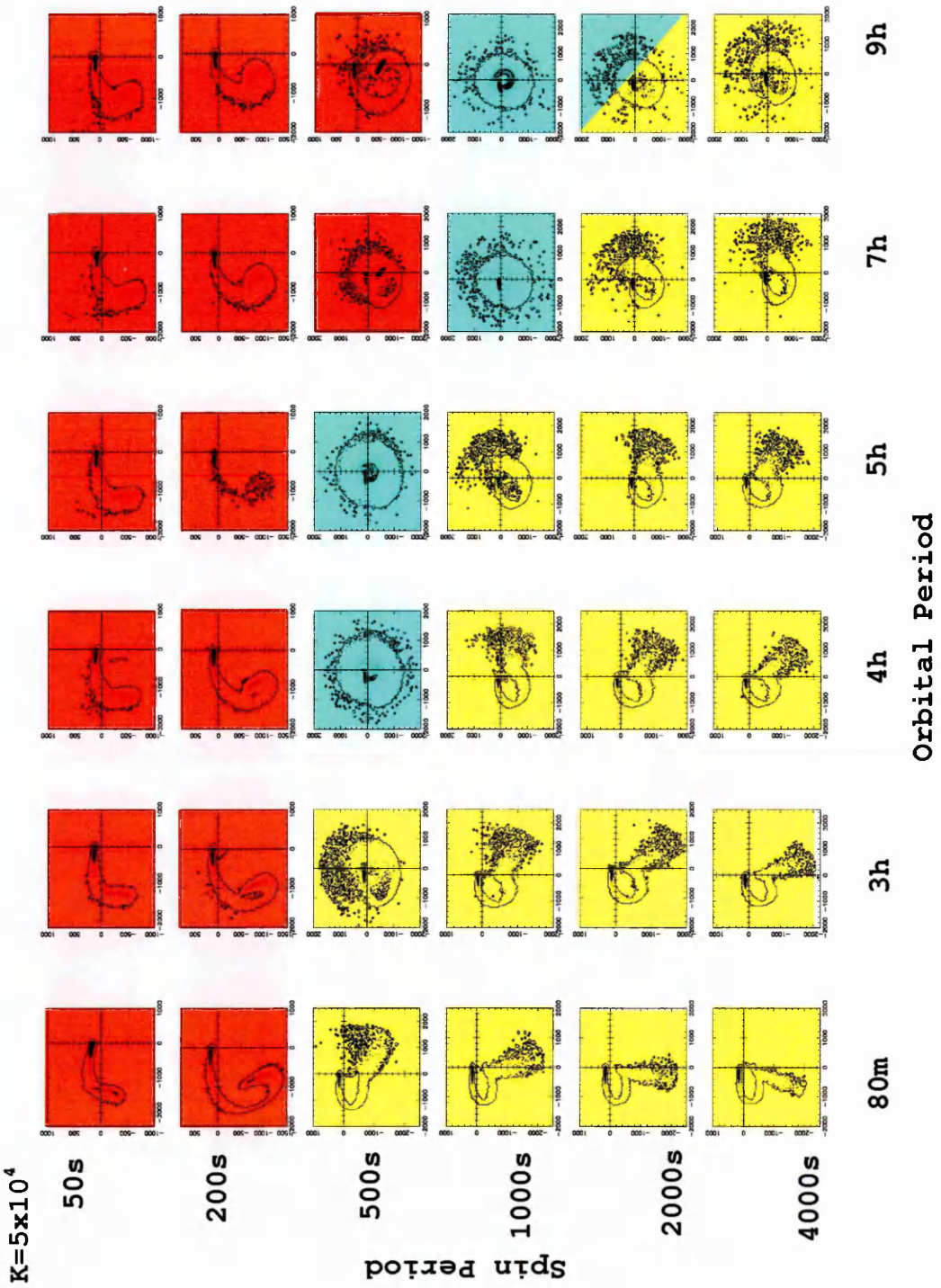
K=5x10^4
Spin Period
50s
200s
500s
1000s
2000s
4000s
Orbital Period
80m
3h
4h
5h
7h
9h

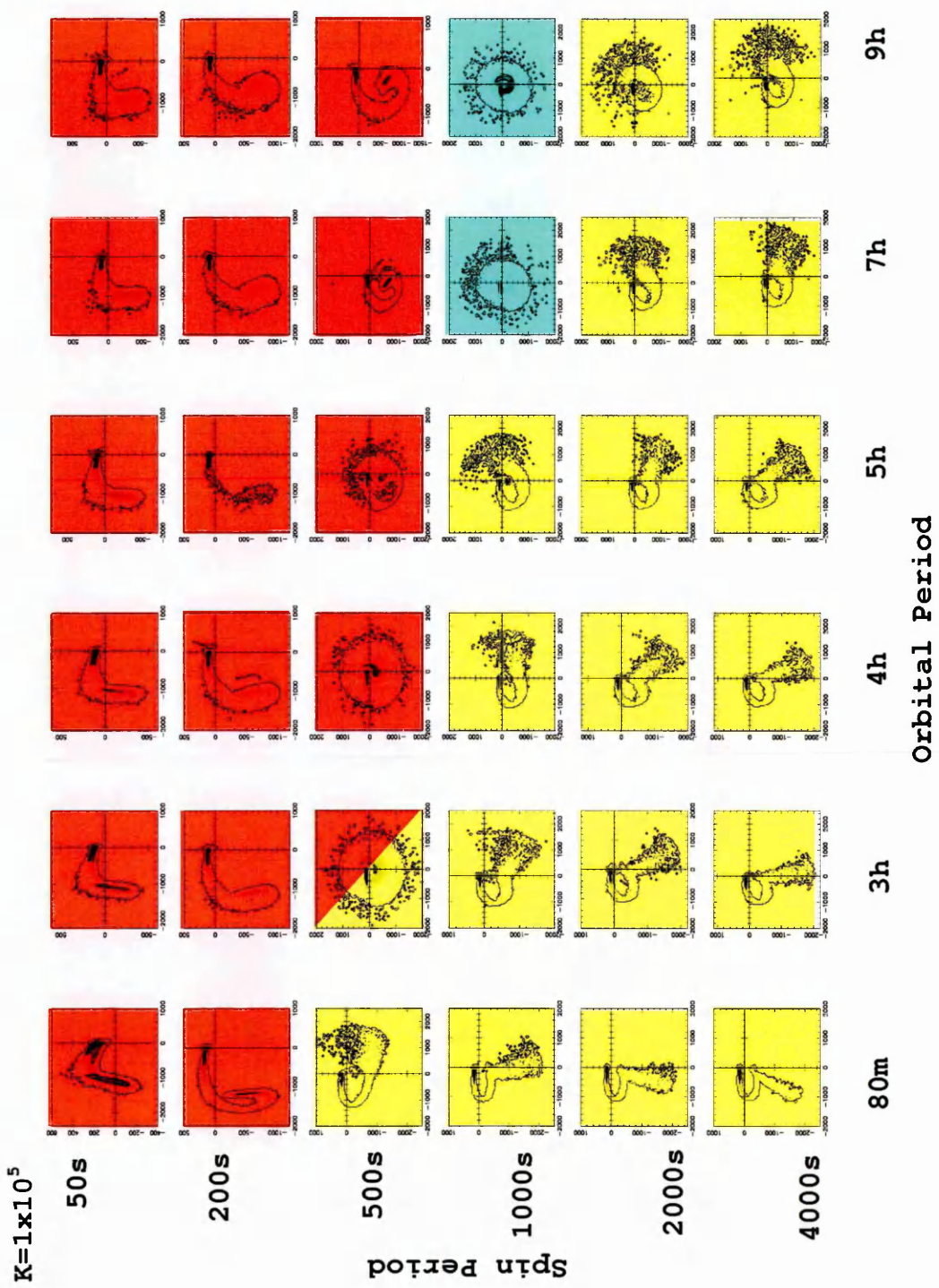
K=1x10^5
Spin Period
50s
200s
500s
1000s
2000s
4000s
Orbital Period
80m
3h
4h
5h
7h
9h

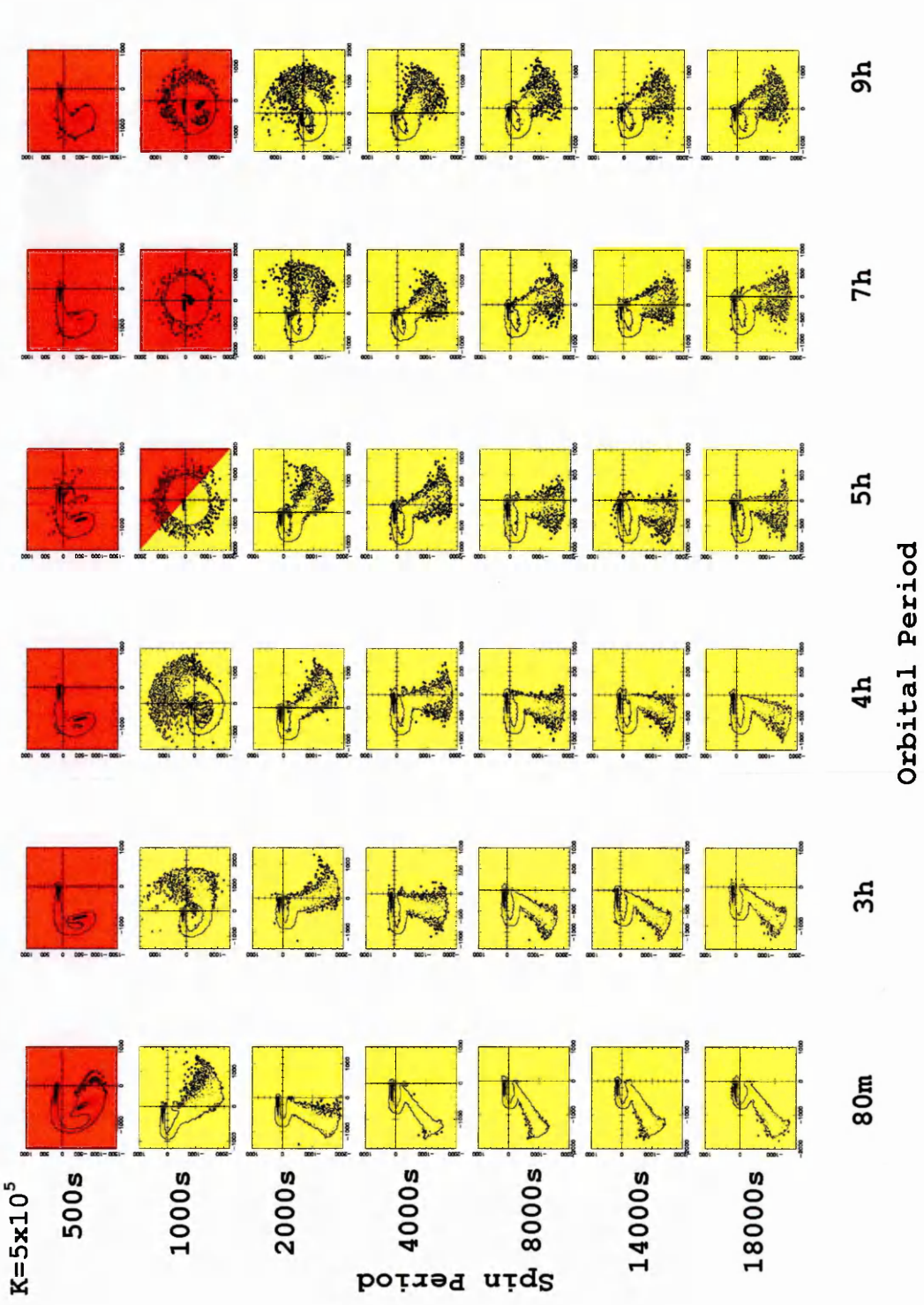
K=5x10^5
500s
1000s
2000s
4000s
8000s
14000s
18000s
Spin Period
80m
3h
4h
5h
7h
9h
Orbital Period

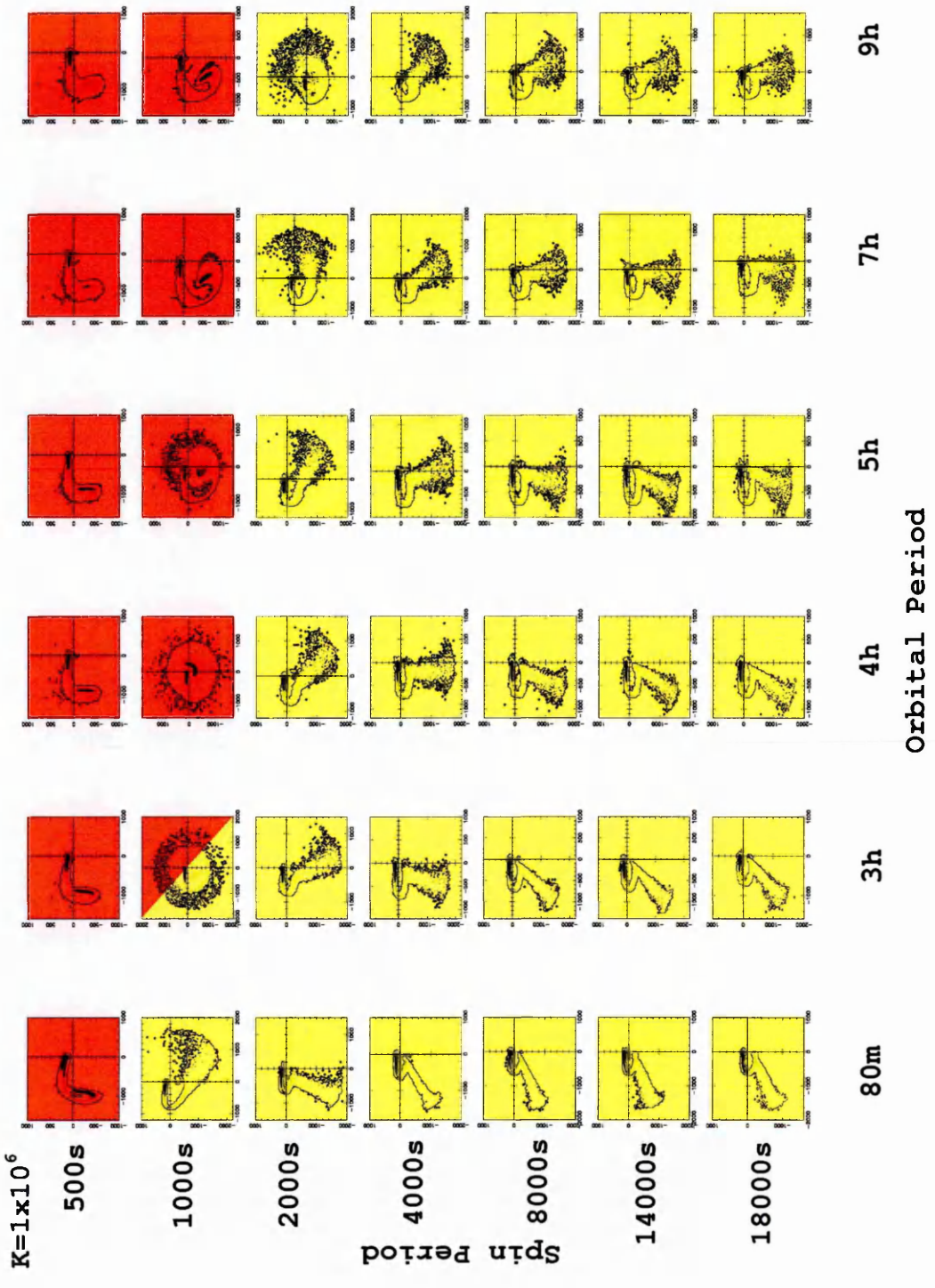
K=1x10^6
500s
1000s
2000s
4000s
8000s
14000s
18000s
Spin Period
80m
3h
4h
5h
7h
9h
Orbital Period

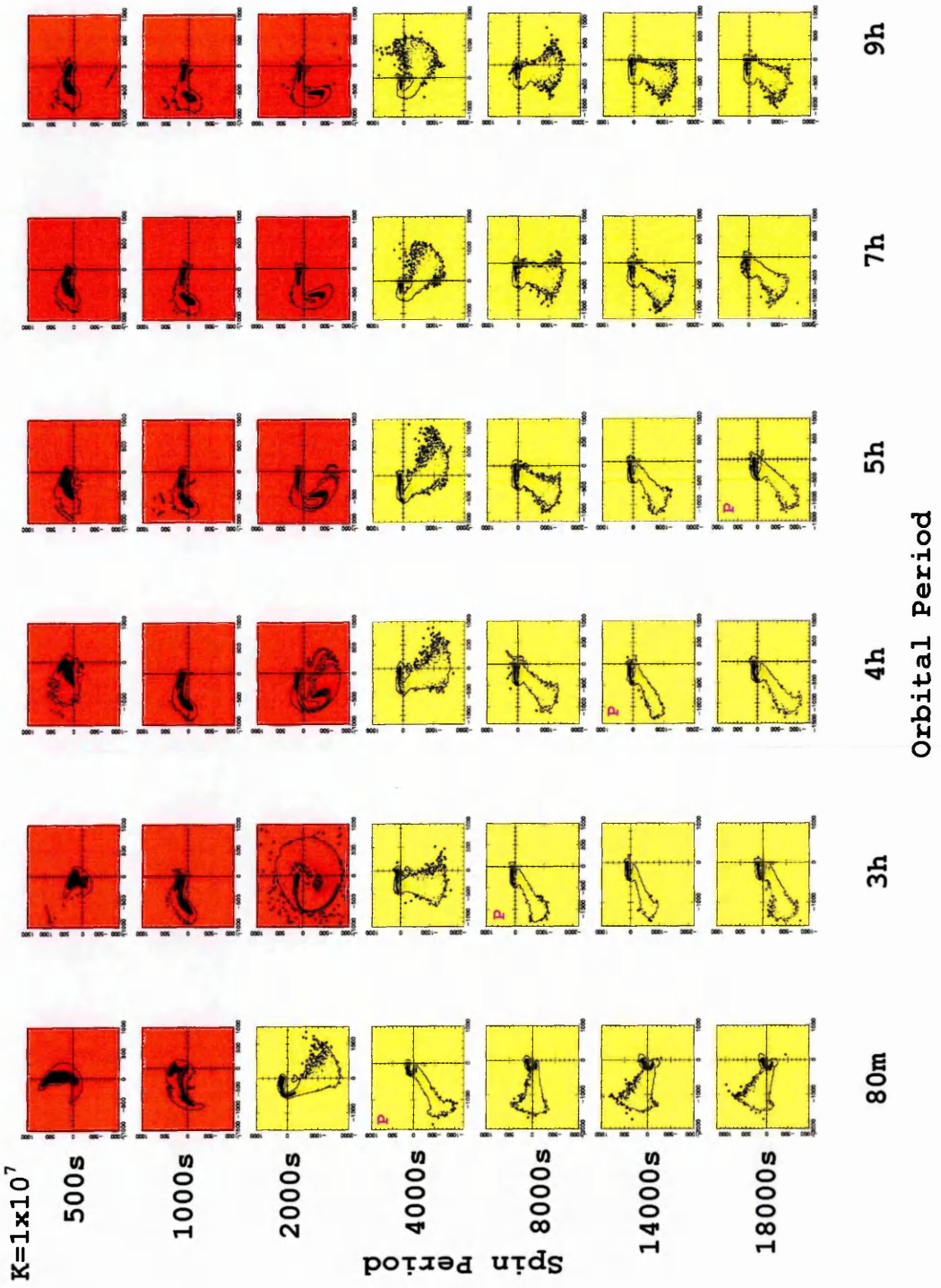
K=1x10^7
500s
1000s
2000s
4000s
8000s
14000s
18000s
Spin Period
80m
3h
4h
5h
7h
9h
Orbital Period

5.5.1 Discussion of the Doppler Tomograms for the n^6 model

- k_o=1×10^2

At k_o=1×10^2 we see that in this slice of parameter space all the accretion flows are disk fed accretion. At P_{spin}=50s for all orbital periods and at P_{orb}=9h for all spin periods we see that the disk systems are much more diffuse in the Roche lobe as we get two rings in the tomograms. One at high velocity which corresponds to the material circling close to the WD, the other at very low velocity corresponding to material circling further out in the Roche lobe. For P_{spin}=50s this small inner ring is a lot denser than the ones at longer orbital periods. If we compare these tomograms to their flows we can see that there is a disk feature formed, but it is a fairly weak one with the blobs very scattered in the Roche lobe, the majority circling at the outer edge at low velocity. At P_{orb}=9h we see that as the spin period of the WD gets longer more material interacts with the magnetic field and is forced to rotate closer to the WD. We see this in the tomogram as the inner ring gets less dense and starts to break up.

All the other systems except the ones at $P_{spin} \gtrsim$500s for P_{orb}=80m show a concentrated disk structure. We see a small emission region from the L_1 point and a ring circling at high velocity hence the magnetosphere is large, attracting the material as soon as it leave the L_1 point forcing it to go straight into a disk.

At $P_{spin} \gtrsim$500s for P_{orb}=80m we see the centre of the ring breaking up, a hole in the middle and a stream moving out from the emission at the L_1 point starting to curl round and join the big outer ring. This shows that the flow is becoming more stream like, travelling a fair distance before it starts to circulate the WD. In these systems we do not see a concentrated disk but a long stream that goes round the WD and produces a scattered disk at high velocity.

- k_o=5×10^2

Increasing the magnetic field strength increases the variety of accretion mechanisms and we now see, propeller, stream and disk systems. We see that the propeller trajectories are almost all at $\gtrsim$90° as they travel round the WD and are expelled away. We see this in the tomogram by the 'hook' shape it produces. This comprises dense emission from the L_1 point, a loop at high velocity where the magnetic field interacts with the blobs and the loop changing direction and coming back on itself at small V_x and V_y decreasing towards zero for the material expelled from the binary system. As the orbital period increases the blobs that are expelled must start following similar paths as we start getting a denser region at the end of the loop at low velocity. At $P_{\rm orb}$=7h and 9h not only do we see this second denser region but we now see a lot of low density material around the centre as well. By 9h it is a medium velocity ring, meaning we also have a large number of scattered blobs staying in the Roche lobe beginning to form a disk in the outer region. A lot of the material being propelled seems to disperse and move back towards the Roche lobe forming a diffuse disk around the edge.

For the disk system we see the same characteristics as before, namely a high velocity ring around all the features in the tomograms from the material circling close to the WD, an inner dense ring at low velocity for the diffuse disks and the small emission region from near the L_1 point.

The stream systems show one just developing from a disk at $P_{\rm spin}$=200s, $P_{\rm orb}$=80m. Hence we still see a ring structure in the tomogram spreading out from low to high velocity but the stream feature is also seen as a curl starting to form from the emission at the L_1 point. Increasing the spin period we see the curl in the tomograms is a lot more defined, curling less anticlockwise into the upper quadrants as the stream itself

curls less round the WD.

- k_o=1×10^3

  This section of parameter space is almost identical to the previous one. The propeller trajectories are close to 90° but seem to expel more material than before as the edge of the loop in the tomogram is much wider with no dense region, so more material is scattered in various directions and at slightly larger -V_x velocities than the previous. The disk systems show the same features of high ring velocity, low ring velocity and emission from the L_1 point depending on how well formed the disk is. We also see at $P_{\rm spin}$ of 200s, $P_{\rm orb}$=80m and $P_{\rm spin}$ $\gtrsim$1000s at $P_{\rm orb}$=3h stream to disk evolution beginning as we see the curls of the stream in the tomograms starting to form into the existing disk structure. In the corresponding accretion flows we see a more stream-like flow with a small disk forming around the WD. One interesting feature that needs to be pointed out is that in the tomogram at $P_{\rm spin}$=200s at $P_{\rm orb}$=5h we suddenly go from a small ring feature forming in the middle at low velocity with a high velocity ring around it to a very dense ring in the middle with a slower velocity ring around it. At longer orbital periods, this then reverts back to the original form of an even denser ring at the centre and high velocity ring on the outside, and yet the accretion disks all look very similar in the simulated flows. Why there is a sudden decrease in the velocity of the outer ring, returning to a large velocity after, is very strange.

  The streams are similar to before, but impacting the WD further back round towards the secondary in the flow as the curls in the tomograms have moved further down in the upper-right quadrant.

- k_o=5×10^3

  In this slice of parameter space we see a greater number of conditions suitable for

propeller and stream fed accretion than for disk and we see more disks starting to evolve into streams.

The propeller trajectories span a much larger range for the angle in which the material is expelled, ranging from ~30° to $\gtrsim$ 90°. We see the 'hook' feature in most of them as it loops round from the high velocity magnetically controlled region to the lower velocity region expelled out of the binary. As the angle is increased for $P_{\rm spin}$=50s we see the loop at the end getting larger as it decreases in the -V_x direction. This indicates the material is getting expelled sooner and becoming very scattered to give such a large low density region slowly approaching zero in the -V_y direction. At $P_{\rm spin}$=200s, $P_{\rm orb}$=3h we see a disk system being formed as well as a propeller. We get a mid velocity ring of material, indicating that not all the material is expelled. A lot of material is captured staying in the Roche lobe, circulating in a weak disk, as seen in the corresponding simulated accretion flow. At $P_{\rm spin}$=200s, $P_{\rm orb}$ $\gtrsim$4h we see a more defined hook feature as all these propellers have trajectories $\gtrsim$90°. There is an interesting feature at $P_{\rm spin}$=200s, $P_{\rm orb}$=5h where we see just the outline of a 'hook' feature. We have the stream, loop and curl round of the tail and we clearly see a strong propeller system in the simulation of the flow. The only explanation being that at these particular parameters the flow is very scattered throughout.

For the disk system we see the same characteristics as before corresponding to concentrated and diffuse disks, (see section k_o=1×10^2 for full explanation).

The stream systems also give similar patterns curling round further into the upper quadrants the further they go round the WD, forming a ring back with the original stream as it travels almost round the WD. As the spin period increases at constant orbital period we see the tail move further down from the upper-quadrant to the lower-quadrant and the stream moving less round the WD. As the orbital period

increases at constant spin we see the tail move further up and curl round, eventually into a ring as the stream curls round the WD almost forming a disk close to the WD.

- k_o=1×10^4

The pattern at k_o=1×10^4 for the accretion mechanisms is extremely similar to k_o=5×10^3. We have the same number of propeller systems showing similar features, a decreased number of disk systems to just 10, two of which show signs of becoming streams, so stream fed accretion is the dominant flow in this slice of parameter space.

The propellers have a large angular trajectory range from ~20° to ~ 90°, they show the 'hook' like feature with the end getting larger as the orbital period increases at $P_{\rm spin}$=50s, indicating the material is expelled sooner from the system. We see the one at $P_{\rm spin}$=200s, $P_{\rm orb}$=3h has become a much more defined propeller system as the 'hook feature now appears in the tomogram where before we saw it just barely coming through and a lot of material still within the Roche lobe. The outline 'hook' feature at $P_{\rm spin}$=200s, $P_{\rm orb}$=5h is still present, but again when we look at the simulated accretion flow there appears to be no reason for causing this feature to look the way it does (see previous section for further particulars on the other propeller systems).

The disks show both concentrated and diffuse systems, with high velocity rings in them all, with some showing low velocity dense emission rings at the centre for the weaker systems. We can also just see the stream fed features in the two tomograms at $P_{\rm spin}$=2000s and 4000s at $P_{\rm orb}$=7h. The curl from the stream is quite clearly forming a ring as the material circulates the WD (see section k_o=1×10^2 for full details of the disk tomogram features).

The streams show the typical characteristics we have seen before. The position of the tail relating to the position of the stream onto the WD. The further round the tail is from the lower-left quadrant the further round the WD the stream travels before

it impacts (see the previous section for further details of stream tomograms).

- k_o=2×10^4

  At k_o=2×10^4 stream fed accretors are still the dominant flow, followed by propellers and disk systems. We also have a system that is undefined at $P_{\rm spin}$=200s, $P_{\rm orb}$=80m. In its tomogram it looks like a clear well defined disk accretor but in the simulated flow it quite clearly shows a propeller system with a lot of scattered material. However this would be from a low velocity ring and so produce a ring near the centre of the tomogram and not at high velocities.

  The propellers trajectory increases from ~10° to just greater than 90° and the same features are seen in the tomograms including an outline of the 'hook' feature at $P_{\rm spin}$=200s, $P_{\rm orb}$=5h but getting slightly denser than before (see section k_o=5×10^3 for details of the propeller tomograms).

  The disk systems show a couple with strong disk accretion, the ones at longer orbital periods however show a reduced velocity in the outer ring even though they appear close to the WD. We see diffuse disk systems indicated by the dense region in the centre of the fairly high velocity ring structures (see section k_o=1×10^2 for explanation of disk tomograms further).

  The streams show characteristic features of a curl from the L_1 point that loops round depending on how far the stream travels around the WD ending in a tail of scattered material (see section k_o=1×10^4 for a more detailed analysis on the stream tomograms).

- k_o=5×10^4

  We have just four disk systems left at this magnetic field strength. The combination of $P_{\rm spin}$ and $P_{\rm orb}$ that was undefined before is now a clear propeller system. One of

the weak disks has become a propeller, one a stream fed accretor and one close to changing, making stream fed accretion still very dominant.

All three types of flow show characteristics previously seen. In propellers, the greater the trajectory angle, the greater the curl of the 'hook' feature and the larger the end is, the more material is scattered out of the binary and the sooner. The disk systems show very diffuse disks that are mostly dense at the outer edges at slower velocities. The streams have the loop region with a long tail that spreads out, the impact site determining how far the feature curls round. Increasing the spin period brings the impact site towards the secondary, increasing the orbital period moves the impact site away from the secondary further round the WD until a slight disk is created (see section k_o=5×10^3 for more details on propellers, section k_o=1×10^2 for disks and section k_o=1×10^4 for the streams).

- k_o=1×10^5

At a magnetic field strength this strong, the flows are evenly split between propeller accretion at fast spin rates $\lesssim$500s and stream fed accretors at slower spin rates $\gtrsim$500s. Two very weak disk systems are also present still able to just form at this high k_o value.

For the propeller systems, we see their trajectories starting to almost move out of the Roche lobe of the WD but also still round to ~95°. A new feature appears in the propellers whose trajectories are a fair distance past the WD. Instead of curling round, we start seeing a denser blob region moving from the upper-left quadrant to the lower-left quadrant which means part of the magnetically controlled region must be collimated as well as scattered to get both a dense and low density region at those velocities together. In the other systems we see similar features to before with a 'hook' like feature developing. As the expelled material is scattered more and

sooner we see the 'hook' expand and get larger at the end. The greater the angular trajectory the more of a curl we see. At $P_{\rm spin}$=200s, $P_{\rm orb}$=5h we still get the very broken up feature of the same shape but no obvious explanation in the accretion flow as to why. We see weak propeller systems at $P_{\rm spin}$=500s as we see the large ring forming in the tomograms at high velocity much the same as we see in disk tomograms indicating material must also be circulating the WD at an inner disk close to the WD. The accretion flows clearly still show material being ejected away but also a lot staying within the Roche lobe of the WD.

The last two disk systems show both concentrated and diffuse disks. At $P_{\rm spin}$=1000s, $P_{\rm orb}$=7h we see the small dense feature from the L_1 point and a ring at fairly high velocities indicating a disk at fairly high velocity round the WD. At $P_{\rm orb}$=9h we see a small very dense ring at the centre which means there must be a lot of blobs at low velocity circulating at larger distances from the WD, near the edge of the Roche lobe with a few a little closer in giving us the ring at medium velocity.

The stream systems typically follow the same characteristics as they have been following previously. As before, the positioning of the scattered tail in the tomogram quadrant relates to the position of the impact onto the WD in the accretion flows (see sections k_o=5×10^3 and k_o=1×10^4 for a more detailed analysis of the tomograms for the propellers and streams respectively).

- k_o=5×10^5

As we increase the magnetic field strength and look at longer spin periods we see no disk systems exist with these combinations. Stream fed accretion is dominant but several combinations produce propeller accretion.

The propeller trajectories have an angle of expulsion of material from ~30° to ~ 95°. They show the typical hook feature that depends on the scatter of material and how

soon it is ejected. We also have weak propellers at $P_{\rm spin}$=1000s for $P_{\rm orb}$=3h and 7h where the ejected material is very disperse near the edge of the Roche lobe so it gets captured and circulates giving a ring of material at medium velocity in the tomograms.

With the greater dominance of stream accretion it becomes clearer in the tomograms how they are related to the accretion flow. We see clearly how the straight tail part curls further and further round anticlockwise from the lower-left quadrant round to the upper-right quadrant as the orbital period increases and that increasing the spin period causes the opposite to happen. In addition, the straight tail moves clockwise back round to the lower-left quadrant indicating the position of the accretion stream on to the WD (see section k_o=5×10^3 and k_o=1×10^4 for a more detailed description of the propeller and stream tomograms respectively).

- k_o=1×10^6

  Apart from the addition of two propeller systems at $P_{\rm spin}$=1000s this section of parameter space at the high k_o value of 1×10^6 is almost identical to that of k_o=5×10^5.

- k_o=1 × 10^7

  At the highest k_o value considered, we see a great increase in propeller systems whose trajectories travel at -90° out of the binary system. At this high k_o value we also see polars exhibiting stream accretion.

  The propeller trajectories start by being expelled sideways out of the binary system and as the orbital period increases the flow moves back towards the Roche lobe of the WD. The ejection at -90° is the first time we have seen this particular trajectory and is shown in the tomograms by a very dense region that is vertically upward in the +V$_y$ direction. The amount of low density material around this region depends

on how scattered the material is further down the trajectory and how soon it is expelled. As the trajectory moves further round towards the WD Roche lobe, the vertical emission region curls further round anticlockwise in the upper-left quadrant and then also into the lower-left.

At P_{spin}=2000s, P_{orb}=3h we see a very long dense emission region embedded in a large low density region. The propeller flows must be highly collimated to greater distances for the emission to be so far round. We also see a large amount of scattered material in the outer edge of the Roche lobe curling round so we see a disk type feature in the tomogram.

The stream systems clearly show the behaviour discussed in the section for k_o=5×10^5.

5.5.2 Overall Conclusions

For the n^6 tomograms, like the n^3 version, we see many interesting features with a large diversity among each of the accretion mechanisms of propeller, stream and disk. There are however some subtle differences.

For the propeller tomograms at a large trajectory angle and weak magnetic field strength we see the 'hook' feature. We see dense emission from the L_1 point surrounded by lower density material looping round as the blobs in the flow interact with the magnetic field. It then finally loops back on itself at low velocity. However in this n^6 model, hardly any of the 'hook' features show a second dense emission region. The material is ejected early on from the binary and in numerous directions so we see this curl in the tomograms very large and wide and consisting of only low density blobs. As the trajectory of the flow decreases in angle we see the 'hook' feature becoming shorter and no longer a hook shape. The blobs are ejected much sooner and dispersed quicker so we don't see the long loop that we have been seeing from the interaction of the magnetic field with the blobs. This

is due to the n^6 model scalling as proportional to $1/r^6$ which means the magnetic field has less influence on material at large distances from the WD. At negative angles, the feature is shorter still with just a slight bend from the upper-left quadrant into the lower-left one. Towards the very high magnetic field strength we start seeing the trajectory flow at -90° and as before we see a very dense vertical emission structure in the tomograms. Only in a very few do we also see the transition to disk and see the high velocity ring forming round the dense regions in the centre as the dispersed material is trapped in the Roche lobe of the WD and forced to rotate. One other interesting feature is the one in which we see just the outline of the hook. This is quite dense but very broken up within the feature, but we can think of no reasonable explanation as to why such a feature should come about. Figure 5.8 depicts these flow and tomogram scenarios. We have the 'hook' feature at high angle trajectories, the shorter feature as the angle decreases, the slight bend for negative angle trajectories, again the vertical emission from a -90° trajectory and finally the broken up 'hook' feature.

The first propeller flow in figure 5.8 is seen at a low magnetic field strength of k_o=5×10^2 at very fast spin periods of 50s at all the orbital period parameters. As the magnetic field strength increases to k_o=5×10^3 these flows are seen at slower spin periods of $P_{\rm spin}$=200s for orbital periods of 3h and longer. The previous spin/orbit combinations at a 50s spin period now give the second type of propeller accretion flow, with the material moving at an angle of $\sim$ 45° out of the system. By k_o=2×10^4 this propeller flow in turn moves to the next as depicted in figure 5.8, at $P_{\rm spin}$=50s, $P_{\rm orb}$=80m. The first type of propeller accretion also forms at slower $P_{\rm spin}$ values of 500s at this magnetic field strength. Stronger field strength at k_o=5×10^5 sees propeller accretion now forming at $P_{\rm spin}$=1000s at the longer orbital periods. Only at k_o=1×10^7 do we see the final propeller flow of -90° out of the system at $P_{\rm spin}$=500s for the two shortest orbital periods of 80m and 3h. At this field

strength propeller accretion also now forms at $P_{\rm spin}$=2000s for orbital periods of $\geq$ 3h along with the propeller flows at $P_{\rm spin}$=500s and 1000s for all the orbital periods. By this strength we only see the last two propeller scenarios.

For the disk accretion we see both diffuse and concentrated disks, with the same features as we saw for the n^3 model. For the diffuse disk we see a large velocity ring circling a very dense low velocity ring in the tomograms, inside-out to that of the accretion geometry where we get the material at high velocity circling close to the WD and that at slower velocity circling further out. In the concentrated disk case, we see again in the tomogram a large velocity ring from material close to the WD but we only see one small emission region in the centre corresponding to the material leaving the L_1 point, due to the large magnetosphere capturing material early on. Both of these disk features are presented in Figure 5.8.

At k_o=1×10^2 we see the diffuse disk accretion only at $P_{\rm spin}$=50s for orbital periods of $\geq$ 4h. For all the other spin/orbital parameter combinations we see the more concentrated disk scenario. As the magnetic field strength is increased the diffuse disk that was at $P_{\rm spin}$=50s makes way for propeller accretion with diffuse disks now at $P_{\rm spin}$=200s for the whole orbital period range. The more concentrated disks are seen at spin periods of 500s and slower at orbital periods of 4h and greater. At k_o=5×10^3 most of the disks are diffuse with the exception of two that are more concentrated at $P_{\rm spin}$=1000s, $P_{\rm orb}$=7h and 9h. The disks are now only seen for spin periods greater than 500s and orbital periods greater than 4h. Stronger field strength makes way for stream fed accretion where the disks once were, with disk accretion forming at increasingly longer orbital periods of 7h and 9h for spin periods of 500s and slower. Increasing the magnetic field strength yet further we see the diffuse disk now turning to propeller flow at $P_{\rm spin}$=500s, with disks at the slowest spin periods existing at 9h orbital periods. By k_o=1×10^5 only two disks remain with

the others at $P_{\rm spin}$=500s turning to propeller accretion and those at slower spin periods becoming streams.

In the tomograms for the stream, the determining factor is not necessarily which direction the flow moves out of the L_1 point, but where it impacts the WD and the trajectory it takes in the Roche lobe. The same features exist as in the n^3 case, dense emission from the L_1 point, the stream interaction with the magnetic field curling round in the tomogram and the ballistic trajectory, with the scattered end to the curl. When interpreting the tomograms for the n^6 model we use the same three criteria as in the n^3 case as stated in the overall conclusions in section 5.4 and depict these situations in Figure 5.8.

Stream accretion occurs first at k_o=5×10^2 at spin periods of 200s and slower only for an orbital period of 80m. It is the last of the four stream scenarios shown that we see existing at longer orbital periods for spin periods of 200s and slower as the magnetic field strength gets stronger. By k_o=5×10^4 stream accretion is seen at spin periods of 500s and slower for all the orbital period parameters. At still stronger k, stream accretion is seen at 1000s spin periods and slower, still at all the orbital period parameters. Only at the strongest magnetic field strength of k_o=1×10^7 do we see the accretion stream move in a fairly straight line from the L_1 point to the WD, at $P_{\rm spin}$=8000s, 14000s and 18000s at an orbital period of 80m. The third stream accretion scenario we see only once at the same magnetic field strength, at $P_{\rm spin}$=200s for $P_{\rm orb}$=80m.

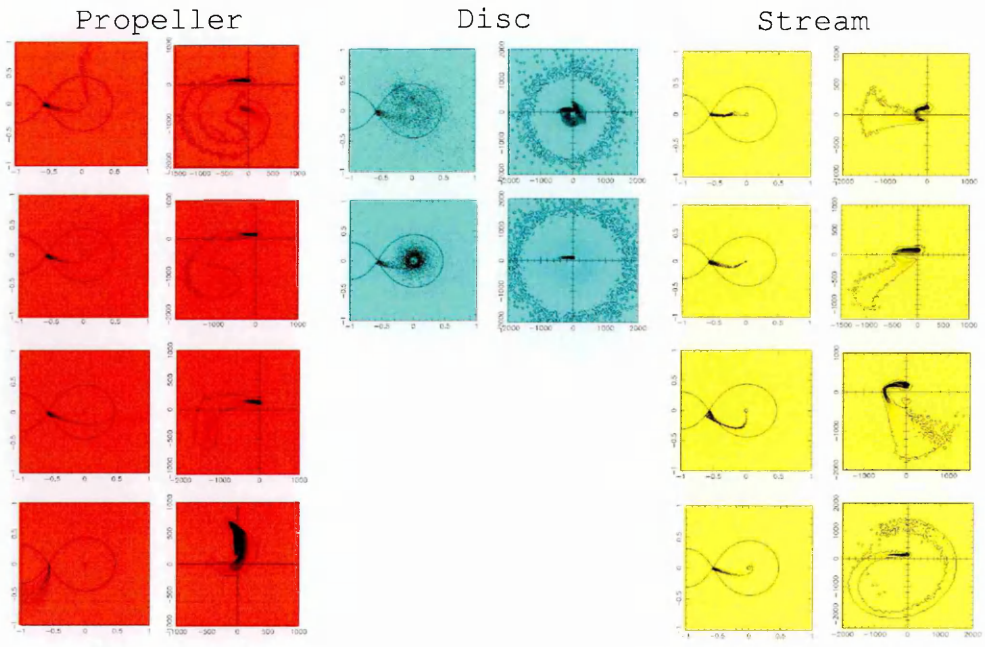

Figure 5.8: Overall result features from the n^6 field tomograms. Each pair of panels shows the simulated flow on the left and its corresponding tomogram on the right.

5.6 Equilibrium Tomograms

In chapter 4 section 4.4 we investigated the situation of simulated accretion flows for systems in equilibrium. In this section we present the corresponding tomograms which these accretion systems produce. Figure 5.9 shows the tomograms relating to the n^3 model, while Figure 5.10 shows the tomograms for the n^6 model.

Figure 5.9: Tomograms for the simulated equilibrium accretion flows for the n^3 model presented in chapter 4. Blue tomograms indicate disk accretion, red indicate weak propeller accretion, yellow for stream accretion and green for ring accretion.

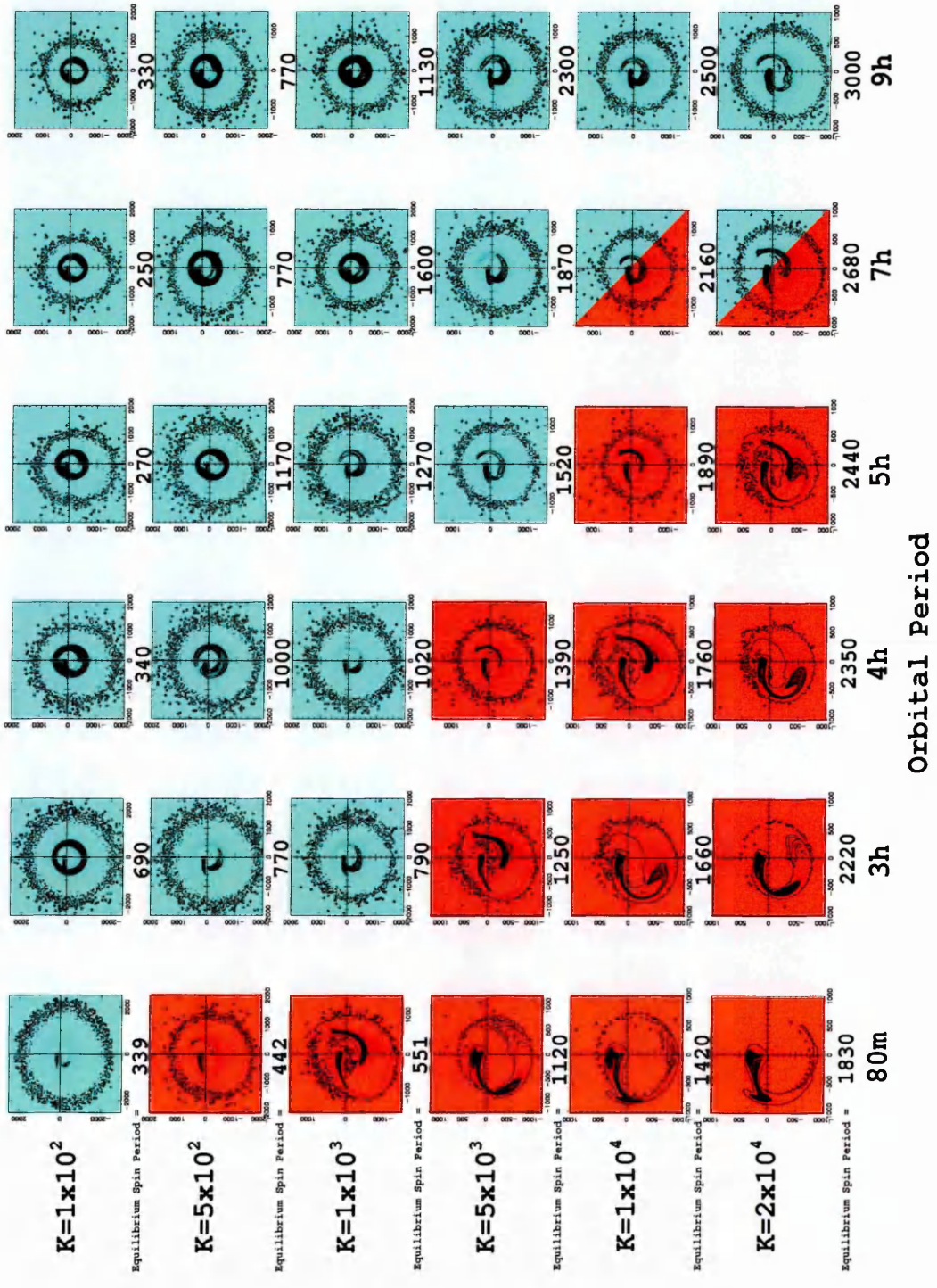

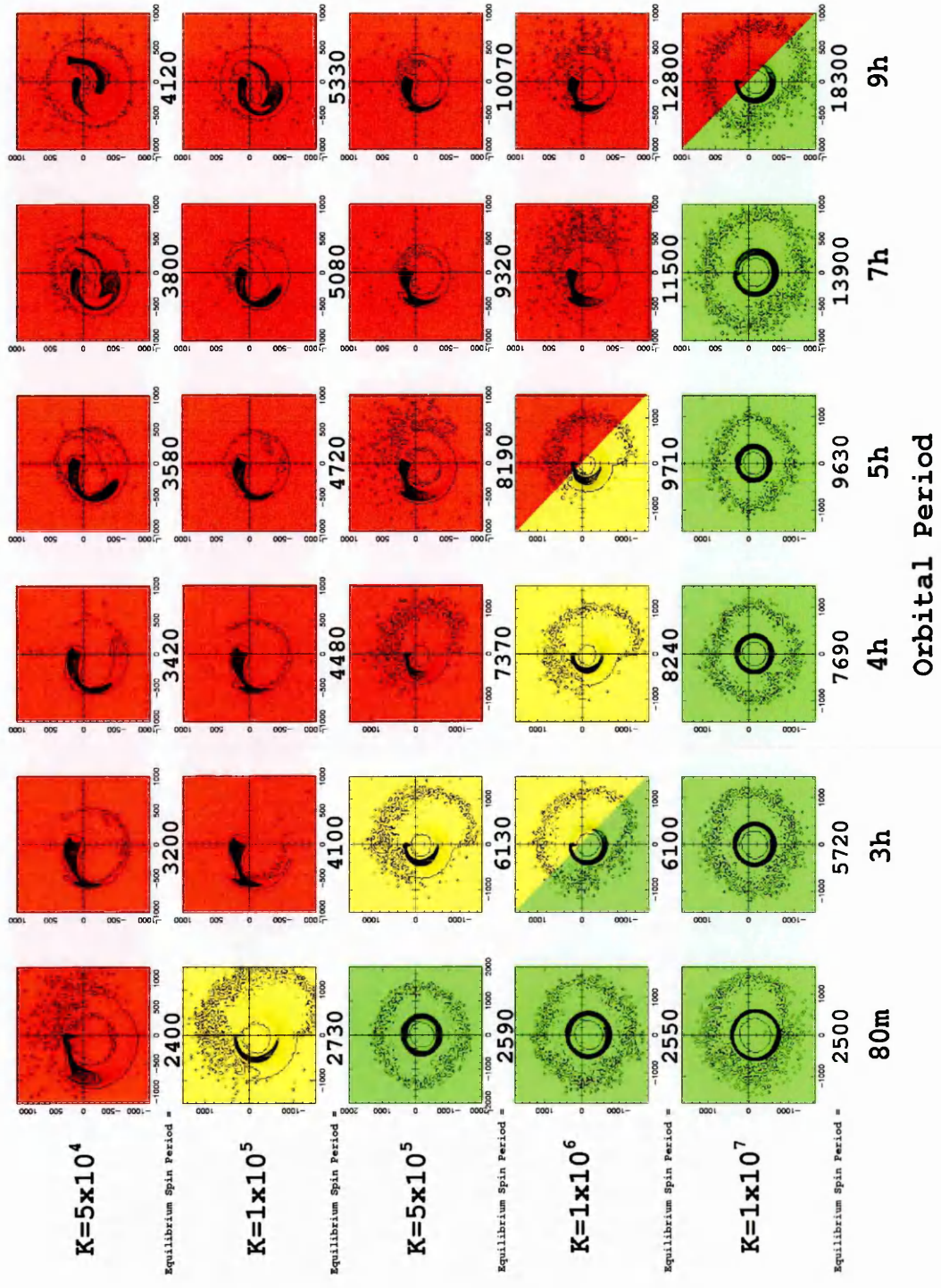
K=5x10^4
K=1x10^5
K=5x10^5
K=1x10^6
K=1x10^7
Equilibrium Spin Period =
2400
2730
2590
2550
2500
3200
4100
6130
6100
5720
3420
4480
7370
8240
7690
3580
4720
8190
9710
9630
3800
5080
9320
11500
13900
4120
5330
10070
12800
18300
80m
3h
4h
5h
7h
9h
Orbital Period

Figure 5.10: Tomograms for the simulated equilibrium accretion flows for the n^6 model presented in chapter 4. Blue tomograms indicate disk accretion and yellow indicate stream accretion.

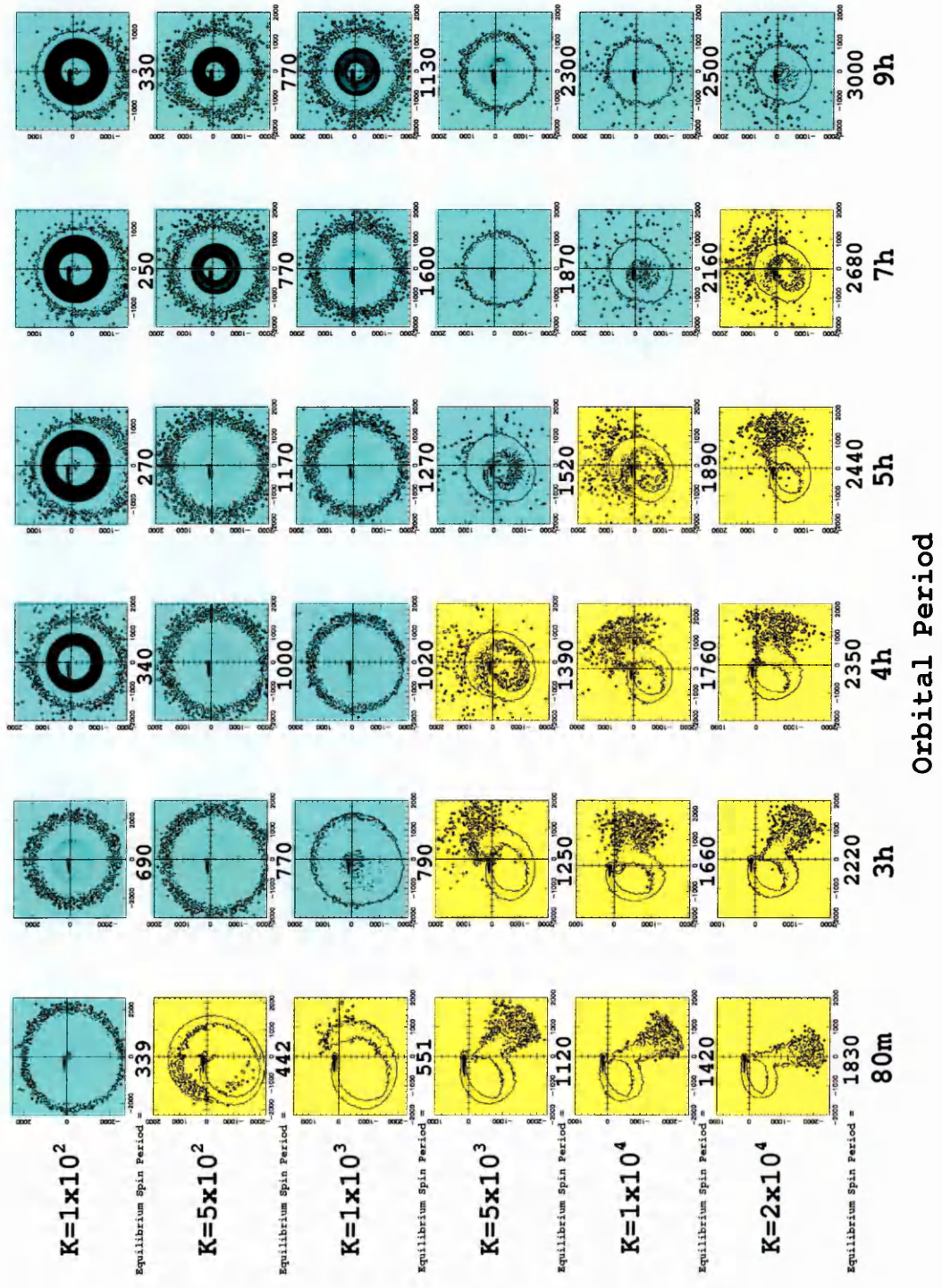

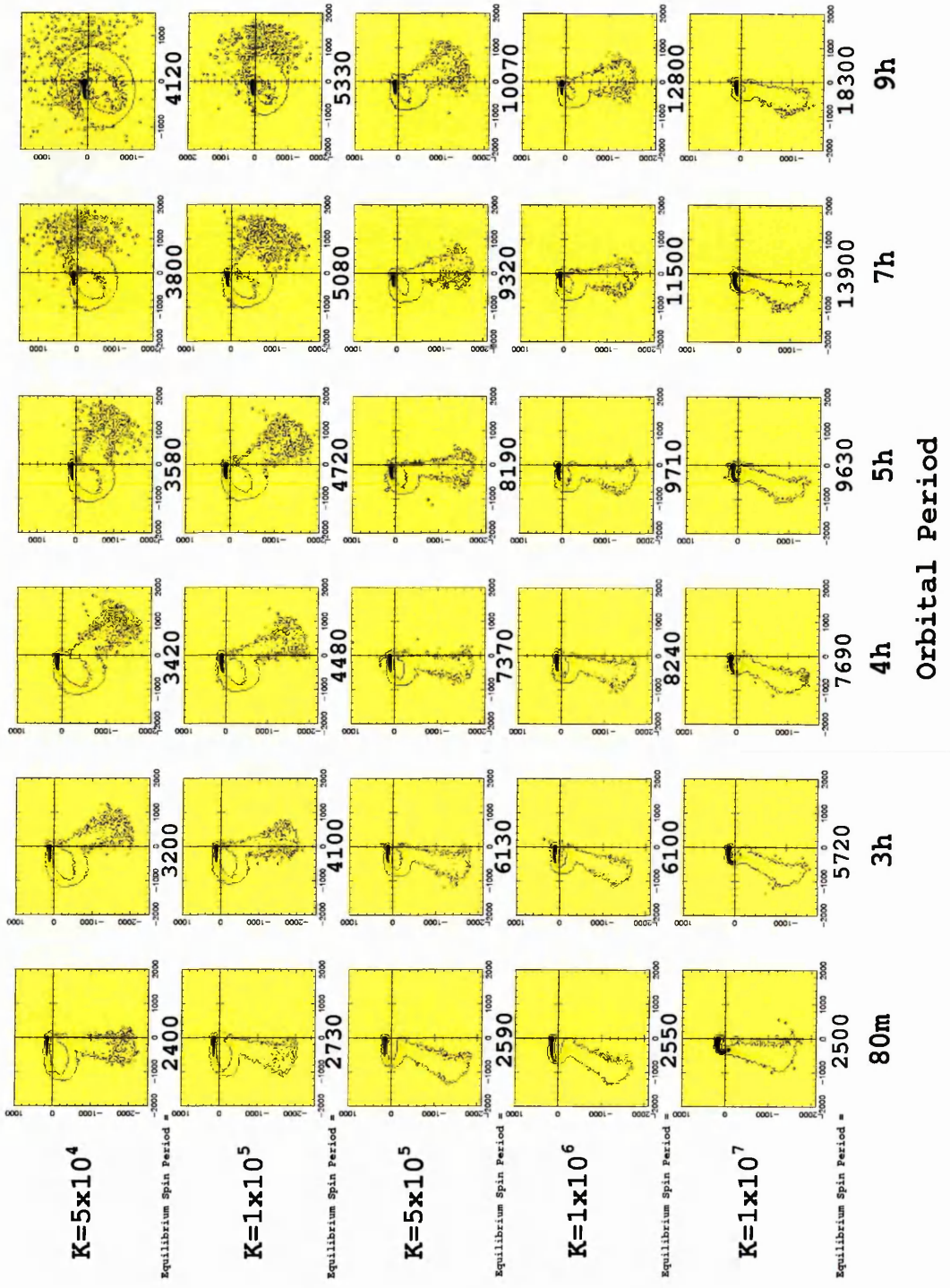
K=5x10^4
K=1x10^5
K=5x10^5
K=1x10^6
K=1x10^7
Equilibrium Spin Period =
80m
3h
4h
5h
7h
9h
Orbital Period

5.6.1 Discussion of equilibrium tomograms for the n^3 model

For the equilibrium situation we see disk accretion changing to weak propeller accretion, which in turn develops in to stream accretion and then finally to ring accretion as the magnetic field strength is increased. The corresponding tomograms to these systems depict some interesting features.

In the previous general tomograms we saw two types of disk systems, diffuse and concentrated, we see the same scenario here in the equilibrium flows but with a slight difference. In half of the tomogram disk systems we see a very dense thick ring feature in the centre at low velocity, surrounded by lower density emission at higher velocity. In the corresponding flows we see a highly collimated, concentrated disk at large distances from the WD at low velocity, with dispersed material around the inner edge of the disk closer to the WD thus moving with a higher velocity. As the collimated disk starts to disperse so too does the dense inner ring in the tomogram, and we see a diffuse disk forming. There are still many dispersed blobs at small radii so we still see a high velocity ring around the centre emission region in the tomograms.

If we move to the most widespread accretion mechanism, the weak propellers, we see in all of them a very dense region from the L_1 point. In some we see just this region, appearing very dense and long curling anticlockwise into the lower-left quadrant, corresponding to a very long collimated flow in the accretion. In others we see two dense regions, one from the L_1 point, the other from the ejected material moving at low velocity. In most of these systems we also see a large amount of low density material surrounding both these dense emission regions, curling round anticlockwise from the position of the L_1 point right round and back on themselves. In the simulated propeller accretion flows we see very dispersed flows, some of this dispersed material must stray close to the magnetosphere of the WD, where it is captured and then forced into rotation round it. The only way we can see such

low density material circling round and forming a ring in the tomograms is if this situation is true. Even in the tomograms that do not posses a complete ring, we still see small blobs closing the gap between the ends of the loop to form the ring, so material must still also be circling the WD in these situations.

For the simulated stream fed accretors we see that all of them have a highly dispersed flow that both accretes onto the WD and is dispersed outside the Roche lobe as well. The geometry of this flow is clearly depicted in the corresponding tomograms. We see a long curled dense emission region from the L_1 point, the collimated stream from the L_1 point in the flows. Lower density material surrounds this region and then curls further, anticlockwise in the lower-left quadrant, the ballistic stream in the flow. This curl then opens out and gets thicker in the lower-right quadrant. The whole flow is now very dispersed moving both onto the WD and away from the binary system. The curl continues into the upper-right quadrant at lower velocity finally merging back round to the original emission at the L_1 point at an even slower velocity so forming a ring in the tomograms. In the flows we see that the dispersed material does in fact move round the whole Roche lobe inside and out giving the ring feature at different velocities in the tomogram.

Finally we also see ring accretion forming at equilibrium and again we see a very dense ring at low velocities in the tomogram, with lower density material circling the inside of this ring as well as large amounts circling at high velocities around the outside. In the accretion flow we see clearly the strong collimated ring structure around the outside of the Roche lobe, so moving at very slow velocity but we also see material dispersed into the Roche lobe towards the WD. Hence we also get many blobs circling close to the WD at high velocity thus explaining the high velocity ring of material.

5.6.2 Discussion of equilibrium tomograms for the n^6 model

In the equilibrium parameter space for the n^6 model we see that only disk and stream fed accretion arises. In the disk accretors we see both diffuse and very concentrated disks, both depicted clearly in the tomograms. In the very concentrated disks we see a highly dense thick ring structure at fairly high velocity and see the collimated stream from the L_1 point joining the disk. These thick dense rings are also surrounded by lower density material in a ring at higher velocity. If we look at the simulated accretion flows we see a very concentrated disk circling close to the WD hence the ring in the tomogram at fairly high velocity. We also see the concentrated stream from the L_1 point joining the disk. For the more diffuse disk in the simulated flows, we see material spreading out through the Roche lobe and the stream from the L_1 point becoming more dispersed as it enters the Roche lobe. Hence in the tomograms we still see a high velocity ring as this is where the disk was most concentrated but at a much lower density and we see a low density region moving from around the centre out to this ring. We still see the dense emission from the L_1 point as it is still collimated before it enters the Roche lobe. Where this dense region ceases is where the stream starts to disperse into the material in the outer region of the disk at lower density, hence merging with it in the tomogram.

As we increase the magnetic field strength we see that more of the disk accretion systems become stream accretors. With such a large number of stream systems it is easy to see the effect in the tomograms of increasing the magnetic field strength and the orbital period for the spin period equilibrium values. Like the stream scenarios in the two previous models from non-equilibrium systems, the same criteria can be applied in interpreting these systems. For stream tomograms we see dense emission from the L_1 point, the stream interaction with the magnetic field curling round in the tomogram and the ballistic trajectory, with the scattered end to the curl. As before, three main features

exist with interpreting the stream tomograms: 1) The further round the stream impacts the WD in the accretion flow, the further round we see the stream curl in the tomograms. If the stream rotates all the way round the WD then we will see the curl merge with itself at the beginning in the tomograms and we start to see a similarity with the disk tomograms. 2) As the spin period is increased, we see the curl in the tomogram moving further round anticlockwise, hence in the simulated flow the stream is moving further round the WD. 3) As the orbital period is increased, we see the curl feature in the tomogram moving further back round clockwise, the stream in the flow moving further back round the WD towards the L_1 point.

5.7 Dipole angle and Inclination angle variations for a n^3 field

The inclination angle of a star is the angle between the orbital plane of the star and our line-of-sight. An angle of 0° corresponds to a face on view, while an angle of 90° gives us an edge on view. By varying the inclination angle we can see how the tomograms are affected and whether our perception of the accretion flow from the tomograms is changed giving us spurious results. We used n^3 model simulations at equilibrium for the four different orbital periods of 2h, 3h, 5h and 7h, at each of the five different k_o values for the three angles of magnetic co-latitude that were presented in chapter four, namely 10°, 40° and 70°. We then constructed tomograms for each system at inclinations of 10°, 50° and 90°. The results of this are shown in Figure 5.11.

Figure 5.11: Doppler Tomograms from the n^3 model for magnetic co-latitudes of 10°, 40° and 70° for varying inclination angles of 10°, 50° and 90° for each k_o value in parameter space at equilibrium. The red figures indicate propeller accretion, yellow figures indicate stream, blue figures indicate disk accretion and green figures are ring structure accretion.

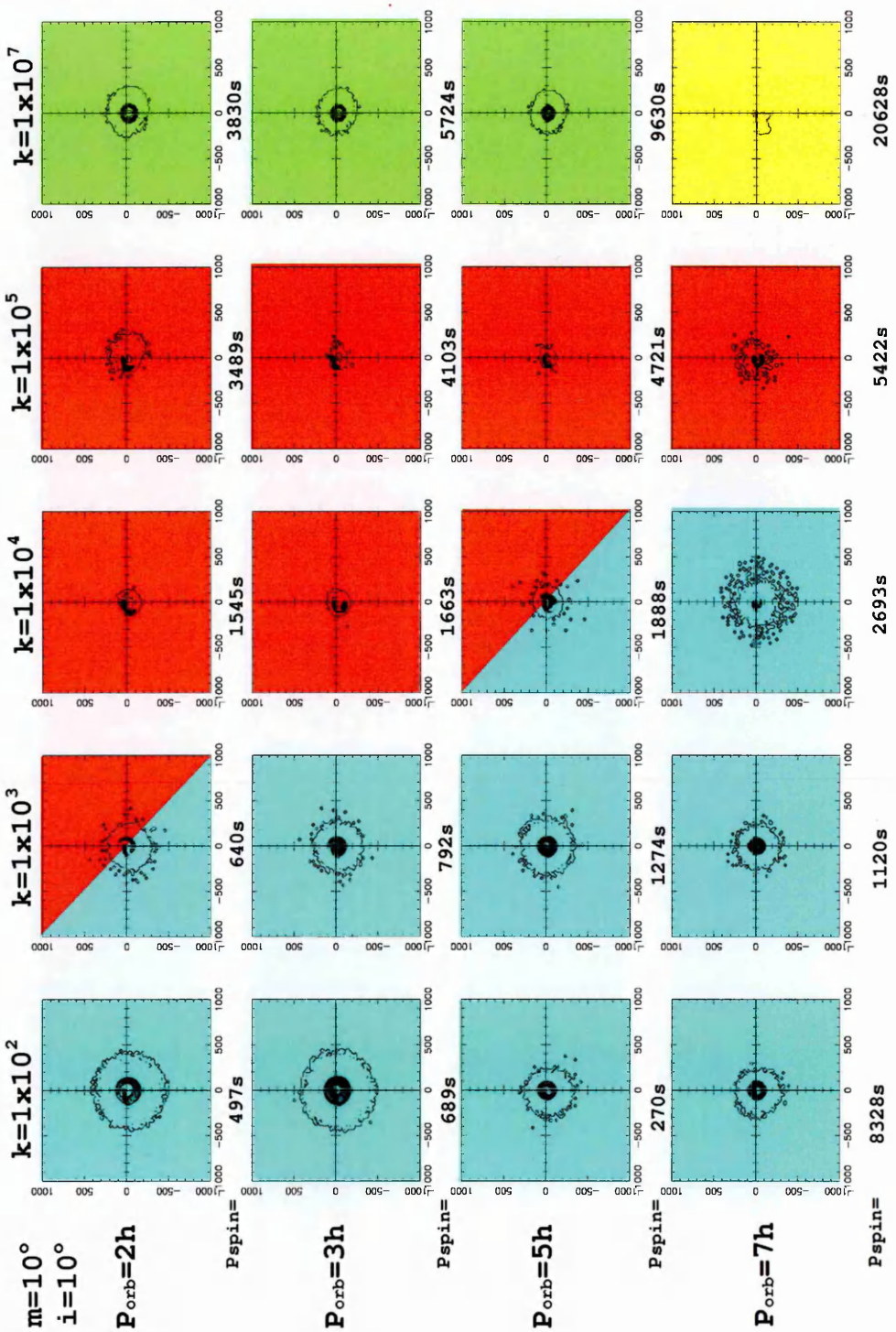
m=10°
i=10°
k=1x10^2
k=1x10^3
k=1x10^4
k=1x10^5
k=1x10^7
Porb=2h
Porb=3h
Porb=5h
Porb=7h
Pspin=
497s
640s
1545s
3489s
3830s
689s
792s
1663s
4103s
5724s
270s
1274s
1888s
4721s
9630s
8328s
1120s
2693s
5422s
20628s

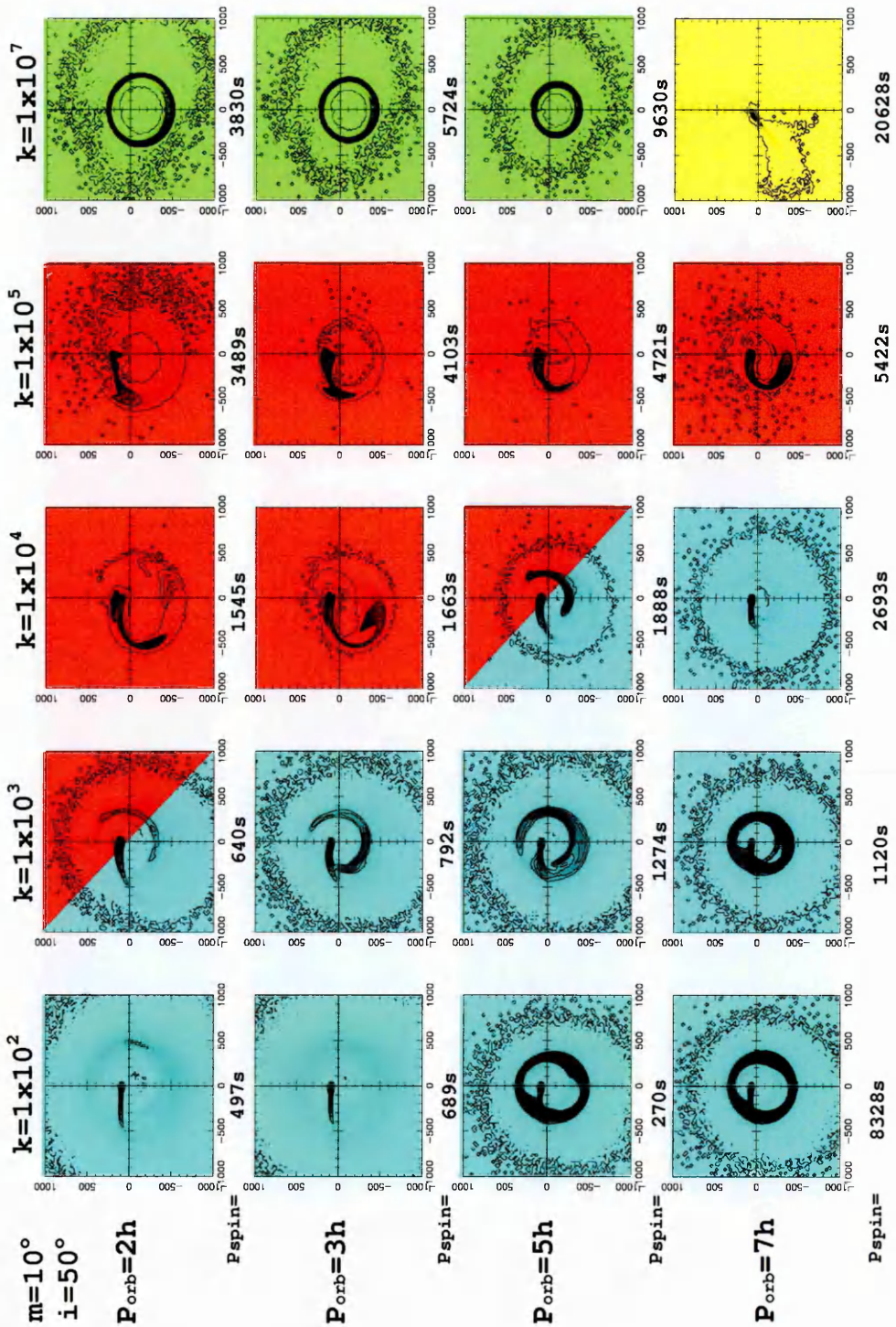
m=10°
i=50°
k=1x10^2
k=1x10^3
k=1x10^4
k=1x10^5
k=1x10^7
Porb=2h
Porb=3h
Porb=5h
Porb=7h
Pspin=
497s
640s
1545s
3489s
3830s
Pspin=
689s
792s
1663s
4103s
5724s
Pspin=
270s
1274s
1888s
4721s
9630s
Pspin=
8328s
1120s
2693s
5422s
20628s

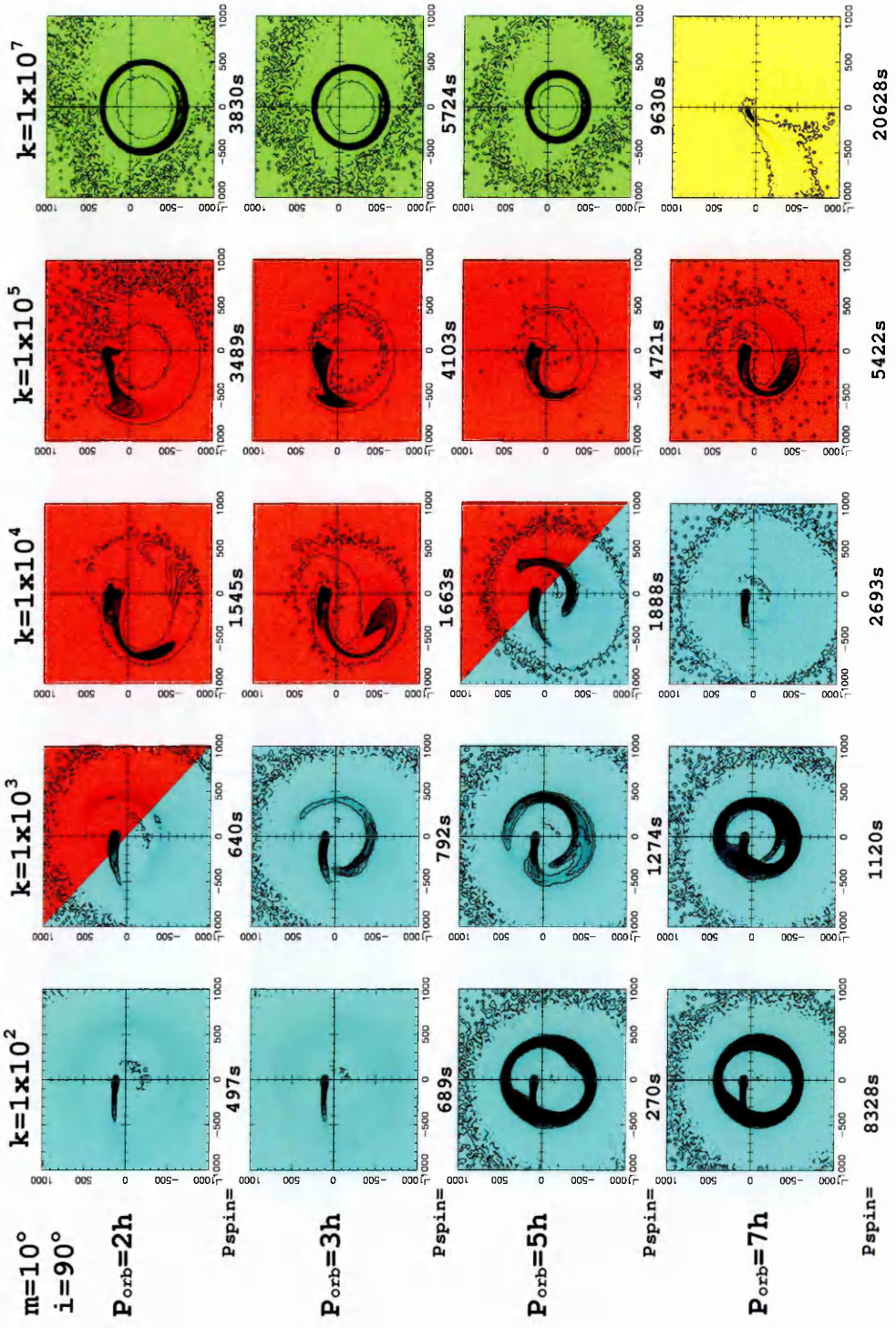
m=10°
i=90°
k=1x10^2
k=1x10^3
k=1x10^4
k=1x10^5
k=1x10^7
Porb=2h
Porb=3h
Porb=5h
Porb=7h
Pspin=
497s
640s
1545s
3489s
3830s
Pspin=
689s
792s
1663s
4103s
5724s
Pspin=
270s
1274s
1888s
4721s
9630s
Pspin=
8328s
1120s
2693s
5422s
20628s

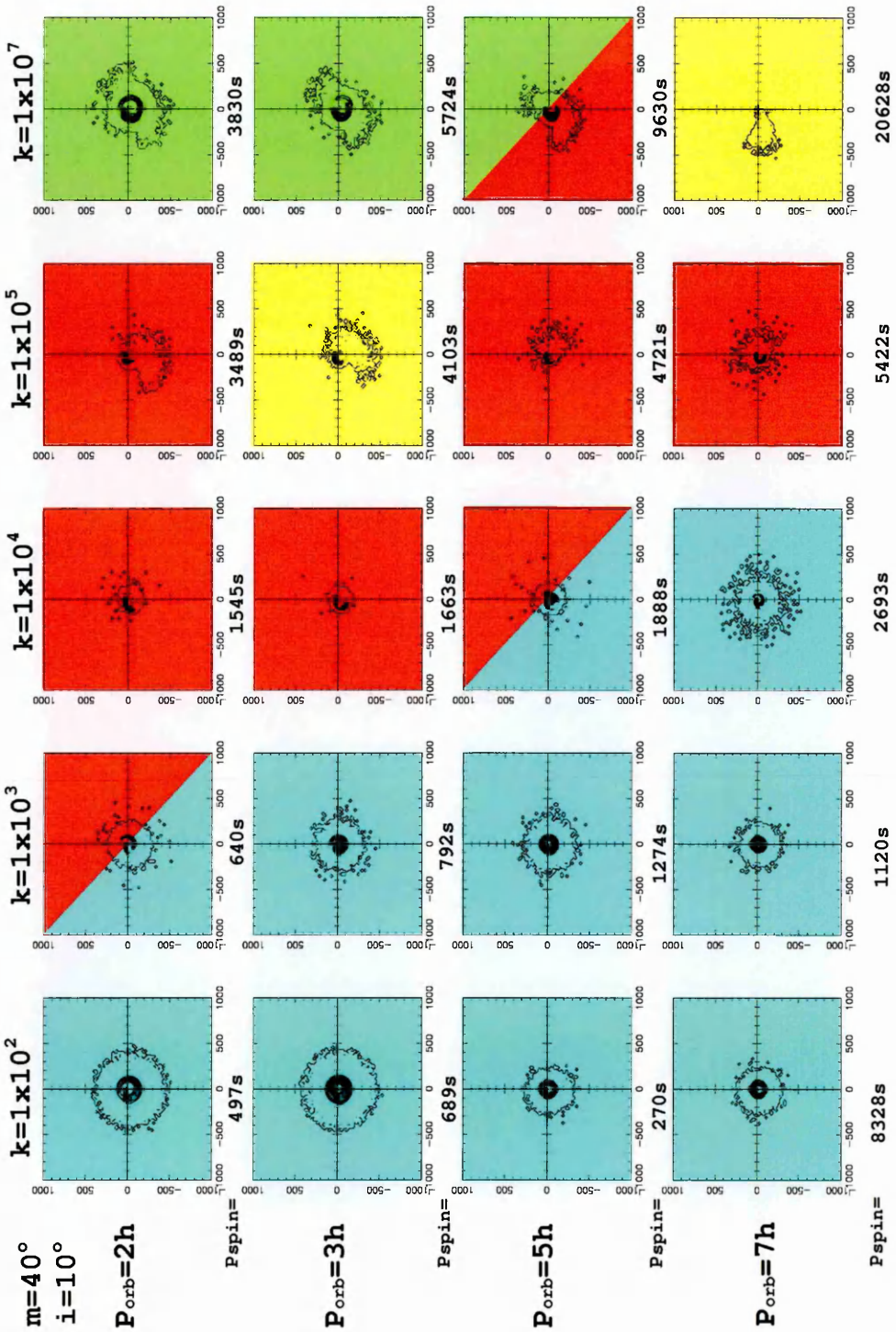
m=40°
i=10°
k=1x10^2
k=1x10^3
k=1x10^4
k=1x10^5
k=1x10^7
Porb=2h
Porb=3h
Porb=5h
Porb=7h
Pspin=
497s
640s
689s
792s
1545s
1663s
1888s
2693s
3489s
4103s
4721s
5422s
3830s
5724s
9630s
20628s
1120s
1274s
270s
8328s

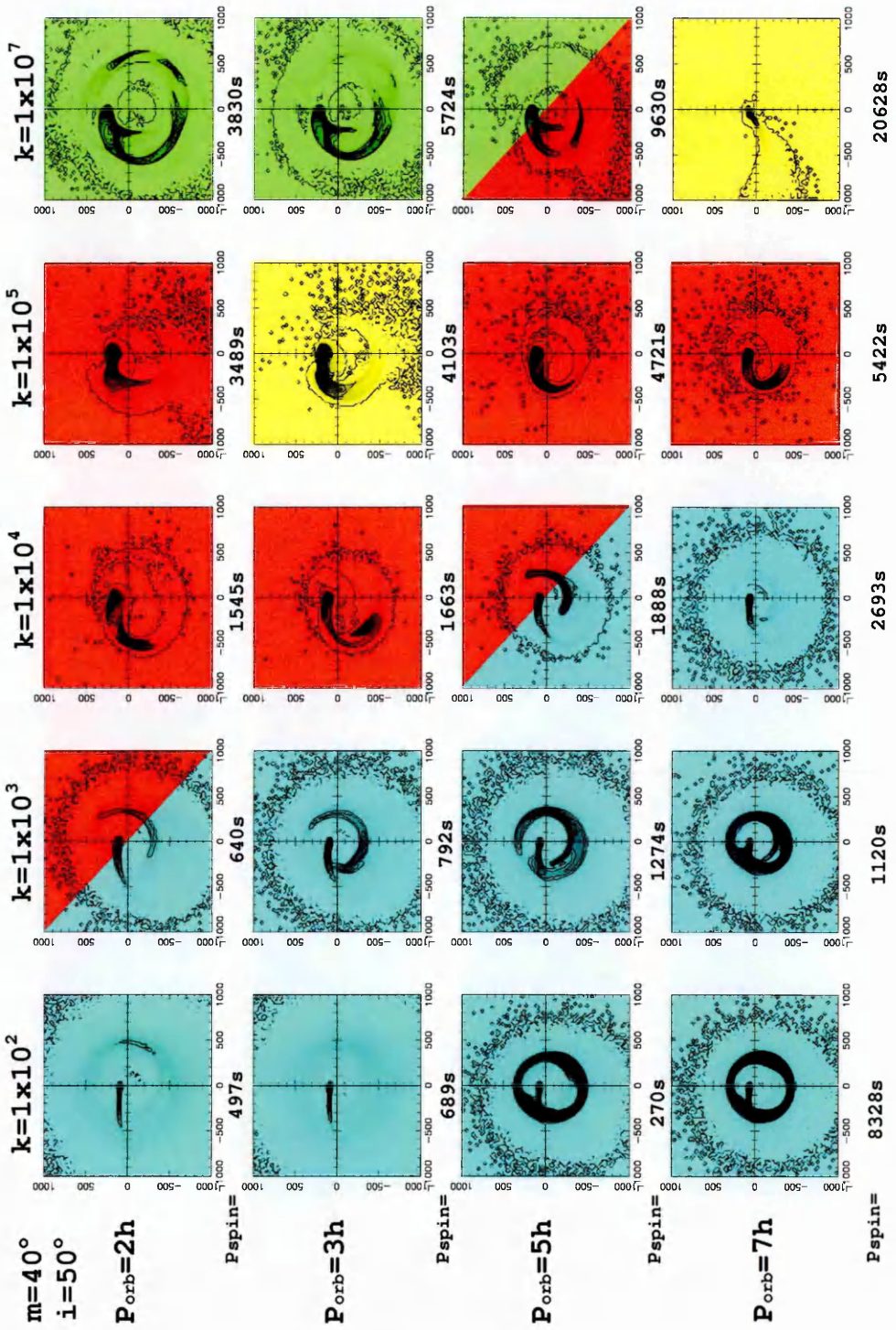
m=40°
i=50°
k=1x10^2
k=1x10^3
k=1x10^4
k=1x10^5
k=1x10^7
Porb=2h
Porb=3h
Porb=5h
Porb=7h
Pspin=
497s
640s
1545s
3489s
3830s
689s
792s
1663s
4103s
5724s
270s
1274s
1888s
4721s
9630s
8328s
1120s
2693s
5422s
20628s

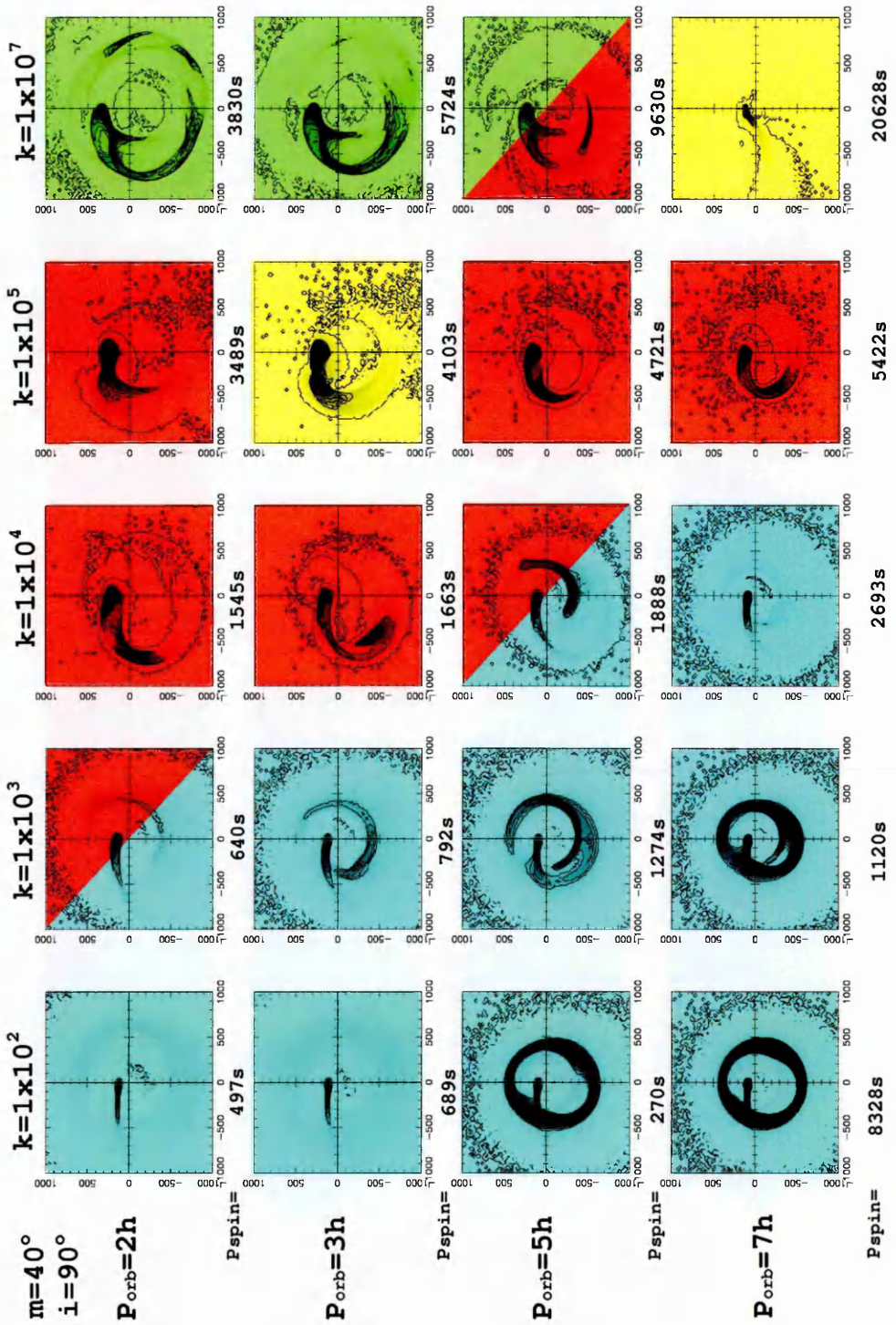
m=40°
i=90°
k=1x10^2
k=1x10^3
k=1x10^4
k=1x10^5
k=1x10^7
Porb=2h
Porb=3h
Porb=5h
Porb=7h
Pspin=
497s
640s
1545s
3489s
3830s
Pspin=
689s
792s
1663s
4103s
5724s
Pspin=
270s
1274s
1888s
4721s
9630s
Pspin=
8328s
1120s
2693s
5422s
20628s

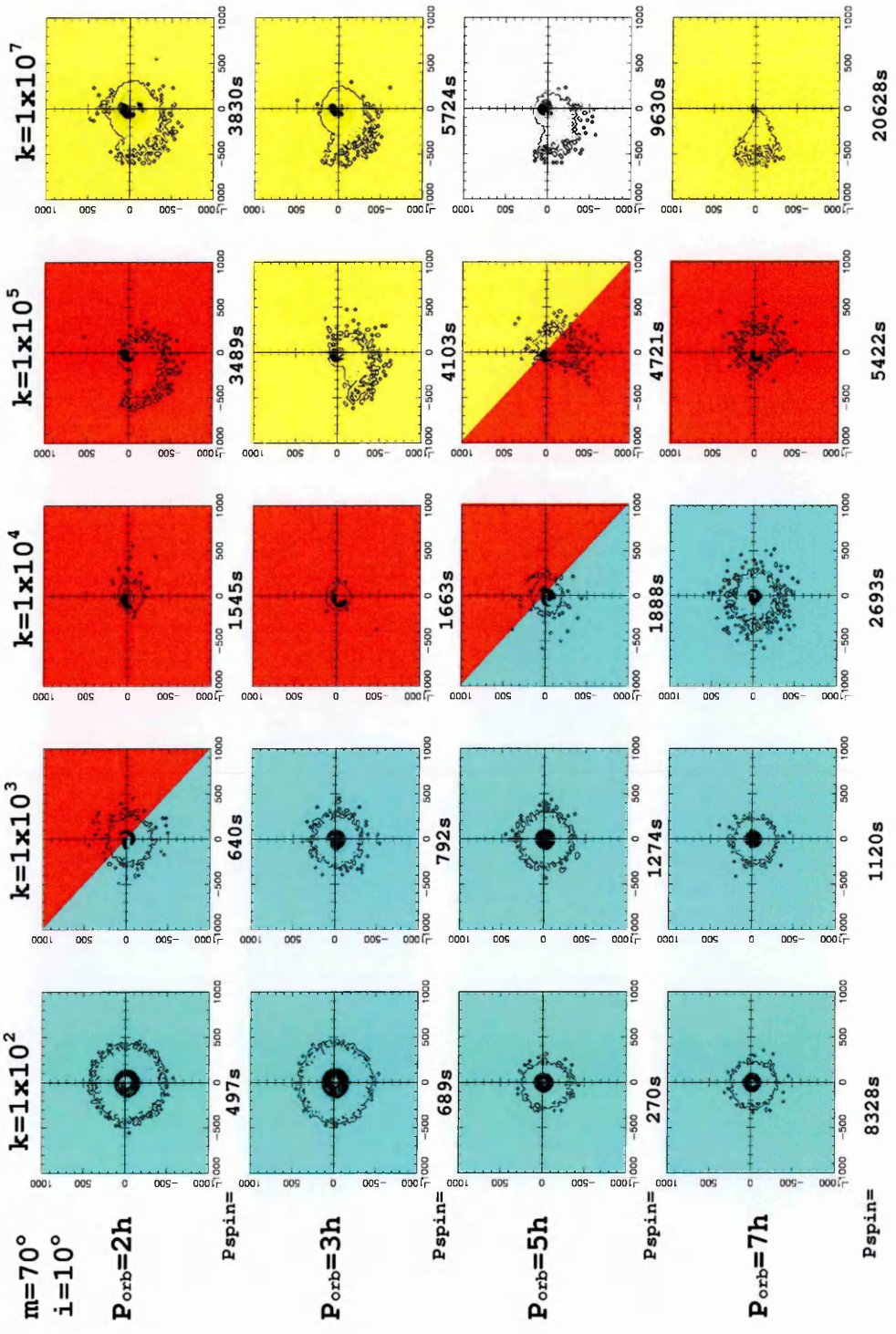
m=70°
i=10°
k=1x10^2
k=1x10^3
k=1x10^4
k=1x10^5
k=1x10^7
Porb=2h
Porb=3h
Porb=5h
Porb=7h
Pspin=
497s
640s
689s
792s
270s
1274s
1545s
1663s
1888s
3489s
4103s
4721s
3830s
5724s
9630s
8328s
1120s
2693s
5422s
20628s

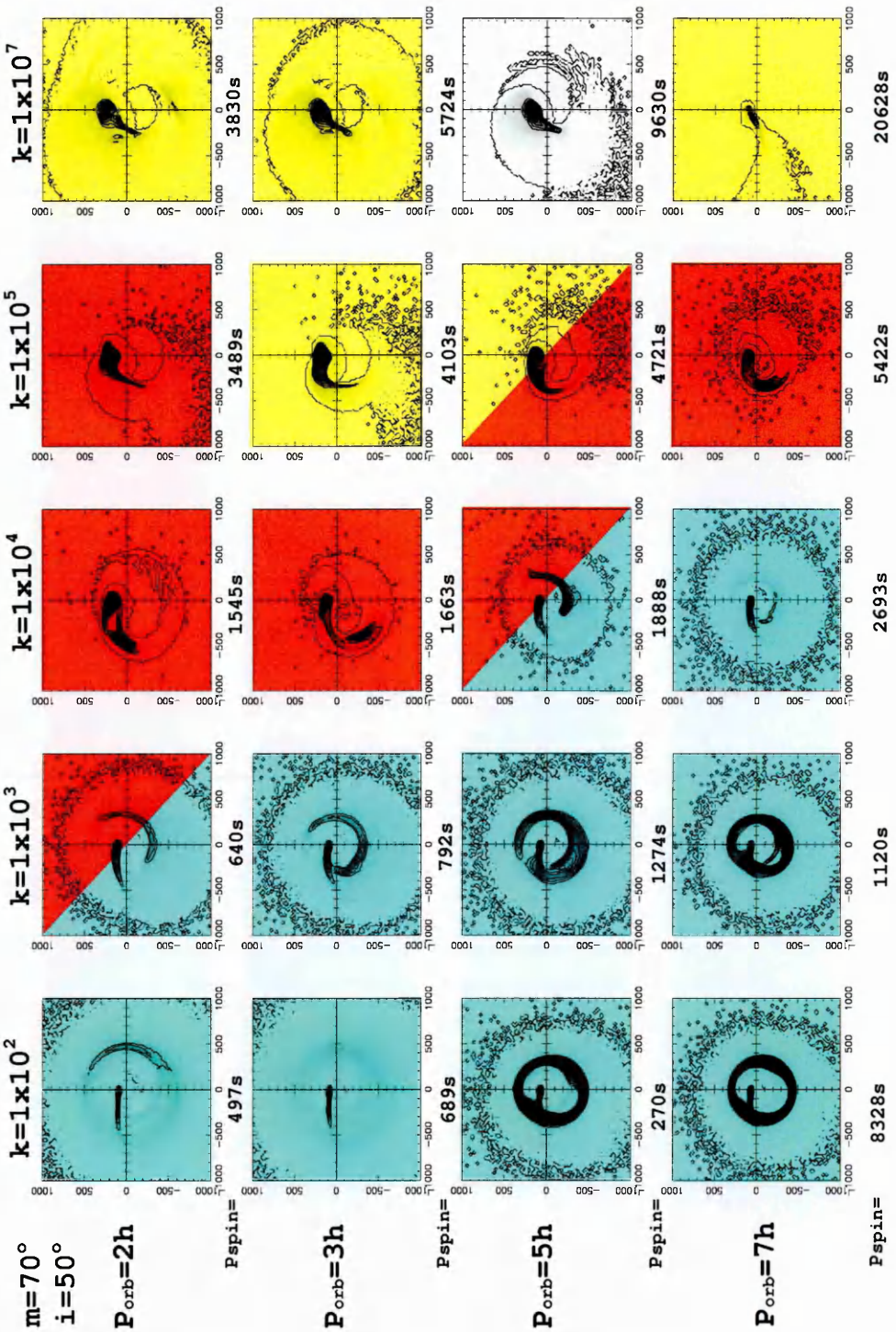
m=70°
i=50°
k=1x10^2
k=1x10^3
k=1x10^4
k=1x10^5
k=1x10^7
Porb=2h
Porb=3h
Porb=5h
Porb=7h
Pspin=
497s
640s
1545s
3489s
3830s
689s
792s
1663s
4103s
5724s
270s
1274s
1888s
4721s
9630s
8328s
1120s
2693s
5422s
20628s

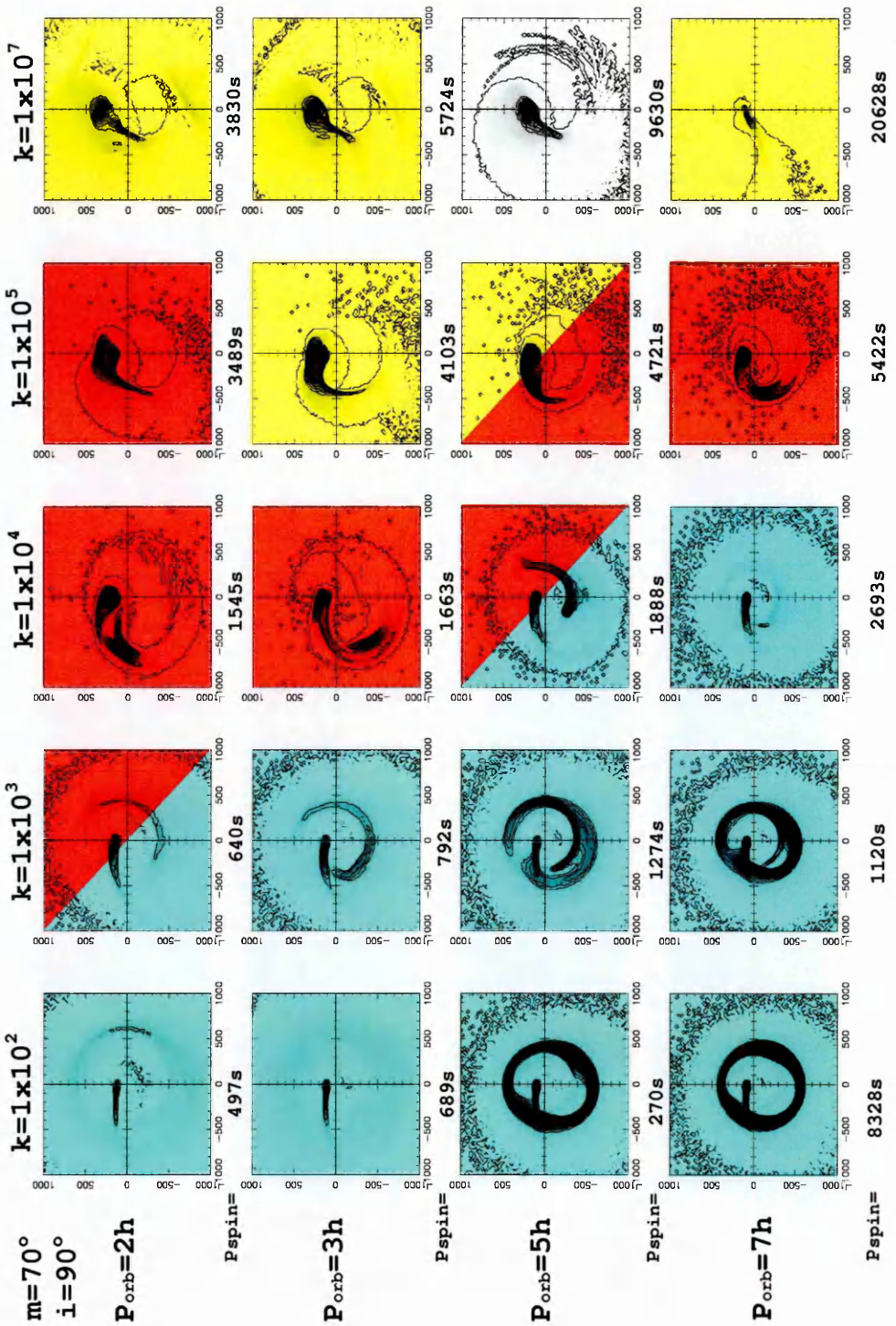
m=70°
i=90°
k=1x10^2
k=1x10^3
k=1x10^4
k=1x10^5
k=1x10^7
Porb=2h
Porb=3h
Porb=5h
Porb=7h
Pspin=
497s
640s
1545s
3489s
3830s
689s
792s
1663s
4103s
5724s
270s
1274s
1888s
4721s
9630s
8328s
1120s
2693s
5422s
20628s

5.7.1 Discussion of Dipole angle and inclination angle variations

In the previous chapter, section 4.5 we looked at the effect on the accretion flow if the dipole angle was changed. In this section we look at the corresponding tomograms for each of the n^3 simulations but we have also viewed them at different inclination angles of 10°, 50° and 90° to see if the tomograms we perceive could be misinterpreted due to the inclination of the system.

- m=10°

  If we look first at the m=10°, i=10° parameter slice, we see the colour coding as for their corresponding simulated accretion flows, disks, propellers, rings and stream. In the accretion flows it is easy to clarify the type of accretion taking place just by looking, in the tomograms however it is very different.

  If we compare the disk tomograms to the ring tomograms we see that they are incredible similar. Both have a dense small ring at low velocity in their centres surrounded by a higher density ring. The velocity of this outer ring in the disk ranges from 400kms^{-1} to $\sim$ 250kms^{-1} decreasing in velocity with increasing orbital period. The ring systems however have outer ring velocities from 300kms^{-1} to $\sim$ 250kms^{-1} with increasing orbital period. The ring systems have some slight low density material on the inside of the dense ring, but this is too slight a feature to make use of in interpretation. The only way a disk tomogram could be identified over a ring tomogram is by the magnetic field strength at which the system is at and this cannot be determined observationally. At high magnetic fields, the tomogram must belong to a ring accretors, at low to medium fields it would belong to a disk. However at medium strength fields another problem arises in distinguishing between propeller tomograms and disk tomograms. Most of the propeller tomograms show a small dense region from small velocity in the V_y axis curling round into the lower-

left quadrant (the collimated flow from the secondary), surrounded by a small less dense region also at low velocity (the dispersed ejected material). Material from the propeller must have been caught up by the magnetosphere and circling the WD, but still clearly being ejected. If we compare the two tomograms at k_o=1×10^4, $P_{\rm orb}$=7h and k_o=1×10^5 at $P_{\rm orb}$=7h we see that they are very alike, in fact the only differences are the dense emission region being slightly bigger in the propeller case and the surrounding material moving at lower velocity. For the propeller the materials speed is $\sim$ 200kms^{-1} whilst the disk is up to $\sim$ 500kms^{-1} but is that enough of a significant difference to tell them apart?

The stream tomogram is easier to identify as the features are not like any of the others. A very small dense emission region from the L_1 point is seen and lower density material moving from it at low-velocities in the lower-left quadrant, corresponding to the magnetically controlled stream.

Increasing the inclination to 50° brings up features in the tomograms we have seen previously for each of the types of systems. The features corresponding to the type of accretion in each system become clear. For the disks we see both diffuse and collimated flows. There is a dense emission ring in the centre at low velocity for the collimated disk and just a small dense region in the upper-left quadrant from the L_1 point in the diffuse situation. Both have high velocity rings circling these features, corresponding to the material circulating close to the WD in both cases.

For propeller systems we see a large curling dense emission region from the upper-left quadrant to the lower one at slow velocity corresponding to the propeller flow, which is highly collimated out of the L_1 point till it starts to interact with the magnetic field where we see the curl in the tomogram carried on by less dense material. In all the propeller tomograms we also see a ring structure which tells us that some of the

material that has been ejected away must have been expelled into the Roche lobe of the WD and caught by the magnetic field causing it to rotate. The majority of the material however is ejected and dispersed out of the binary system.

The ring accretors show their characteristic dense ring at low velocities in the tomograms, as the collimated ring forms round the outside of the Roche lobe of the WD in the corresponding flows. All the ring tomograms also show low velocity material on the inside and outside of the dense ring. We see in the flow that material is accreted on to the WD from the ring at higher velocity as well as the ring itself being a little dispersed in places so giving even slower moving material.

The only stream accretor still shows dense emission from the L_1 point, but now the less dense material coming away from it has spread out more in the lower-left quadrant. The stream itself in the flow is very dispersed and we see it impacts the WD in the side towards the secondary, hence the tail opening up in the lower-left quadrant.

At i=90° we see all the same features as just previously described, except for a few changes. At this inclination angle in the disk systems, the inner dense ring has increased in velocity both the inner and outer edges, making the dense region of the disk seem closer to the WD than it appears at an inclination of 50°. The outer less dense material has also moved further out in the tomograms to higher velocity so appears closer to the WD when viewed at this inclination angle. The same is true for the propeller systems, the ring systems and the stream system. All the tomogram features appear the same as they did at an inclination of 50°, but they have all increased in velocity, moving further out in the tomograms. Hence viewing the systems at either 50° or 90° can lead to misinterpretation as to the nature of the accretion flow and its velocity. At 90° all the system features appear to be closer to

the WD.

- m=40°

At a magnetic co-latitude of 40° there are some interesting accretion scenarios, (See section 4.8.1 for full details) producing even more interesting features in the tomograms. At a quick glance of the tomograms it is quite hard to distinguish one type of accretion system from another if they were not colour coded, except perhaps for the stream fed accretion at $P_{\rm orb}$=7h for k_o=1×10^7.

Most of the disk features appear with a dense ring at small velocities in the centre of the tomogram surrounded by a region of lower density, slightly broken up on its outer edge. The ring tomograms also appear very similar to this. They have a dense emission region in the centre, one of which is a full ring surrounded by less dense material at slightly higher velocity. If we look at the propeller systems we see a similar case, namely a small emission region at the centre surrounded by slight higher velocity lower density material. We also see a stream system in the middle of the propellers that, although it looks like a stream in the simulated flows, in the tomograms it looks remarkably similar to a propeller feature. So how do we tell the different accretion mechanisms from these tomograms? Although both the disk and ring accretors have central dense rings at low velocity, the disk system's outer ring of lower density material is much more uniform and circular than that of the ring. At this magnetic co-latitude we see in the accretion flow that the disk accretion has still kept the disk shape, whilst the rings are rather broken up in places leading to the non-uniformity of the outer material in the tomogram. Again the disk systems appear at low to medium magnetic field strengths, the rings at high strength only.

The propeller systems, like the rings, have a non-uniform spread around their central dense emission features, distinguishing them from the disks. The rings un-like the

propellers have either a ring or semi-circle of dense material at their centres, whereas the propellers have just a small dense region from the L_1 point curling round slightly into the lower-left quadrant. The less dense material surrounding them comes from some of the material accreting onto the WD or circulating around it a large distances hence at low velocity, keeping the system in equilibrium.

At an inclination angle of 50°, like the previous case we see more characteristics in the tomogram features that we have previously identified. This enables us to interpret the accretion flows that accompany these tomograms more easily.

We see the familiar dense rings at low velocity in the disk tomograms with the emission from the L_1 point and the high velocity less dense material surrounding it, corresponding to the concentrated disk accretion. We see the more diffuse disk as well, showing just the dense emission from the L_1 point and the high velocity, low density material surrounding it. The diffuse disk in the flows spans the whole of the Roche lobe from high velocity near the WD to slower velocity further out.

In the propeller systems there is a highly collimated flow from the L_1 point as we see the long curled dense region. It is also apparent that material in the flow is circling the WD as we see the low density material in the tomograms forming rings. The same must also be true for the stream at $P_{\rm orb}$=3h, circulating at great distances as the low density material curls round at low velocity. In the other stream system we see a fairly collimated stream to the WD with a slight scatter from the L_1 point in the simulated flow, depicted by the flow in the tomogram fanning out into the lower-left quadrant due to the direction of the flow.

For the ring accretor systems in the simulated flow we do not see full rings form outside the Roche lobe. Instead we see a broken ring feature as the material curls most of the way round the Roche lobe, then breaks up and disperses, finally getting

slightly denser close to the secondary. In the tomograms we see a similar picture, the dense low velocity ring for the material orbiting around the outside of the Roche lobe is also broken up. We see a large amount from the L_1 point then breaking up but still moving anticlockwise round the quadrants. This region is surrounded by a lower density ring moving from low to high velocity. If we look closely at the flows we can see material streaming down onto the WD so it must be circulating near the WD for us to see low density material a high velocity in the tomogram.

At i=90° we see the same features as before and see the same effect as for the m=10° situation. All the features in the tomograms have got larger and increased in velocity. Hence at this inclination angle we see the systems closer to either the Roche lobe of the WD, or the WD itself to create the sudden increase in velocity.

- m=70°

At m=70°, we see the same pattern emerging for the different inclination angles. At i=10° some of the disk tomograms look like the propeller ones which in turn look similar to some of the streams. As we increase the inclination to 50° we see clear features in the tomograms that allow us to define the accretion geometry. By 90° we see these same features yet they have all become bigger in the tomograms increasing their velocity. So our perceptions are different at 90° to that of 50°, the material in the accretion flow would appear closer to the Roche lobe of the WD or the WD itself for us to see the higher velocities.

For the i=10° case, we see a small dense ring at low velocity in the centre of the disk tomograms with a ring of slightly lower density material surrounding it. These originate from the dense outer region of the disk at low velocity, with the scattered material on the inside, scattered closer and around the WD so appearing at higher velocity. The propeller systems show a small dense region at the centre of the tomo-

gram from the upper-left quadrant curling round anticlockwise from the L_1 point. They are also surrounded by low density material as seen at low velocity. In all the simulated propeller accretion systems we see some of the material either being propelled away and moving into the Roche lobe of the WD, or we see the material being accreted onto the WD and being propelled away. Hence the lower density material in the tomogram along with a small collimated flow from the L_1 point. The stream systems are much the same as the propellers, showing a small dense region in the centre of the tomogram from the L_1 point in the flow, surrounded by a less dense region in the centre of the tomogram from the interaction with the magnetic field and the ballistic trajectory.

At i=10°, telling the difference between the three accretion modes is tricky. The disks occur at lower magnetic field strength and the lower density material surrounding the denser material in the centre is again uniform unlike that for the other systems. For the propellers we see small emission in the centre surrounded by lower density, less uniform material. The streams also show a small emission region in the centre from the L_1 point, but their low velocity emission is generally longer and wide in just one direction, where the streams interact with the magnetic field in the flow and where it impacts the WD.

At i=50° we see more characteristic features of the accretion flows in the tomograms. The dense inner ring and outer lower density ring are seen in the disk tomograms for collimated disk accretion. Conversely, just the dense feature from the L_1 point surrounded by lower density material is seen for the more diffuse disk accretion. A long collimated curl moving anticlockwise form the upper to the lower-left quadrant and a ring of low density material is seen in the propeller tomograms. The collimated stream from the L_1 point before it interacts with the magnetic field is also seen and

the ejected flow with material dispersed into in the Roche lobe of the WD is seen as well. Finally the stream tomograms show a large dense emission area from the L_1 point in the flow, surrounded by either a large ring of lower density material in two cases, or lower density material moving away from the dense emission and fanning out. The stream flow material in the two ring case tomograms must be captured and forced to rotate around the WD to give the lower density ring structure, as well as having slightly collimated streams from the L_1 point which disperse from the ballistic trajectory and then interact with the magnetic field.

At i=90° as for the previous two situations, the velocity of each feature increases and the overall feature gets larger, due to our perception of how close the material is to the WD and the magnetic effects.

5.7.2 Overall Conclusions

For each dipole angle variation we see a similar pattern arising in the tomograms at the three different inclination angles. At an inclination of 10° it is very hard to identify the type of accretion flow geometry that would correspond to each simulated tomogram, with disk tomograms looking like the propeller ones which in turn look similar to some of the streams. Only very subtle difference give the type of accretion flow that would come from the particular tomogram. For example, in the disk systems, their outer ring of lower density material is much more uniform and circular than that of the ring and they only form at low to medium magnetic field strengths, whereas the rings form at high magnetic field strength only. As the inclination angle is increased to 50°, we see more characteristics in the tomogram features that have previously been identified. Enabling us to interpret the accretion flow geometry that accompanies the tomograms more easily. At an inclination of 90° however all the tomogram features appear the same as they did at an inclination

of 50°, but they have increased in size and increased in velocity, moving further out in the tomograms. Thus at this inclination angle we see the systems closer to either the Roche lobe of the WD, or the WD itself to create the sudden increase in velocity. Viewing the systems at either 50° or 90° could lead to misinterpretation as to the nature of the accretion flow and its velocity.

5.8 Published observations of Doppler Tomography of IPs

The following table (Table 5.1) shows the published tomograms for IPs to date (adapted from T.R. Marsh Astrotomography - Indirect Imaging Methods in Observation Astronomy 2001). In the rest of this section we discuss the specific papers in turn.

- Stroboscopic Doppler Tomography of FO Aqr Marsh & Duck (1996).

  Marsh & Duck (1996) took 938 spectra of FO Aqr and found that, HeII 4686 showed an 'S'-wave on the orbital period with sharp features on top that ran across from red-to-blue and blue-to-red, reversing direction with orbital phase. They applied the method of Doppler tomography to try and understand these features. They computed the Doppler images as a function of the orientation of the WD relative to the binary system to cope with the variations as the WD rotated. The process was analogous to how a stroboscope worked, in freezing the motion of rotating objects.

  Some of the most important features of their results can only really be seen from viewing their images as an animation[1], however they displayed a set of 'stills' in their paper. They showed a sequence of eight images spaced equally around the sideband cycle and saw strong emission concentrated in the gas stream/secondary star region (see Figure 5.12). They found that this component changed significantly with side-band phase. The flux of this component changed by a large amount with

[1]See Figure 16 of the electronic version of this paper, http://www.elsevier.nl/locate/newast

Table 5.1: Published Doppler maps of IPs

Source	Line(s)	Features	Ref.
FO Aqr	HeII	2a;3?	[1]
"	HeII		[2]†
BG CMi	Hβ, HeII	2	[2]†[3]
PQ Gem	Hβ, HeII	2	[2]†[3]
EX Hya	Hβ	1;2a	[4]
"	Hβ		[2]†
AO Psc	HeII		[2]†
V405 Aur	Hα, β, HeI, HeII	1;2b,d	[5]
"	Hα, γ HeII		[6]
AE Aqr	Hα	2b;4	[7]
V1025 Cen	Hβ	2b;d	[8]
RX0757+63	Hβ	1;2b;3?	[9]‡
RX1238-38	Hβ	1;2a	[2]†
RX1712-24	HeII		[2]†

†These maps were computed on the spin phase of the white dwarf rather than the standard orbital phase.

‡These maps were computed on the beat phase of the white dwarf as well as the standard orbital phase.

References: [1] Marsh & Duck (1996), [2] Hellier (1999), [3] Hellier (1997a), [4] Kaitchuck et al. (1994), [5] Still et al. (1998), [6] Szkody et al. (2000), [7] Welsh et al. (1998) [8] Hellier et al. (2002b), [9] Tovmassian et al. (1998). Feature codes: (1) Ring (which may be from a disk), (2) Spot, (3) Secondary Star, (4) Little structure or low signal-to-noise. Type (2) = "spot" does not necessarily imply stream/disk impact, but just refers to the appearance of the image. Entries such as 2a refer to the quadrant the spot is located in (if the orbital phase is known). The quadrants start at the upper-left with "a", and then go anti-clockwise from there.

side-band phase almost disappearing at phase 0.61, with the location of the emission peak shifting back and forth. The shift in location of the emission peak was the equivalent in the Doppler images of the blue-to-red and red-to-blue shifts. There was also more extended emission which showed less change with side-band phase. Some of this is seen to rotate in the animation and could have been from the spin component, but it did not have the correct phase for the disk in their standard model.

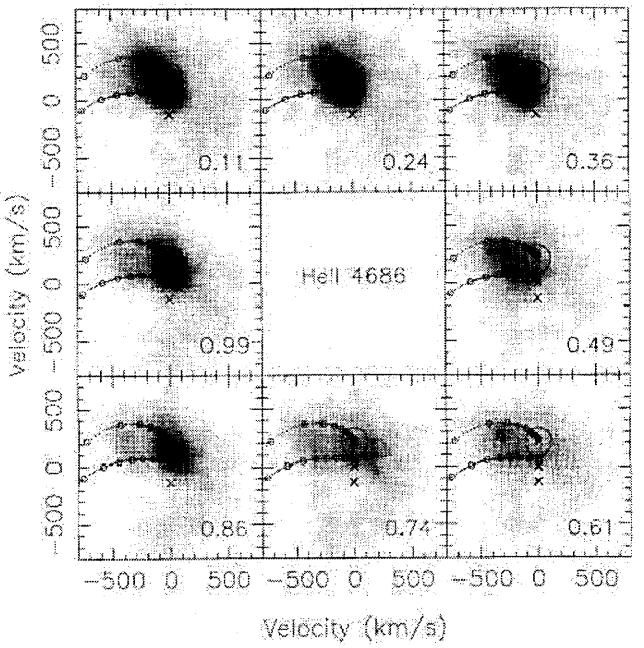

Figure 5.12: A set of 8 images of HeII 4686 around the side-band phase cycle of FO Aqr Marsh & Duck (1996).

The changes in the Doppler images could be understood by imagining the radiation from the WD sweeping round the system. The WD rotates in the same direction as the binary orbits so the gas stream region is ahead of the secondary and lights up after it, as was seen. In order to understand the features in the images better, they

carried out simulations based on a model where radiation from the WD sweeps the system exciting emission in various structures such as the secondary and gas stream. The model went some way to explaining the 'S' wave emission.

Their Doppler images however showed no sign of an illuminated disk component. With the only arguments in favour of it being indirect. There did appear to be a bright spot which could have come from the impact of the gas stream with a disk. However as it is not understood how the stream threads onto the magnetic field of the WD they could not say that it was not this that produced the feature. The images did have persistent extended emission, but it was low velocity and very asymmetric so it seemed unlikely that it was a disk. The images did however provide an explanation for the side-band modulation that was visible in the trailed spectra. A structure which subtends a significant azimuth as the WD lights up as the beam from the WD sweeps round. The structure has a range of velocities, so as the beam sweeps across it, a velocity shift is seen. The direction of the shift agreed with what was expected from structures related to the secondary star and gas stream in that the spot shifts towards the left in the Doppler images rather than in some other direction. After this point their model no longer agreed with their data.

- Spectroscopy of the intermediate polars BG Canis Minoris and PQ Geminorum, Hellier (1997a).

  BG CMi and PQ Gem both showed an orbital cycle S-wave caused by the impact of the accretion stream with an accretion disk. They are both believed to be disk fed accretors. The emission line in PQ Gem showed complex changes over the spin cycle which arise in accretion curtains falling on to both magnetic poles of the WD. Hellier presented the first Doppler tomography of these curtains, see Figure 5.13.

  Spectroscopy of BG CMi showed no double peaked emission lines arising from an accretion disk but HeII λ4686 showed an obvious S-wave and the Hβ line was enhanced at all velocities. When a component from the accretion disk is clearly seen in the emission lines it is usual to attempt to measure the WDs orbital velocity from the line wings which presumably originate closest to the WD. The Hβ line profile however as a whole was too poorly understood to measure a velocity reliably. The Doppler tomogram of the line was also hard to interpret consisting mainly of low-velocity emission caused by the single-peaked component.

  The PQ Gem line profiles were similar to those of BG CMi with no obvious double peaks. The Hβ showed a single peaked profile, with clear orbital motion and the HeII λ4686 showed the same component as well as an obvious S-wave which brightened up twice per orbital cycle. For PQ Gem it was the S-wave velocity from the HeII λ4686 that was measured from the tomogram though it underestimates the S-wave velocity because it assumes that components do not change in intensity round the cycle. As the S-wave had two brightenings per cycle, both at low velocity, the tomogram would be misleadingly bright at velocities lower than the true velocity so the S-wave was then measured directly from the line profiles.

  Hellier then went on to look at the spin period profiles of the two systems and used

Doppler tomography to compare spin cycle tomograms of a model that consisted of two equally visible accreting poles with opposite velocities to that of the PQ Gem line HeII λ4686. Hellier found that they both showed a division into two emission regions (each corresponding to one of the spin waves) which Hellier attributed to the two accreting poles. The upper right region appeared to have a lower velocity than the other regions, however this was misleading again since the spin wave was clearly varying in intensity. Hellier went on to assume that the brighter of the spin waves came from the upper-pole, since this was the more visible pole. The brighter spin-wave was seen in the lower-left quadrant of the tomogram, which implied that it was the upper pole that pointed towards them at that phase in the spin cycle variations.

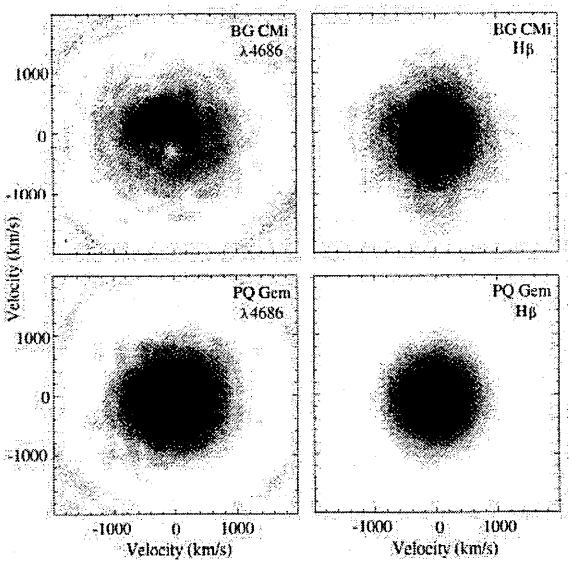

Figure 5.13: The Doppler tomograms of the He II λ4686 and Hβ lines of BG CMi and PQ Gem, Hellier (1997a)

- Doppler Tomography of Intermediate Polar Spin Cycles, Hellier (1999).

  Hellier collected emission line profiles for seven IPs, phase-resolved over the spin cycles and presented the first systematic application of Doppler tomography to the spin cycles, with the aim to investigate whether it would be a useful diagnostic tool, see Figures 5.14-5.17.

  For AO Psc, the HeII λ4686 line showed a low-velocity component, that brightened and faded over the cycle as well as a higher velocity S-wave phased with maximum blueshift at phase 1. This mapped on to a diffuse area of emission at "3 o'clock" in the tomogram.

  The finding of maximum blueshift at phase 1 led to the "accretion curtain" model of IPs, where optical and X-ray maximum occurred when, the upper-magnetic pole pointed away from the observer, emission moving toward the observer onto the upper pole was predominantly seen (Hellier et al. 1987 1991). Thus the tomogram shows a velocity image of the upper accretion curtain. Since there was little or no emission to the left of the y-axis, it meant no HeII λ4686 was being seen from the lower pole. Since the velocities were low compared to the escape velocity of the WD at 3000kms^{-1} it meant they were seeing emission from relatively far out in the accretion curtains at a few WD radii (see Hellier et al. (1991) for more discussion on this). Also the fact that the emission subtended $\sim$180° at the origin suggested that the accretion curtain was extended over this angle, picking up material from the disk over a wide range of azimuth (Figure 5.14).

  FO Aqr gave similar results to that of AO Psc. The tomogram again showed diffuse emission centred on 3 o'clock suggesting the emission appeared from just one pole. However it subtended at a greater angle than that for AO Psc which suggested that the accretion curtain was even more azimuthally extended. The low velocities again

implied emission from the outer parts of the magnetosphere (Figure 5.14).

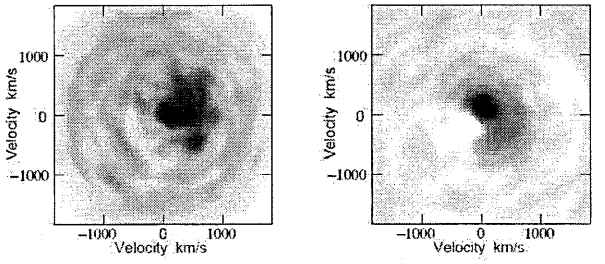

Figure 5.14: Doppler tomograms of He II λ4686 for AO Psc on the left and FO Aqr on the right, Hellier (1999).

BG CMi showed a lower signal-to-noise ratio version of the behaviour seen in both AO Psc and FO Aqr again with greater emission around 3 o'clock but broken up into separate blobs because of the greater noise. The tomogram also picked up a weak spin-wave (Figure 5.15).

PQ Gem's tomogram showed clear evidence for emission from both the upper and lower accretion curtains which was interpreted as showing a nearly complete azimuthal ring of emission, brightening at the locations where the upper and lower poles point. Again the low velocities implied that they were seeing emission from several WD radii out. They noted however that these curtains that they saw in the tomogram appeared rotated by ∼40° ahead of the location at which it hits the WD. They expected that the brighter of the poles was the upper pole, since in the tomogram the brighter pole was the lower-left, this implied that the upper pole pointed towards them at blue-optical and hard X-ray pulse maximum (5.15).

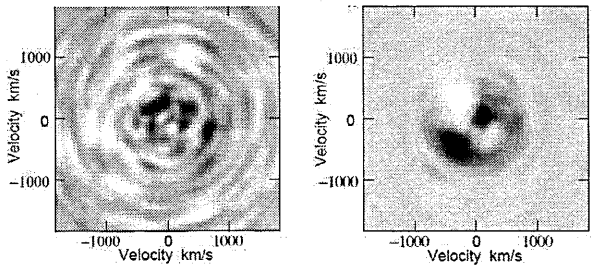

Figure 5.15: Doppler tomograms of He II λ4686 for BG CMi on the left and PQ Gem on the right, Hellier (1999).

RX 1712-24 probably does not have an accretion disk as stated by Hellier. Unfortunately this system violated one of the rules of tomography, that of constant-brightness, which meant the tomogram was again hard to interpret (Figure 5.16).

Unfortunately for EX Hya, changes in the intensity dominated over velocity variations which meant the tomogram was again hard to interpret (Figure 5.16).

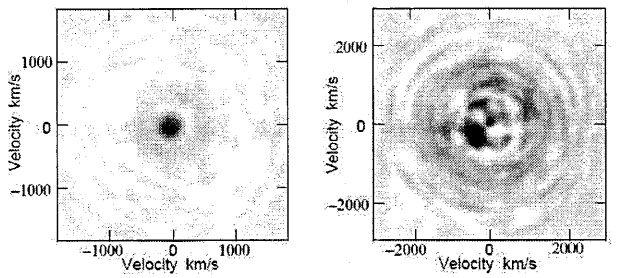

Figure 5.16: Doppler tomograms of He II λ4686 for RX 1712 on the left and Hβ for EX Hya on the right, Hellier (1999).

For RX1238-38, again, intensity changes dominated over velocity changes and the tomogram was of no help (Figure 5.17).

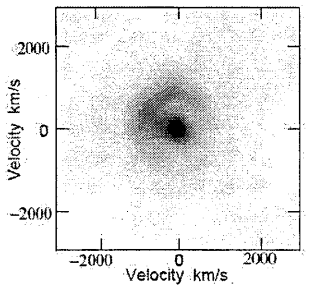

Figure 5.17: Doppler tomogram of He II β for RX 1238-38, Hellier (1999).

- Tomography of Cataclysmic Variable Stars, Kaitchuck et al. (1994).

  In the atlas, Kaitchuck et al. (1994) analysed the tomogram of EX Hya, see Figure 5.18. They found a clear disk feature with central absorption and strong S-wave emission which appeared to be spread azimuthally over a considerable fraction of the disk. The brightest emission occurred at (-170, 290) and it was found that the bright spot fell on the expected stream trajectory. This suggested that there maybe a stream/disk collision for the location of the S-wave emission.

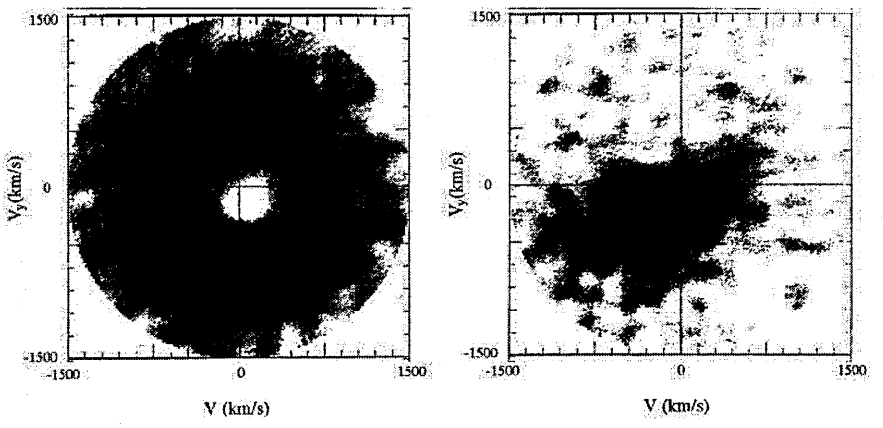

Figure 5.18: Doppler tomogram for the Hβ emission line of EX Hya, Kaitchuck et al. (1994).Unfortunately, it is difficult to draw any conclusions from the figure as presented.

- Spectroscopic evidence for two-pole accretion in the intermediate polar, RX J0558+5353 Still et al. (1998).

  Still et al. took Doppler tomograms of 4 lines for RX J0558+5353 namely Hα, Hβ, HeI λ5876 and HeII λ4686, see Figure 5.19. By assuming a velocity field for the emitting gas, the tomograms provided maps of orbitally coherent accretion structure. All the lines shared a common asymmetric feature with a semi amplitude of 300kms^{-1}. The features they were seeing were usually interpreted as emission from places such as the hot-spot or the inner face of the secondary. The feature in the tomograms was broad and the fit that they used generally smoothed the feature over azimuth for the tomograms of the low excitation lines.

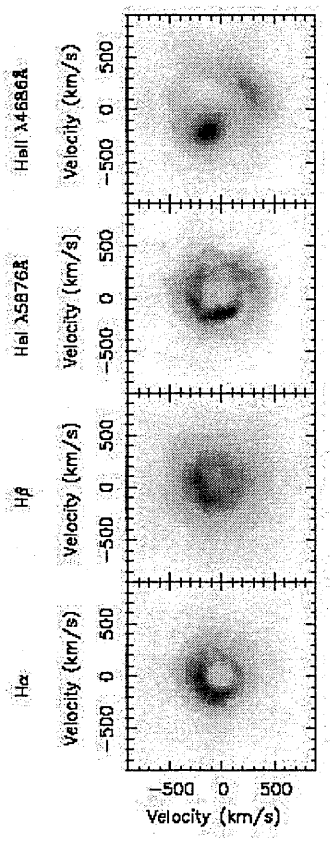

Figure 5.19: Doppler tomograms of the Hα, Hβ, He I λ5876 and HeII λ4686 emission lines for RX J0558+5353 (V405 Aur), Still et al. (1998).

- *Extreme Ultraviolet Explorer* and Optical Observations of the Magnetic Cataclysmic Variables RX J1015.5+0904 and V405 Auriga (RX J0558+5353), Szkody et al. (2000).

  Szkody et el. constructed Doppler maps of the Balmer and HeII lines for V405 Auriga, see Figure 5.20. They found that their tomograms showed different emission for each line. Hα showed nearly uniform disklike emission, with a large amount near the location of the WD. Hβ showed a disk with a large concentration of emission near the stream location. There was also another spot of enhanced emission that

was however 180° out of phase. Hγ showed the strong component with the second component barely visible. HeII was similar to Hγ, again not showing much of another enhanced region. As the excitation energy increased, the disk structure became less pronounced, and the spot emission appeared to be closest to the stream. Advancing the phasing to the zero point measured from the Hβ and γ lines, put the spot even closer to the stream. Their Balmer tomograms showed axisymmetric emission, with most of it concentrated to lower velocities. Their HeII tomograms showed the strongest emission from a location almost consistent with the stream interaction zone and less emission from the second component. So they favoured a location of the HeII with the stream interaction zone, which was easier to displace with variations in mass transfer rate than irradiation zones on the secondary.

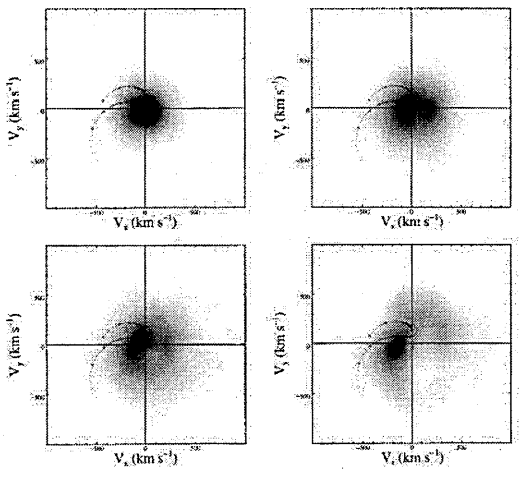

Figure 5.20: Doppler tomograms for Hα (upper left), Hβ (upper right), Hγ (lower left) and He II (lower right) of V405 Aur, Szkody et al. (2000).

- Doppler signatures of Hα flares in AE Aquarii, Welsh et al. (1998).

  In their tomograms it was immediately clear that they did not resemble those for an accretion disk, see Figure 5.21. The emission was not centred on the WD, but was clearly clumpy and did not show azimuthal symmetry with the strongest emission region occurring at low velocities. They believed that the tomograms had definitely been contaminated by flaring activity.

  Their tomograms from each night showed a different appearance, indicating that the emission was not stable, however they did have one feature in common. Most of the emission arises from a region with a small negative V_x and V_y component. There was a substantial amount of emission from near the centre of mass and from the inner face of the secondary star. There was no obvious feature of the gas stream. Thus, the Doppler tomograms showed none of the expected signatures of an accretion disk, and they concluded that there was no evidence for an accretion disk in AE Aqr.

  The propeller model however can make some qualitative predictions about Doppler tomograms: (i) the tomograms will look nothing like a standard disk tomogram; (ii) the blob trajectory is such that it forms a 'loop' in the ($-V_x$,$-V_y$) velocity quadrant, and as this is where the interaction of the blobs with the magnetic field is greatest, the bulk of the line emission will be expected to come from this region; (iii) material that has been ejected from the system will have low velocities, and so the central area of the tomogram should show a large amount of the emission. These predictions were in agreement with their observed tomograms. However, they concluded that although the propeller model was a better fit to their data, they were unable to produce conclusive evidence for its validity. As quantitative prediction do not exist for the model, the comparison with their data could only weakly test the theory.

- On the accretion mode of the intermediate polar V1025 Centauri, Hellier et al.

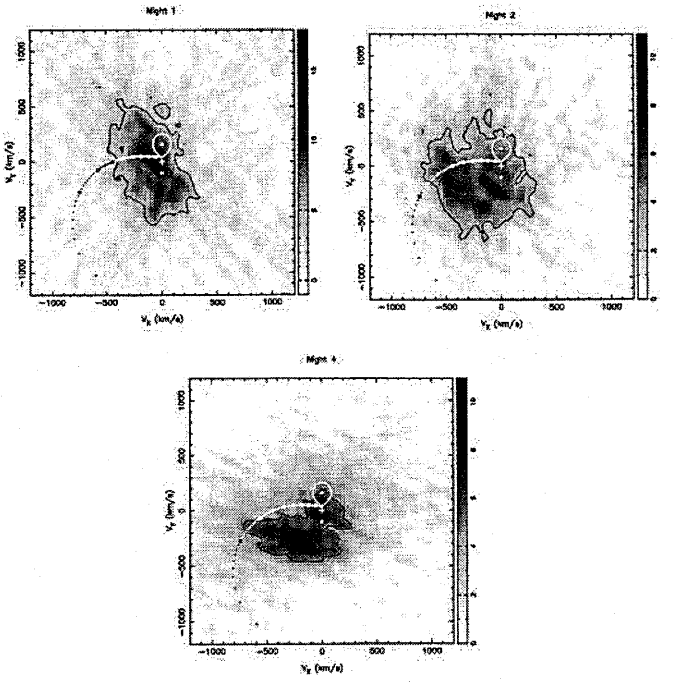

Figure 5.21: Doppler tomograms for three nights observations. Night 1 (upper left), Night 2 (upper right) and Night 4 (bottom) for AE Aqr, Welsh et al. (1998).

(2002b).

Hellier et al. used line profiles of Hβ folded on the orbital period, with phase 1 of the orbit cycle corresponding to a guess of inferior conjunction of the secondary. In the line centre was an S-wave that appeared as the brightest region of the tomogram. Conventionally this would be interpreted as arising from the heated face of the secondary, or from the accretion stream, especially where it impacts the disk.

There was also a higher velocity feature in the line which was not very well defined, but it gave rise to a brightening in the lower-left hand quadrant of the tomogram see Figure 5.22.

Hellier et al. also found weak evidence for a disk structure, seeing a double-peaked structure in the line. As this would form a ring feature in the tomogram, centred on

the velocity of the WD they stipulated that it was not well defined and incomplete.

Hellier et al. interpreted the tomograms first based on a conventional partial disk. The high-velocity emission was not symmetric about the WD and was enhanced in the lower-left hand quadrant. Thus the higher-velocity regions are not symmetric over the orbital phase. Since V1025 Cen is not eclipsing the likely explanation for this was from the accretion stream overflowing the outer disk, continuing into the inner disk and creating a localized disturbance in orbital phase. The idea was previously proposed in IPs to explain X-ray beat periods (Hellier (1991)) and may also occur in SW Sex stars Hellier & Robinson (1994).

In SW Sex stars, high-velocity line wings are at a maximum redshift at an orbital phase of $\approx$0.9 which matched with that of V1025 Cen with Hellier et al's adopted phasing. Thus the brightest region in the tomogram is at the right phase to correspond to emission from either the secondary star or the bright spot from the stream/disk impact site or a mixture of the two due to the phase uncertainty. Weaker emission looping leftwards towards the higher-velocity feature, could be emission from the overflowing stream.

Hellier et al. had insufficient information to interpret the velocities in the tomogram directly but they carried out a plausibility check against SW Sex star data and found that the overall line profiles were consistent with the stream-overflow idea.

Hellier et al. then went on to consider the alternative diskless model. However, a diskless flow is dependent primarily on the beat cycle, rather than the orbital or spin cycle tomograms. So they went further and found orbital-cycle tomograms that were sampled from particular beat phases, the same analysis technique used for FO Aqr by Marsh & Duck (1996), see Figure 5.23. The tomograms showed a hook-like feature that varied with beat phase. They found that the tail of the hook became

less pronounced during the ejection events, and re-formed during accretion episodes once per beat cycle. They also compared their beat-resolved tomograms back to the partial-disc model. They concluded that the emission they saw near a velocity of (0,300)kms^{-1} in all the beat phases, was probably from the secondary star. The 'hook' feature was caused by the stream flowing from the L_1 point, colliding with the disk, and then overflowing the disk (moving to the lower-left hand quadrant). They saw that the velocities in the lower-left hand quadrant were approximately half that of those of a free-falling stream, so it meant that the overflowing stream was slowed down by its interaction with the disk.

The stream would be lit once per beat cycle by the spin-pulsed X-ray beam, which explained why it was only seen for certain beat phases. As they did not have an ephemeris for the X-ray pulse though, they could not predict which phases these would be.

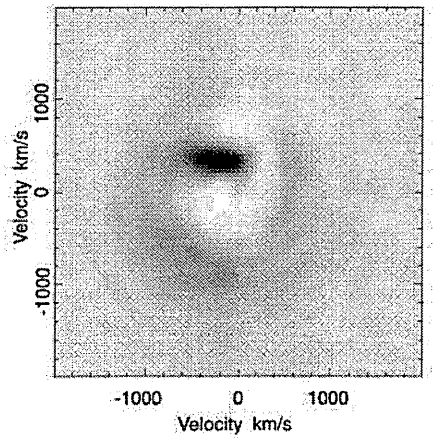

Figure 5.22: Doppler tomograms of the Hβ line for V1025 Cen, Hellier et al. (2002b)

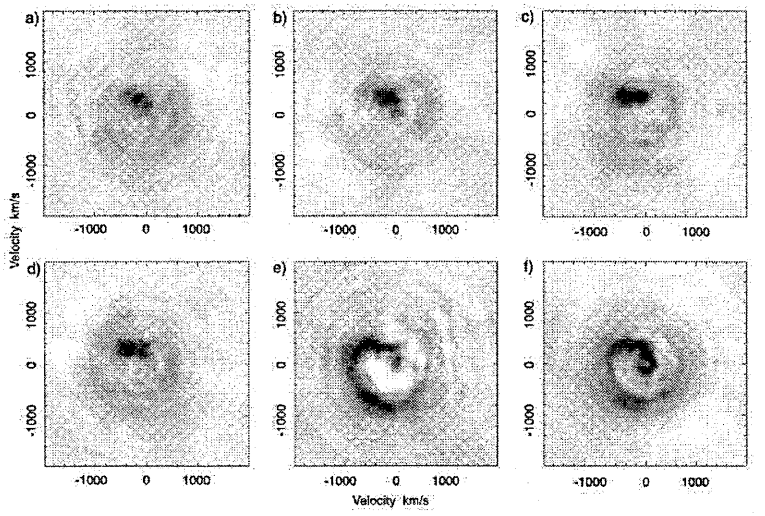

Figure 5.23: Orbital-cycle tomograms of the Hβ line from selected ranges of beat-cycle phase for V1025 Cen, Hellier et al. (2002b).

- A new cataclysmic variable RX J0757.0+6306: candidate for the shortest period intermediate polar, Tovmassian et al. (1998).

  Tovmassian et al. used the Doppler tomography technique to try and aid in determining whether the new CV RXJ0757.0+6306 was a candidate for the shortest period IP, see Figure 5.24. From their assumed parameters, the tomogram produced a dense spot which they interpreted as corresponding to the hot spot, as the phase was picked arbitrarily, it also meant that the position of this feature was arbitrary but it was evidence for the presence of a large accretion disk by a "doughnut" structure that appeared with the prominent hot spot on its edge.

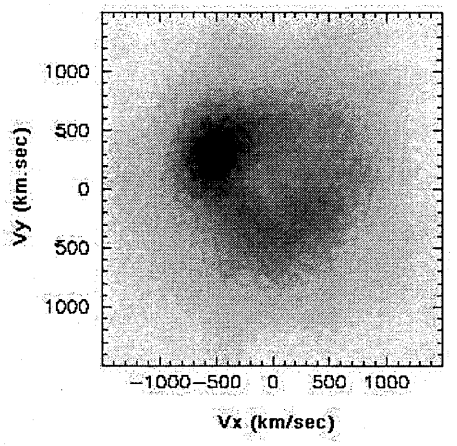

Figure 5.24: Doppler tomogram of the Hβ line for RXJ0757.0+6306, Tovmassian et al. (1998).

5.9 Observational tomograms vs. model tomograms

We compare some of the observed tomograms to that of the calculated tomograms produced by the model in which the parameters are almost similar. Although this is not a perfect match due to the assumptions of the model, there are some important similarities that are seen between the tomograms.

5.9.1 V1025 Centauri

Figure 5.25 shows eight images taken from the two magnetic models at parameters of $P_{\rm spin}$=2000s, $P_{\rm orb}$=80m close to the actual spin and orbital periods of V1025 Cen of 2146s and 1.41hr respectively. For the n^3 model the tomograms are taken at k_o values of 1×10^2, 5×10^2, 2×10^4, 5×10^5 and 1×10^6 from upper left top row to lower right middle row. In the n^6 case the k_o values are 1×10^2, 5×10^2 and 1×10^3 for the bottom row left to right.

These images were chosen for their closest resemblance to the observational tomogram. As we do not know the exact magnetic field strength of the system or how the magnetic field behaves we can only speculate at this stage as to which parameters best suit the actual binary system. If we compare them with the observed tomogram in Figure 5.26, taken from Hellier et al. (2002b) we see that both the tomograms from the model and the observational tomogram have a large concentration of emission at the L_1 point that then curls round into the lower left quadrant, lower right quadrant and then up into the upper right quadrant. Each model tomogram has its similarities to the observed one and each has its differences.

If we start with the first tomogram on the top row, we see that both model and observed tomogram have strong emission at the L_1 point with less dense material curling round into the three quadrants named above. However the model tomogram curls further round and almost back on itself which is not indicated in the observed tomgoram, but the basic characteristic is there. The second image of the top row again shows the strong emission from the L_1 point but yet does not curl round far enough into the lower or upper right quadrants to match that of the observed tomogram. The third image shows a much better resemblance having strong emission from the L_1 point curling round into the lower left quadrant. The observed tomogram also shows this with a dark grey curl from the dense emission region of the L_1 point. The first image of the middle row shows this feature better with less dense material from the L_1 point curling round through all three quadrants as in the observed tomogram. However the emission from the L_1 point in the model tomogram is seen as a vertical region from 200kms^{-1} to 600kms^{-1} before it curls round into the three quadrants, whereas in the observed tomogram the dense emission from the L_1 point is horizontal before curling round. The second image of the middle row shows similar features to that just describe except the dense emission carries further round than before

and further than that seen in the observed tomogram, but still the features are similar.

Finally we come to the n^6 model tomograms. All again have some slight resemblance to the observed tomogram. The all share the common feature of strong emission from the L_1 point though it is more pronounced in the second and third image. They share the curl feature into the three quadrants as the observed one does, with the first and second images curling slightly further round. However this curl feature is a dense region indicated by the greyness of the curl in the observed tomogram, which is not seen as strong in the model n^6 images.

The best fit to the observed tomogram is then that of the n^3 model tomograms at intermediate to high k_o values of 2×10^4, 5×10^5 and 1×10^6 consistent with the parameters used in the model that are the most accurate to V1025 Cen. This then indicates a moderate magnetic field strength of $10^{33} - 10^{34}\mathrm{Gcm}^3$ for this type of system.

Hellier et al. also used the magnetic model HyDisc (see section 3.4) to create simulated tomograms of V1025 Cen. However for their model they assumed white-dwarf and red-dwarf masses of 0.7 and $0.1\mathrm{M}_\odot$, respectively, an orbital period of 5077s, tweaked the k parameter until they obtained a spin period of 2147s and used a field of $\approx$ 1MG so they could carry out a direct comparison. The model we used however is for different regions of parameter space to investigate the accretion flows in IPs. As we do not use specific parameters set by each individual IP we can not make a direct comparison at this stage but can still pick out the similarities between the observed tomograms of V1025 Cen and our simulated tomogorams at parameters close to the real values of V1025 Cen.

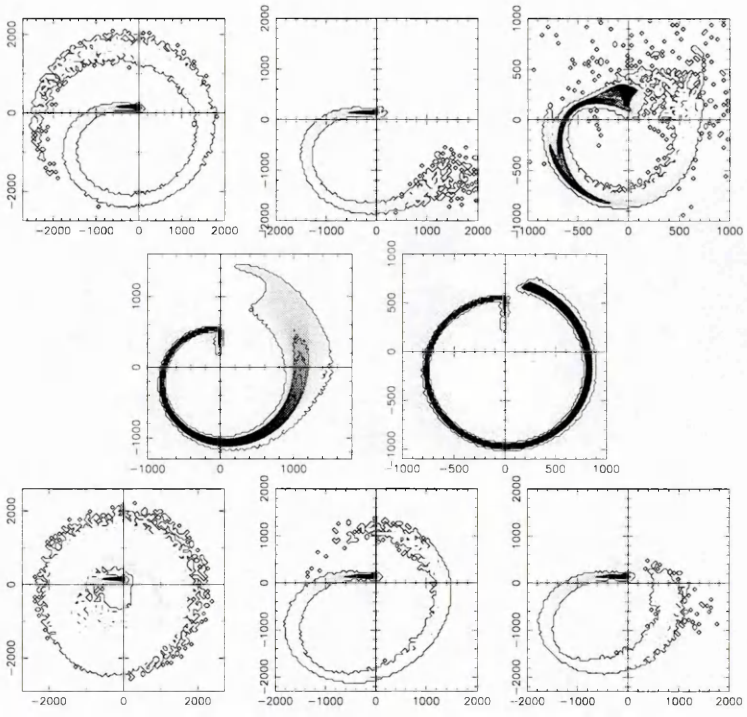

Figure 5.25: Model tomograms of V1025 Cen. The top and middle row are from the n^3 model and the bottom from the n^6 model.

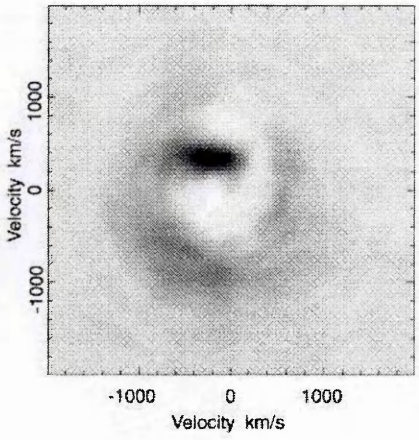

Figure 5.26: Doppler tomogram of the Hβ line for V1025 Cen, Hellier et al. (2002b)

5.9.2 V405 Aurigae

As for V1025 Cen, the model tomograms were taken from both magnetic models at parameters that were closest to the actual values of V405 Aur spin and orbital periods of 545.5s and 4.16hr respectively. The model tomograms were taken at the parameters of $P_{\rm spin}$=500s, $P_{\rm orb}$=4hr at k_o values of 5×10^2 and 1×10^3 for the n^3 model and 5×10^4 and 1×10^5 for the n^6 model shown in figure 5.27.

The first and second model tomograms are taken from the n^3 model and we can see that the strong emission in the center of the tomograms compares well to the observed tomograms taken by both Szkody et al. (2000) figure 5.28 and Still et al. (1998) figure 5.29, though more so to Still et al.. The observed tomograms of Szkody et al. show a very large dense circle of emission around the center of three of the tomograms with the fourth having the region as a small oval crossing the upper left to the lower left quadrants. Still et al. however show more of a defined curled region from the upper left quadrant to the lower left emerging from the L_1 point, this is similar to what is seen in the model tomograms. The first with strong emission curling round into all four quadrants at low velocity as in the 1st, 2nd and 3rd images of Szkody et al. The second and fourth model tomograms are similar to Still et al. in that they show strong emission at low velocity in the four quadrants but they are broken up some what with less dense emission in between. The third image bears a very strong resemblance to both the fourth image of Szkody et al. and the fourth of Still et al.. All show strong emission from the L_1 point curling round at low velocity into the lower left quadrant, less dense emission then curls round from this point into the upper right quadrant though there is a slight break in the less dense emission in the lower right quadrant in Szkody et al's tomogram.

Thus in the case of V405 Aur although most of the model tomograms in some way or another have large similarities to at least one of the observed tomograms, we would say

that the the first model tomogram from the n^3 model with a k_o value of 5×10^2 indicating a relatively weak magnetic field of $\leq 10^{33}$Gcm^3, is the most alike to the observed V405 Aur tomgorams.

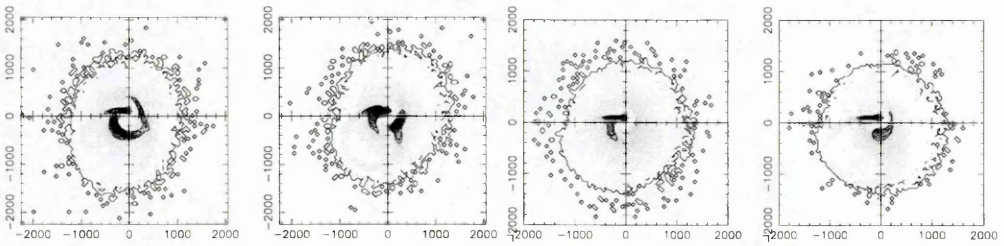

Figure 5.27: Model tomograms of V405 Aur. The first and second tomograms are from the n^3 model and the third and fourth from the n^6 model.

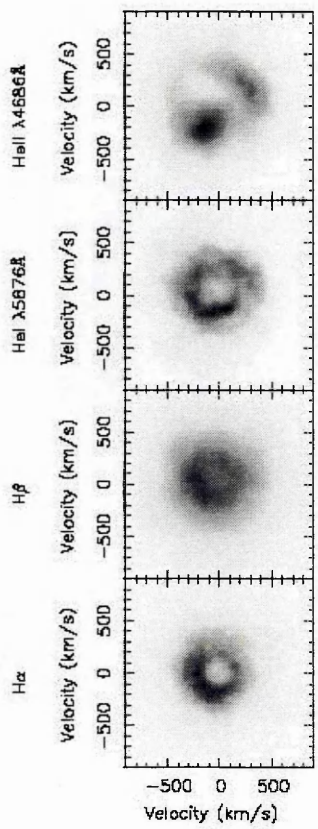

Figure 5.28: Doppler tomograms of the Hα, Hβ, He I λ5876 and HeII λ4686 emission lines for RX J0558+5353 (V405 Aur), Still et al. (1998).

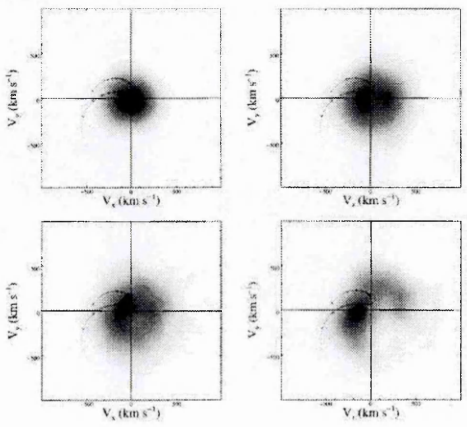

Figure 5.29: Doppler tomograms for Hα (upper left), Hβ (upper right), Hγ (lower left) and He II (lower right) of V405 Aur, Szkody et al. (2000).

5.10 Overall Chapter Conclusion

In this chapter we have seen that both the n^3 and n^6 models produce similar results in the simulated Doppler tomograms. We see interesting characteristic features for the particular systems. For propellers the tomogram feature depends on the trajectory of the flow and the angle at which material is expelled from the binary. For the stream fed accretor tomograms, we see that their features depend on the direction of the stream flow out of the L_1 point, as well as where they impact the WD. For the disk systems we see two distinct types of tomograms. A diffuse disk with a high velocity, low density ring and a low velocity, high density ring feature and a concentrated disk with just the emission from the L_1 point and the high velocity, low density ring. For the ring systems we see a ring in the tomograms that clearly moves faster in the bottom two quadrants than it does in the top two.

For the specific equilibrium situation we still see the characteristics mentioned above but with slight differences. In the n^3 case, the disk systems still show both a low and high velocity ring with the inner dense ring becoming less pronounced as the disk becomes more diffuse. For the weak propeller systems, we see the hook emission feature characteristic to propeller accretion but we also see less dense material curling round the quadrants as the material must also be being accreted onto the WD to have these propellers in equilibrium. The streams are similar in feature to the propellers in that there is emission from the L_1 curling round as well as less dense material forming a ring around it, more so in the two right quadrants where the stream is becoming scattered. The ring systems still showed their typical ring feature surrounded by a high velocity, low density ring.

For the n^6 model at equilibrium only disk and stream accretion is observed. The disk tomograms show the same features as mentioned for the n^3 case, the streams show their characteristic feature of the slight hook out of the L_1 point, with a straight or curled tail

from this hook (depending on how far round the WD the stream impacts) spreading out towards the end.

Doppler tomography interpretation relies heavily on knowing the inclination angle to interpret the feature correctly and deduce the correct accretion mechanism. At small inclinations most of the features in the tomograms all appear the same. As the inclination angle increases we see more characteristic features in the tomograms allowing us to interpret the accretion flow better, but there is a caution, this can also be misleading. At high inclinations the features all increase in size and velocity, which we would interpret as the accretion flow being closer to the WD. Knowing these small details through these simulations will allow true accretion flows to be interpreted from the tomograms instead of giving a false perspective.

If we compare the simulated tomograms with the observed tomograms, we see some similarities in the features they produce:

- Strong emission concentrated in the gas stream/secondary star region.
- A bright spot, corresponding perhaps to the stream/disk collision.
- Axisymmetric emission seen for a disk feature.
- A strong emission region seen occurring at low velocities, arising from a region with small negative V_x and V_y component, with substantial emission from near the center of mass and the from the inner face of the secondary star. This is similar to what we observed for our simulated propeller tomograms.
- A ring feature is seen in the tomograms for a disk, centered on the velocity of the WD.
- A large accretion disk is represented by a "doughnut" structure, with a prominent hot spot on its edge.

Thus the simulated Doppler tomograms can really be an asset for distinguishing and interpreting the types of accretion flow that take place in IPs. We can comment on the angles of trajectories in these flows, the sites of impact regions and how diffuse the accretion spread is, thus giving us further insight into their accretion geometry. We re-enforce the fact that the doppler tomograms in this chapter are based on the velocity components of all the particles present in the simulated accretion flow at a given instant, giving the assumption that all parts of the accretion flow have a uniform temperature and level of flux emission. In true systems this is of course not the case. If we were to look at the emission lines of the systems, we would most certainly see lines from the hottest regions, the inner most regions of the flow. We would only see emission at higher velocities and so would probably see these strong areas in the tomograms and not that of the lower velocity regions. Thus these simulated tomograms are just the start to a means of interpreting observational tomograms of IPs.

Further work on Doppler tomography techniques and other aids to understanding the accretion flow geometry better in IPs are discussed in the final chapter.

Chapter 6

Conclusions and Further Work

6.1 Conclusions

The object of this thesis was to investigate the characteristic accretion flows that occur in IPs, to study them further and produce an Atlas of simulated data which observers could refer back to in order to better understand the systems they are observing. This thesis has partly begun that process with the compilation of the simulated accretion flows and Doppler tomograms.

By looking firstly at the X-ray orbital modulations in IPs, we have been able to clarify one aspect of the accretion geometry. From analysing 30 archival *ASCA* and *RXTE* X-ray observations of 16 IPs, we showed that X-ray orbital modulation were widespread amongst these systems, but not ubiquitous. Only seven of the sixteen systems (BG CMi; FO Aqr; TV Col; TX Col; V1223 Sgr; AO Psc and V405 Aur) showed a clearly statistically significant modulation depth whose amplitude decreased with increasing X-ray energy. Two further IPs (EX Hya and XY Ari) are known to show eclipses. Interpreting this orbital modulation as due to photoelectric absorption in material at the edge of an accretion disk

implied that such modulations are visible for all system inclination angles in excess of 60 degrees, in agreement with previously published simulations. However, it is also apparent that the presence of an X-ray orbital modulation can appear and disappear on a timescale of ~years or months in an individual system. This may be evidence for the presence of a precessing, tilted accretion disk, as inferred in some low mass X-ray binaries. From this study we were able to determine that these IPs contain accretion disks, or at least structures that resemble disks.

By using the particle hydrodynamical code HyDisc we were able to simulate the parameters in which IPs exist, and assess the type of accretion flow that takes place in the systems. We inferred that at a spin to orbital period ratio of <0.1 disk accretion usually takes place, between 0.1 and ~0.5 we see propeller accretion and above this at strong magnetic field strengths ring accretion takes place. By plotting this simulated data against known IP systems and using the information gathered from the findings of the orbital modulation we were able to ascertain that BG CMi; FO Aqr; V1223 Sgr; AO Psc and V405 Aur are all in agreement for containing accretion disks. TV Col and TX Col are border line cases, appearing just on the edge of the border between weak propeller flow and disk accretion. By compiling the simulated accretion flows, a basis of comparison has begun into identifying the accretion mechanism at work in IPs. The simulated flows also showed the variation in accretion flows depending on the structure of the magnetic field. We still do not know whether the WD field is a pure dipole or a much more complex field. The simulated flows show just how vast a difference this can make. For the n^6 case, at a spin to orbital ratio of < 0.1, the systems are still disk accretors like that of the n^3 case. Above this value they are all stream-fed, no weak propellers and no ring accretion is seen.

Doppler tomography allows us to get a much greater understanding of the accretion flows, with the main benefit being able to interpret features out of the orbital plane, vital

for the study of the accretion curtains in IPs. The simulated tomograms produced features that have been seen in observed tomograms, making the model relatively viable. From interpreting the simulated Doppler tomogams we can infer certain types of flow patterns. We were able to ascertain the angle of projection of material in propeller accretion, how far the stream travels round the WD before impacting it and in which direction the flow travels out of the L_1 point. We could determine whether the system contained a concentrated disk or a diffuse disk and the features that ring accretion displays. Altering the inclination angle showed that the Doppler tomograms can be misleading and misinterpreted, unless you have some basis for comparison. At an inclination of 10°, the tomogram features are all similar no matter what parameter space values they occur at. Constructing this atlas of such varying values and investigating all the possible scenarios at which IPs occur allows us to interpret observed tomograms to a much higher level of accuracy and ascertain the correct accretion flow mechanism operating in the system.

We have presented a number of methods for determining the characteristics of accretion in the magnetic cataclysmic variable subclass of Intermediate Polars. It is hoped that with the numerous accretion flows and Doppler tomograms produced in this thesis a complete simulated reference atlas can be composed and used as a basis for comparison to observed data. To establish this further, there are a number of directions which we can take.

6.2 Further Work

- The Doppler tomograms from HyDisc are produced from simulated accretion flows by simply looking at the velocity of each "blob" and then projecting this on a Doppler map. To continue the simulated Doppler tomography further we need to look at realistic tomograms from HyDisc, where we look at the temperature and emission from each "blob" and construct the Doppler tomogram maps from these values,

giving us a better comparison to observed tomograms.

- More Doppler tomograms are needed of optical observations of IPs to compare to the data we present in this thesis and as was explained in Chapter 5 not many have been calculated.

- Spin cycle tomography could also aid in the further understanding of the accretion mechanism on to the WD; our tomograms deal with the orbital cycle. Hellier (1999) carried out a study on seven IPs to see if this technique would be a useful diagnostic tool. We could again compare and contrast our data with simulated spin-cycle tomograms and compare with real data to see if any conclusive connections can be made.

- A lot of the observed tomograms picked up an emission region corresponding to the disk/stream impact site. This is not modelled explicitly in HyDisc. A comparison of tomograms to that of the data we used in determining the X-ray orbital modulations may yield further in sights.

- The work should also be extended with newly recognised intermediate polar systems, for population statistics and investigation into intermediate polar to polar evolution, as surveys such as SLOAN and HQS are finding many new intermediate polars.

- Another interesting study to add to the numerous models would be to compile a data set of simulated X-ray lightcurves that would be expected from each of the systems we studied in parameter space for both models to also aid in a comparison to real data.

- IPs display a range of accretion mechanisms, depending on the mass-transfer rate, field strength and spin of the WD. The latter two have been investigated in this thesis, the third, mass-transfer rate is another criteria to be looked at. Using a

similar model and parameter space it would be useful to investigate what type of accretion would happen if we vary the rate of diamagnetic blobs proceeding from the secondary to the WD.

In conclusion, it is encouraging that progress has been made, and the atlas is starting to take shape, but there are still plenty more areas of research still to be investigated concerning the intriguing Intermediate Polars.

APPENDIX A

Current Information on Known Intermediate Polars

In this section of the appendix we present a brief summary of the observational history and background information on each known or suspected intermediate polar.

A.0.1 Aqr1

Listed in Downes et al. (2001) as Aqr1, it is also known as 2236+0052 and was identified spectroscopically as a CV by Berg et al. (1992) in a bright QSO survey. Woudt & Warner (2004) observed Aqr1 over four nights in 2002 November. From their light curves and taking the FT of the combined data set they found an unambiguous peak at ω=2477.1μHz which they inferred as the spin frequency i.e. $P_{\rm spin}$ = 403.7s. There were also two prominent sidebands, however the orbital frequency could not be determined unambiguously from the data. A more thorough study of Aqr1 is needed in order to determine its orbital period. The classification as an IP however, is secure due to the presence of the orbital sidebands.

A.0.2 AE Aquarii

AE Aquarii is classified as a nova-like star belonging to the DQ Herculis subclass of magnetic cataclysmic variables at a distance of D $\sim$ 100 $\pm$ 30pc (Welsh et al. (1995), Friedjung (1997)). The variable star is a low mass non-eclipsing binary system, where the normal component (secondary) is a K3-K5 main sequence red dwarf (Bruch (1991a),Welsh et al. (1995)) and the primary is a magnetised WD rotating with a period of 33s (Patterson (1979a), Eracleous et al. (1994). Optical photometric and spectroscopic studies indicate that it has an orbital period of ~9.88hr (Joy (1954)). The inclination angle of the system is limited to $50° < i < 70°$ and the mass ratio is $0.58 \lesssim (q = M_2/M_1) \lesssim 0.89$ with a WD mass evaluated as $0.8 \lesssim M_1 \lesssim 1 M_\odot$ (Reinsch & Beuermann (1994),Welsh et al. (1995)) and a red dwarf mass of $0.41 M_\odot$. The system has an orbital eccentricity of e $\approx$0.02 (Chincarini & Walker (1981)). AE Aqr is one of the longest period cataclysmic variables, the 33s spin period of the primary is the shortest among CVs (often referred to as a "WD pulsar"), and it exceeds the minimum period of a WD rotating close to the breakup speed by a factor of less than three. It emits detectable radiation in almost all parts of the spectrum and was observed as a powerful non-thermal flaring source in radio (Bastian et al. (1988)) and gamma rays (Bowden et al. (1992); Meintjes et al. (1994)). The optical, UV and X-ray radiation of the system is predominantly thermal and is coming from at least three different sources. The visual light is dominated (up to 95%) by the secondary, (Bruch (1991b); Welsh et al. (1995)), whilst the contribution of the primary is observed mainly in the form of 33s coherent oscillations detectable in the optical, UV and X-rays (Patterson (1979b); Patterson et al. (1980). Whereas the X-ray spectra of most IPs are hard, AE Aqr has a soft X-ray spectrum. AE Aquarii is a propeller system where the magnetospheric radius is larger than the co-rotation radius.

A.0.3 FO Aquarii

Discovered as a hard X-ray source (H2215-086) by Marshall et al. (1979), FO Aqr was identified as a cataclysmic variable by Patterson and Steiner (1983). It has a binary orbital period = 4.84hr whereas the WD spins with a period = 1254s. Optical photometry obtained by Patterson & Steiner (1983) showed the presence of three periodicities in its light curve. The dominant photometric feature is a coherent variation at a period of 1254s. The strong modulation with a consistent period and consistent phase was also detected in X-rays with the EXOSAT observatory which confirmed the earlier anticipation that the 1254s period is the rotation period of the WD. Modulations have also been seen at the sideband period (beat period) of 1350s in the optical and X-ray bands (e.g Patterson & Steiner (1983); Norton et al. (1992c)).

A.0.4 V1425 Aquilae

Nova V1425 Aquilae 1995 was discovered on 1995 February 7 by K.Takamizawa (Nakano et al. (1995)), at a magnitude of 8.1. Mason et al. (1996) used its similarity to Nova V1668 Cygni 1978 to extrapolate a maximum brightness of $M_v \sim 6.2$. This classifies Nova Aquilae as a fast nova. They also deduced from infrared considerations that the dust shell of the nova was optically thin shortly after its outburst. Retter et al. (1996) and Leibowitz et al. (1997)) reported the discovery of two photometric periods in the light curve of Nova Aquilae 1995, and pointed out the resemblance of this object to intermediate polar systems. Retter et al. (1998) found three periods in the power spectrum 0.2558d, 0.06005d (with its first harmonic) and 0.079d the beat period between the first two periods. The inter-relations among the frequencies of the three periods are characteristic of intermediate polar systems. Based on this they suggest that V1425 Aquilae belongs to this group. They interpret the longer 6.14hr period as the orbital period of the binary system, the 5190sec

period as the spin period of a magnetic WD and the 1.9hr period as the beat period between them. Lyke et al. (2001) determined that the WD in the V1425 Aql system has a CO composition and is at a distance of 3.0±0.4kpc.

A.0.5 XY Arietis

XY Ari also known as H0253+193 was discovered as an X-ray source using the *Einstein* satellite (Halpern & Patterson (1987)). It lies within 5 arcsec of the core of the molecular cloud Lynds 1457 and was initially suggested to be an X-ray emitting protostar. However, Patterson & Halpern (1990) noted that the X-ray properties of XY Ari strongly resemble those of an intermediate polar and the binary nature of the system was confirmed with the discovery of X-ray eclipses recurring with a 6.06hr orbital period (Kamata et al. (1991)). XY Ari is the only intermediate polar to exhibit deep X-ray eclipses. High extinction through the molecular cloud means that XY Ari is not observable at optical wavelengths. X-ray and infrared studies (Zuckerman et al. (1992); Allan et al. (1996a)) showed it to have a 6.06hr orbital period and a 206s spin period, and revealed deep eclipses implying an inclination of $80° < i < 87°$. It's mass ratio $q = M_2/M_1$ is in the range 0.43-0.71 with a WD mass of 0.91-1.17$M_\odot$ and a red dwarf mass $\sim 0.62M_\odot$.

A.0.6 V405 Aurigae

V405 Aur was classified as an intermediate polar (V=14.6 mag), soon after its discovery during the *ROSAT* All-Sky Survey, which also showed a soft X-ray spectrum more similar to that of polars. A pointed observation by Haberl et al. (1994) revealed a 272.74s soft X-ray periodicity, optical spectroscopy from the same paper found the orbital period to be 4.15h. The 273s period was first detected in optical photometry by Ashoka et al. (1995) and was subsequently determined to be a harmonic of the WD spin period of 545.46s by Allan et al. (1996b) and Skillman (1996b). A re-analysis of the *ROSAT* data by Allan

et al. (1996b) proved that the 545s fundamental was also present in the hard X-rays.

A.0.7 HT Camelopardaris

HT Camelopardalis, is a recently discovered X-ray-bright cataclysmic variable from the *ROSAT* All-Sky Survey, Tovmassian et al. (1998) identified RX J0757.0+6306 as an 18th magnitude blue star with emission lines and suggested periods of 1.35hr and 510s (candidates for $P_{\rm orb}$ and $P_{\rm spin}$, respectively). The star was later renamed HT Camelopardalis. The spectrum shows bright lines of H, He I, and He II, all moving with a period of 1.433hr, which Kemp et al. (2002) interprets as the orbital period close to that suggested above by Tovmassian and the star's brightness varies with a strict period of 514.8s as suggested. These properties qualify it as an intermediate polar. Normally at V=17.8, the star shows rare and brief outbursts to V=12-13.

A.0.8 BG Canis Minoris

BG Canis Minoris is a well known intermediate polar, whose optical counterpart, a blue cataclysmic variable of about 15th mag, was identified with the hard X-ray source 3A 0729+103 by McHardy et al. (1984). It has positively detected circular polarisation in the optical and infrared (Penning et al. (1986), West et al. (1987), providing evidence for a strong (~4MG) magnetic field of the WD in the system. Optical studies and X-ray observations of the system with *Einstein* and *EXOSAT* established its orbital period to be ~3.25hr and determined a pulse period of ~913s which was taken to represent the spin period of the WD (McHardy et al. (1982 1984 1987); Penning (1985)). It belongs to a group of seven intermediate polars whose rotational periods of their white dwarfs are known to be changing, in the case of BG CMi it has a decreasing rotation period. de Martino et al. (1995c) inferred from the orbital motion of the WD in BG CMi that it was a moderate inclination system of $i \sim 55° - 75°$.

A.0.9 V709 Cassiopeia

The X-ray source RX J0028.8+5917 was detected in the *ROSAT* All-Sky Survey and identified as an intermediate polar on the basis of its spectral characteristics by Haberl & Motch (1995b). A further 18ksec pointed observation by the ROSAT satellite led to the detection of X-ray pulsations at 312.8s and a conventional 'hard' intermediate polar spectrum. Motch et al. (1996) identified the X-ray source with a 14th magnitude blue star, V709 Cas. The optical spectrum of this star showed radial velocity variations with periods of P=5.4±0.2hr and P=4.45±0.15hr, one of these periods was assumed to be the orbital period. From a study of the emission line radial velocities, Bonnet-Bidaud et al. (2001c) removed the uncertainties on the different aliases of the orbital period and a best value is found at (5.34±0.0048)hr. V709 Cas also exhibits a double-peaked X-ray pulse profile and shows no evidence for X-ray beat period or orbital modulation, so must be a disk-fed accretor seen at low inclination angles. The short spin period of the WD of V709 Cas indicates that it has a weak magnetic field, so the radius at which material is captured by the field lines is relatively small (Norton et al. (1999)).

A.0.10 V1025 Centauri

V1025 Cen was discovered by Buckley et al. (1998b). Follow up X-ray observations (Hellier et al. (1998)) found a spin period of 2147s (revealed by an optical and X-ray pulsation), and suggested an orbital period near 1.417-1.5hr. Other than this V1025 Cen is little studied, with, as yet, no emphemerides for the periodicities, no estimate of the field strength, and no determination of the binary inclination or of the component mass.

A.0.11 RR Chamaeleontis

RR Cha is the remnant of Nova Chamaeleontis 1953 a moderately fast nova (rapid rise to maximum brightness). A recent photometric study puts it at V=18.3 (Woudt & Warner (2002)). It is an eclipsing system with an orbital period of $P_{\rm orb}$=3.362hr showing both positive and negative superhumps. In two independent data sets Woudt and Warner identified a photometric periodicity at 1950s, suggesting this might be the spin period of the WD. Recent polarimetric observations of RR Cha (Rodríguez-Gil & Potter (2003)) revealed circular polarisation at the 1950s periodicity, supporting the classification as an IP.

A.0.12 DD Circinus

DD Cir was discovered as Nova Cir on the 23rd of August 1999 at an apparent magnitude of 7.7 (Liller et al. (1999)). It proved to be a very fast nova, with a pre-eruption brightness of V $>$ 21 (Downes et al. (2001)). From the light curves produced by Warner et al. (2003), DD Cir is an eclipsing system with an orbital period of 2.339hrs, hence lying within the 'period gap'. It shows a mean magnitude V $\sim$ 20.1 when out of eclipse and has an inclination $\sim$70°. There is a consistent photometric modulation at $\sim$670s which is either the spin period of the WD, or its orbital sideband.

A.0.13 DW Cnc

DW Cnc was discovered in the Byurakan blue-galaxy survey and identified as a CV from its Balmer emission lines (Stepanian 1982; Kopylov et al. (1988)). Patterson et al. (2004) radial-velocity searches found strong detections at two periods, 1.43hr and 2315s which they interpreted as the orbital period of the binary and the spin period of the WD respectively. They also found an additional strong period at 4195s which conincided with the

difference frequency $1/P_{\rm spin}$ - $P_{\rm orb}$.

A.0.14 TV Columbae

TV Col is a 13th magnitude intermediate polar with multiple periods found in its light curves. Recently completed *Hubble Space Telescope* fine guidance sensor interferometric observations determine the first trigonometric parallax to TV Col which puts it at a distance of 368^{+15}_{-17} McArthur et al. (2001b). It was first discovered as the high-latitude hard X-ray source 2A 0526−328 with the *ARIEL V* satellite by Cooke et al. (1978). The X-ray source was optically identified with TV Col by Charles et al. (1979) on the basis of its accurate HEAO-1 position (Schwartz et al. (1979) and its optical emission-line spectrum, being the first CV discovered by its X-ray emission. It has an orbital binary period of 5.486hr (Hutchings et al. (1981) detected from the emission-line radial velocities. TV Col shows four additional periods: a 1911s X-ray period representing the rotation period of the WD (Schrijver et al. (1985); a 4 day nodal precession of the accretion disk period (Hellier (1993); a ∼5.2hr period that is the beat between the two longer periods (Motch (1981)) - interpreted as a negative superhump Retter et al. (2003); and a photometric period of 6.36hr (Retter et al. (2003) - interpreted as positive superhump. It has the longest orbital period of any permanent superhump system. Even after a larger number of photometric and spectroscopic observations in the ultraviolet and optical, the detailed nature of TV Col is still unclear.

A.0.15 TX Columbae

The X-ray source 1H0542−407 was discovered by the *HEAO* 1 X-ray satellite and optically identified with a cataclysmic variable by Tuohy et al. (1986) on the basis of strongly variable light curves and optical emission line spectra. TX Col exhibits a number of periodicities in its optical and X-ray light curves. *EXOSAT* observations (Tuohy et al.

(1986)) revealed a strong soft X-ray modulation at ~1920sec, which was later seen in the radial velocities, at a low amplitude. This period was identified as the WD spin period and refined to 1911sec (Buckley & Tuohy (1989)). Optical photometry from 1984-1985 showed the dominant period to be at 2106sec which is also the strongest period in the harder X-rays, interpreted to be the $\omega - \Omega$ sideband, or beat period (where ω is the WD spin frequency, and Ω is the orbital frequency). An orbital period of ~5.72hr was determined from the radial velocity curve, which was consistent with the value obtained from the *EXOSAT* observations. The high soft X-ray flux and the absence of a modulation at the spin period in optical data are quite unusual among intermediate polars, nevertheless all the presumed low inclination ($i< 30°$) systems such as TX Col show their dominant optical period at the beat period.

A.0.16 UU Columbae

Burwitz et al. (1996)reported the discovery of a new magnetic cataclysmic variable, identified as the V~17.6 mag optical counterpart of the bright, soft, high-galactic latitude X-ray source RX J0512.2−3241 detected during the *ROSAT* All-Sky Survey. From optical follow-up B and V CCD photometry Burwitz et al. (1996) derived the most probable spin and orbital periods to be (863.5±0.7)s and (3.45±0.03)hr respectively and set a lower limit for the distance to the system of $d>$ 740pc.

A.0.17 AP Crucis

AP Cru was Nova Crucis 1936 and is currently at V ~18. Woudt & Warner (2002), used four high-speed photometric runs to produce light curves that determined the orbital period to be 5.1hr. Their FT showed a significant band of power which on examination was found to be a result of a coherent modulation, broadened by amplitude modulation. This signal was present in all four light curves and was seen to have a period of 1837s.

A persistent signal of this kind is characteristic of an IP. However AP Cru is at a low Galactic latitude (2°) and at a distance 500pc, such that it is unlikely to be detectable in the X-ray region, and so difficult to confirm.

A.0.18 V2306 Cyg

Israel et al. (1998) discovered that 1WGAJ1958.2+3232 was a pulsating X-ray source. Strong modulations of this source in X-rays were obtained from the ROSAT PSPC (Positions Sensitive Proportional Counter) (721±14s) and a more accurate period of 734±1s from ASCA was presented by Israel et al. (1998) and Israel et al. (1999). Photometric observations of the optical counterpart of 1WGAJ1958+3232 known as V2306 Cyg, exhibited strong optical variation, compatible with the X-ray period (Uslenghi et al. (2000). This modulation was interpreted as evidence of the spin period of the WD. Uslenghi et al. (2000) detected a circular polarisation from the source in the R and I bands, with evidence for a possible modulation of the polarisation at twice the previously observed pulsation period. On the basis of optical photometry and low resolution spectroscopy, Israel et al. (1999) proposed a $m_w = 15.7$ star as the optical counterpart of 1WGAJ1958.2+3232. Further spectroscopic measurements carried out by Negueruela et al. (2000), as well as time resolved optical photometry performed by Uslenghi et al. (2000) (which provided detection of optical modulation at 733.24±0.02s), confirmed the candidate of Israel et al. (1999) and allowed its classification as an Intermediate Polar. Zharikov et al. (2001) obtained time resolved spectroscopy and R-band photometry from which they deduced an orbital period of 4.36hr and confirmed the pulsation period of 733s. Later, Norton et al. (2002) obtained UBVRI photometry and reported that the orbital period was 5.387±0.006h, corresponding to the -1 day alias of the period found by Zharikov et al. (2001). Evidence from the detection of an optical beat pulse shows that the true spin period is in fact 1466s.

A.0.19 YY Draconis

YY Dra is a 16th mag dwarf nova and is one of a small number of intermediate polars that show outburst behaviour. It was discovered by Tsesevich (1934) and originally misclassified as an Algol-like system. Detected as an X-ray source by *Ariel V* (3A 1148+719) and *Einstein* (2E 1140.7+7158), it was subsequently reclassified as a cataclysmic variable. The intermediate polar nature of YY Dra was eventually recognised by Patterson et al. (1992), who discovered optical photometric modulation at periods of about 265s and 275s. Indications of sub-harmonics at periods of 529s and 550s suggested that the spin period of the WD might actually be 529s, and that 550s was the beat period between the orbital and spin periods, (Norton et al. (1999)). Mateo et al. (1991) deduced that it yielded an orbital period of 3.96hr, with a spectral type of dM4±1 for the secondary star based on the strength of its near-infrared spectral features. The spectroscopic mass ratio of YY Dra is q=M_2/M_1 = 2.1 ± 0.3. Assuming the secondary obeys the mass-radius relation for late type dwarfs, they derived the following parameters: $M_2 = 0.39 \pm 0.08 M_\odot$, $M_1 = 0.83 \pm 0.18 M_\odot$, i=42° ± 5° and the distance 155±35pc based on an application of Bailey's method (a method for determining the distance of a cataclysmic variable by making use of the $K(2.2\mu m)$ magnitude of the secondary star. This is achieved by calibrating surface brightness in this band as a function of effective temperature).

A.0.20 PQ Geminorum

PQ Gem (RE 0751+14) was discovered in the extreme-ultraviolet (70-200Å) all-sky survey by the UK Wide Field Camera on the *ROSAT* satellite (Mason et al. (1992)). It was soon realised that this star was not a typical magnetic CV in that it could not be placed uniquely into the AM Her or the Intermediate Polar category. In common with IP systems, PQ Gem has an asynchronously spinning WD (P_{spin} = 13.9min); much shorter than its

orbital period of 5.2hr, a strong, spin-modulated hard X-ray pulse, and optical variations modulated on the beat frequency. However, it also shows spin modulated polarisation and a photometric orbital variation in the red part of the optical spectrum, typical of AM Hers and indicative of a magnetic field strength stronger than in typical IPs. Also, unusually for an IP system, PQ Gem has an observable soft X-ray component with a flux that is modulated with the spin period and that contains a narrow "dip" feature. These dip features are seen quite often in the X-ray light curves of AM Her stars and are attributed to the obscuring of the accretion region by the gas stream very near the WD surface.

A.0.21 DQ Herculis

DQ Her was first studied as Nova 1934 Herculis, it is an eclipsing binary star, consisting of a WD and a late-type cool star presumed to be on the main sequence (Patterson (1994b)). The mass of the WD is about $0.60\pm 0.07 M_{\odot}$ and the secondary $0.40\pm 0.05\ M_{\odot}$ (Horne et al. (1993)). On the basis of photometric observation of its optical pulsations, Walker (1954 1956)) reported the then record-setting orbital period of 4hr 39min and also the bewildering 71s signal. Warner et al. (1972) noted that this signal showed significant and repeatable phase variations during eclipse ingress and egress, but it was Bath et al. (1974) and Lamb (1974) who first suggested the now-accepted magnetic rotator model for DQ Her, identifying the source of the 71s signal as the magnetic white dwarf primary's spin period, and the pulse itself as reprocessed radiation from the X-ray emitting accretion column sweeping the inner accretion disk. However recent investigations suggest that the true period must be 142s (Patterson (1994b), Zhang et al. (1995)). The optical pulsations in DQ Her are universally believed to be due to emission from the magnetic poles of the WD. However, there is no way for a pulsation to be seen if the magnetic axis and the spin axis are aligned; whether the optical pulsation is seen directly from the poles or as a result

of re-processing this beam from sides in an accretion disk, the magnetic and spin axes must be offset. This fact explains why the oblique rotator model has been adopted as a standard model for the DQ Her primary (Bath et al. (1974)). DQ Her is only very weakly detected in soft X-rays, and there is no evidence of pulsations in the X-rays. Most likely this is due to the accretion disk blocking a direct view of the WD, as would be expected in a system with an inclination this high, (i=86.5°; Horne et al. (1993)).

A.0.22 V533 Herculis

V533 Her is the stellar remnant of Nova Herculis 1963. Patterson (1979b) detected coherent photometric oscillations at 63.633s, but these oscillations have not been detected for some years now. Coherent oscillations suggest the presence of a rotating magnetised WD (Patterson (1994b)), making this a DQ Her star (or intermediate polar). However Thorstensen & Taylor (2000) report a spectroscopic orbital period for V533 Her of 0.147d (=3.53hr) and find that its spectrum intermittently shows symptoms of an SW Sextantis type star.

A.0.23 V795 Herculis

Historically V795 Her (PG1711+336) is a noneruptive 13th magnitude nova-like cataclysmic variable. Several spectroscopic periods, and one photometric period, have been observed in this system. The 2.6hr spectroscopic period places V795 Her inside the CV 'period gap', if interpreted as the binary orbital period. However there is an important feature with the apparent difference between this period and the 2.8hr photometric period. Shafter et al. (1990) and Zhang et al. (1991) conclude that the difference in periods supports an IP model, where the photometric modulation is related to the beat period between the orbital period and the (undetected) spin period. However, with the reported disappearance of this period by Patterson & Skillman (1994) the data may not support

the idea.

A.0.24 EX Hydrae

EX Hya was discovered by Kraft (1962) and quickly recognised as an eclipsing binary. It is a bright (V$\sim$ 13), high inclination (i=77° $\pm$ 1°), eclipsing IP with an orbital period of 98.26min and a WD spin period of 67.03min. The mass of the WD is measured by both dynamical (Hellier (1996)) and X-ray spectroscopic (Fujimoto & Ishida (1997)) methods to be $M_2 = 0.49 M_\odot$, while details of the accretion geometry are established by the optical and X-ray observations of Hellier et al. (1987)and Rosen et al. (1988). The secondary star is of spectral type M4$\pm$1 and is detected by its ellipsoidal modulation. Eisenbart et al. (2002) derived a distance of 65$\pm$11pc making EX Hydrae one of the closest cataclysmic variables with a known distance.

A.0.25 V2400 Oph

Buckley et al. (1995 1997) reported the first secure evidence for a diskless IP, with the discovery of the *R*OSAT source V2400 Oph (RX J1712.6-2414). They found that polarised light from the system varies at 927s, which is interpreted as the spin period of the magnetic dipole and thus of the WD. The X-rays, though, are pulsed at 1003s, which is the beat period between the 3.42hr orbital and 927s spin cycles, thus V2400 Oph shows the signature of pole-flipping accretion, as expected in a diskless IP. V2400 Oph is at a low inclination, estimated as 10° (Hellier & Beardmore (2002)). We only ever see the upper magnetic pole. The stream-fed accretion flips from pole to pole on the beat cycle. However, only $\sim$ 25% of the accreting material participates in this motion, the rest appears to be circling the WD.

A.0.26 LS Pegasi

LS Peg is an X-ray emitting CV with a low inclination and optical signatures of unusual stream flow. LS Peg (formerly known as S193), is a V=12th-14th magnitude CV with an orbital period of 4.2hr and an inclination of 30°. It has recently been proposed as an SW Sex star. Its X-ray light curve shows a low but constant count rate throughout its orbit which may be evidence for material thrown high above the disk by the disk-stream interaction or a magnetic accretion funnel sometimes suggested to explain other SW Sex stars (Szkody et al. (1997); Taylor et al. (1999); Martínez-Pais et al. (1999)). It also shows a large-amplitude (1700kms^{-1}) component in its radial velocity curve, absorption in the Balmer and He I lines at some phases, and quasiperiodic oscillations in its light curve at a period close to 20 minutes. Rodríguez-Gil et al. (2001) report on the discovery of variable polarisation in LS Peg. The observed modulation has an amplitude of $\sim$ 0.3% and a period of 29.6 minutes, which they assumed as the spin period of the magnetic WD. They also detected periodic flaring in the blue wing of Hβ, with a period of 35.5 minutes. The difference between both frequencies is just the orbital frequency, so they relate the 35.5min modulation to the *beat* between the orbital and spin period. They estimate a magnetic field strength of $B_1 \sim$ 5-15 MG. Their results indicate that magnetic accretion plays an important role in SW Sex stars, and they suggest that these systems are probably intermediate polars with the highest mass accretion rates. Taylor et al. (1999) also identify LS Peg as a low-inclination SW Sex star. Their model suggests i=30°, and the observed absence of any photometric signal at the orbital frequency establishes $i<$ 60°. This constraint puts a severe strain on interpretations of the SW Sex phenomenon which rely on disk structures lying slightly out of the orbital plane.

A.0.27 GK Persei

GK Per (Nova 1901/A 0327+43) is one of a few old novae known to undergo dwarf nova outbursts. It was discovered as a classical nova system in 1901 when it outburst and reached a maximum of $V = 0.2$mag. As a close binary system GK Per has an unusually long orbital period, in fact the longest known orbital period for a classical nova at 1.997days (Crampton et al. (1986)). The system has a coherent 351s X-ray pulsation (Watson et al. (1985); Norton et al. (1988); Norton & Watson (1989); Ishida et al. (1992)) representing the spin period of the white dwarf that has also been detected in ultraviolet light curves. GK Per is also unique among classical nova in that it contains a WD primary with an evolved K2 sub giant secondary, with an estimated mass of $0.25M_{\odot}$ (Watson et al. (1985)). The mass of the WD is a subject of controversy as the inclination of GK Per is not well established. Estimates for the inclination range from 45° Cannizzo & Kenyon (1986) to 86° (Kim et al. 1992) but a common range is $60° - 73°$ giving an estimate for the WD mass at $0.9\pm0.2M_{\odot}$ Crampton et al. (1986). Despite a great deal of observations, many properties and physical parameters of GK Per are not well understood. The nature of the optical counterpart of the X-ray periodicity, the orbital inclination and/or the mass of the primary, the nature of the optical outburst, for example, are still subjects of debate.

A.0.28 AO Piscium

The X-ray source AO Psc (H2252-035) was identified with a 13th magnitude cataclysmic variable by Griffiths et al. (1980). Persistent modulation at optical wavelength with a period of 859s and a binary orbital period of 3.59hr were found (Warner et al. (1981) Patterson & Price (1981)). X-ray pulsations with a period of 805s were detected by White & Marshall (1981)from X-ray light curves, and a small optical modulation (0.02-0.04 mag) at the X-ray period was identified by Warner et al. (1981). In the presently favoured model

of the system, the X-ray and optical pulsations at 805s period come from the vicinity of the spinning WD, while the optical modulation at the beat period of 859s arises from the reprocessing of X-ray flux into optical emission from a region of the system co-rotating with the orbital period. The reprocessing region could be the atmosphere of the companion star (Patterson & Price (1981)) or a hot spot where the accretion column from the companion star strikes the disk (Hassall et al. (1981)).

A.0.29 HZ Puppis

HZ Pup (also know as N Pup 1963 No 1) was identified as a fast nova by C.Hoffmeister (1964), with a maximum brightness of m_{pg}=7.7. In 1994 March and 1995 February, Abbott & Shafter (1997) observed HZ Puppis as part of a program of photometric period searches among old novae. HZ Pup appeared to be an IP whose light curve displayed an exceptionally rich selection of photometric periodicities arising from spin and orbital variations and beating between the two. They then went on to clearly state that HZ Pup was actually an IP, as they had identified three signals in the light curves as the spin period of the magnetic WD and two orbital sidebands. They also postulated that possible signals also detected could be a further two sidebands. The frequency separation of the three unambiguous signals implied an orbital period for the system of 5.11±0.03hr. They proposed that the true nature of the system may only be revealed by a concentrated campaign of time series spectroscopy.

A.0.30 VZ Pyxidis

Kato & Nogami (1997) observed VZ Pyx (H0857-242), a suspected intermediate polar, during a bright outburst in 1996 May. Time resolved CCD photometry revealed superhumps with a period of 0.07576 ±(0.00003)d, confirming the SU UMa-type nature of the object. Unlike other intermediate polars, the superhump and outburst properties of VX Pyx are

quite similar to those of non-magnetic dwarf novae, (de Martino et al. (1992); Remillard et al. (1994)), suggesting a minor effect of global magnetism on the outburst mechanism of this system. The orbital period of 1.78±0.09hr, which is well below the CV period gap, and the existence of a bright, superoutburst-like outburst (Remillard et al. (1994)) make VZ Pyx a good candidate for an SU UMa-type dwarf nova, although no known IPs below the period gap has been shown to exhibit superoutbursts or superhumps. Photometric variations (Remillard et al. (1994)), also seem to occur at a period $\sim$ 2940s, which may be the spin period of a magnetic WD. If VZ Pyx is really proven to be an IP by future detection of X-ray pulses, this system might provide a unique opportunity to investigate what mechanisms regulate the accretion process and disk instabilities in magnetic dwarf novae.

A.0.31 WX Pyxidis

WX Pyx was discovered in the *Einstein* Galactic plane X-ray survey. It aquired its name on the 71st Namelist of Variable Stars Kazarovets et al. (1993). O'Donoghue et al. (1996) presented optical observations of WX Pyx and showed that it has a choerent period of 1557.5±0.02s. The existence of this period was discovered by Koen & O'Donoghue (1995), but only a few cycles were observed. Photometric analysis by O'Donoghue et al. (1996) revealed a large amplitude signal, as well as its first harmonic at a period of 26min. The most probable cause is that it is the WD spin period, or the sideband period. The XMM Newton data of Schlegel (2005) indicated a spin period of 1557.3s. With the strength of the spin component relative to the $\omega \pm \Omega$ components suggesting that disk accretion occurs in WX Pyx given the weak orbital modulation Norton et al. (1996), but must be confirmed. The weak orbital modulation indicates probably also a low inclination system. If the estimated period of $\sim$19933s is confirmed, then the $P_{\rm spin}/P_{\rm orb}$ ratio is $\sim$0.08. They

found provisional evidence for an orbital period of ~0.25-0.4d in their photometry and spectroscopy, but a more reliable determination is needed. To date however the spin and orbital periods remain unconfirmed.

A.0.32 V1223 Sagittari

V1223 Sgr is among the brightest X-ray magnetic cataclysmic variables in the 1-10keV band. It was identified as the optical counterpart of the X-ray source 4U 1849-31 by Steiner et al. (1981). Photometric observations showed that this object varies with a 3.36hr period and has a 794.38s optical beat period. This feature, as well as the star's optical spectrum, are very similar to those of AO Psc (Patterson & Price (1981)). Using *EXOSAT*, Osborne et al. (1985) discovered a 745.6s X-ray pulsation. The difference between the optical and X-ray oscillation frequencies is equal to the orbital frequency of the binary system. Spectroscopy shows it to be a typical cataclysmic variable with strong emission lines superposed on a blue continuum. UV observations by Bonnet-Bidaud et al. (1982) using *IUE* show a spectrum consistent with that expected from an optically thick accretion disk and allow them to estimate a distance of 600pc from the ultraviolet interstellar extinction.

A.0.33 V697 Scorpii

Nova Scorpii 1941 was discovered by Margaret Mayall on objective prism plates at a photometric magnitude of 10.2 (Mayall 1947), it is faint at V~20 and is situated in a star-crowded region. The orbital period determined from optical photometry by Warner & Woudt (2002), gives $P_{\rm orb}$= 4.49hr. The spin period at 11916s puts V697 Sco as an asynchronous magnetic rotator with a high $P_{\rm spin}/P_{\rm orb}$ ratio, similar to EX Hydrae and V1025 Centauri, but at a much larger orbital period.

A.0.34 V1062 Tauri

With the assistance of X-ray positions from the *HEAO 1* Modulation Collimator and the Large-Area Sky Survey, Remillard et al. (1994) made the discovery of V1062 Tauri (H0459+246). It was observed optically during faint states ($V\sim16$), in which there were spectral features of both an accretion disk and a K star. The light curves in the V and I bands were consistent with ellipsoidal variations in the secondary star with a binary period of 9.952hr. X-ray observations with *EXOSAT* revealed a strong pulsation with a period ~62 mins, which confirmed an intermediate polar classification for V1062 Tau. The long orbital period opens up the possibility that V1062 Tau is a relatively young IP that might evolve into a polar.

A.0.35 V381 Velorum

The optical counterpart of this X-ray source RX J1016.9-4103 was identified by Greiner & Schwarz (1998). They estimated the orbital period to be 2.23hrs. Tovmassian et al. (2004) carried out a complete orbital coverage, which allowed them to conclude that the system has two accreting poles and after folding the data they were in strong favour of this orbital period and a spin period of the WD of 7320s. The spin to orbital period ratio is therefore 0.910 and they believed this to be a polar that is not synchronised. In contrast, Norton et al. (2004a) believed it to be an IP in the process of attaining synchronism and evolving into a polar.

A.0.36 RX J0944.5+0357

The source RX J0944.5+0357(=1RXS J094432.1+035738), in the constellation Sextans, was observed spectroscopically by Jiang et al. (2000).Mennickent et al. (2002) from further spectroscopic studies determined the orbital period $P_{\rm orb}$=3.581hr as reported to them by

Thorstensen and Fenton. Woudt & Warner (2003a) determined from the FT of their entire data set from high speed photometry that RX J0944.5+0357 is of quite low inclination as no power at the spectroscopic period or its first harmonic were seen. Mennickente *et al.* proposed that the inclination probably lies within the range $30° - 60°$ to which Woudt and Warner conclude that it is probably more the lower end of this range. Their FT also determined the best spin period to be 2162s. RX J0944.5+0357 is most probably an IP with a highly variable two-pole accretion. Quantitatively it is similar to FO Aqr and TV Col, however it most resembles YY Dra (as it has a double-humped light curve).

A.0.37 1RXS J154814.5-452845

Haberl et al. (2002) reported the identification of the *ROSAT* All-Sky Survey source 1RXSJ154814.5-452845 as a new intermediate polar. The source shows pulsations with a period of 693s both in the optical and X-ray light curves and the detection of a beat frequency strongly suggests that this is the rotation period of the WD. Although the one day aliasing and the sparse optical data coverage does not allow the orbital period to be identified unambiguously, the most likely values of 9.37hr and 6.72hr add 1RXSJ154814.5-452845 to the intermediate polars with the longest orbital period known. The optical spectrum displays features from the late type secondary and shows the presence of broad absorption lines at Hβ and higher order Balmer lines which may be a signature of the WD atmosphere, very similar to V709 Cas (RXJ0028.8+5917 (Bonnet-Bidaud et al. 2001a)). The average X-ray spectrum as obtained by the EPIC instruments on board XMM-Newton shows hard emission but also the presence of soft blackbody-like emission similar to that seen from soft intermediate polars and thought to arise from the WD surface heated by the hard X-rays.

A.0.38 RX J0153.3+7446

Haberl & Motch (1995a) reported on the discovery of RX J0153.3+7446, detected during the ROSAT Galactic Plane Survey project Motch et al. (1991) characterized by hard ROSAT spectra. It has $P_{\rm spin}$=1414s and $P_{\rm orb}$=3.94hr.

A.0.39 RX J1039.7-0507

RX J1039.7-0507 is a weak *ROSAT* X-Ray source in the constellation of Sextans that was identified as a V=18.5 CV star by Appenzeller et al. (1998) on the basis of positional agreement and an emission line spectrum. Woudt & Warner (2003c) showed from high speed photometry that the variable star has an orbital period of 1.574hr. The system has a nearly sinusoidal photometric modulation with a range of 1.1mag which they interpreted as the reflection effect caused by a very hot WD primary. It has in addition periodic signals at 1932.5s and 721.9s which, with the aid of other periods present at low amplitude is interpreted as an orbital sideband and the first harmonic of the primary's spin period. It is therefore an IP with a spin period of 1444s.

A.0.40 RX J2133.7+5107

Bonnet-Bidaud *et al.* (2005) reported the first time-resolved photometric and spectroscopic optical observation of RX J2133.7+5107. The source was discovered from the ROSAT Galactic Plane Survey and identified as a reletively bright ($m_B \sim 16$) CV Motch et al. (1998). Bonnet-Bidaud *et al.* (2005) found the spin period to be 570.823±0.013s and the orbital period to be 7.193±0.016hr. It is a unique IP as the orbital period is in the middle of the (6-10)hr IP gap and shows a significant degree of asynchronism with a ratio of $P_{\rm spin}/P_{\rm orb}$ of 0.02. It has a probable inclination of $\lesssim 45°$ with a WD mass of M_{WD}= (0.6 -1)$M_\odot$ and a secondary star mass of M_s *gtrsim* (0.27 - 0.37)$M_\odot$.

A.0.41 HS0943+1404

Rodríguez-Gil et al. (2005) identified HS0943+1404 in the Hamburg Quasar Survey. They found an orbital period of 4.17hr from time-resolved photometry and a spin period of 4150.26S from time-resolved spectroscopy, giving a spin to orbit ratio of $\simeq$0.3. This ratio and the long orbital period is very unusual compared to the other known IPs. Rodríguez-Gil et al. (2005) photometry also showed that HS0943+1404 enters into deep ($\sim$ 3mag) low states, suggesting that the system is a true "intermediate" polar that will eventually synchronise.

A.0.42 Recently discovered IPs

1RXS J063631.9+353537, 1RXS J070407.9+262501, 1RXS J173021.5-055933 and 1RXS J180340.0+401214 have all been recently identified as IPs using a combined X-ray (ROSAT) / infrared (2MASS) target selection that discriminates against background AGN by Gänsicke et al. (2005). 1RXS J063631.9+353537 has an orbital period of $P_{\rm orb} \simeq$ 201min and a spin period of $P_{\rm spin}$ = 1008.3408s. The orbital period of 1RXS J070407.9+262501 is $P_{\rm orb} \simeq$ 250min with a spin period of $P_{\rm spin}$ = 480.708s. 1RXS J173021.5-055933 has $P_{\rm orb}$ = 925.27min, with $P_{\rm spin}$ = 128.0s and 1RXS J180340.0+401214 has an orbital period $P_{\rm orb}$ = 160.21min with the spin period being $P_{\rm spin}$ = 1520.51s. Other than this, nothing is yet known of these systems.

APPENDIX B

RXTE and ASCA Data Reduction

B.1 Archival data from *RXTE* and *ASCA*

All mission data from both RXTE and ASCA is archived at the Laboratory for High Energy Astrophysics at NASA Goddard Space Flight Center. The data is freely available for download over the internet via front-end web pages.

The extraction of data from the archives involves a number of programs specifically designed for each satellite. The following section gives some background behind the programs, a brief overview of the programs used and the structure for obtaining lightcurves.

FTOOLS

Ftools is the main program that holds the many sub programs used to extract the lightcurves and spectra from the X-ray satellite data. It is a collection of utility programs used to create, examine, or modify the contents of FITS data files, it forms the core of the HEASARC software system for reducing and analysing data in FITS format. FITS stands for 'Flexible Image Transport System' and is the standard astronomical data format endorsed by both NASA and the IAU and is primarily designed to store scientific

data sets consisting of multi-dimensional arrays (1-D spectra, 2-D images or 3-D data cubes) and 2-dimensional tables containing rows and columns of data.

Each FTOOLS task is a separate program that performs a single simple operation. The FTOOLS are primarily a Unix based package, although a Windows version was created. Scripts are available for combining several FTOOLS to perform complex tasks. All of the core FTOOLS programs share several common design features:

- All are written in ANSI Fortran or C;
- All use a simple standardised subroutine interface for getting the value of program parameters (e.g., the name of the input FITS file);
- All data I/O is restricted to FITS files via the FITSIO (a library of C and Fortran subroutines for reading and writing data files in FITS data format) subroutine interface (or to simple ASCII format in certain cases).
- All scripts are written in Perl5 (The 5(.004) release of Perl - a high-level programming language)
- The GUI (graphical user interfaces) tools are written in Tcl/Tk [(Tool Command Language)/(graphical user interface toolkit)]: Currently there are fv (an interactive FITS file browser/editor), flaunch (a powerful GUI interface to the FTOOLS), and xdf (the XTE Data Finder).

These design decisions have resulted in a software package that is exceptionally portable and can be integrated into new environments with a minimum of modification to the source code.

B.2 *RXTE* data reduction

The Basic Scheme

Between receiving RXTE data from the ground station and sending the data to Guest Observers, the XTE Science Data Center (XSDC) converts the data to FITS format, arranges the FITS files into a hierarchical set of directories and performs a set of standard calibrations. Also produced at this stage are filter files which contain the time-histories of various parameters in reference to which good data can be identified and screened.

RXTE data reduction involves first navigating the directory structure with the GUI-driven program XDF (XTE Data Finder) to identify the files which contain the data you want to reduce. Next, the user manipulates the FITS files by a set of tasks. Using a filter file for the observation a list is produced of good time intervals based on various selection criteria applied. At this stage, filters can be specified to single out parts of the good data. The final step is to apply the good time intervals and extract data products (light curves or spectra) through the filters. These products can be read into the appropriate data analysis programs (e.g. XRONOS, XSPEC - or any others equipped to handle the formats).

Xselect may be used to perform most of these tasks for reducing data in PCA Standard 2 configuration.

The reduction process

The user obtains an auxiliary directory of tools (available as a small tar file), places it in the working directory, and runs the script as outlined below.

1. un-tar the raw data obtained from the HEASARC website.

2. run **xtefilt** to produce an updated filter file; this filter file will be put in the pro-

posal/ObsId/stdprod/ directory, named with the suffix ".xfl", and listed in the standard products index file (the FIST... file) for that ObsId; An XTE filter file contains most of the housekeeping data deemed useful for creating Good Time Interval (GTI) files to filter unwanted events from XTE science data.

3. make a directory for the ObsId in both the aux directory (for file lists, GTIs, background files, etc.) and in the working directory (for resulting light curves and spectra); compile a list of Standard2 files by dumping FIPC index file;

4. run **maketime** to produce a list of Good Time Intervals (GTI) to be extracted; it uses the filter file; the result is checked for good time, and if no time fits those criteria;

5. run **pcabackest** to produce modelled background data for each Standard 2 file found in the ObsId/pca/ directory's index file; use the background models listed in aux/model.txt and the SAA history file there; the output background files go into the aux/ObsId directory along with a list of all files successfully created;

6. run **saextrct** to produce spectra and/or lightcurves for source and background files (assuming GTI and background files were created successfully) using the defaults below*;

7. next the data has to be converted from fits lightcurves to ASCII data.

8. the background data then needs to be subtracted.

9. finally the user may examine the data with a plotting package that reads ASCII data, such as **qdp**.

*Default extraction criteria::

The default extracted products are light curves and spectra extracted from the PCA Standard 2 data using:

- layer 1 only, for better signal to noise;
- PCUs 0, 1, and 2, since PCUs 3 and 4 go on and off regularly;
- absolute channels 0 to 27 (light curves only), or approximately 1-10 keV for epoch 3 data.

and times when:

- the Earth elevation angle is greater than 10 degrees (bright Earth effects have been seen near 5 degrees, thus the conservative cut);
- the pointing offset is less than 0.02 degrees;
- the time since the peak of the last SAA passage is greater than 30 minutes;
- the electron contamination is less than 0.1.

These criteria are the conservative cuts the GOF and PCA team recommend to ensure the best background subtraction and highest signal to noise in the data. Any of them can be changed to suit specific analysis situations. It's recommended to examine the data carefully to be sure than no spurious effects creep in.

B.3 *ASCA* data reduction

The Basic Scheme

Between receiving ASCA data from ISAS and sending the data to Guest Observers, the ASCA Guest Observer Facility (GOF) converts the data to FITS format and performs a set of standard calibrations. Also produced at this stage are mkf files, which contain the time-histories of various parameters to which good data can be referenced, identified and screened. The name mkf comes from the program mkfilter used to produce the files.

ASCA data reduction, as performed by GOs, involves the manipulation of these FITS files by a set of tasks - FTOOLS, which can be called from XSELECT by higher level tasks.

When screening data, XSELECT consults the events data files and the accompanying mkf files to produce a list of selected good time intervals (GTI). These good time intervals are used for extracting a list of screened events (in the same FITS format as before). The final stage, when the GO is happy with the screening, is the filtering (spatial, temporal or spectral) of the events list, which is then binned and projected appropriately for extraction, as data products in their own FITS formats. The products, usually spectra, light curves, or images, can be read into the data analysis programs XSPEC, XRONOS and XIMAGE, respectively, or into any others equipped to handle these formats. Since many of the basic XSELECT commands required to clean data are repetitive, a script called ascascreen has been produced to take care of this task. ascascreen is the usual starting point in the reduction of ASCA data.

The reduction process

The user obtains an auxiliary directory of tools (available as a small tar file), places it in the working directory, and runs the script as outlined below.

The data files which contain events detected by ASCA have three key properties:

- They are in FITS format.
- They are time-ordered events lists.
- Each file contains data from only one of the four instruments and in only one instrument mode.

Note that different methods to the script may be used, this is just a guideline used to reduce ASCA data, other programs that the user is more accustomed to may be substituted where appropriate.

GIS reduction and SIS reduction

SIS data reduction is similar to that for GIS except that some of the following prompts are appropriate to that instrument only (as indicated).

- First make a set of directories: crv, evt, flt, log and spc, in the obsID directory to house files created further in the script.
- un-tar the raw data obtained from the HEASARC website
- run **ascascreen** to generate cleaned data to create a script that can be fed to xselect.

  You will then be asked for the following prompts:

  1. Enter data directory:
  2. Which instrument do you want to process?
  3. Enter product filename root [xsel]
  4. Which Bit Rates do you want to use?
  5. Enter Maximum allowed angular deviation [0.01 recommended]:
  6. Enter minimum elevation angle [5-10 recommended]
  7. Enter angle from Bright Earth [20-40 recommended]: (SIS ONLY)
  8. Enter minimum cutoff rigidity [6 recommended]:
  9. Enter PIXL rejection threshold [50 recommended]: (SIS ONLY)
  10. Start up SAOimage, and remain in XSELECT at the end? (y/n):
  11. Remove ring and calibration source? (y/n): (GIS ONLY)
  12. Use Rise Time window background rejection? (y/n): (GIS ONLY)
  13. Remove hot and flickering pixels? (y/n): (SIS ONLY)
  14. Select based on grade (this will keep only grades 0,2,3 and 4)?: (SIS ONLY)

- run **saoimage** - a program for displaying astronomical images to identify the source region and background region
- run **xselect** - this will examine the event files (source and background files), and filters them to include events of intrest, then creates data product for further analysis. A simple text file can be written and fed to the xselect commmand to perform all these tasks.
- **filter region ../flt/(g2s/s0s).reg** - uses the region created earlier in the script (source region).
- **filter region ../flt/(g2b/s0b).reg** - uses the region created earlier in the script (background region)
- do **fkeyprint** on both the source and background data. looks for a specified keyword(s) in the header of the input FITS file(s). When the keyword is found it is printed out to the requested output ASCII format file.
- create a program suitable to convert fits lightcurves to ASCII data and run on both the source and background data.
- create a program that will then subtract the background data from the source.
- The data may then be examined using **qdp**, a plotting package that reads the ASCII lightcurve data.

B.3.1 *RXTE* data reduction in comparison with *ASCA* Data Reduction

Data Files

Both ASCA and RXTE data files are in FITS format. Where appropriate, the keywords are identical and follow the same OGIP standards. However, there are several differences:

- RXTE datasets are generally larger. Mostly because of the higher temporal resolution, typical RXTE datasets are about 100 times bigger than typical ASCA datasets.
- RXTE data files contain either regularly accumulated arrays or event-by-event bitmasks. Neither format used in ASCA (except for the little-used GIS MPC mode).
- RXTE data files are arranged in a hierarchical directory structure. RXTE has more subsystems and instruments than ASCA and its observations are more likely to be split up. Accordingly, a hierarchical directory structure was devised to keep better order of individual files - unlike the case with ASCA.

REFERENCES

Abbott, T. M. C. & Shafter, A. W. 1997, in ASP Conf. Ser. 121: IAU Colloq. 163: Accretion Phenomena and Related Outflows, 679

Allan, A., Hellier, C., & Ramseyer, T. F. 1996a, MNRAS, 282, 699

Allan, A., Horne, K., Hellier, C., et al. 1996b, MNRAS, 279, 1345

Appenzeller, I., Thiering, I., Zickgraf, F.-J., et al. 1998, ApJS, 117, 319

Ashoka, B. N., Marar, T. M. K., Seetha, S., Kasturirangan, K., & Bhattacharyya, J. C. 1995, A&A, 297, L83

Barrett, P., O'Donoghue, D., & Warner, B. 1988, MNRAS, 233, 759

Baskill, D., Wheatley, P., & Osborne, J. 2005, MNRAS, 000, 000

Bastian, T. S., Dulk, G. A., & Chanmugam, G. 1988, ApJ, 324, 431

Bath, G. T., Evans, W. D., & Pringle, J. E. 1974, MNRAS, 166, 113

Beardmore, A. P., Mukai, K., Norton, A. J., Osborne, J. P., & Hellier, C. 1998, MNRAS, 297, 337

Beardmore, A. P., Osborne, J. P., & Hellier, C. 2000, MNRAS, 315, 307

Berg, C., Wegner, G., Foltz, C. B., Chaffee, F. H., & Hewett, P. C. 1992, ApJS, 78, 409

Bildsten, L. 1998, in NATO ASIC Proc. 515: The Many Faces of Neutron Stars., 419

Bildsten, L., Chakrabarty, D., Chiu, J., et al. 1997, ApJS, 113, 367

Bonnet-Bidaud, J. M., Mouchet, M., de Martino, D., Matt, G., & Motch, C. 2001a, A&A, 374, 1003

—. 2001b, A&A, 374, 1003

—. 2001c, A&A, 374, 1003

Bonnet-Bidaud, J. M., Mouchet, M., & Motch, C. 1982, A&A, 112, 355

Bowden, C. C. G., Bradbury, S. M., Chadwick, P. M., et al. 1992, Astroparticle Physics, 1, 47

Bradt, H. V., Rothschild, R. E., & Swank, J. H. 1993, A&As, 97, 355

Bradt, H. V. D. & McClintock, J. E. 1983, ARAA, 21, 13

Bruch, A. 1991a, A&A, 251, 59

—. 1991b, A&A, 251, 59

Buckley, D. A. H., Cropper, M., Ramsay, G., & Wickramasinghe, D. T. 1998a, MNRAS, 299, 83

—. 1998b, MNRAS, 299, 83

Buckley, D. A. H., Haberl, F., Motch, C., et al. 1997, MNRAS, 287, 117

Buckley, D. A. H., Sekiguchi, K., Motch, C., et al. 1995, MNRAS, 275, 1028

Buckley, D. A. H. & Sullivan, D. J. 1992, in ASP Conf. Ser. 29: Cataclysmic Variable Stars, 387

Buckley, D. A. H. & Tuohy, I. R. 1989, ApJ, 344, 376

Burwitz, V., Reinsch, K., Beuermann, K., & Thomas, H.-C. 1996, A&A, 310, L25

Cannizzo, J. K. & Kenyon, S. J. 1986, ApJ Lett, 309, L43

Casares, J., Mouchet, M., Martinez-Pais, I. G., & Harlaftis, E. T. 1996, MNRAS, 282, 182

Charles, P., Thorstensen, J., Bowyer, S., & Middleditch, J. 1979, ApJ Lett, 231, L131

Chincarini, G. & Walker, M. F. 1981, A&A, 104, 24

Choi, C., Dotani, T., & Agrawal, P. C. 1999, ApJ, 525, 399

Cooke, B. A., Ricketts, M. J., Maccacaro, T., et al. 1978, MNRAS, 182, 489

Corbet, R. H. D. 1986, MNRAS, 220, 1047

Crampton, D., Fisher, W. A., & Cowley, A. P. 1986, ApJ, 300, 788

Cropper, M., Wu, K., & Ramsay, G. 2000, New Astronomy Review, 44, 57

de Jager, O. C., Meintjes, P. J., O'Donoghue, D., & Robinson, E. L. 1994, MNRAS, 267, 577

de Martino, D., Gonzalez-Riestra, R., Rodriguez, P., et al. 1992, IAU Circ, 5481, 2

de Martino, D., Matt, G., Mukai, K., et al. 2002, in Astronomical Society of the Pacific Conference Series, 143

de Martino, D., Mouchet, M., Bonnet-Bidaud, J. M., et al. 1995a, A&A, 298, 849

—. 1995b, A&A, 298, 849

—. 1995c, A&A, 298, 849

Downes, R. A., Webbink, R. F., Shara, M. M., et al. 2001, PASP, 113, 764

Duerbeck, H. W. 1987, Space Science Reviews, 45, 1

Eisenbart, S., Beuermann, K., Reinsch, K., & Gänsicke, B. T. 2002, A&A, 382, 984

Eracleous, M. 1999, in Astronomical Society of the Pacific Conference Series, 343

Eracleous, M., Horne, K., Robinson, E. L., et al. 1994, ApJ, 433, 313

Friedjung, M. 1997, New Astronomy, 2, 319

Fujimoto, R. & Ishida, M. 1997, ApJ, 474, 774

Gänsicke, B. T., Marsh, T. R., Edge, A., et al. 2005, MNRAS, 361, 141

Gierliński, M. & Done, C. 2002, MNRAS, 331, L47

Greiner, J. & Schwarz, R. 1998, A&A, 340, 129

Griffiths, R. E., Lamb, D. Q., Ward, M. J., et al. 1980, MNRAS, 193, 25P

Haberl, F. & Motch, C. 1995a, A&A, 297, L37

—. 1995b, A&A, 297, L37

Haberl, F., Motch, C., & Zickgraf, F.-J. 2002, A&A, 387, 201

Haberl, F., Throstensen, J. R., Motch, C., et al. 1994, A&A, 291, 171

Halpern, J. P. & Patterson, J. 1987, ApJ Lett, 312, L31

Harlaftis, E. T. & Horne, K. 1999, MNRAS, 305, 437

Harvey, D., Skillman, D. R., Patterson, J., & Ringwald, F. A. 1995, PASP, 107, 551

Hasinger, G. 1994, in AIP Conf. Proc. 308: The Evolution of X-ray Binariese, 611

Hasinger, G. & van der Klis, M. 1989, A&A, 225, 79

Hassall, B. J. M., Pringle, J. E., Ward, M. J., et al. 1981, MNRAS, 197, 275

Haswell, C. A., Patterson, J., Thorstensen, J. R., Hellier, C., & Skillman, D. R. 1997, ApJ, 476, 847

Hayakawa, S. 1985, physrep, 121, 317

Hellier, C. 1991, MNRAS, 251, 693

—. 1993, MNRAS, 264, 132

Hellier, C. 1996, in ASSL Vol. 208: IAU Colloq. 158: Cataclysmic Variables and Related Objects, 143

—. 1997a, MNRAS, 288, 817

—. 1997b, MNRAS, 291, 71

—. 1999, ApJ, 519, 324

—. 2000, New Astronomy Review, 44, 131

Hellier, C. & Beardmore, A. P. 2002, MNRAS, 331, 407

Hellier, C., Beardmore, A. P., & Buckley, D. A. H. 1998, MNRAS, 299, 851

Hellier, C., Beardmore, A. P., & Mukai, K. 2002a, A&A, 389, 904

Hellier, C., Cropper, M., & Mason, K. O. 1991, MNRAS, 248, 233

Hellier, C., Garlick, M. A., & Mason, K. O. 1993, MNRAS, 260, 299

Hellier, C., Mason, K. O., Rosen, S. R., & Cordova, F. A. 1987, MNRAS, 228, 463

Hellier, C., Mukai, K., Ishida, M., & Fujimoto, R. 1996, MNRAS, 280, 877

Hellier, C. & Robinson, E. L. 1994, ApJ Lett, 431, L107

Hellier, C., Wynn, G. A., & Buckley, D. A. H. 2002b, MNRAS, 333, 84

Horne, K. & Marsh, T. R. 1986, MNRAS, 218, 761

Horne, K., Welsh, W. F., & Wade, R. A. 1993, ApJ, 410, 357

Howell, S. B., Sirk, M. M., Ramsay, G., et al. 1997, ApJ, 485, 333

Hutchings, J. B., Crampton, D., Cowley, A. P., Thorstensen, J. R., & Charles, P. A. 1981, ApJ, 249, 680

Ikhsanov, N. R. 2000, aa, 358, 201

—. 2001, A&A, 374, 1030

Ishida, M., Sakao, T., Makishima, K., et al. 1992, MNRAS, 254, 647

Israel, G. L., Angelini, L., Campana, S., et al. 1998, MNRAS, 298, 502

Israel, G. L., Covino, S., Polcaro, V. F., & Stella, L. 1999, A&A, 345, L1

Jablonski, F. & Steiner, J. E. 1987, ApJ, 323, 672

James, C. H., Ramsay, G., Mark Cropper, M. C., & Branduardi-Raymont, G. 2002, MNRAS, 336, 550

Jiang, X. J., Engels, D., Wei, J. Y., Tesch, F., & Hu, J. Y. 2000, A&A, 362, 263

Joy, A. H. 1954, ApJ, 120, 377

Kahabka, P. & van den Heuvel, E. P. J. 1997, ARAA, 35, 69

Kaitchuck, R. H., Schlegel, E. M., Honeycutt, R. K., et al. 1994, ApJS, 93, 519

Kalogera, V. & Webbink, R. F. 1996, ApJ, 458, 301

—. 1998, ApJ, 493, 351

Kaluzny, J. & Semeniuk, I. 1988, Informational Bulletin on Variable Stars, 3145, 1

Kamata, Y., Tawara, Y., & Koyama, K. 1991, ApJ Lett, 379, L65

Kato, T. & Nogami, D. 1997, PASJ, 49, 481

Katysheva, N. A. & Pavlenko, E. P. 2003, Astrophysics, 46, 114

Kazarovets, E. V., Samus, N. N., & Goranskij, V. P. 1993, Informational Bulletin on Variable Stars, 3840, 1

Kemp, J., Patterson, J., Thorstensen, J. R., et al. 2002, PASP, 114, 623

King, A. R. 1988, QJRAS, 29, 1

—. 1993, MNRAS, 261, 144

King, A. R. & Wynn, G. A. 1999, MNRAS, 310, 203

Koen, C. & O'Donoghue, D. 1995, ApJS, 101, 347

Kolb, U. 1996, in ASSL Vol. 208: IAU Colloq. 158: Cataclysmic Variables and Related Objects, 433

Kopylov, I. M., Lipovetsky, V. A., Somov, N. N., Somova, T. A., & Stepanian, J. A. 1988, Astrofizika, 28, 287

Kraft, R. P. 1962, ApJ, 135, 408

Kunze, S., Speith, R., & Hessman, F. V. 2001, MNRAS, 322, 499

Lamb, D. Q. 1974, ApJ Lett, 192, L129

Larwood, J. 1998, MNRAS, 299, L32

Leibowitz, E. M., Retter, A., & Kovo-Kariti, O. 1997, in ASSL Vol. 218: Astronomical Time Series, 215

Lewin, W. H. G., van Paradijs, J., & Taam, R. E. 1993, Space Science Reviews, 62, 223

Liller, W., Pearce, A., Stubbings, R., & Jones, A. 1999, IAU Circ, 7242, 1

Lipkin, Y. M., Leibowitz, E. M., & Orio, M. 2004, MNRAS, 349, 1323

Littlefair, S. P., Dhillon, V. S., & Marsh, T. R. 2001, MNRAS, 327, 669

Liu, Q. Z., van Paradijs, J., & van den Heuvel, E. P. J. 2000, A&As, 147, 25

Lubow, S. H. 1991, ApJ, 381, 268

Lyke, J. E., Gehrz, R. D., Woodward, C. E., et al. 2001, Aj, 122, 3305

Maraschi, L., Treves, A., & van den Heuvel, E. P. J. 1976, NAT, 259, 292

Marsh, T. R. 2001, LNP Vol. 573: Astrotomography, Indirect Imaging Methods in Observational Astronomy, 573, 1

—. 2005, APSS, 296, 403

Marsh, T. R. & Duck, S. R. 1996, New Astronomy, 1, 97

Marsh, T. R. & Horne, K. 1988, MNRAS, 235, 269

Marshall, F. E., Boldt, E. A., Holt, S. S., et al. 1979, ApJS, 40, 657

Martínez-Pais, I. G., Rodríguez-Gil, P., & Casares, J. 1999, MNRAS, 305, 661

Mason, C. G., Gehrz, R. D., Woodward, C. E., et al. 1996, ApJ, 470, 577

Mason, K. O. 1997, MNRAS, 285, 493

Mason, K. O., Watson, M. G., Ponman, T. J., et al. 1992, MNRAS, 258, 749

Mateo, M., Szkody, P., & Garnavich, P. 1991, ApJ, 370, 370

Mauche, C. W. 1999, ApJ, 520, 822

McArthur, B. E., Benedict, G. F., Lee, J., et al. 2001a, ApJ, 560, 907

—. 2001b, ApJ, 560, 907

McHardy, I. M., Pye, J. P., Fairall, A. P., & Menzies, J. W. 1987, MNRAS, 225, 355

McHardy, I. M., Pye, J. P., Fairall, A. P., et al. 1982, IAU Circ, 3687, 1

—. 1984, MNRAS, 210, 663

Meintjes, P. J. 2002, MNRAS, 336, 265

Meintjes, P. J., de Jager, O. C., Raubenheimer, B. C., et al. 1994, ApJ, 434, 292

Meintjes, P. J. & Venter, L. A. 2005, MNRAS, 360, 573

Mennickent, R. E., Tovmassian, G., Zharikov, S. V., et al. 2002, A&A, 383, 933

Mirabel, I. F. & Rodriguez, L. F. 1998, Nature, 392, 673

Motch, C. 1981, A&A, 100, 277

Motch, C., Belloni, T., Buckley, D., et al. 1991, A&A, 246, L24

Motch, C., Guillout, P., Haberl, F., et al. 1998, A&A Suppl., 132, 341

Motch, C., Haberl, F., Guillout, P., et al. 1996, A&A, 307, 459

Mouchet, M., Bonnet-Bidaud, J. M., Buckley, D. A. H., & Tuohy, I. R. 1991, A&A, 250, 99

Mukai, K., Ishida, M., & Osborne, J. P. 1994, PASJ, 46, L87

Munari, U., Zwitter, T., & Bragaglia, A. 1997, A&As, 122, 495

Muno, M. P., Remillard, R. A., & Chakrabarty, D. 2002, ApJ Lett, 568, L35

Murray, J. R. & Armitage, P. J. 1998, MNRAS, 300, 561

Murray, J. R., Chakrabarty, D., Wynn, G. A., & Kramer, L. 2002, MNRAS, 335, 247

Nakano, S., Takamizawa, K., Kushida, Y., et al. 1995, IAU circ, 6133, 1

Negueruela, I., Reig, P., & Clark, J. S. 2000, A&A, 354, L29

Norton, A. J., Beardmore, A. P., Allan, A., & Hellier, C. 1999, A&A, 347, 203

Norton, A. J., Beardmore, A. P., & Taylor, P. 1996, MNRAS, 280, 937

Norton, A. J., Hellier, C., Beardmore, A. P., et al. 1997, MNRAS, 289, 362

Norton, A. J., McHardy, I. M., Lehto, H. J., & Watson, M. G. 1992a, MNRAS, 258, 697

Norton, A. J., Quaintrell, H., Katajainen, S., et al. 2002, A&A, 384, 195

Norton, A. J., Somerscales, R. V., & Wynn, G. A. 2004a, in ASP Conf. Ser. 315: IAU Colloq. 190: Magnetic Cataclysmic Variables, 216–+

Norton, A. J. & Watson, M. G. 1989, MNRAS, 237, 853

Norton, A. J., Watson, M. G., & King, A. R. 1988, MNRAS, 231, 783

Norton, A. J., Watson, M. G., King, A. R., Lehto, H. J., & McHardy, I. M. 1992b, MNRAS, 254, 705

—. 1992c, MNRAS, 254, 705

Norton, A. J., Wynn, G. A., & Somerscales, R. V. 2004b, ApJ, 614, 349

O'Donoghue, D., Koen, C., & Kilkenny, D. 1996, MNRAS, 278, 1075

Osaki, Y. 1989, PASJ, 41, 1005

Osborne, J. P., Rosen, R., Mason, K. O., & Beuermann, K. 1985, Space Science Reviews, 40, 143

Paczynski, B. 1976, in IAU Symp. 73: Structure and Evolution of Close Binary Systems, 75

Patterson, J. 1979a, ApJ, 234, 978

—. 1979b, ApJ, 234, 978

—. 1994a, PASP, 106, 209

—. 1994b, PASP, 106, 209

Patterson, J. 1999, in Disk Instabilities in Close Binary Systems, 61

Patterson, J., Branch, D., Chincarini, G., & Robinson, E. L. 1980, ApJ Lett, 240, L133

Patterson, J. & Halpern, J. P. 1990, ApJ, 361, 173

Patterson, J., Kemp, J., Richman, H. R., et al. 1998, PASP, 110, 415

Patterson, J., Kemp, J., Saad, J., et al. 1997, PASP, 109, 468

Patterson, J. & Price, C. M. 1981, ApJ Lett, 243, L83

Patterson, J. & Richman, H. 1991, PASP, 103, 735

Patterson, J., Schwartz, D. A., Pye, J. P., et al. 1992, ApJ, 392, 233

Patterson, J. & Skillman, D. R. 1994, PASP, 106, 1141

Patterson, J. & Steiner, J. E. 1983, ApJ Lett, 264, L61

Patterson, J., Thorstensen, J. R., Vanmunster, T., et al. 2004, PASP, 116, 516

Penning, W. R. 1985, ApJ, 289, 300

Penning, W. R., Schmidt, G. D., & Liebert, J. 1986, ApJ, 301, 881

Plavec, M. & Kratochvil, P. 1964, Bulletin of the Astronomical Institutes of Czechoslovakia, 15, 165

Poyner, G. 2001, Journal of the British Astronomical Association, 111, 350

Rana, V. R., Singh, K. P., Schlegel, E. M., & Barrett, P. 2004, AJ, 127, 489

Rappaport, S., Verbunt, F., & Joss, P. C. 1983, ApJ, 275, 713

Reinsch, K. 1994, A&A, 281, 108

Reinsch, K. & Beuermann, K. 1994, aa, 282, 493

Remillard, R. A., Bradt, H. V., Brissenden, R. J. V., et al. 1994, ApJ, 428, 785

Retter, A., Hellier, C., Augusteijn, T., et al. 2003, MNRAS, 340, 679

Retter, A., Leibowitz, E. M., & Kovo-Kariti, O. 1996, IAU Circ, 6527, 2

—. 1998, MNRAS, 293, 145

Revnivtsev, M., Lutovinov, A., Suleimanov, V., Sunyaev, R., & Zheleznyakov, V. 2004, A&A, 426, 253

Ritter, H. 1990, A&As, 85, 1179

Ritter, H. 1996, in NATO ASIC Proc. 477: Evolutionary Processes in Binary Stars, 223

Ritter, H. & Kolb, U. 1998, A&AS, 129, 83

—. 2005, VizieR Online Data Catalog, 1, 2018

Rodríguez-Gil, P., Casares, J., Martínez-Pais, I. G., Hakala, P., & Steeghs, D. 2001, ApJ letter, 548, L49

Rodríguez-Gil, P., Casares, J., Martínez-Pais, I. G., & Hakala, P. J. 2002, in ASP Conf. Ser. 261: The Physics of Cataclysmic Variables and Related Objects, 533

Rodríguez-Gil, P., Gänsicke, B. T., Hagen, H.-J., et al. 2005, A&A, 440, 701

Rodríguez-Gil, P. & Potter, S. B. 2003, MNRAS, 342, L1

Rosen, S. R., Mason, K. O., & Cordova, F. A. 1988, MNRAS, 231, 549

Rosen, S. R., Mason, K. O., Mukai, K., & Williams, O. R. 1991, MNRAS, 249, 417

Schlegel, E. M. 1999, in Astronomical Society of the Pacific Conference Series, 60

Schlegel, E. M. 2005, A&A, 433, 635

Schmidt, G. D., Harris, H. C., Liebert, J., et al. 2003, ApJ, 595, 1101

Schmidtke, P. C. 1988, AJ, 95, 1528

Schrijver, J., Brinkman, A. C., van der Woerd, H., Watson, M. G., & King, A. R. 1985, Space Science Reviews, 40, 121

Schwartz, D. A., Fabbiano, G., Griffiths, R. E., et al. 1979, AJ, 84, 1560

Schwarz, R., Schwope, A. D., Staude, A., et al. 2004, in ASP Conf. Ser. 315: IAU Colloq. 190: Magnetic Cataclysmic Variables, 230

Schwope, A. D. 1995, Reviews of Modern Astronomy, 8, 125

Shafter, A. W., Robinson, E. L., Crampton, D., Warner, B., & Prestage, R. M. 1990, ApJ, 354, 708

Silber, A. D., Anderson, S. F., Margon, B., & Downes, R. A. 1996, AJ, 112, 1174

Skillman, D. R. 1996a, PASP, 108, 130

—. 1996b, PASP, 108, 130

Smale, A. P., Mason, K. O., White, N. E., & Gottwald, M. 1988, MNRAS, 232, 647

Solheim, J.-E. 1995, Baltic Astronomy, 4, 363

Spruit, H. C. & Ritter, H. 1983, A&A, 124, 267

Steeghs, D. 1996, Masters Thesis, 4

Steiner, J. E., Schwartz, D. A., Jablonski, F. J., et al. 1981, ApJ Lett, 249, L21

Still, M. D., Duck, S. R., & Marsh, T. R. 1998, MNRAS, 299, 759

Szkody, P., Armstrong, J., & Fried, R. 2000, PASP, 112, 228

Szkody, P., Garnavich, P., Holberg, J., Silber, A., & Pastwick, L. 1997, AJ, 113, 2276

Szkody, P., Nishikida, K., Erb, D., et al. 2002, AJ, 123, 413

Szkody, P., Nishikida, K., Long, K. S., & Fried, R. 2001, AJ, 121, 2761

Taff, L. G., Lattanzi, M. G., Bucciarelli, B., et al. 1990, ApJ Lett, 353, L45

Tanaka, Y., Inoue, H., & Holt, S. S. 1994, PASJ, 46, L37

Taylor, C. J., Thorstensen, J. R., & Patterson, J. 1999, PASP, 111, 184

Taylor, P., Beardmore, A. P., Norton, A. J., Osborne, J. P., & Watson, M. G. 1997, MNRAS, 289, 349

Thorstensen, J. R., Ringwald, F. A., Wade, R. A., Schmidt, G. D., & Norsworthy, J. E. 1991, AJ, 102, 272

Thorstensen, J. R. & Taylor, C. J. 2000, MNRAS, 312, 629

Tovmassian, G., Zharikov, S., Mennickent, R., & Greiner, J. 2004, in ASP Conf. Ser. 315: IAU Colloq. 190: Magnetic Cataclysmic Variables, 15

Tovmassian, G. H., Greiner, J., Kroll, P., et al. 1998, A&A, 335, 227

Tuohy, I. R., Buckley, D. A. H., Remillard, R. A., Bradt, H. V., & Schwartz, D. A. 1986, ApJ, 311, 275

Ultchin, Y., Regev, O., & Wynn, G. A. 2002, MNRAS, 331, 578

Urpin, V., Konenkov, D., & Geppert, U. 1998, MNRAS, 299, 73

Uslenghi, M., Bergamini, P., Catalano, S., Tommasi, L., & Treves, A. 2000, A&A, 359, 639

van den Heuvel, E. P. J. & Rappaport, S. 1987, in IAU Colloq. 92: Physics of Be Stars, 291–307

van der Klis, M. 1998, in NATO ASIC Proc. 515: The Many Faces of Neutron Stars., 337

van Paradijs, J. 1983, in Accretion-Driven Stellar X-ray Sources, 231

Walker, M. F. 1954, PASP, 66, 230

—. 1956, ApJ, 123, 68

Warner, B. 1995a, Cataclysmic variable stars (Cambridge Astrophysics Series, Cambridge, New York: Cambridge University Press, —c1995)

—. 1995b, APSS, 226, 187

—. 1995c, APSS, 225, 249

Warner, B., Odonoghue, D., & Fairall, A. P. 1981, MNRAS, 196, 705

Warner, B., Peters, W. L., Hubbard, W. B., & Nather, R. E. 1972, MNRAS, 159, 321

Warner, B. & Woudt, P. A. 2002, PASP, 114, 1222

Warner, B., Woudt, P. A., & Pretorius, M. L. 2003, MNRAS, 344, 1193

Watson, M. G., King, A. R., & Osborne, J. 1985, MNRAS, 212, 917

Watts, D. J., Giles, A. B., Greenhill, J. G., Hill, K., & Bailey, J. 1985, MNRAS, 215, 83

Webbink, R. F., Rappaport, S., & Savonije, G. J. 1983, ApJ, 270, 678

Welsh, W. F., Horne, K., & Gomer, R. 1993, ApJ Lett, 410, L39

—. 1995, MNRAS, 275, 649

—. 1998, MNRAS, 298, 285

West, S. C., Berriman, G., & Schmidt, G. D. 1987, ApJ Lett, 322, L35

White, N. E. 1994, in AIP Conf. Proc. 308: The Evolution of X-ray Binariese, 53

White, N. E. & Marshall, F. E. 1981, ApJ Lett, 249, L25

Whitehurst, R. 1988a, MNRAS, 233, 529

—. 1988b, MNRAS, 232, 35

Wickramasinghe, D. T. & Ferrario, L. 2000, PASP, 112, 873

Wijnands, R. 2001, Advances in Space Research, 28, 469

Wood, M. A., Montgomery, M. M., & Simpson, J. C. 2000, ApJ Lett, 535, L39

Woudt, P. A. & Warner, B. 2002, MNRAS, 335, 44

—. 2003a, APSS, 288, 573

—. 2003b, MNRAS, 339, 731

—. 2003c, MNRAS, 339, 731

Woudt, P. A. & Warner, B. 2004, in ASP Conf. Ser. 315: IAU Colloq. 190: Magnetic Cataclysmic Variables, 39

Wynn, G. A., King, A. R., & Horne, K. 1997, MNRAS, 286, 436

Yazgan, E. & Balman, Ş. 2002, in Astronomical Society of the Pacific Conference Series, 177

Zhang, E., Robinson, E. L., Ramseyer, T. F., Shetrone, M. D., & Stiening, R. F. 1991, ApJ, 381, 534

Zhang, E., Robinson, E. L., Stiening, R. F., & Horne, K. 1995, ApJ, 454, 447

Zhang, W., Giles, A. B., Jahoda, K., et al. 1993, in Proc. SPIE Vol. 2006, p. 324-333, EUV, X-Ray, and Gamma-Ray Instrumentation for Astronomy IV, Oswald H. Siegmund; Ed., 324–333

Zharikov, S. V., Tovmassian, G. H., & Echevarría, J. 2002, A&A, 390, L23

Zharikov, S. V., Tovmassian, G. H., Echevarría, J., & Cárdenas, A. A. 2001, A&A, 366, 834

Zuckerman, B., Becklin, E. E., McLean, I. S., & Patterson, J. 1992, ApJ, 400, 665